

Quantum Computation and Simulation with Trapped Ions

Dissertation Submitted to

Tsinghua University

in partial fulfillment of the requirement

for the degree of

Doctor of Philosophy

in

Physics

by

ZHANG Xiang

Dissertation Supervisor: Associate Professor Kim Kihwan

June 2015

Quantum Computation and Simulation with Trapped Ions

by

ZHANG Xiang

Submitted to the Institute for Interdisciplinary Information Sciences
in partial fulfillment of the requirements for the degree of

Doctor of Philosophy

at

TSINGHUA UNIVERSITY

June 2015

© TSINGHUA UNIVERSITY 2015. All rights reserved.

Author

Institute for Interdisciplinary Information Sciences

April 20, 2015

Certified by

Kim Kihwan

Associate Professor

Thesis Supervisor

Quantum Computation and Simulation with Trapped Ions

by

ZHANG Xiang

Submitted to the Tsinghua University
on April 20, 2015, in partial fulfillment of the
requirements for the degree of
Doctor of Philosophy

Abstract

Trapped ion quantum system is one of the most promising architectures for the realization of a universal quantum computer mainly because of its high fidelity of fundamental operations, long coherence of qubits, and scalability for the large quantum system. With current techniques, it already shows great capabilities of demonstrations for quantum computation algorithms and quantum simulation models. To explore and study these important features in our experiment platform, I built a $^{171}\text{Yb}^+$ trapped-ion system that are capable of high fidelity quantum operations and great controllability based on our integrated control system.

Several fundamental and important experiments about quantum computation and simulation are demonstrated with our system. We first explore the hyperfine levels of a single $^{171}\text{Yb}^+$ ion with microwaves and take a experimental test of quantum contextuality. We test the state-dependent version as well as the state-independent version of Kochen-Specker inequalities. It's the first time to test quantum contextuality in a 3-level indivisible system without detection loophole. The successful observation of experimental violation of Kochen-Specker inequalities shows quantum contextuality is rooted in the fundamental structure of quantum mechanics.

After this, with the key technique of multi-fold microwaves, we achieve full controllability over the Hilbert space spanned by all of the four internal states. We make an experimental quantum simulation of “unphysical” operations beyond the regime of unitary and dissipative evolutions through the embedding quantum simulator

scheme. Our experiment demonstrates new direction of quantum simulation by successfully realizing the fundamental useful anti-linear operations such as the complex conjugate and symmetry operations, whose implementations in a quantum device were considered to be impossible due to the linear character of quantum mechanics.

For a higher degree of control in quantum regime, motional degrees of freedom are then added to our system with stimulated Raman transitions implemented by a mode-locked pulsed laser. With this new functionality, we make an experimental quantum simulation of interacting bosonic and fermionic quantum field modes, which reveals interesting features such as self interactions, particle creation and annihilation and non-perturbative regimes. Our experimental scheme is a scalable approach and can be extended beyond the limit of classical computation of quantum field theory when more fermions and bosons are included.

Dissertation Supervisor: Associate Professor Kim Kihwan

Acknowledgments

This is the acknowledgements section. You should replace this with your own acknowledgements.

THIS PAGE INTENTIONALLY LEFT BLANK

Contents

Contents	XIV
List of Figures	XIX
List of Tables	XXI
1 Introduction	1
1.1 Quantum computation and simulation	2
1.2 Quantum algorithms and physical implementations	5
2 Trapped-ion system	11
2.1 Trap system	14
2.1.1 Principle of Paul ion trap	14
2.1.2 Construction of 4-rod trap	17
2.1.3 Characterization of helical resonator	20
2.2 Vacuum system	21
2.2.1 Preparation of UHV	21
2.2.2 Estimation of background gas collision rates	26
3 Daily operations of trapped ions	33

3.1	Main optical transitions of trapped ion	34
3.2	Ionization and “load”	37
3.3	Doppler cooling and optical pumping	39
3.4	State detection	42
3.5	Excess micromotion compensation	44
3.6	Laser frequency stabilization	46
4	Quantum manipulation of trapped ions	55
4.1	Quantum dynamics of a trapped ion	56
4.1.1	Quantum picture of a trapped ion	56
4.1.2	Interaction Hamiltonian	57
4.2	Microwave system	61
4.3	Raman laser system	65
4.3.1	Stimulated Raman transition	65
4.3.2	Mode-locked pulse laser	69
4.3.3	Sideband cooling	79
5	Control system	87
5.1	Equipment control	89
5.2	Data acquisition	93
5.3	Waveform generation	97
5.4	Software architecture	98
6	Experimental tests of quantum contextuality	103
6.1	Quantum contextuality	103
6.2	State-independent experimental test	106
6.3	Experimental measurements	108

7	Quantum simulation of symmetry operations	117
7.1	Majorana equation and “unphysical” operation	119
7.2	Realization of embedding quantum simulator	124
7.3	Experimental procedures	130
7.3.1	Stimulated Raman couplings	131
7.3.2	Mapping between original and enlarged spaces	132
7.3.3	Quasi-quantum treatment of the momentum	135
7.3.4	Physical observables	135
7.3.5	Diagonal operators in the momentum space	136
7.3.6	Off-diagonal operators in the momentum space	138
7.3.7	Charge conservation and charge conjugation	141
7.4	Experimental results	143
7.4.1	Majorana dynamics	143
7.4.2	Symmetry operations	149
7.5	Conclusion	151
8	Quantum simulation of quantum field theory	153
8.1	Quantum field theory simulation	154
8.2	Experimental results	160
9	Conclusion and outlook	167
A	Control software	169
A.1	Code snippets	169
A.2	Software screenshots	181
B	Quantum contextuality experimental data	185

C Ququad Operations	199
Bibliography	214

List of Figures

2.0.1 Picture of a trapped-ion system in CQI. We can see ion pump, Ti sublimation pump, DC voltage filter box, microwave horn, magnetic coil, helical resonator, observation tubes and some lens mounted in 3D transition stages around the trap.	13
2.1.1 Diagram of a linear 4-rod Paul trap.	14
2.1.2 4-rod trap and vacuum chamber used in CQI.	18
2.1.3 Finding the best match of ceramic tubes pair.	19
2.2.1 Design of our vacuum system.	22
2.2.2 Assembling of vacuum system in Autodesk Inventor.	23
2.2.3 Vacuum pumps and big oven for baking ion trap and other vacuum components.	24
2.2.4 Effective potential and inelastic collisions.	28
3.1.1 Hyperfine structures and optical transitions of the main optical cycle.	34
3.2.1 Loading and trapping of $^{171}\text{Yb}^+$ ions. Yb atoms are ionized and Doppler cooled by laser beams. A chain of 23 ions are observed with CCD camera.	38
3.3.1 Relevant $^{171}\text{Yb}^+$ level diagrams of 369.5 nm laser and 935 nm laser.	40
3.3.2 Optical paths for 369.5 nm laser.	41

3.4.1 PMT counts before and after optical pumping.	42
3.4.2 Diagram of detection system with CCD and PMT.	43
3.4.3 Image of trapped ions. The distance between two adjacent ions in first image is around 10 μm . The second image shows ions' crystal structure.	44
3.6.1 Picture of the Iodine lock system.	47
3.6.2 Diagram of cavity and Iodine laser stabilization.	48
3.6.3 Graph for EOM frequency sweep, with a step of 0.1 MHz.	52
4.1.1 Resonant transitions between ion's motional levels.	59
4.2.1 Microwave transitions and state detection of $^{171}\text{Yb}^+$	62
4.2.2 Zeeman levels' resonant frequencies. The zero point of vertical axis is 12.642812118466 GHz. Dots are experimental data and solid lines are fitted curves.	64
4.2.3 Rabi flopping from $ 1\rangle \rightarrow 2\rangle$. The data is averaged over 1000 repeated experiments. Points or bars are real data, while dark solid lines are fitted curves.	65
4.3.1 Raman transition in a three level system.	66
4.3.2 Raman transition between ion's motional levels.	68
4.3.3 Diagram of optical paths for 355 nm pulse laser.	71
4.3.4 Frequency difference generated by pulse laser's frequency comb.	73
4.3.5 Polarization configurations of different Raman beams. The first po- larization setup does not drive a transition between $ 1\rangle \leftrightarrow 3\rangle$	75
4.3.6 Raman spectrum depending on the frequency of AOM2.	77

4.3.7 Raman spectrum of carrier transition, first blue sideband transitions and first red sideband transitions. We can see the two different trap modes along X and Y axis.	78
4.3.8 Carrier transitions (cyan), first blue sideband transitions (blue) and first red sideband transitions (red).	80
4.3.9 Diagram of sideband cooling. Dashed lines and dotted lines stand for optical pumping transitions. Solid lines stand for red sideband transitions.	81
4.3.10 Performance of sideband cooling with different estimation of maximal phonon numbers.	84
4.3.11 Heating rate measurement after sideband cooling. The solid line is fitted curve.	85
5.1.1 Left figure shows a 24 ports pulse sequencer on top of the RF switches box it controls. Right figure shows the inside FPGA board designed by Dizmitry.	89
5.1.2 Example sequence file for microwave experiments.	92
5.1.3 Time sequence diagram for the sequence file in Fig. 5.1.2.	93
5.2.1 The main control program written in LabVIEW.	94
5.2.2 Screen shot of lab temperature website.	96
5.4.1 Diagram of IonTrap package written in Mathematica.	100
6.0.1 Microwave operations for qutrit system.	104
6.1.1 Simultaneously measurement & contextuality	105
6.2.1 State-independent measurement basis and orthogonal relationships.	107
6.2.2 The $^{171}\text{Yb}^+$ ion system and the measurement scheme.	109
6.3.1 State-independent test of the KS inequalities for a qutrit system.	115

7.2.1 Schematic of the EQS.	127
7.3.1 Microwave Raman transition	133
7.3.2 Text excluding the matrix	144
7.4.1 Global phase effect	145
7.4.2 Orthogonality non-preservation	146
7.4.3 Momentum <i>Zitterbewegung</i> and helicity conservation	146
7.4.4 Majorana dynamics.	147
7.4.5 Time reversal and charge conjugation.	150
8.1.1 Diagram of interactions between fermion, antifermion and bosons.	156
8.1.2 Diagram of QFT experiment.	158
8.1.3 Diagram of displacement operator with σ_+ polarization Raman beams. 159	
8.2.1 Experimental data of self-interaction process. Solid curve is theoretical simulation curve.	161
8.2.2 Experimental data of phonon number fitting at $t = 2/\omega_0$. The upper histogram is phonon number distribution. The lower data and curve are experimental data and theoretical curve of blue sideband time sweep.	162
8.2.3 Experimental data of pair annihilation process. Solid dots and hollow dots are data of two experiments. Solid curve is theoretical simulation curve.	163
8.2.4 Experimental data of non-perturbative regimes interaction process. Solid curve is theoretical simulation curve.	164
8.2.5 Experimental data of quantum field theory simulation.	165
A.2.1 Another picture of the main control program.	182

A.2.2 Automated data taking with Mathematica.	183
A.2.3 Data analysis and plot with Mathematica.	184

THIS PAGE INTENTIONALLY LEFT BLANK

List of Tables

3.1	All transition terms between ${}^2S_{1/2} \leftrightarrow {}^2P_{1/2}$	37
4.1	An example wave file of Ramsey interferometry measurement.	62
6.1	The pulse sequences to prepare initial states and unitary rotations. . .	110
B.1	Density matrices of the 12 initial states.	186
B.2	ψ_1	187
B.3	ψ_2	188
B.4	ψ_3	189
B.5	ψ_4	190
B.6	ψ_5	191
B.7	ψ_6	192
B.8	ψ_7	193
B.9	ψ_8	194
B.10	ψ_9	195
B.11	ρ_{10}	196
B.12	ρ_{11}	197
B.13	ρ_{12}	198

Chapter 1

Introduction

At the age that Moore's law almost reaches to its limit and already slows down, mainly due to quantum tunnelling [1]. Quantum computer becomes more and more important as one of the most optimistic solution to enhance or even replace current integrated-circuit technology based classical computer [2]. Not only because of its' ability to do reversible computation to minimize heat loss and maximize running speed [3], but also due to its intrinsically different working principle that provides unique new capabilities for computation such as Shor's factoring algorithm [4] and quantum simulation algorithms [5]. There are a lot of different physical systems that can be used as platforms to implement quantum computers, such as quantum optics, NMR (nuclear magnetic resonance) systems, trapped ions, quantum dots, optical lattices, NV centers in diamond, superconducting josephson-junctions, Rydberg atoms. Among them, trapped ion quantum computer system is one of the most promising architectures for a scalable, universal quantum computer mainly because of its high fidelity ($> 99.9\%$) of fundamental operations, long coherence of qubits [6], and scalability [7] for the large quantum system. With current techniques, it already

shows great capabilities of demonstrations for quantum computation algorithms and quantum simulation models.

1.1 Quantum computation and simulation

When Feynman first introduced the concept of quantum computer in his famous talk “Simulating Physics with Computers” [8], several experiments have just demonstrated that the predictions of quantum mechanics about EPR’s hypothetical paradox are correct, although relying on local realism loopholes [9]. The fact that no physical theory of local hidden variables can ever reproduce all of the predictions of quantum mechanics ensures quantum entanglement and contextuality to be the unique resource of quantum computation. Another fact that a classical computer needs exponential resource to simulate a system of many particles makes quantum simulation essential since it only requires quantum bits number similar to the number of particles [5].

A quantum bit or qubit, which describes a two state quantum system, is the basic information unit of quantum computation and simulation. A single qubit can be in a superposition of its two basis states unlike its classical analogue, while with a measurement it outcomes one of the basis states just like a classical bit. Except its measurement property, the qubit shares the same mathematical model with the polarized beam, thus can be represented as a complex coefficient linear combination of its two basis states $|0\rangle$ and $|1\rangle$:

$$|\psi\rangle = \alpha |0\rangle + \beta |1\rangle, |\alpha|^2 + |\beta|^2 = 1.$$

If we measure qubit ψ in its basis states, the probability that we get outcome $|0\rangle$ is

$|\alpha|^2$ and is $|\beta|^2$ for outcome $|1\rangle$. The concept of qubit can be naturally extended to qudit if we increase the number of basis states.

In similar situation to classical computation, there are a lot of computational equivalent models for quantum computation, including quantum Turing machines and quantum circuit families. The common philosophy behind all these models is to find and use a small complete set of basic quantum operations to build a full functional quantum computer without any possible loss of “quantum power”. Any quantum operation can be implemented or approximated by applying a sequence of operations from this finite set. So far within the quantum circuit model, after the experimentally realization of the quantum reversible version of the classically universal Toffoli gate, we already know that quantum computers can be at least as powerful as classical computers [10].

Just like a classical logic gate for digital circuits, the basic building block of quantum circuits is a quantum logic gate operating on a small number of qubits, which can be represented by unitary matrices. The simplest quantum gate is the single qubit gate, whose unitary property restricts it to be just a rotation on the Bloch sphere representation of a single qubit. The Pauli matrices represent single qubit gates that perform π radian rotations along X,Y or Z axis. The Hadamard gate is a π radian rotation along the angular bisector of X and Z axis. And the θ phase shift gate is a θ rotation along Z axis. Any single qubit gate can be decomposed into a sequence of single qubit gates along X,Y and Z axis, or can be approximated by a sequence of Hadamard gates and $\pi/8$ phase shift gates [11]. Among two qubit gates, The CNOT (controlled NOT) gate is the most important one. If the first qubit is $|1\rangle$, the CNOT gate performs the NOT operation (single qubit Pauli-X gate) on the second qubit, otherwise it does nothing. In standard computational basis $|00\rangle$, $|01\rangle$,

$|10\rangle$ and $|11\rangle$, it is represented by the matrix

$$\text{CNOT} = \begin{pmatrix} 1 & 0 & 0 & 0 \\ 0 & 1 & 0 & 0 \\ 0 & 0 & 0 & 1 \\ 0 & 0 & 1 & 0 \end{pmatrix}.$$

Arbitrary quantum gates acting on any number of qubits can be constructed or approximated to arbitrary precision with a small number of one and two qubits gates: single qubit gates and the CNOT gate [12]. So the Hadamard gate, the $\pi/8$ phase shift gate, and the CNOT gate, forms a simple but complete universal quantum gates set. A quantum computer with the capability of performing universal quantum gates can actually act as a universal quantum simulator. Applying the digital quantum simulation scheme, a quantum computer can simulate different kinds of evolution process by different quantum programs [13]. However, for specific problems, we can build much simpler problem-specific quantum machines, which are shipped with more specific and efficient quantum operations, or are even in an analog manner. Unlike digital quantum simulation, which uses a finite set of restricted quantum operations to construct quantum computation sequence, analog quantum simulation directly mimics arbitrary hamiltonian in an analog way. It's also known as continuous-variable quantum computation [14], from which we can measure physical observables after evolving the initial state with some Hamiltonian for some time.

1.2 Quantum algorithms and physical implementations

Quantum algorithms becomes really popular only after Peter Shor invented a polynomial time quantum algorithm for interger factorization [15]. Shor's algorithm actually acts as one of main motivations behind the huge investment on the development of quantum computers, because of its potential to break the widely used RSA cryptography system. No polynomial time integer factorization algorithms have been invented for classical computers yet [16]. Recently even a record of factoring a 232 decimal digits number (RSA-768) takes about 2 years with hundreds of powerful computers, with a highly optimized implementation of the best ever classical algorithm [17]. Meanwhile, it is estimated that a 1024-bit RSA key could be broken with only several thousands quantum logic qubits [18]. Shor's algorithm is based on the quantum Fourier transform (QFT), which takes only a polynomial number of quantum gates and acts as the basis of many important quantum algorithms including Deutsch-Jozsa boolean function judge algorithm, Simon's decision tree algorithm and hidden subgroup algorithms.

Another famous quantum algorithm is Grover's database search algorithm, which is proven to lead a quadratic speedup over all classical algorithms [19]. Grover's algorithm is based on amplitude amplification, which also acts as the basis of quantum counting algorithm. Other than these deterministic quantum algorithms, probabilistic quantum algorithms such as quantum random walks and quantum annealing contribute speedups to many practical problems, including a hard protein-folding problem which is solved by a commercial quantum processor [20]. Polynomial time quantum algorithms have been developed for simulating both Bosonic and Fermionic

systems, chemical processes, quantum field theory and even “unphysical” systems, with a claim that a few hundred qubits will beat the capabilities of current classical supercomputers [21].

There are a lot of different physical systems that can be used as platforms to implement quantum computers, such as quantum optics, NMR (nuclear magnetic resonance) systems, trapped ions, quantum dots, optical lattices, NV centers in diamond, superconducting Josephson-junctions, Rydberg atoms, as long as they can satisfy the requirements nowadays known as the DiVincenzo criteria [22]:

1. A scalable physical system with well-characterized qubits
2. The ability to initialize the state of the qubits to a simple fiducial state, such as $|00 \cdots 0\rangle$
3. Long coherence time, much longer than the gate operation time
4. An universal set of quantum gates
5. The ability to measure specific qubits.

Among them, trapped ion quantum computer system is one of the most promising architectures for a scalable, universal quantum computer. Not only because of the high fidelity ($> 99.9\%$) of fundamental operations, but also because of promising schemes in development to scale the system to arbitrarily large numbers of qubits, which include shuttling ions in an array of ion traps, building large entangled states via photons connected networks of remotely entangled ion chains, and combinations of these two ideas [7].

To explore and study these important features in experiment platform, I start my PhD training with building our own $^{171}\text{Yb}^+$ trapped-ion systems. They are the first

$^{171}\text{Yb}^+$ trapped-ion systems in China. Fancy techniques are so heavily improved in all areas related to trapped ions that an elaborated study of every single one will become a separated monograph. The contribution I make to trapped ions community in this building process actually starts from the “software” parts, which is mainly about quantum manipulation of trapped ions with our integrated control system.

Several fundamental and important experiments on quantum computation and simulation are demonstrated with these systems. We first explore the hyperfine levels of a single $^{171}\text{Yb}^+$ ion with microwaves and take a experimental test of quantum contextuality. We test the state-dependent version as while as the state-independent version of Kochen-Specker inequalities. It’s the first time that people test quantum contextuality in a 3-level indivisible system without detection loophole. The successful observation of experimental violation of Kochen-Specker inequalities shows quantum contextuality is rooted in the fundamental structure of quantum mechanics.

After this, with the key technique of multi-fold microwaves, we achieve full controllability over the Hilbert space spanned by all of the four internal states. We make an experimental quantum simulation of “unphysical” operations beyond the regime of unitary and dissipative evolutions through the embedding quantum simulator scheme. Our experiment demonstrates new direction of quantum simulation by successfully realizing the fundamental useful anti-linear operations such as the complex conjugate and symmetry operations, whose implementations in a quantum device was considered to be impossible due to the linear character of quantum mechanics.

For a higher degree of control in quantum regime, motional degrees of freedom are then added to our system with stimulated Raman transitions implemented by a mode-locked pulsed laser. With this new functionality, we make an experimental quantum simulation of interacting bosonic and fermionic quantum field modes, which

reveals interesting features such as self interactions, particle creation and annihilation and non-perturbative regimes. our experimental scheme is a scalable approach and can be extended beyond the limit of classical computation of quantum field theory when more fermions and bosons are included.

My thesis is organized as follows:

Chapter 2 is mainly the basic principle and construction procedures of a trapped-ion system related to the ion trap and vacuum system. Since there are very good references for almost all aspects about this, I will focus on how I build our trapped-ion system.

Chapter 3 is about daily operations we performed with our trapped-ion system, from ionization, Doppler cooling, optical pumping to state detection. Some related techniques, e.g. micromotion compensation and laser frequency stabilization, are also described.

Chapter 4 is about quantum manipulation of trapped ions. We start with the microwave system which only couples to ions' internal states. Later a Raman laser system is discussed based on a mode-locked pico-second pulse laser, which couples to both internal states and motional states. All these quantum manipulation systems and the basic trapped-ion system constitute most necessary setups for trapped-ion experiments.

Chapter 5 describes a detailed implementation of our integrated control system, which have integrated control over all these apparatus and provides a powerful software interface to experimentalists.

Chapter 6 is about experimental test of quantum contextuality with microwave operations. We experimentally observed state-dependent and state-independent violations of Kochen-Specker inequalities for the simplest indivisible quantum system manifesting quantum contextuality. We performed the experiment with a single

trapped $^{171}\text{Yb}^+$ ion, by mapping three ground states of the $^{171}\text{Yb}^+$ ion to a 3-level (qutrit) system and carrying out quantum operations by applying microwaves resonant to the qutrit transition frequencies.

Chapter 7 is about the first experimental quantum simulation of “unphysical” operations beyond the regime of unitary and dissipative evolutions through the embedding of the dynamics in the electronic multi-levels of an $^{171}\text{Yb}^+$ ion.

Chapter 8 is about experimental quantum simulation of interacting bosonic and fermionic quantum field modes with a trapped ion system, by manipulating a single $^{171}\text{Yb}^+$ ion’s 4 internal levels and motional states, with a Raman laser system.

Chapter 9 is the conclusion and outlook.

THIS PAGE INTENTIONALLY LEFT BLANK

Chapter 2

Trapped-ion system

A trapped-ion system uses the ion trap to cool down and trap ions while the ions' internal and motional quantum states are coherently manipulated by microwave or laser beams. Generally an ion trap is a manual designed combination of electric or magnetic fields that captures and confines ions in a free space region inside a vacuum system. Other than trapped ion quantum computers, ion traps have a number of important applications including mass spectrometer, precise measurement, and even world's most accurate atomic clocks [23]. Two common types of ion traps are the Penning trap and the Paul trap (quadrupole ion trap). When using ion traps for scientific studies of quantum state manipulation, the Paul trap is most often used [24].

In a trapped ion quantum computer, quantum bits are mainly stored in long-lived stable electronic levels of ions. A universal set of quantum gates is implemented with manipulating each ion's internal states and collective quantized motional states of ion chains. Multiple ions' entanglement are prepared through the Coulomb force interactions and can be measured and transmitted with high fidelity. Quantum

projection measurement is done by collecting quantized fluorescence photons from laser-induced emissions. The ultra high vacuum ($< 10^{-11}$ torr) and well designed harmonic trapping potential make trapped ions perfect pure quantum systems. Effective isolation from the outside environment noise and a rich set of operations make them constitute one of the most promising systems to implement scalable quantum computation and simulation.

Physically a trapped-ion experiment system consists of at least this two parts.

1. **Trap system** This part is the kernel of the system. All quantum operations happen here.
 - (a) Ion trap. 4-rod trap, blade trap, chip trap, etc.
 - (b) Atom oven. Atom beam source heated up by electricity or laser.
 - (c) RF helical resonator. Homemade RF amplifier with high output voltage for radial confinement.
 - (d) Filtered DC circuit. Controllable voltage source and DC filter for axial confinement and movement.

2. **Vacuum system** This part provides a well isolated environment with ultra-high vacuum (UHV, $10^{-9} \sim 10^{-12}$ mbar) and low background collision rate.
 - (a) Vacuum components. Vacuum chamber, flanges, copper gaskets, feed-through and vacuum gauges.
 - (b) Vacuum pumps. Mechanical rough pump, turbomolecular pump, Ti sublimation pump and ion pumps.
 - (c) Baking oven. A big oven to bake out waters and gases.

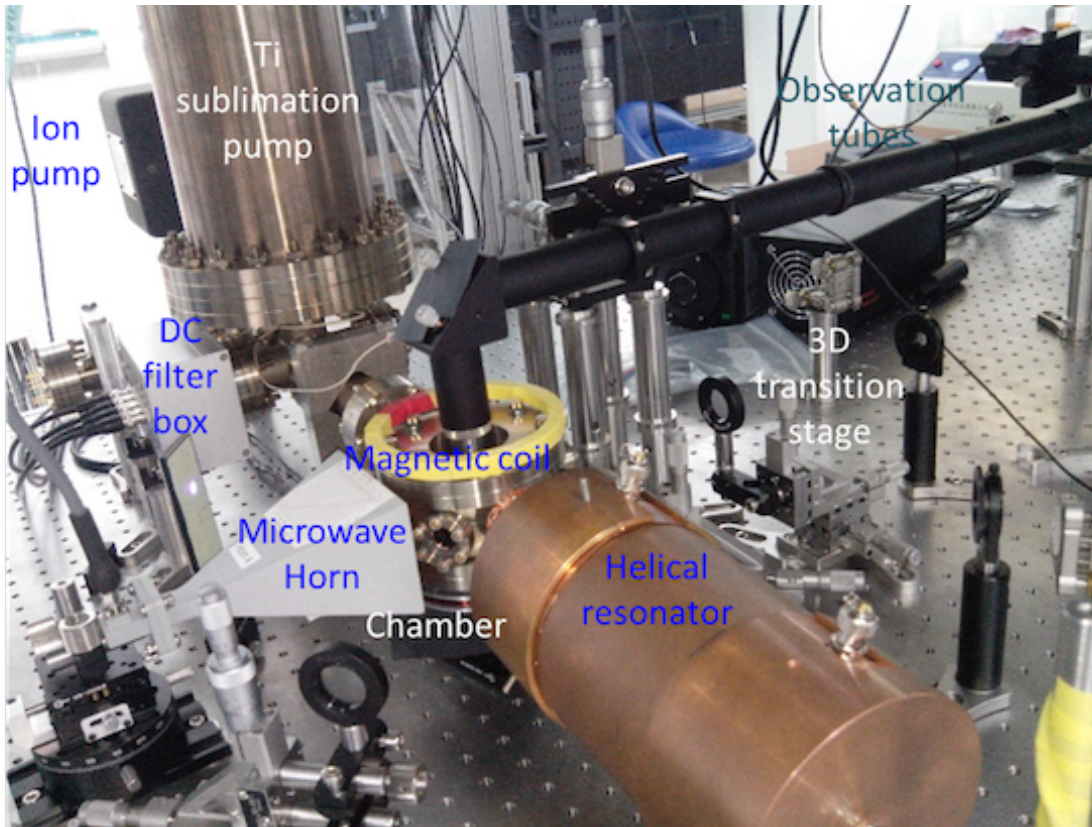


Figure 2.0.1: Picture of a trapped-ion system in CQI. We can see ion pump, Ti sublimation pump, DC voltage filter box, microwave horn, magnetic coil, helical resonator, observation tubes and some lens mounted in 3D transition stages around the trap.

All these sub systems constitute a basis for quantum manipulation of trapped ions. Fig. 2.0.1 shows a picture of the real using trapped-ion system in our Lab 3. In this chapter, we will mainly describe the basic construction of a trapped-ion system. More details about daily operations, quantum manipulation and related apparatus will be discussed in Chapter 3 and Chapter 4.

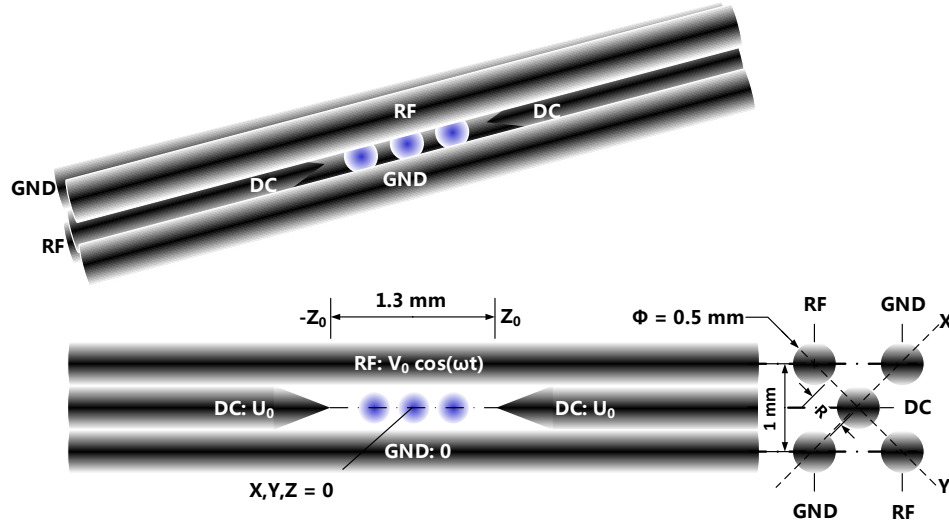


Figure 2.1.1: Diagram of a linear 4-rod Paul trap.

2.1 Trap system

We will start with an introduction of our 4-rod trap, which is the main experiment platform I'm working on. Later I will describe more details about realizing each part of this trap system.

2.1.1 Principle of Paul ion trap

The 4-rod trap is one kind of Paul linear trap. It uses 4 electrodes to form a rotating radio frequency field. The potential of the field can be described as a parabolic pseudo-potential on x, y plane, centered at origin point, which makes the ions elastically bound to z axis. And in the z direction, 2 electrodes are used to generate a static coulomb potential, in which ions are arranged into a string. The diagram of one linear 4-rod trap we used is showed in Fig. 2.1.1.

Near the axis of the trap, the total potential generated by these electrodes can

be written as

$$\begin{aligned}\Phi(x, y, z, t) &= U_0 \frac{1}{Z_0^2} (\alpha x^2 + \beta y^2 + \gamma z^2) \\ &+ V_0 \cos(\omega t) \frac{1}{2R^2} (\alpha' x^2 + \beta' y^2 + \gamma' z^2)\end{aligned}\tag{2.1.1}$$

when $\omega/2\pi > 100$ kHz and $|V_0| < 1000$ V. In free space the Laplace equation of any electrostatic potential must equal zero since charge density is zero in free space. The Laplace condition $\nabla^2\Phi = 0$ implies

$$\begin{aligned}\alpha + \beta + \gamma &= 0 \\ \alpha' + \beta' + \gamma' &= 0\end{aligned}$$

and in Paul trap case [6]

$$\begin{aligned}-(\alpha + \beta) &= \gamma < 0, \\ \alpha' + \beta' &= \gamma' = 0.\end{aligned}$$

The corresponding electric field is

$$\begin{aligned}\mathbf{E}(x, y, z, t) &= -\frac{\partial\Phi}{\partial\mathbf{u}} = -\frac{\gamma U_0}{Z_0^2} (2z\hat{z} - x\hat{x} - y\hat{y}) \\ &\quad -\alpha' V_0 \frac{x\hat{x} - y\hat{y}}{R^2} \cos(\omega t)\end{aligned}\tag{2.1.2}$$

The classical equations of motion of a ion with mass m and charge Q in this field can be decoupled in the spatial coordinates

$$m\ddot{u}_i = QE_i, i = x, y, z$$

The equation of motion along each axis can be rewritten as a Mathieu differential equation

$$\ddot{u}_i + (a_i + 2q_i \cos(\omega t)) \frac{\omega^2}{4} u_i = 0 \quad (2.1.3)$$

where

$$a_x = a_y = -\frac{1}{2} a_z = -\frac{4Q\gamma U_0}{mZ_0^2 \omega^2}$$

and

$$q_x = -q_y = \frac{2Q\alpha' V_0}{mR^2 \omega^2}, q_z = 0$$

As an example, substitute the physical parameters of our 4-rod trap

$$Q = e = 1.6 \times 10^{-19} \text{ C}$$

$$\gamma \approx 1$$

$$U_0 = 30 \text{ V}$$

$$m = \frac{171}{6.02} \times 10^{-23} \approx 2.84 \times 10^{-22} \text{ g}$$

$$Z_0 = \frac{1.3}{2} = 0.65 \text{ } \mu\text{m}$$

$$R = 0.5\sqrt{2} - 0.25 \approx 0.457 \text{ mm}$$

$$\alpha' \approx 1$$

$$V_0 \approx 500 \text{ V}$$

$$\omega = (2\pi) 12\text{MHz}$$

we have

$$a_x \approx 0.028, q_x \approx 0.474.$$

The lowest-order approximation stable solution [25] under the necessary condition

($|a_i|, q_i^2$) $\ll 1$ is

$$u_i(t) \approx A_i \cos(\beta_i \frac{\omega}{2} t + \phi_i) (1 + \frac{q_i}{2} \cos(\omega t)) \quad (2.1.4)$$

where $\beta_i \approx \sqrt{a_i + q_i^2/2}$. This motion solution consists of secular harmonic oscillation at frequency $\omega_i = \beta_i \omega / 2 \ll \omega$ and a fast, small oscillations called “micromotion”, which has the same frequency as the driven RF field. The average kinetic energy of the ion over a period of the secular harmonic oscillation is

$$E_i^{(k)} = \frac{1}{2} m \langle \dot{u}_i^2 \rangle \approx \frac{1}{4} m u_i^2 (\omega_i^2 + \frac{1}{8} q_i^2 \omega^2) \quad (2.1.5)$$

The energy of the secular motion can be reduced by laser cooling. As the amplitude A_i is reduced, the corresponding micromotion is also reduced with the same rate. In this case, ion’s motion can be approximated by only the harmonic oscillator with frequency ω_i . For our trap with above parameters, $\omega_x \approx (2\pi) 2.25$ MHz.

Up to now, we already learn the working principle of an “ideal” 4-rod trap. However the real experiment situation is more complex. More technique details in the real realization are described in following contents.

2.1.2 Construction of 4-rod trap

A near picture of our 4-rod trap and vacuum chamber is showed in Fig. 2.1.2.

We preprocess all 8 electrodes with electro chemical polishing for several minutes to remove rust and get a better cylinder shape. The heads of two DC electrodes in z direction are then ground to cones with sand papers. DC electrodes and RF electrodes are mounted with a pair of 5 holes ceramic tubes which are cut and drilled by laser machining. However, the machining quality is always a limitation of making a stable trap even with a perfect design. As an example of efforts to overcome this

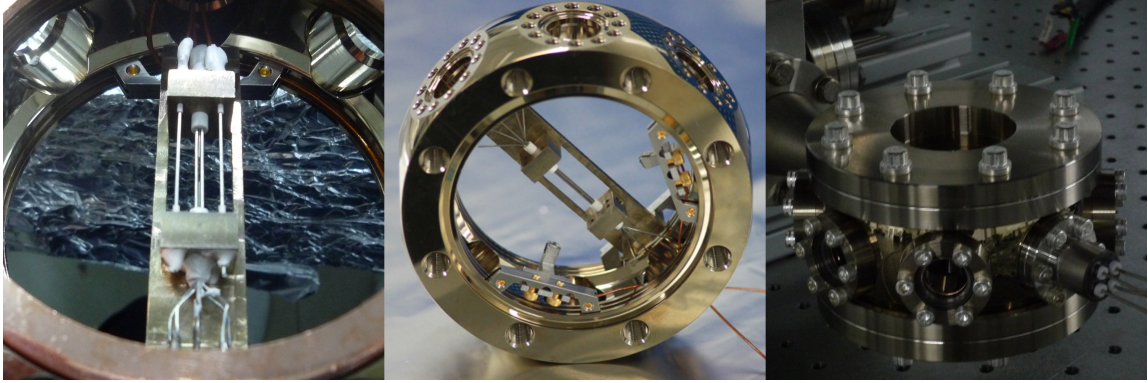


Figure 2.1.2: 4-rod trap and vacuum chamber used in CQI.

kind of limitation, we make a lot of ceramic tubes and only choose the best matched pair for the real use. We take pictures of all tubes' faces (Fig. 2.1.3) and then analyze them with a image processing program written in Mathematica.

The same program has also been used to recognize and fit Gaussian border of each ion within real-time ions crystal images. Usually we use a simulation software called "CPO3D" to simulate and verify the whole static field generated by all these electrodes.

Around the trap, 4 atomic ovens each filled with natural Yb, Yb 171, natural Ba and Ba 137 are mounted as atom sources. Currently most experiments are carried with only $^{171}\text{Yb}^+$ ions. When we load $^{171}\text{Yb}^+$ ion, a DC current of typically 3A is applied to the stainless steel tube with resistance $\sim 0.5 \Omega$. With this parameter, the ion will jump into the trap one by one. The DC current will turn on for several minutes until we finish loading.

In order to bring ion's equilibrium position back to trap's X-Y plane center, 2 extra cylindrical tungsten steel electrodes are added outside the trap to compensate the background electric field. We design the trap holder, atomic ovens and the whole trap assembling procedure with a 3D design software called "Autodesk Inventor".

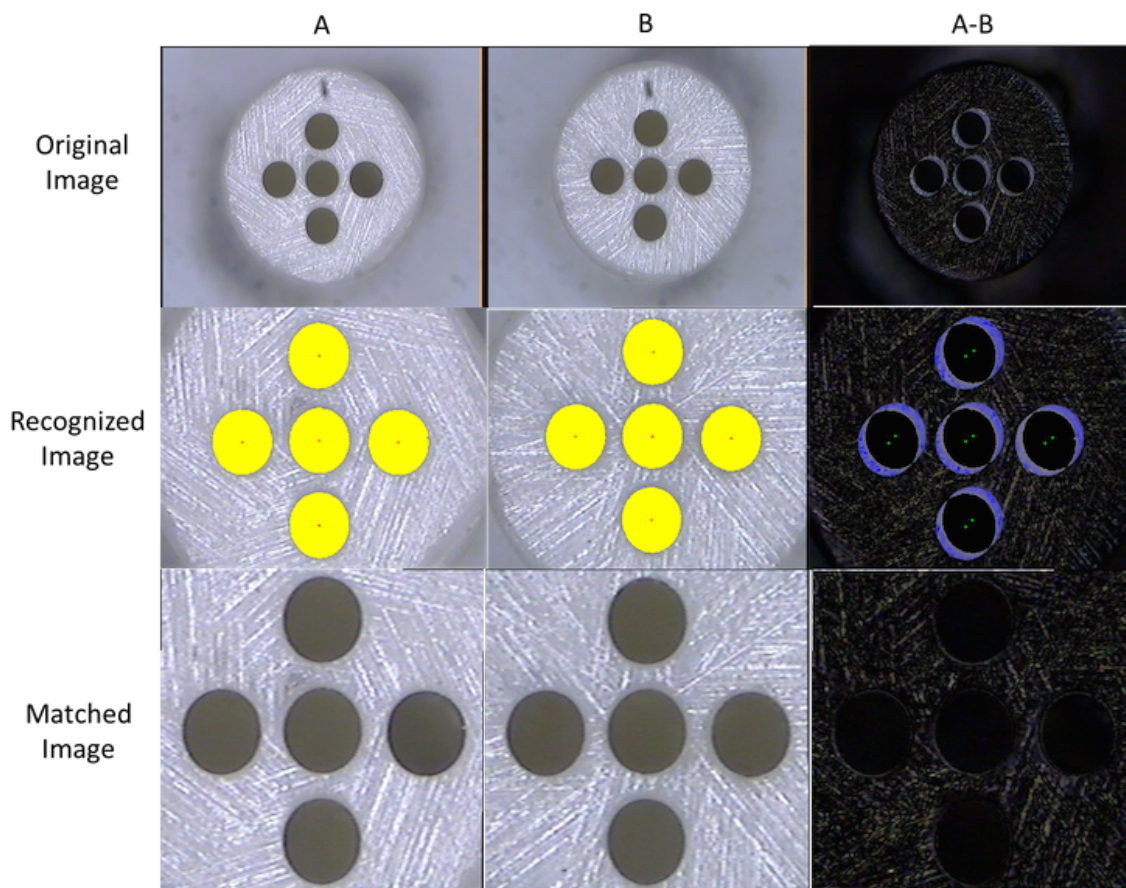


Figure 2.1.3: Finding the best match of ceramic tubes pair.

2.1.3 Characterization of helical resonator

The strong RF field is provided by a homemade high quality amplifier working at around 12 MHz, called “helical resonator” [26], which has a pretty high amplification with low noise. The effective cavity length of helical resonator decides its resonance frequency. Smaller cavity has a higher resonance frequency. The power amplification ratio is proportional to cavity’s quality factor Q . To measure quality factor Q , we sweep the input frequency and measure reflection signal spectrum’s center frequency ω and FWHM $\delta\omega$. Then

$$Q \approx \frac{\omega}{\delta\omega}$$

Lower resistance between the end cap and main tube makes higher quality factor according to our experience. After we polish the cooper surfaces with sand papers and wash them with phosphoric acid, a quality factor of > 200 is obtained with trap connected, and > 400 without trap. The power transmitted to the trap is monitored by a standing wave power meter. We use a fast RF switch to switch between two different power levels. ~ 0.1 W power is used during loading step, and ~ 2 W power is used when we manipulate motional sidebands. The reflection signal is also monitored and indicates “health” status of the helical resonator. Since the cavity length is sensitive to temperature, a shielding box filled with styrofoam peanuts is built to protect helical resonator from lab temperature fluctuation.

Usually the main tube and caps are well connected with a short-circuit BNC cap. This is the standard configuration where the DC level difference between trap’s RF rods and ground rods is 0 and leads to a equal trap frequency along X and Y axis. However, for phonon related experiments we need to split degenerated X mode and Y mode to have individually control over different kinds of phonon. At this time, we replace the short-circuit BNC cap with a capacitor to keep the resonator circuit

still working and apply several volts DC voltage on two ends of this capacitor. This configuration results in different DC levels between RF rods and ground rods and leads to a much bigger mode splitting compared to their Rabi frequencies.

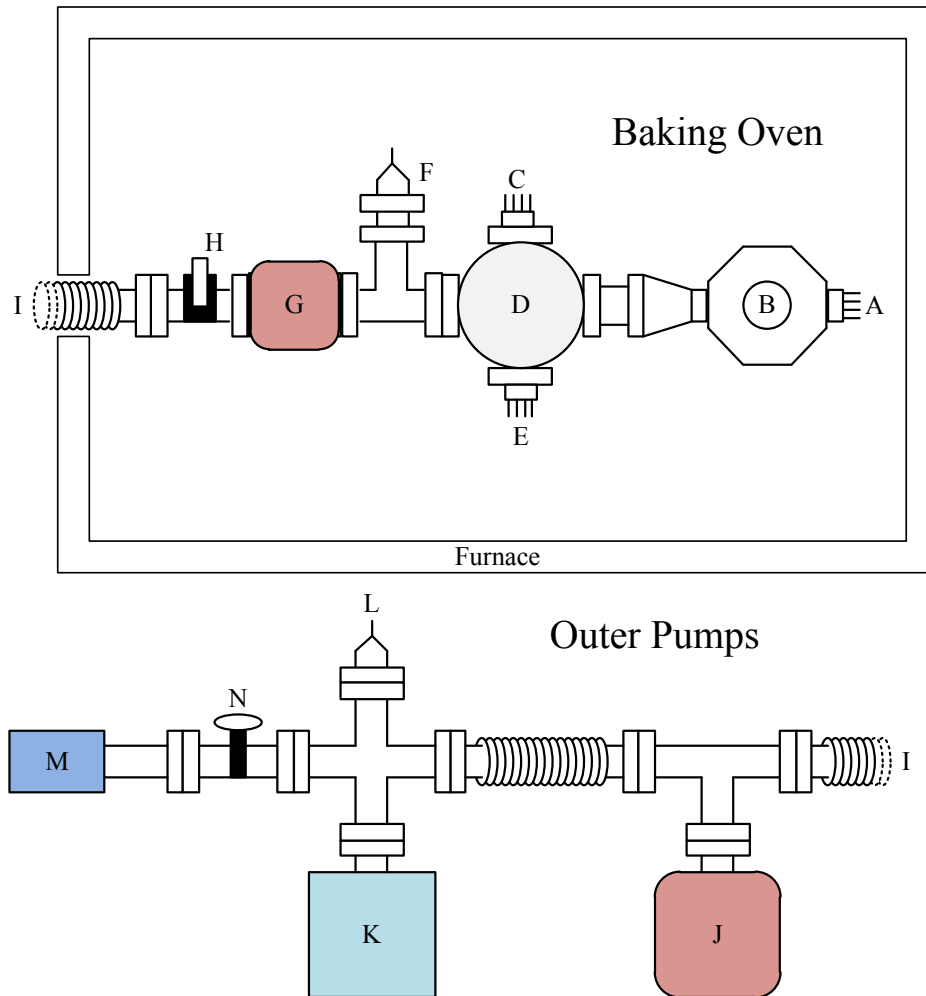
2.2 Vacuum system

2.2.1 Preparation of UHV

The main body of vacuum system is connected by a lot of thick stainless steel tubes. The connection flange between two tubes is sealed by a copper gasket. When we tight the connection with flange bolts and screws, the copper gasket is clamped and tightly surrounded by knife edges because copper is softer than stainless steel. All screws should be tighten in a Zig-Zag star manner to keep a uniform sealing depth. All vacuum components are cleaned several times in alternate baths of ethanol and acetone before the final assembling. We use a ultrasonic generator to clean most of them except some composite components, e.g., feed-through and view ports. All metal components are then air-baked with a big high temperature oven to acquire a chromium oxide coating. This coating is able to prevent the material of vacuum components from absorbing gases in the air, thus decreasing the amount of out gassing [27]. The design diagram of our vacuum system is showed in Fig. 2.2.1.

Before real assembling, the whole system is also testing assembled with Autodesk Inventor, as it shows in Fig. 2.2.2.

After we assemble the vacuum system, 4 levels of vacuum pumps (mechanical rough pump, turbomolecular pump, big ion pump, small ion pump and Ti sublimation pump) are used to prepare the UHV environment. A picture of these vacuum pumps is showed in Fig. 2.2.3.



- | | |
|---|--|
| A feedthrough for RF confinement voltage | H bakeable valve |
| B octagon vacuum chamber for the trap system | I bellows connecting the two systems |
| C feedthrough for DC confinement voltage | J big ion pump |
| D Ti sublimation pump | K turbomolecular / mechanical pump assembly |
| E feedthrough for atomic ovens | L ion gauge |
| F ion gauge | M residual gas analyzer (RGA) |
| G small ion pump | N isolation valve for the RGA |

Figure 2.2.1: Design of our vacuum system.

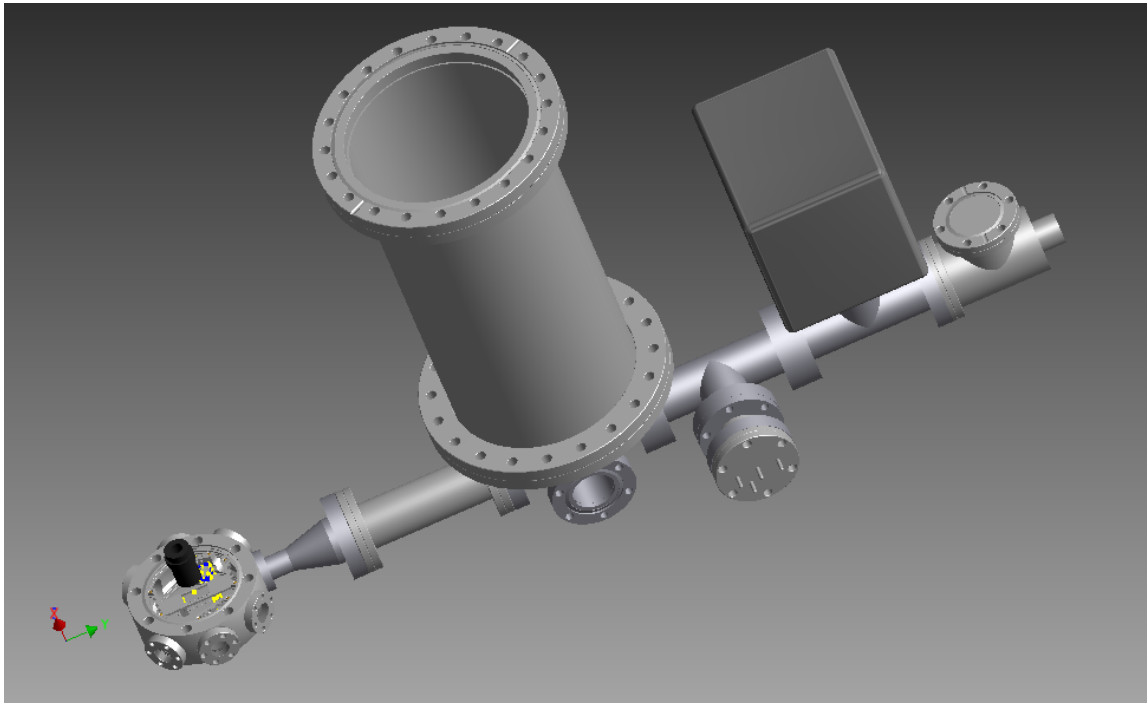


Figure 2.2.2: Assembling of vacuum system in Autodesk Inventor.



Figure 2.2.3: Vacuum pumps and big oven for baking ion trap and other vacuum components.

The mechanical rough pump is first turned on to get the the bulk of air out. When the vacuum is below 10^{-4} torr, the turbomolecular pump on top of the mechanical rough pump is turned on. The turbomolecular pump has a fast rotation speed ($\sim 20,000$ RPM) which enables its blades to achieve a speed comparable to the molecular speed. Molecules are mechanically deflected downward and are then wiped out by the mechanical rough pump. When the vacuum is below 10^{-8} torr, H_2O is one of the mainly remained molecule. So the big oven is again used for vacuum-baking. It heats the vacuum system to around $200\text{ }^\circ\text{C}$ for about one week to speed up the out-gassing process and completely vaporize the water layer. The Ti sublimation pump is degassed and the big ion pump is turned on during baking. The ion pump is basically a Penning trap with electrons fed by HV discharge. Background gas molecules are ionized by high speed electrons. Molecules' fragments are attracted to cathodes and get stuck there. Some neutral constitutes can be absorbed by the "getter" material on walls of pump. When the baking is finished, the bakeable valve is sealed before the temperature starts to decrease. It cuts off the inner vacuum system from the outer pumps. Finally, when the system is at room temperature, the Ti sublimation pump is turned on several times with stepped big currents (~ 40 A) to take out the remaining hydrogen, which is the dominant ingredient in UHV environment. The pump speed can be greatly improved by liquid nitrogen cooling. The small ion pump is always on to keep a vacuum pressure below 10^{-10} torr.

A mass spectrometer called "RGA" and several vacuum gauges are used to check leakage and measure vacuum during the whole vacuum-preparation stage. Leakages occur most often at seals and glass-metal transitions. A quick leakage test at the early stage is by spraying acetone to all possible suspicious places and look for pressure changes in either direction. Acetone can temporarily seal the leak or creep through it, which results in a notably vacuum pressure dropping down or rising up. For more

accurate leakage test, we need to use the high sensitivity Helium leak detection, which can find a leak as small as 10^{-11} torr L/s since the Helium is rare in the natural air. The operation is pretty similar with the acetone method except that we use a mass spectrometer to monitor Helium’s partial pressure inside our vacuum system. The mass spectrometer measures mass-to-charge ratio by ionizing a molecule and accelerating it in a electric-magnetic field. It can detect partial pressure down to 10^{-14} torr. Once we find some suspicious place, we can use a plastic bag filled with Helium to discover the tiniest leaks.

2.2.2 Estimation of background gas collision rates

With this whole procedure we can archive a ultra high vacuum with pressure around 10^{-11} torr. At these pressures, the collisions between the ion and background gas particles were infrequent. In these collisions, the electric field from the trapped ion polarizes the background neutral molecules. We can analyze this process with a basic two body model where an induced electric dipole lives in a single point source electric field. This model has an interaction Coulomb potential [28, 29]

$$V(r) = -\frac{C_4}{2r^4} \quad (2.2.1)$$

, where

$$C_4 = \frac{\alpha q^2}{(4\pi\epsilon_0)^2} \quad (2.2.2)$$

For a given initial velocity \vec{v} in the center-of-mass frame, there exists a critical barrier initial distance b_v , below which the electric dipole will be captured by the ion. This barrier separates “elastic” collisions and “inelastic” collisions. The particles in “inelastic” collisions go cross the angular-momentum barrier and may exchange

charge or even chemically react (e.g., $\text{Yb}^+ + \text{H} \rightarrow \text{YbH}^+$) with trapped ions, which resulted in the effective loss of the ion. But inelastic collisions can occur only if the inter particle spacing of the two colliding partners approaches the critical atomic dimension [30].

Define r as the distance and v as the tangential velocity between the hydrogen dipole and the center $^{171}\text{Yb}^+$. The system should satisfy following equations

$$\begin{cases} \mu v r = L \\ \frac{1}{2}\mu\dot{r}^2 + \frac{1}{2}\mu v^2 + V(r) = E \\ \mu(\ddot{r} - \frac{v^2}{r}) = -\frac{dV(r)}{dr} \end{cases} \quad (2.2.3)$$

where the angular momentum L and total energy E are both conserved quantities. Change to a reference system with the same centripetal acceleration as the hydrogen, then we have an additional centrifugal potential which is always equal to the tangential translational energy

$$V_c(r) = \frac{L^2}{2\mu r^2} = T \left(\frac{b}{r}\right)^2 \quad (2.2.4)$$

where

$$T = \frac{L^2}{2\mu b^2}$$

is the initial translational energy at initial distance b . Note that we can make the initial radial velocity $\dot{r} = 0$ by choosing a proper initial reference system. Define the effective potential

$$V_{\text{eff}}(r) = V(r) + V_c(r)$$

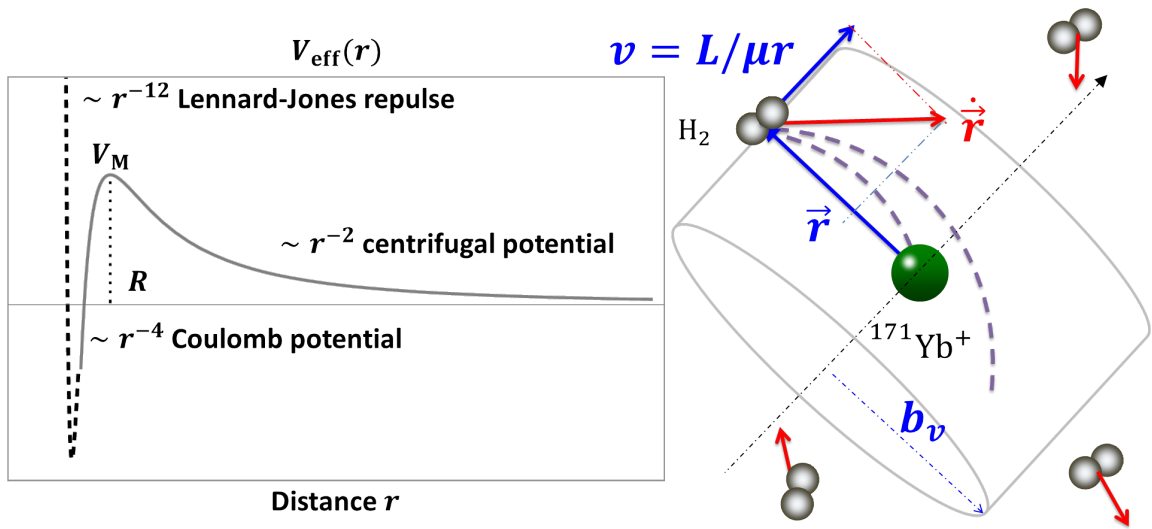


Figure 2.2.4: Effective potential and inelastic collisions.

, then the equations becomes

$$\begin{cases} \frac{1}{2}\mu\dot{r}^2 = E - V_{\text{eff}}(r) \\ \mu\ddot{r} = -\frac{dV_{\text{eff}}(r)}{dr} \end{cases} \quad (2.2.5)$$

A diagram of the effective potential and inelastic collision process is showed in Fig. 2.2.4 [31].

When the effective potential reaches to its maximal value

$$V_M = \frac{T^2 b^4}{2C_4} \quad (2.2.6)$$

at distance

$$R = \sqrt{\frac{C_4}{Tb^2}} \quad (2.2.7)$$

the radial direction acceleration becomes zero. If the total energy E is bigger than

this energy barrier V_M , then there is still remaining radial direction velocity $\dot{r}|_{r=R} < 0$. The dipole definitely collapses to the center ion and an inelastic collision happens. So the critical barrier initial distance b should satisfy

$$V_M = E = V_{\text{eff}}(b) = T + V(b) \quad (2.2.8)$$

Solve this equations and we have

$$b_v = \left(\frac{C_4}{T}\right)^{\frac{1}{4}} = \left(\frac{2C_4}{\mu v^2}\right)^{\frac{1}{4}} \quad (2.2.9)$$

Then an upper limit estimation rate of inelastic collisions from background hydrogen molecules can be derived with this Langevin rate constant

$$k_{\text{Langevin}} = \sigma_{\text{Langevin}} v = \pi b_v^2 v = \pi \sqrt{\frac{2C_4}{\mu}} = \frac{q}{4\epsilon_0} \sqrt{\frac{2\alpha}{\mu}} \approx 5.382 \times 10^{-6} \text{ mm}^3 \text{ s}^{-1} \quad (2.2.10)$$

where the static dipole polarizability of Yb [32] is

$$\alpha = 143 \text{ au} = 2.358 \times 10^{-39} \text{ C}^2 \text{ m}^2 \text{ J}^{-1} \quad (2.2.11)$$

and the reduced mass of hydrogen and Yb is

$$\mu = \frac{(2 \times 171)/(2 + 171) \text{ g/mol}}{N_A} = 3.322 \times 10^{-27} \text{ kg} \quad (2.2.12)$$

Note that the velocity \vec{v} dependency cancels out in Langevin rate constant. At a pressure of 5 nPa ($\approx 4 \times 10^{-11}$ torr) and a room temperature of 300 K, the molecule density of hydrogen is

$$n = \frac{P}{RT} = 1206.73/\text{mm}^3 \quad (2.2.13)$$

We have the Langevin collision rate

$$\gamma_{\text{Langevin}} = nk_{\text{Langevin}} \approx 0.006/\text{s} \quad (2.2.14)$$

or approximately 1 collision every 3 minutes. However, experimentally we observe a lifetime of several days for trapped $^{171}\text{Yb}^+$ ions with Doppler cooling beam always on, which indicates that at least for ground state $^{171}\text{Yb}^+$ ions the probability of chemical reactions with the background gas constituents is small. Other than inelastic collisions, background gas can also heat the trapped ions by transferring energy during an elastic collision. In the quasi-classical limit, The total elastic collision cross section [33] is

$$\sigma_{\text{elastic}} = \pi\Gamma \left(\frac{1}{3}\right) \left(\frac{\alpha'q^2}{16\epsilon_0\hbar v}\right)^{\frac{2}{3}} \quad (2.2.15)$$

where $\alpha' = \alpha/(4\pi\epsilon_0)$. Average over a thermal distribution of background hydrogen velocities

$$f(v) = \frac{4v^2}{\sqrt{\pi}\tilde{v}^3} e^{-(v/\tilde{v})^2} \quad (2.2.16)$$

where square mean root velocity

$$\tilde{v} = \sqrt{\frac{2k_{\text{B}}T}{\mu}} \approx 1578.7\text{m/s} \quad (2.2.17)$$

The elastic collision rate constant

$$\begin{aligned}
k_{\text{elastic}} &= \langle \sigma_{\text{elaststic}} v \rangle \\
&= \int_0^\infty \sigma_{\text{elaststic}} v f(v) dv \\
&= 4\sqrt{\pi} \Gamma\left(\frac{1}{3}\right) \left(\frac{q^2}{16\epsilon_0 \hbar}\right)^{\frac{2}{3}} \int_0^\infty v^{7/3} e^{-(v/\tilde{v})^2} dv \\
&= 1.228 \times 10^5 (\alpha')^{2/3} \tilde{v}^{1/3} \\
&= \approx 1.095 \times 10^{-4} \text{mm}^3 \text{s}^{-1}
\end{aligned} \tag{2.2.18}$$

and the elastic collision rate

$$\gamma_{\text{elastic}} = n k_{\text{elastic}} \approx 0.132/\text{s} \tag{2.2.19}$$

Although each elastic collision on average transfers a large amount of energy to the trapped ion, we conclude that at typical UHV pressures, such collisions will also be rare. The average gap (≈ 10 s) between two elastic collisions is much longer than the time required for a single experiment (< 10 ms), so that elastic heating collisions were negligible. This makes our ions extremely stable: ion seldom disappear during experiments and can survive over nights even without laser cooling.

THIS PAGE INTENTIONALLY LEFT BLANK

Chapter 3

Daily operations of trapped ions

Transitions between a trapped ion's some internal electronic levels can be used as a qubit (or a qudit) to store quantum information. Ion's motional oscillators in trap potential can also be used as a qudit or a quantum bus to transfer quantum information between different ions. Both of these quantum resources can be initialized, manipulated and then measured by utilization of external electronic-magnetic fields generated by lasers or RF sources.

Our daily operations of trapped ions mainly consists of ionization, Doppler cooling, optical pumping and state detection. A lot of lasers related to optical radiative transitions of $^{171}\text{Yb}^+$ are used. Following techniques are mostly involved for these laser operations

1. Optical addressing. Mirrors, beam splitters, lens and transition stages to precisely address each laser beam at ion position.
2. Optical observation. Optical lens train to collect, transfer and magnify ions fluorescence images.

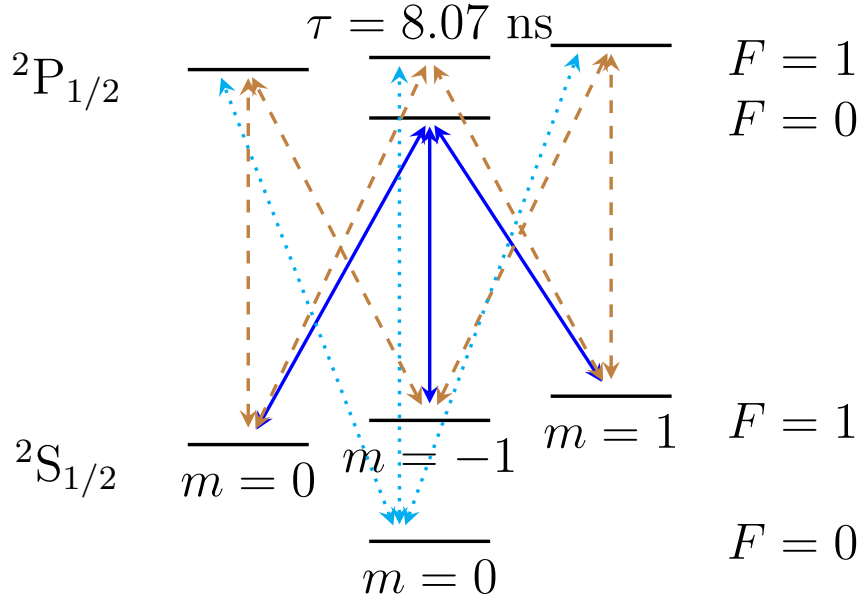


Figure 3.1.1: Hyperfine structures and optical transitions of the main optical cycle.

3. Frequency modulation. EOMs to generate frequency sidebands, AOMs to shift center frequency and act as optical switches.
4. Frequency stabilization. Optical cavities, vapor cells, photo diodes and feedback circuits to stabilize laser frequencies.

3.1 Main optical transitions of trapped ion

For an ion with nuclear spin $I = 1/2$, e.g., $^{171}\text{Yb}^+$, its ground energy levels are degenerated and split into several Zeeman levels. We use optical dipole transitions between $^2S_{1/2} \leftrightarrow ^2P_{1/2}$ as the main cycle for laser cooling, state initialization and state detection. The hyperfine structures and optical radiative transitions are showed in Fig. 3.1.1.

For state detection, we drive transitions labeled as blue solid lines. Ion is excited

from ${}^2S_{1/2} : |F = 1\rangle$ states to ${}^2P_{1/2} : |F = 0\rangle$ state. It can only live there for a short time (life time $\tau = 8.07$ ns). Then it spontaneously emits a photon and go back to one of ${}^2S_{1/2} : |F = 1\rangle$ states. The whole cycle can be rapidly repeated for many times until we collect enough photons. By this process, we can easily distinguish the “dark” state ${}^2S_{1/2} : |F = 0\rangle$ and measure its population, since it’s never touched and emits no photon. We use a π rotation gate to swap other state with “dark” state and then measure its population. For state initialization, we need to drive additional transitions labeled by brown dashed lines. In this case, ion is excited from ${}^2S_{1/2} : |F = 1\rangle$ states to ${}^2P_{1/2} : |F = 1\rangle$ states and has a chance to jump to “dark” state ${}^2S_{1/2} : |F = 0\rangle$ through the cyan dotted lines. However, when ion is in “dark” state, it has no chance to jump back to other states. After many cycles, all the population is transferred and initialized to “dark” state. For laser cooling, what we do is to excite the ion from ${}^2S_{1/2}$ to ${}^2P_{1/2}$ through all possible ways, which can be implemented with transitions labeled by blue solid lines and cyan dotted lines.

The dipole matrix elements of different transitions can be calculated with the useful Wigner-Eckart theorem

$$\begin{aligned} \langle jm|T_q^{(k)}|j'm'\rangle &= \langle j'm'kq|jm\rangle \langle j||T^{(k)}||j'\rangle \\ &= (-1)^{j-m} \langle j||T_k||j'\rangle \begin{pmatrix} j & k & j' \\ -m & q & m' \end{pmatrix} \end{aligned} \quad (3.1.1)$$

where $q = m - m'$ and $k = 1$ for dipole transitions. The reduced matrix element can

be calculated with following formula

$$\begin{aligned} \langle (j_1 j_2) j || T^{(k)} || (j'_1 j'_2) j' \rangle &= (-1)^{j_1 + j_2 + j' + k} \langle j_1 || T^{(k)} || j'_1 \rangle \\ &\quad \sqrt{(2j+1)(2j'+1)} \begin{Bmatrix} j_1 & j & j_2 \\ j' & j'_1 & k \end{Bmatrix} \end{aligned} \quad (3.1.2)$$

when $\vec{j} = \vec{j}_1 + \vec{j}_2$, $T^{(k)}$ commutes with j_2 but not j_1 . For optical transitions between hyperfine levels

$$|l = 0, s = 1/2, j = 1/2, I = 1/2, F, m\rangle \leftrightarrow |l = 1, s = 1/2, j = 1/2, I = 1/2, F, m\rangle$$

, we first apply Eq. 3.1.2 with $j = F$ and then apply Eq. 3.1.3 twice. The first time we use $\vec{F} = \vec{j} + \vec{I}$ to get $\langle (jI)F || T^{(1)} || (j'I')F' \rangle$. The second time we use $\vec{j} = \vec{l} + \vec{s}$ to get $\langle (ls)j || T^{(1)} || (l's')j' \rangle$. Then by representing position operator r with spherical basis we can calculate

$$\langle l || T^{(1)} || l' \rangle = \langle T^{(1)} \rangle (l - l') \sqrt{\max(l, l')} \quad (3.1.3)$$

when $l' = l + 1$. In this way we can finally write the relative transition term

$$\begin{aligned} \Omega(|ljFm\rangle, |l'j'F'm'\rangle) &= (-1)^{1+F_1+F_2+j_1+j_2+l_1-m_1} (l_1 - l_2) \max(l_1, l_2) \\ &\quad \sqrt{(2F_1+1)(2F_2+1)(2j_1+1)(2j_2+1)} \\ &\quad \begin{Bmatrix} j_1 & F_1 & 1/2 \\ F_2 & j_2 & 1 \end{Bmatrix} \begin{Bmatrix} l_1 & j_1 & 1/2 \\ j_2 & l_2 & 1 \end{Bmatrix} \begin{pmatrix} F_1 & 1 & F_2 \\ -m_1 & m_1 - m_2 & m_2 \end{pmatrix} \end{aligned} \quad (3.1.4)$$

A table of all transition terms between ${}^2S_{1/2} \leftrightarrow {}^2P_{1/2}$ is showed in Table. 3.1.

We can easily verify the familiar “selection rules” with this table. A sample

Table 3.1: All transition terms between ${}^2S_{1/2} \leftrightarrow {}^2P_{1/2}$.

${}^{2s+1}l_j : F, m\rangle$	${}^2S_{1/2} : 0, 0\rangle$	${}^2S_{1/2} : 1, -1\rangle$	${}^2S_{1/2} : 1, 0\rangle$	${}^2S_{1/2} : 1, 1\rangle$
${}^2P_{1/2} : 0, 0\rangle$	0	-1/3	-1/3	-1/3
${}^2P_{1/2} : 1, -1\rangle$	1/3	1/3	1/3	0
${}^2P_{1/2} : 1, 0\rangle$	-1/3	-1/3	0	1/3
${}^2P_{1/2} : 1, 1\rangle$	1/3	0	-1/3	-1/3

Mathematica code to calculate transition terms is showed in Appendix A.

3.2 Ionization and “load”

Once we understand these basic things of our trap, next is how to really “load” ions into it. The diagram of this procedure is showed in Fig. 3.2.1.

First the atom oven is heated up around sublimation temperature. For Yb ions, the boiler temperature under UHV is 480 °C [34]. The metal powder inside oven melts and gasifies. Then a beam of several thousand atoms is emitted from the oven and shoot towards the trap. Some of these neutral atoms are hit by strong lasers shining around the trap area and ionized to ions. Once they become ions, they are confined by the strong electro-magnetic trap potential and have to oscillate near the trap center.

A $\sim 500\mu\text{W}$ 398.9108 nm beam provided by Toptica diode laser and a $\sim 5\text{mW}$ 369.5263 nm beam provided by Toptica SHG laser are used for ionization. Both beams are focused to $\sim 50\mu\text{m}$ waist at the center of trap. Neutral Yb atoms passing through these beams are photon-ionized by way of a resonantly assisted dichroic two-photon transition: the 398.9108 nm light excites Yb atoms from the 1S_0 to the 1P_1 level, from which the 369.5263 nm light can promote the electron to the continuum

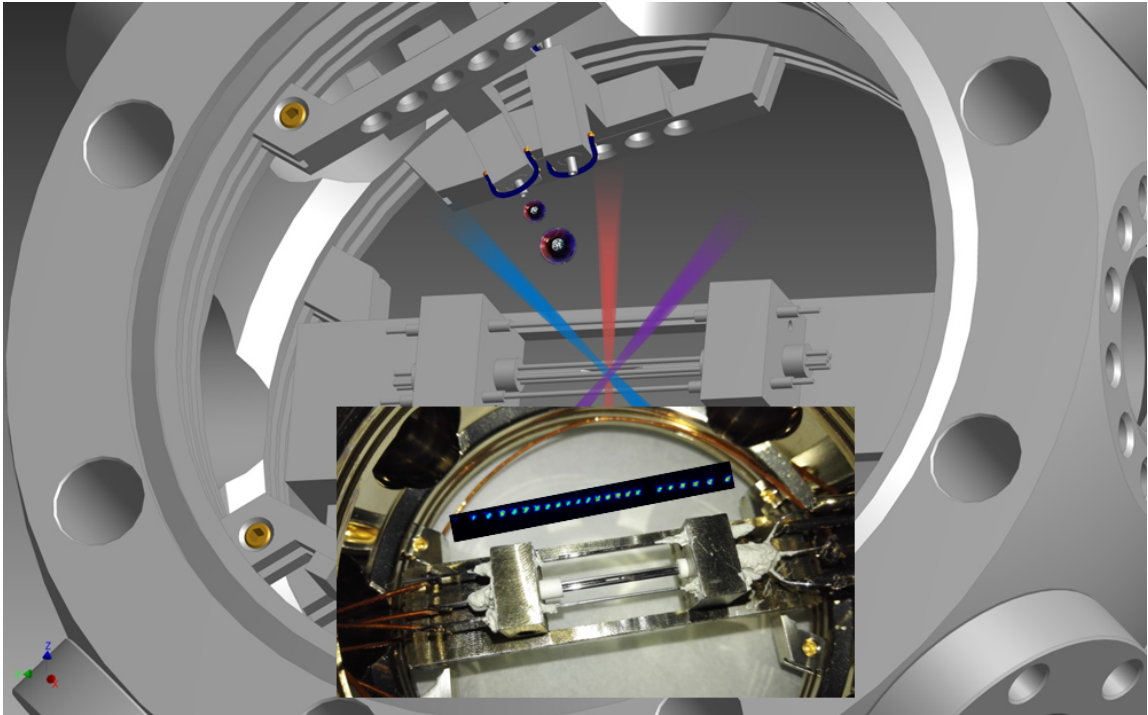


Figure 3.2.1: Loading and trapping of $^{171}\text{Yb}^+$ ions. Yb atoms are ionized and Doppler cooled by laser beams. A chain of 23 ions are observed with CCD camera.

[35]. Additional Doppler frequency shift depending on the angle between atom oven and ionization beams are considered to improve ionization efficiency. Shutters are used to block beams and control the manually loading process.

At this time, these hot ions still have huge motion energies and are not stable in the trap. They absorb photons from a near resonant but red detuned laser beam, then spontaneously emit photons to every direction with uniformly probability distribution. Their momentum along laser beam's direction will be efficiently canceled after hundreds of thousands cycles. This process is called Doppler cooling. The Doppler cooling beam is chosen to be at small angles with 3 axes, thus efficiently cools down ions' oscillation energies.

3.3 Doppler cooling and optical pumping

Another pair of beams are used for Doppler cooling. One of them is a $\sim 50\mu\text{W}$ 369.5263 nm beam, slightly red-detuned from the optical transition $^2\text{S}_{1/2} \leftrightarrow ^2\text{P}_{1/2}$. The ion on $^2\text{S}_{1/2}$ can absorb one laser photon and go up to $^2\text{P}_{1/2}$, the life time of $^2\text{P}_{1/2}$ is only 8.7ns, then it spontaneously emits a photon to every direction with uniformly probability distribution. Typically the Doppler cooling beam is shined for 1ms before any other quantum operations to make sure the ion is cooled down to near Doppler limit. This Doppler cooling beam has a 14.74 GHz sideband provided by a LabBrick driven Electro-Optic Modulator (EOM), to cover all possible transitions between hyperfine levels. The second one is an auxiliary but important $\sim 10\text{mW}$ 935.1882 nm beam. It's used to re-pump 0.5% leakage on metastable $^2\text{D}_{3/2}$ back to the main cycle, thus completes a stable Doppler cooling scheme. This beam also has a 3.1 GHz sideband.

The relevant $^{171}\text{Yb}^+$ level diagrams of 369.5 nm laser and 935 nm laser beams is

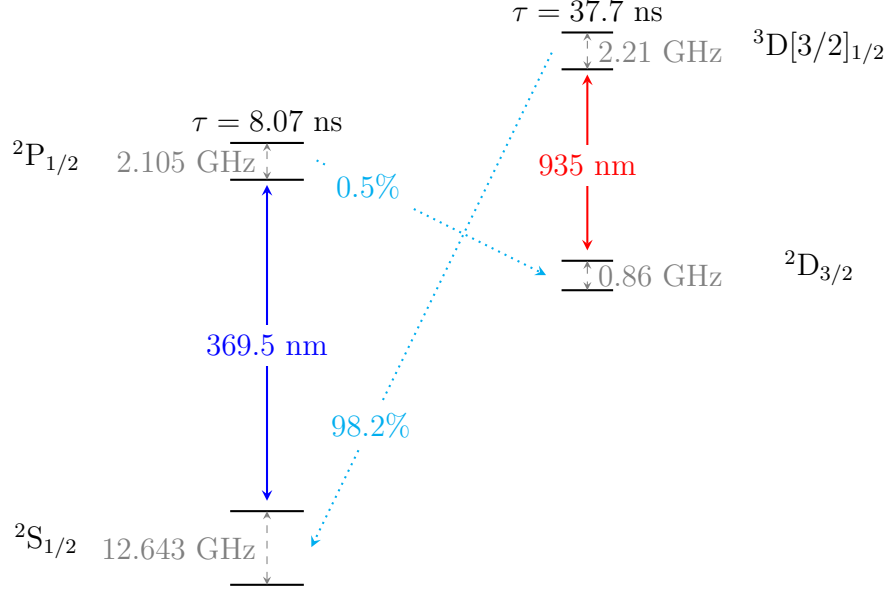


Figure 3.3.1: Relevant $^{171}\text{Yb}^+$ level diagrams of 369.5 nm laser and 935 nm laser.

showed in Fig. 3.3.1 [36].

Sometimes the ion falls into the $^2\text{F}_{7/2}$ state, possibly caused by collisions with residual background gas. A $\sim 1\text{mW}$ laser beam near $638.6101 \sim 638.6151$ nm depopulates the $^2\text{F}_{7/2}$ level and returns the ion to the four-level Doppler cooling scheme. With Doppler cooling, ions' temperature can be lowered down to Doppler limit

$$T_D \approx \frac{\hbar\gamma}{2k_B} \approx 470 \mu\text{K}$$

where $\gamma = (2\pi) 19.7$ MHz is the line width of the cooling transition for $^{171}\text{Yb}^+$. The fluorescence generated by Doppler cooling process also indicates each ion's position and can be observed with a CCD camera. Another 369.5263 nm optical pumping beam is used to initialize $^{171}\text{Yb}^+$ ion to state $|F = 0, m = 0\rangle$, labeled as state |1⟩ in our 4-level system. Unlike Doppler cooling beam, the optical pumping beam is modulated with a 2.105 GHz EOM. Its sideband doesn't cover transitions from

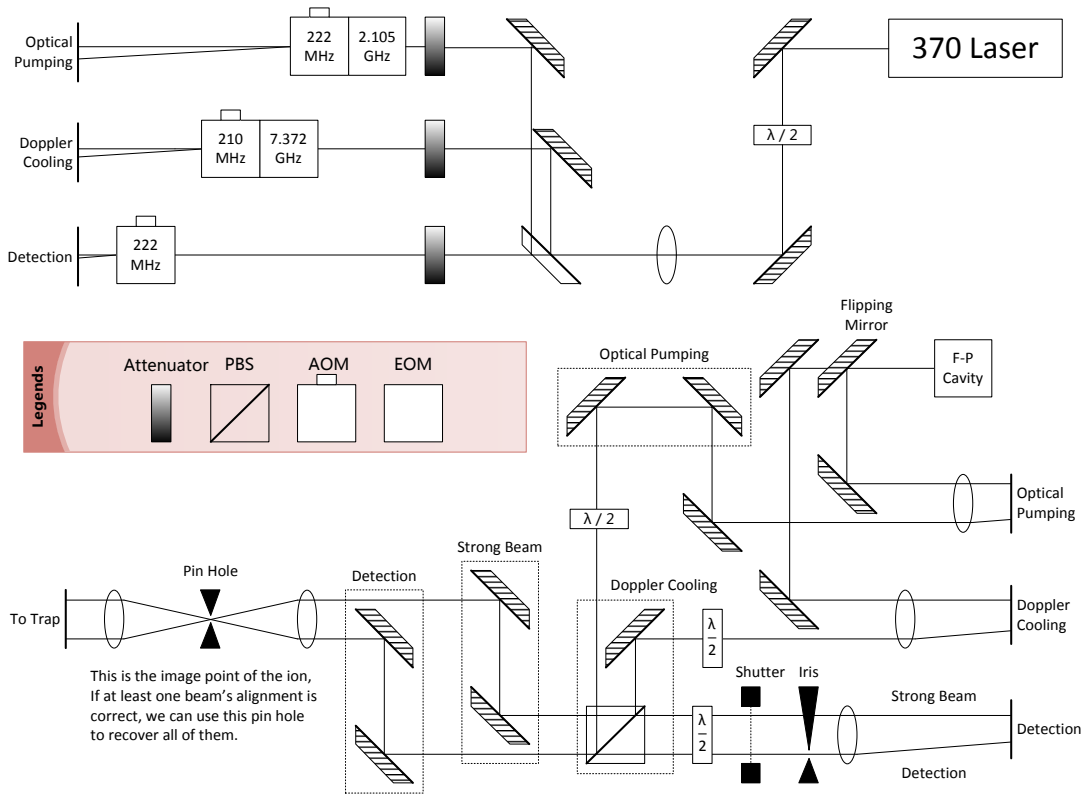


Figure 3.3.2: Optical paths for 369.5 nm laser.

$|F = 0, m = 0\rangle$, which means $|F = 0, m = 0\rangle$ will never be excited, but other states can go down to $|F = 0, m = 0\rangle$ by spontaneously emission. So after a bunch of cycles ($\sim 5\mu s$), the $^{171}\text{Yb}^+$ ion will be on state $|F = 0, m = 0\rangle$ with high fidelity ($> 99.5\%$). All these laser beams are finally applied to trap center through lenses and small view ports on the vacuum chamber. Each lens is mounted to a three dimensional transition stage, which provides a firm support as well as a precise control of the optical system.

The optical paths for all these 369.5 nm laser beams is showed in Fig. 3.3.2.

AOMs are used as quick optical switches and can be automatically controlled by

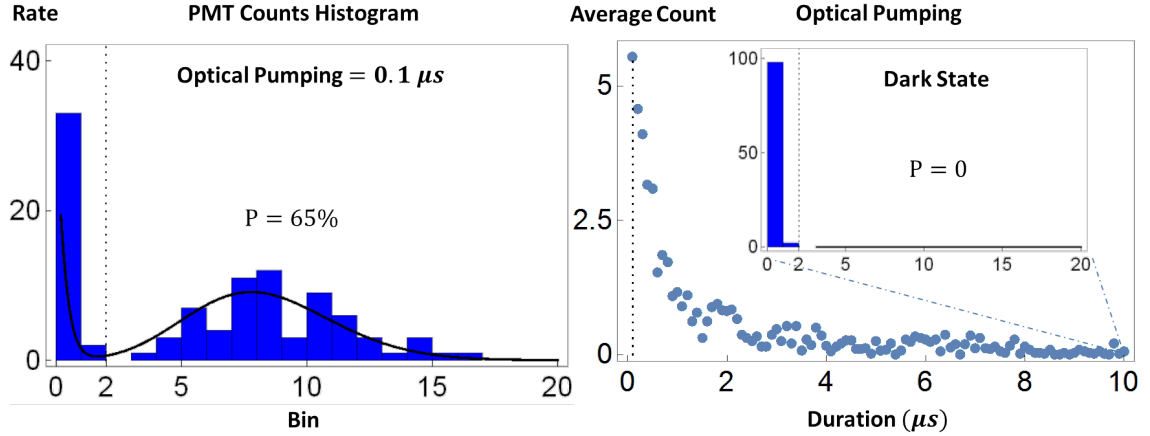


Figure 3.4.1: PMT counts before and after optical pumping.

TTL signals. A good beam profile of strong ionization and Doppler cooling beams should be maintained to minimize possible optical leakages and reduce background scattering, which could lead to a low optical pumping efficiency.

3.4 State detection

According to our quantum state detection scheme, the population of “dark” state $|1\rangle$ can be measured with a 369.5263 nm detection beam which is only resonant to ${}^2S_{1/2} : |F = 1\rangle \leftrightarrow {}^2P_{1/2} : |F = 0\rangle$ transition. If the emitted photons’ counting rate is lower than a detection threshold $\sim 1/300\mu s$, we define the population to be 0, which means the ion is totally at dark state $|1\rangle$. Otherwise the population is 1, which means the ion is at one of bright states $|2\rangle, |3\rangle, |4\rangle$. By averaging the detection results of hundreds of repeated experiments, we can get a pretty accurate population estimation of dark state $|1\rangle$ and bright states. Fig. 3.4.1 shows PMT counts and corresponding bright states populations before and after optical pumping.

A two stage optical observation system designed with the OSLO software is set

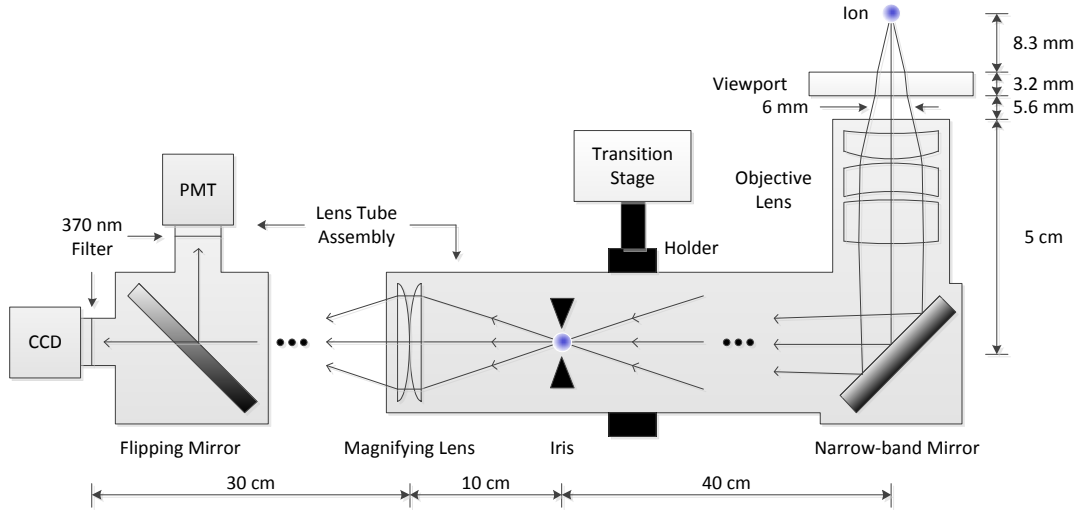


Figure 3.4.2: Diagram of detection system with CCD and PMT.

up to collect fluorescence coming from the ion. The diagram of our optical observation system is shown in Fig. 3.4.2.

A microscopic objective lens with a short focal length and a large numerical aperture is used as the first stage of detection, to maximize the solid angle ($\approx 0.77\%$ in our case) of the detection lens to the ion. A group of magnifying lenses at the second stage casts the image to the sensitive surface of optical detection devices. We put a CCD camera at one end of the second stage to observe the airy disk of ions and a PMT at another end to count emitted photons. Observation with CCD or PMT is switchable by a flipping mirror. Two 370 nm narrow-band filters are inserted into the optic tubes to filter out background noise introduced by photons of other wavelength. Fig. 3.4.3 shows a CCD image of ions' Doppler cooling spots.

For ion addressing alignment, usually we use shadows or CCD camera images of rods and needles to help determine the geometry center of our trap. Unfortunately, this geometry center is usually not exactly the trap's center. So for the first time of

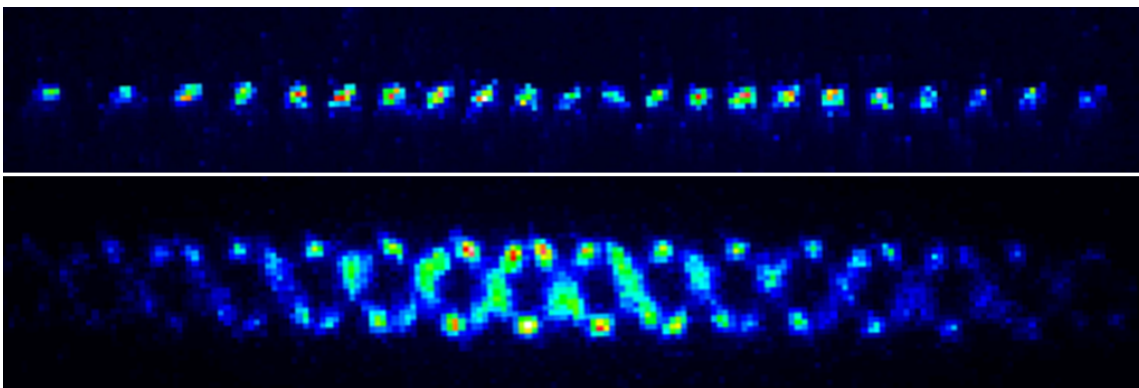


Figure 3.4.3: Image of trapped ions. The distance between two adjacent ions in first image is around $10\ \mu\text{m}$. The second image shows ions' crystal structure.

ion addressing, we always use a big current to load a lot of $^{174}\text{Yb}^+$ ions until all ions forms a wide crystal structure. This wide crystal structure looks like a cloud on our CCD camera. Then it's possible to see some edges of ions' cloud at trap's geometry center. Following this signal we can move the objective lens and all laser beams to cloud's center step by step. The alignment procedure is finalized by loading a single $^{171}\text{Yb}^+$ ion and maximize its detection count.

3.5 Excess micromotion compensation

For multiple ions, the small leaked alternating electric field along our 4-rod trap's z axis can not be neglected. This component will add an additional micromotion term to the motion solution. Other than this, there could be also other additional micromotion terms caused by

1. imperfect geometry configuration caused by machining or assembling
2. additional external field

3. phase difference between AC electrodes

Different from previous unavoidable micromotion, these kinds of “excess” micromotions can not be significantly reduced by cooling [37] and must be eliminated as small as possible. In the first two cases, ion’s default equilibrium position are shifted from the z axis of the trap. When we change trap depth, i.e., the power of driven RF field, ion’s position will change accordingly. We can use this phenomenon to estimate the amplitude of excess micromotion, by quickly switch the power of driven RF field between high level and low level. The rising time of this RF switch must be less than a trap period ($\sim 8\text{ns}$) so that the ion is not released.

A 2 ns resolution FPGA-based Time to Digit Converter(TDC) is built to measure the time correlation of ion’s micromotion frequency and its Doppler cooling fluorescence rate along certain direction. The arrival time of the photons on the PMT is recorded and compared to the phase of the RF trap drive voltage. If the ion’s movement is influenced by micromotion, the absorption and emission process of photons by the ion will be modulated at that frequency due to the Doppler effect. The ion will absorb more photons when the velocity is low, and vice versa. In TDC’s histogram this shows as a sine curve whose frequency equals to micromotion’s frequency (also equals to driven RF’s frequency). We use this time correlation pattern as a directional indicator to adjust voltages that applied on these micromotion compensation electrodes. The micromotion can be effectively reduced by eliminating the correlation peaks in the TDC spectrum. Another accurate micromotion compensation method is based on reduction of the motional sidebands in the spectrum of stimulated Raman transitions or the 935nm laser [38].

To isolate variables, voltages applied on compensation electrodes must be changed in pair to move ion only along or only perpendicular to certain direction. For ion’s

position scheme, this direction is objective lens plane. For TDC scheme, this direction is Doppler cooling beam's incidence direction. For motional sidebands scheme, this direction is X and Y axis of the trap. Final compensation voltages can range from several volts to several hundred volts, mainly depending on trap electrodes' geometry. Sometimes even after a strong laser beam hit trap's ceramic insulator part, or too many atoms are hanging around after a failed "loading", the micromotion condition will change a lot.

The voltage of each micro-motion compensation electrode as well as axial confinement electrode in our trap can be individually controlled through an ISEG high voltage module. A custom control program written in LabVIEW is used to change some of these electrodes' voltages simultaneously with arbitrary ratio.

3.6 Laser frequency stabilization

Efficient quantum operations on $^{171}\text{Yb}^+$ ions require that the 369.5263 nm and 935.1882 nm lasers are stable in frequency, especially the 369.5263 nm laser, to well within the linewidths of the relevant transitions in the experiment. Normally diode lasers are very sensitive to temperature and current and will have huge fluctuation without further stabilization. So we lock the 739.0526 nm laser (after SHG becomes a 369.5263nm laser) to a Fabry-Pérot(F-P) cavity using Pound-Drever-Hall(PDH) method to compensate fast fluctuation. The F-P cavity's length is then externally locked to an absolute frequency reference provided by an Iodine vapor cell system, to compensate long term drift, mainly caused by temperature. A ~ 13 GHz fiber EOM is used to shift laser frequency to Iodine's spectrum. A picture of the Iodine lock system is showed in Fig. 3.6.1.

This lock system works well and results in a high precision < 1 MHz. Lock

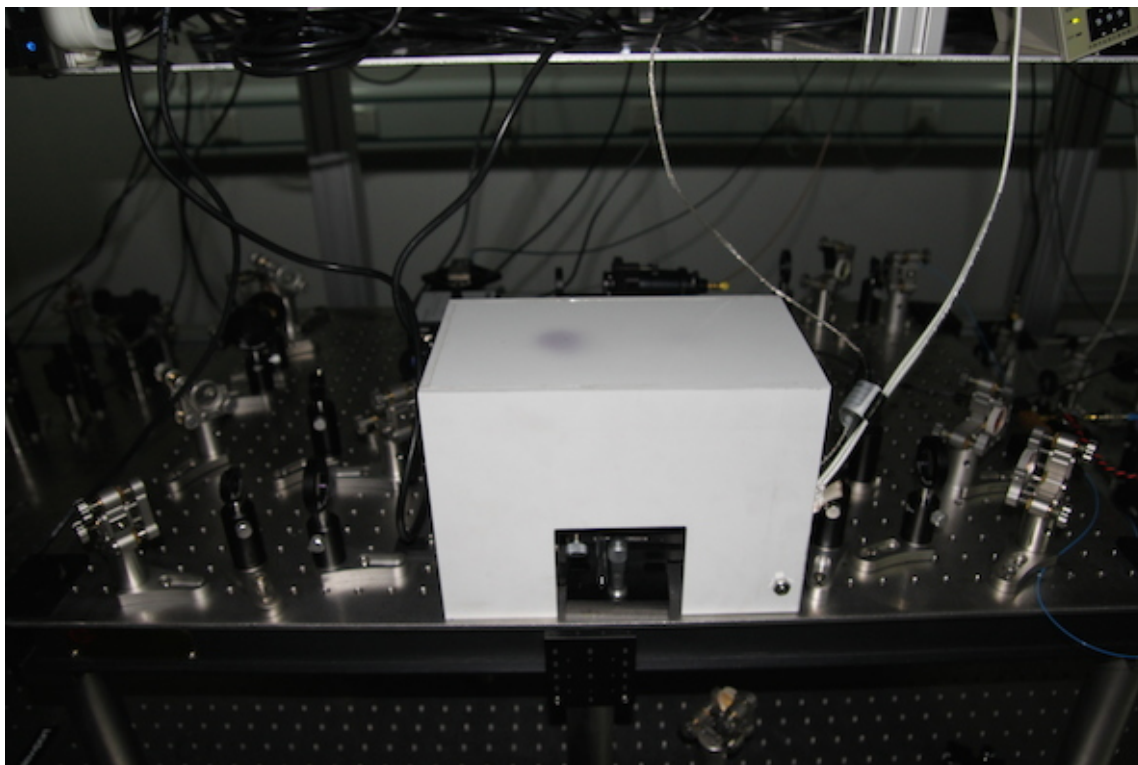


Figure 3.6.1: Picture of the Iodine lock system.

an automatic feedback loop for arbitrary system by setting appropriate coefficients of 3 components. Another important kind of device is the Lock-In amplifier, which is very useful to pick up weak signals from a noisy background. It takes advantage of the orthonormality of trigonometric functions:

$$\int_{-\pi}^{\pi} \cos(mx) \cos(nx) dx = \pi \delta_{mn}, \quad m, n \geq 1.$$

If we multiply a noisy signal with a reference signal and do integration, then all signals except the one with the same frequency as the reference signal vanish. The Lock-In amplifier is just the device that can simulate this mathematical process, which has a mixer to do multiplication, a low pass filter to throw away high frequency components, and an integrating circuit to do the final integration. The directly measured deviation signal is always very noisy because of power fluctuation and loses directional information which is essential for a feedback loop. So in a lock system, we usually apply some low frequency modulation on the source signal, then use a Lock-In amplifier to pick up the carried amplitude envelope of that low frequency, which can be seen as the directional derivative signal with respect to frequency.

In our cavity lock system, the PDH module inside controller box of 740nm Toptica diode laser puts voltage modulation with frequency ω_m on the diffraction grating piezo of external cavity diode laser. The output laser light of frequency ω is then phase-modulated by $\beta \sin(\omega_m t)$, which can be represented by its electric field with

one carrier and two sidebands

$$\begin{aligned}
 E &= E_0 e^{i(\omega t + \beta \sin(\omega_m t))} \\
 &\approx E_0 e^{i\omega t} [1 + i\beta \sin(\omega_m t)] \\
 &= E_0 e^{i\omega t} \left[1 + \frac{\beta}{2} e^{i\omega_m t} - \frac{\beta}{2} e^{-i\omega_m t} \right].
 \end{aligned}$$

Phase modulation is also widely implemented by EOMs or Acoustic-Optic Modulator(AOM)s in our laser setup to enrich frequency components. The reflection power signal about laser frequency for our F-P two mirror cavity is a single peak function with a similar shape to a sharp normal distribution function. The PDH module takes this reflection signal from the photodetector and extracts the directional derivative signal with a circuit consists of a phase shifter, a mixer and a low pass filter, which has a similar function to a Lock-In amplifier. For certain cavity length, the sharp center slope of derivative signal indicates how far laser's frequency is deviated from cavity's resonance laser frequency. The signal's sign is always the same as the sign of target frequency minus current frequency, and is suitable as an error signal for the PID to compensate laser's frequency. The PID's DC output is then added to the piezo of external cavity diode laser, thus keeps output laser's frequency synchronized with, i.e., locked to cavity's resonance laser frequency. More formal and mathematical description of this PDH method can be found in PDH's original paper [39].

With the one body high finesse confocal cavity designed by ourself and made of hard indium steel, the cavity lock system is really stable, which can even tolerate huge mechanical hit while keep the lock. The ultra low heat expansion rate of indium steel material also makes our cavity's length insensitive to lab temperature. However,

to lock the 739.0526 nm laser in 1 MHz(≈ 1.8 fm) region, for a 15 cm cavity, the desired cavity length's fluctuation should be within

$$\frac{2L}{\lambda} \Delta\lambda = \frac{2L\lambda}{c} \Delta f \approx 0.74\text{nm}.$$

To fulfill this requirement, one way is to put our cavity into a highly isolated environment, such as vacuum or cryostat, which is also helpful to cavity's finesse. Another simpler way is to use some absolute frequency reference to lock cavity's length, like a Rb-stabilized cavity. This way depends on the existence of absolute reference near your target frequency. Fortunately, Iodine molecule has a absorbing peak at $13531.2773 \text{ cm}^{-1}$, which is corresponding to wavelength 739.028532 nm and is close to our target wavelength [40]. Iodine is solid under normal condition. It's put into a vacuum vapor with a cold finger. The vapor is surrounded with heating tapes to keep it in around ~ 300 °C high temperature, under which Iodine gasify and fill into whole vapor. The directly measured absorbing peak of hot Iodine molecules is shifted by Doppler effect because of their quick motion. So we use two opposite laser beams to get the saturated Doppler-free signal. One of the beam is also phase modulated with a 15 KHz signal for the usage of Lock-In amplifier, through a 80 MHz center frequency AOM. The error signal outputs from the Lock-In amplifier indicates laser frequency deviation from Iodine's absorbing peak. This error signal is feed into another PID and feedbacks to the ± 75 V high voltage board which finally stabilizes, i.e., locks the length of cavity.

All EOMs for adding frequency sidebands or changing lock points are controlled by LabBrick signal generators, which are connected to control computers through USB cables. By changing input frequency of the fiber EOM which bridges the lock target frequency with Iodine's absorbing peak, we can precisely control our laser's

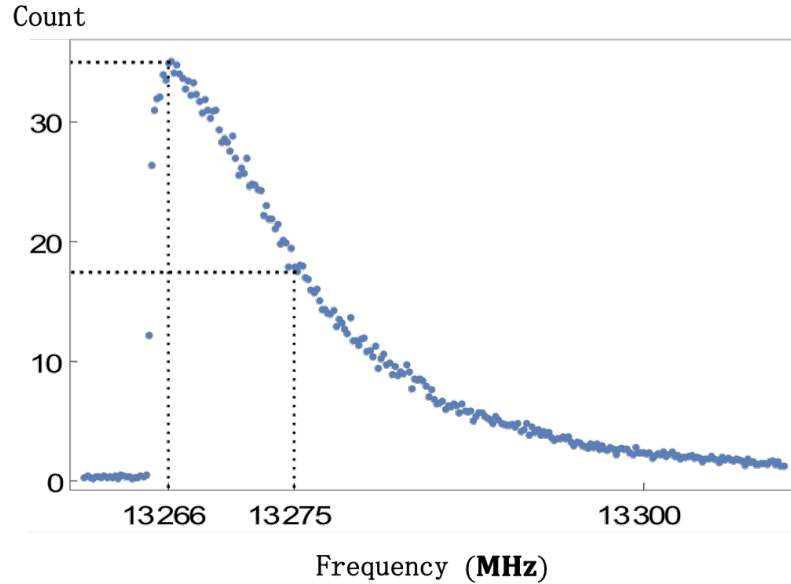


Figure 3.6.3: Graph for EOM frequency sweep, with a step of 0.1 MHz.

frequency relative to some absolute reference. Fig. 3.6.3 shows a Doppler cooling counts graph when we sweep EOM's input frequency from 13310 MHz to 13260 MHz.

From the graph we can clearly find ion's resonance point when the EOM frequency is around 13266 MHz. When EOM frequency is lower than this, which means the laser's lock frequency is higher than ion's resonance point, the ion is heated by this blue detuned laser and becomes melted. The PMT count also quickly drops to nearly zero. Usually we choose the half maximal height point of the red detuning side as laser's working lock frequency, which is around 13275 MHz for this graph. At this frequency, the counting rate has a nearly maximal increasing slope, which corresponds to a nearly maximal Doppler cooling efficiency. However, both optical pumping and detection beams require a near resonance laser frequency. So we use a higher AOM frequency for them, e.g., for Doppler cooling beam's AOM frequency

200 MHz, we set optical pumping and detection beam's AOM frequency to be $200 + 2 \times (13275 - 13266) = 218$ MHz. Here the factor 2 is because the laser lock frequency is for 740nm seed laser while AOMs are for the frequency doubled 370nm laser. Note that this EOM frequency sweep experiment should be done after micromotion compensation. Otherwise the ion will be melted before its resonance point and we will see a flat slope near to the peak of the graph.

The 935.1882 nm is directly locked to a HighFinesse wavelength meter with precision ~ 10 MHz. A custom program written in Visual Basic is used to auto-calibrated the wavelength meter every 10 seconds to compensate wavelength meter's long term drift, using the already stabilized 739.0526 nm laser's wavelength as a reference.

THIS PAGE INTENTIONALLY LEFT BLANK

Chapter 4

Quantum manipulation of trapped ions

On top of daily operations discussed in the last chapter, now we can introduce the whole working procedure of our $^{171}\text{Yb}^+$ ion system:

1. **Doppler cooling.** Cool down the ion.
2. **Optical pumping.** Initialize to state $|1\rangle$.
3. **Quantum manipulating.** Rotate state coherently with microwave or Raman laser beams (include a leading sideband cooling if needed).
4. **Florescence detecting.** Measure population of state $|1\rangle$.

For the quantum manipulation of trapped ions, following systems are used

1. **Microwave system** Manipulate internal states with direct hyperfine transitions driven by a microwave horn antenna.

2. **Raman laser system** Manipulate both internal and motional states with stimulated Raman transitions driven by a mode-locked pulse laser.

4.1 Quantum dynamics of a trapped ion

Before we start discussing quantum manipulation, some necessary theory preparations for quantum dynamics of trapped $^{171}\text{Yb}^+$ is needed.

4.1.1 Quantum picture of a trapped ion

The internal electronic structure of the ion can be approximated by a 2-level system with levels $|g\rangle$ and $|e\rangle$ of energy difference $\hbar\omega = \hbar(\omega_e - \omega_g)$. The corresponding two level system Hamiltonian $\hat{H}^{(e)}$ is

$$\begin{aligned}\hat{H}^{(e)} &= \hbar(\omega_g |g\rangle \langle g| + \omega_e |e\rangle \langle e|) \\ &= \hbar \frac{\omega_e + \omega_g}{2} (|g\rangle \langle g| + |e\rangle \langle e|) \\ &\quad + \hbar \frac{\omega}{2} (|e\rangle \langle e| - |g\rangle \langle g|) \\ &= \hbar \frac{\omega_e + \omega_g}{2} \mathbf{I} + \hbar \frac{\omega}{2} \sigma_z\end{aligned}$$

Since we will consider the evolution in the interaction picture, the constant part can be safely eliminated and only the σ_z part remains. This elimination can be easily extend to a N-level system

$$\hat{H}^{(e)} = \hbar \sum_{i=1}^N \omega_i |i\rangle \langle i| \rightarrow \hbar \sum_{i=1}^N (\omega_i - \omega_1) |i\rangle \langle i| \quad (4.1.1)$$

For the quantum-mechanical treatment of the motion, replacing the coordinate x by the respective operator \hat{x} , we can write the time-dependent potential $V(t)$ as

$$V(t) = \frac{m}{2}W(t)\hat{x}^2$$

where

$$W(t) = \frac{\omega^2}{4}(a_x + 2q_x \cos(\omega t))$$

can be thought of as a time-varying spring constant that will play a role similar to ω_m^2 in the static potential harmonic oscillator. With these definitions, the Hamiltonian of the motion $H^{(m)}$ takes a form very similar to the familiar Hamiltonian of a static potential harmonic oscillator

$$\hat{H}^{(m)} = \frac{\hat{p}^2}{2m} + \frac{m}{2}W(t)\hat{x}^2 \rightarrow \omega_m a^\dagger a \quad (4.1.2)$$

where $\omega_m = \beta_x \omega / 2$ equals to the classical secular motion frequency.

4.1.2 Interaction Hamiltonian

We can interact with ion by applying an external wave field from either microwave horn or laser beam. For dipole allowed transitions the field will be treated in the familiar dipole approximation, while for dipole forbidden transitions only the quadrupole component of the field is considered. For Raman transitions, the near-resonant intermediate level will be adiabatically eliminated, making these transitions formally equivalent to the other transition types.

Electric dipole allowed transitions, electric quadrupole allowed transitions, and stimulated Raman transitions can be described in a unified framework that associates

a certain on-resonance Rabi frequency Ω , effective light frequency ν , and effective wave vector \vec{k} with each of these transition types. The effective light frequencies and wave vectors are identical to the frequency and wave vector of the coupling light field for dipole and quadrupole transitions, but equal to the frequency difference $\nu = \nu_1 - \nu_2$ and wave vector difference $\vec{k} = \vec{k}_1 - \vec{k}_2$ of the two light fields driving the stimulated Raman transitions. For traveling wave light fields all three transition types can be described by a coupling Hamiltonian of the form

$$\hat{H}^{(i)} = \hbar\Omega(\hat{\sigma}_+ + \hat{\sigma}_-) \cos(k\hat{x} - \nu t + \phi) \quad (4.1.3)$$

$$= \frac{\hbar}{2}\Omega(\hat{\sigma}_+ + \hat{\sigma}_-)e^{i(\eta(\hat{a} + \hat{a}^\dagger) - \nu t + \phi)} + h.c. \quad (4.1.4)$$

where the Lamb-Dicke parameter $\eta = \vec{k} \cdot \vec{x}_0$, $|\vec{x}_0| = \sqrt{\hbar/(2m\omega_m)}$ is the extension along the x axis of the ground-state wave function. As we will mention later, we manipulate a $^{171}\text{Yb}^+$ ion in a $\omega_m \approx (2\pi) 3$ MHz trap with a pair of 355nm pulse laser beams, then we have $\eta \approx 0.111 \cos \theta$, where θ is the angle between laser beam and trap's X axis.

Now we have the total Hamiltonian in Schoedinger picture

$$\hat{H} = \hat{H}^{(e)} + \hat{H}^{(m)} + \hat{H}^{(i)}$$

If we label spin ground state as $|\downarrow\rangle$, excited state as $|\uparrow\rangle$, motional state as $|n\rangle$, then for transition $|\downarrow, n\rangle \leftrightarrow |\uparrow, m\rangle$, we can choose the interaction picture with respect to external field's frequency. The base Hamiltonian

$$\hat{H}_0 = \hat{H}^{(e)} + \hat{H}^{(m)} + \frac{\hbar\delta}{2}\sigma_z$$

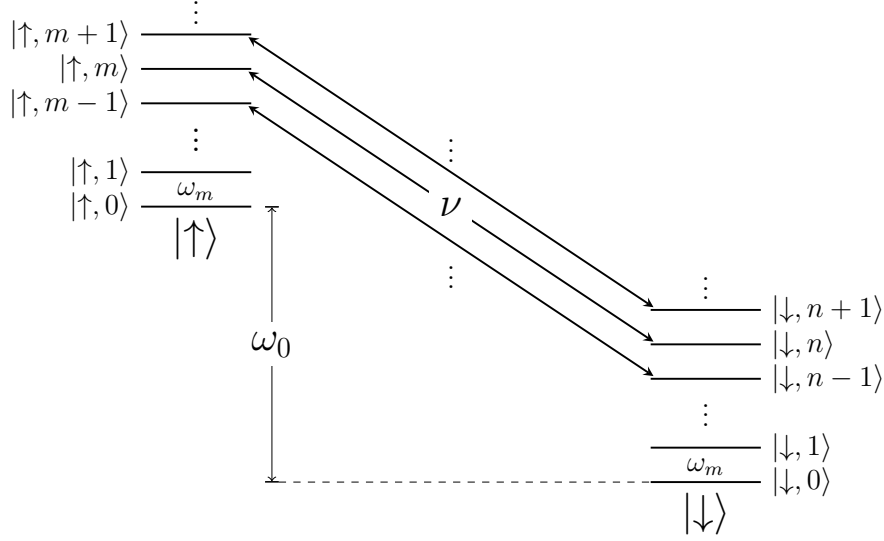


Figure 4.1.1: Resonant transitions between ion's motional levels.

where the detuning from resonance transition $\delta = \nu - \omega_0 - (m-n)\omega_m$. The transition diagram for resonant case is showed in Fig. 4.1.1. The coupling term

$$\begin{aligned}
\langle \uparrow, m | \hat{H}_I | \downarrow, n \rangle &= \langle \uparrow, m | e^{i\hat{H}_0 t/\hbar} (\hat{H} - \hat{H}_0) e^{-i\hat{H}_0 t/\hbar} | \downarrow, n \rangle \\
&= e^{i(1/2(\omega_0+\delta)+m\omega_m+1/2(\omega_0+\delta)-n\omega_m)t} \langle \uparrow, m | \hat{H}^{(i)} - \frac{\hbar\delta}{2}\sigma_z | \downarrow, n \rangle \\
&= e^{i\nu t} \langle \uparrow, m | \frac{\hbar}{2}\Omega(\hat{\sigma}_+ + \hat{\sigma}_-) e^{i(\eta(\hat{a}+\hat{a}^\dagger)-\nu t+\phi)} + h.c. | \downarrow, n \rangle \\
&= \frac{\hbar\Omega}{2} \langle m | e^{i(\eta(\hat{a}+\hat{a}^\dagger)+\phi)} + e^{i(-\eta(\hat{a}+\hat{a}^\dagger)+2\nu t-\phi)} | \downarrow, n \rangle
\end{aligned}$$

Apply rotating-wave approximation, then

$$\langle \uparrow, m | \hat{H}_I | \downarrow, n \rangle \approx \frac{\hbar\Omega}{2} e^{i\phi} \langle m | e^{i\eta\hat{a}^\dagger + i\eta\hat{a}} | n \rangle$$

Apply Baker-Campbell-Hausdorff formula

$$e^{A+B} = e^A e^B e^{-\frac{1}{2}(A,B)} e^{\frac{1}{6}(2[B,[A,B]]+[A,[A,B]])} \dots$$

and note that $[a^\dagger, a] = -1$, the result becomes

$$\begin{aligned}
& \frac{\hbar\Omega}{2} e^{-\frac{\eta^2}{2} + i\phi} \langle m | e^{i\eta a^\dagger} e^{i\eta a} | n \rangle \\
&= \frac{\hbar\Omega}{2} e^{-\frac{\eta^2}{2} + i\phi} \left(\sum_{j=0}^{\infty} \frac{(\eta\eta)^j}{j!} (a^\dagger)^j \langle m | \right) \cdot \left(\sum_{j=0}^{\infty} \frac{(\eta\eta)^j}{j!} a^j | n \rangle \right) \\
&= \frac{\hbar\Omega}{2} e^{-\frac{\eta^2}{2} + i\phi} \left(\sum_{j=0}^m \frac{(\eta\eta)^j}{j!} \sqrt{\frac{m!}{(m-j)!}} \langle m-j | \right) \cdot \left(\sum_{j=0}^n \frac{(\eta\eta)^j}{j!} \sqrt{\frac{n!}{(n-j)!}} | n-j \rangle \right) \\
&= \frac{\hbar\Omega}{2} e^{-\frac{\eta^2}{2} + i\phi} \left(\sum_{k=0}^m \frac{(\eta\eta)^{m-k}}{(m-k)!} \sqrt{\frac{m!}{k!}} \langle k | \right) \cdot \left(\sum_{k=0}^n \frac{(\eta\eta)^{n-k}}{(n-k)!} \sqrt{\frac{n!}{k!}} | k \rangle \right) \\
&= \frac{\hbar\Omega}{2} e^{-\frac{\eta^2}{2} + i\phi} \sum_{k=0}^{n_<} \frac{(\eta\eta)^{m+n-2k} \sqrt{m!n!}}{(m-k)!(n-k)!k!} \\
&= \frac{\hbar\Omega}{2} e^{-\frac{\eta^2}{2} + i\phi} (\eta\eta)^{n_>-n_<} \sqrt{\frac{n_<!}{n_>!}} \sum_{k=0}^{n_<} \frac{(\eta\eta)^{2(n_<-k)} n_>!}{(n_<-k)!(n_>-k)!k!} \\
&= \frac{\hbar\Omega}{2} e^{-\frac{\eta^2}{2} + i\phi} (\eta\eta)^{n_>-n_<} \sqrt{\frac{n_<!}{n_>!}} \sum_{k=0}^{n_<} (-1)^{n_<-k} \binom{n_>}{k} \frac{(\eta^2)^{n_<-k}}{(n_<-k)!} \\
&= \frac{\hbar\Omega}{2} e^{-\frac{\eta^2}{2} + i\phi} (\eta\eta)^{|m-n|} \sqrt{\frac{n_<!}{n_>!}} \sum_{j=0}^{n_<} (-1)^j \binom{n_< + |m-n|}{n_<-j} \frac{(\eta^2)^j}{j!} \\
&= \frac{\hbar\Omega}{2} e^{-\frac{\eta^2}{2} + i\phi} (i\eta)^{|m-n|} \sqrt{\frac{n_<!}{n_>!}} L_{n_<}^{|m-n|}(\eta^2)
\end{aligned}$$

where the definition of Laguerre polynomial is

$$L_n^\alpha(x) = \sum_{j=0}^n (-1)^j \binom{n+\alpha}{n-j} \frac{x^j}{j!} = \binom{n+\alpha}{n} - \binom{n+\alpha}{n-1} x + \dots$$

Finally we have

$$\langle \uparrow, m | \hat{H}_I | \downarrow, n \rangle \approx \frac{\hbar\Omega}{2} e^{-\frac{\eta^2}{2} + i\phi} (i\eta)^{|m-n|} \sqrt{\frac{n_{<}!}{n_{>}!}} \left(\binom{n_{>}}{n_{<}} - \binom{n_{>}}{n_{<-} - 1} \eta^2 \right) \quad (4.1.5)$$

4.2 Microwave system

For a lot of experiments, the hyperfine level $|1\rangle = |F = 0, m = 0\rangle$ and Zeeman splitting levels $|2\rangle = |F = 1, m = -1\rangle$, $|3\rangle = |F = 1, m = 0\rangle$, $|4\rangle = |F = 1, m = 1\rangle$ are used together as a 4-level system. The energy gap between hyperfine states $|1\rangle$ and $|3\rangle$ is

$$\omega_{\text{HF}} = 12.642812118466 + \delta_{2z} \text{ GHz} \quad (4.2.1)$$

where the second order Zeeman shift

$$\delta_{2z} = (310.8)B^2 \text{ Hz} \quad (4.2.2)$$

and the unit of magnetic field B is gauss. Standard commercial microwave signal sources can easily generate this frequency and drive transitions. The transition diagram is showed in Fig. 4.2.1.

We put magnets or Helmholtz magnetic coils on top of vacuum chamber to maintain a quantization axis and certain Zeeman splittings. The energy gap between $|3\rangle, |2\rangle$ and $|4\rangle, |3\rangle$ is both $1.4B$ MHz. The static magnetic field strength B at ion's position is typically ~ 10 gauss with coil current $\sim 3A$. Two pairs of auxiliary magnetic coils are installed to compensate static magnetic fields' direction. For the quantum operations with microwaves, the main device we control is a 1 GHz sampling rate PCI-board Arbitrary Waveform Generator(AWG) ¹. It's used to generate

¹<http://www.chase-scientific.com>

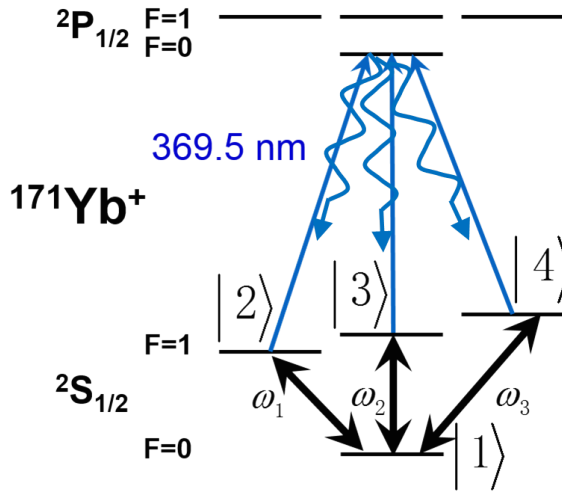


Figure 4.2.1: Microwave transitions and state detection of $^{171}\text{Yb}^+$.

arbitrary waveforms from 150 ~ 250 MHz. The output of AWG is then mixed with a ~ 12.44 GHz microwave provided by an Agilent microwave source. Both them are externally referenced by a 10 MHz Rb atomic clock.

The AWG board is another main device in our system and is the key part to both microwave and Raman laser operations. The board's driver library accept a number array and output the interpolation voltages with a fixed 1 GHz sampling rate. In reality, the quantum gates or Hamiltonians we implement can always be represented as a piecewise analytic function. So we define a CSV-based wave file format which has a segments structure and each segment has several standard parameters. An example wave file is showed in Table 4.1.

Table 4.1: An example wave file of Ramsey interferometry measurement.

Frequency	Duration	Amplitude	Phase	Gap	Formula
189.4681	1.156	0.4	0	1.	
189.4681	1.156	0.4	0.5	1.	$a*\cos(w*(t-g0)+p)$

The first line with a empty “Formula” field represents a standard cosine waveform “ $a*\cos(w*t+p)$ ”, where “a” refers to Amplitude field 0.4, “w” refers to 2π times the “Frequency” field 189.4681 MHz and “p” refers to “Phase” field 0. The second line has a similar explanation, except that “g0” refers to “Gap” field in the first/0th line. This wave file is used for Ramsey measurement of state $|2\rangle$, we can scan the “Gap” parameter of the first line. Note that the phase defined in wave file is the relative phase with respect to the start time of each line. Then the data we get should be a sine curve about this “Gap” and population of state $|2\rangle$, whose frequency is just the frequency gap between the Ramsey frequency of $|2\rangle$ and the “Frequency” field in the wave file. We can then use sine curve data fitting to calculate the correct Ramsey frequency. There are a lot of other functions and variables can be used in the formula field, thus makes this wave file format expressive enough for our quantum operations. The segment and parameter structure also makes it highly compatible with the linear scanning operation pattern. Multiple segments wave file can be defined by adding a blank line between different segments. Segments can be sequentially triggered in one experiment by pulse sequencer. We keep track of all start times to maintain the phase continuation and simulate the behavior of a continuous signal source. Finally the wave file is sampled to arrays of discrete voltage values and programmed to the AWG board.

After amplification with fan and water cooled 2-level amplifier system, the mixed microwave finally applies to the trap through a horn antenna. The maximal output power of the last amplifier ² is around 10 W. The output microwave forms a standing wave inside the chamber. The horn is mounted on a translation stage. We can adjust its height or direction by moving or rotating stage, thus changing microwave’s polarization or strength. With a careful optimization of transition stage, currently

²<http://www.bonn-elektronik.com>

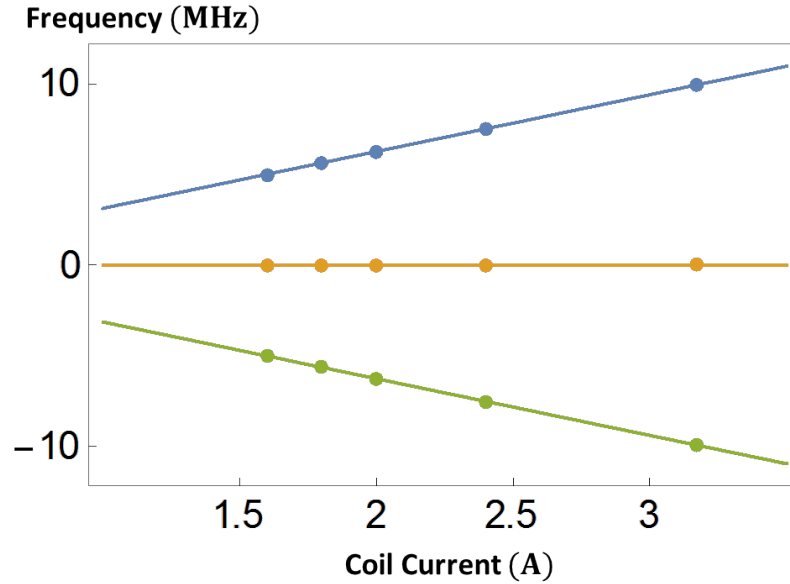


Figure 4.2.2: Zeeman levels' resonant frequencies. The zero point of vertical axis is 12.642812118466 GHz. Dots are experimental data and solid lines are fitted curves.

the Rabi flopping π times between $|1\rangle$ and $|2\rangle$, $|3\rangle$, $|4\rangle$ are $\sim 1.5\mu s$, $4\mu s$, $1.5\mu s$, with fidelity $\sim 99\%$. Further improvement can be achieved by replacing the normal mixer with an IQ mixer.

In experiments, we can scan AWG's frequency to find resonance peaks and scan AWG's duration to find resonance strength. A graph of Zeeman levels' resonant AWG frequencies with different coil currents ranging from 1.6A to 3.2A is showed in Fig. 4.2.2.

Fig. 4.2.3 shows a typical averaged Rabi flopping data from $|1\rangle \rightarrow |2\rangle$ with microwaves.

We fit left figure with a sine curve and find its $1/2$ Rabi period to be $2.25 \mu s$. Right figure shows a Poisson distribution histogram of actually PMT counts for the highest point where all population is transfered from $|1\rangle$ to $|2\rangle$.

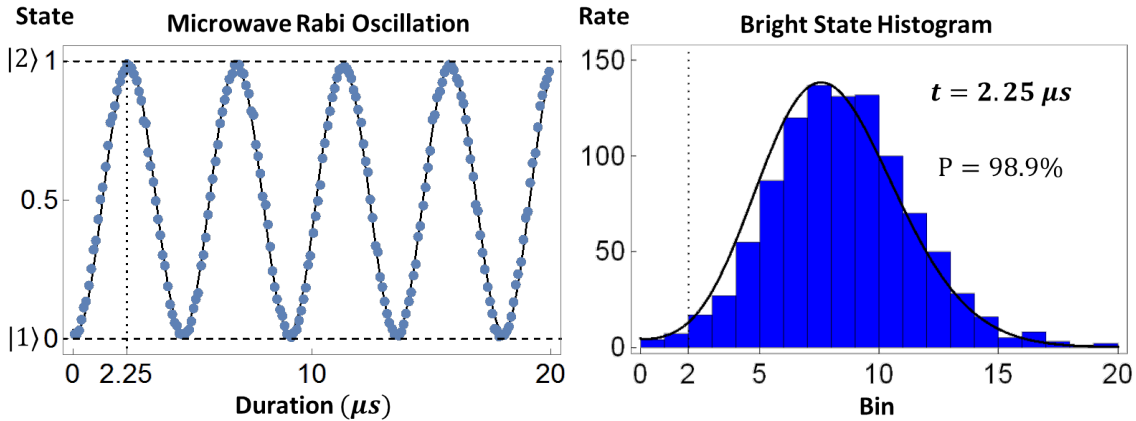


Figure 4.2.3: Rabi flopping from $|1\rangle \rightarrow |2\rangle$. The data is averaged over 1000 repeated experiments. Points or bars are real data, while dark solid lines are fitted curves.

4.3 Raman laser system

For a higher degree of control in quantum regime, motional degrees of freedom are then added to our system with stimulated Raman transitions implemented by mode-locked pulse lasers.

4.3.1 Stimulated Raman transition

The well-known Raman transition happens between two levels who both have interactions with a common third level. A good analytic way to study Raman transition is the “effective Hamiltonian” method [41]. Consider the case of a three level system in Fig. 4.3.1.

There are interactions between $|1\rangle \leftrightarrow |3\rangle$ and $|2\rangle \leftrightarrow |3\rangle$, each with a Rabi frequency Ω_i and a detuning Δ_i from resonance frequency ω_i , $i = 1, 2$, e.g., the interaction by a wave field with frequency $\nu_i = \omega_i + \Delta_i$. The static Hamiltonian for this

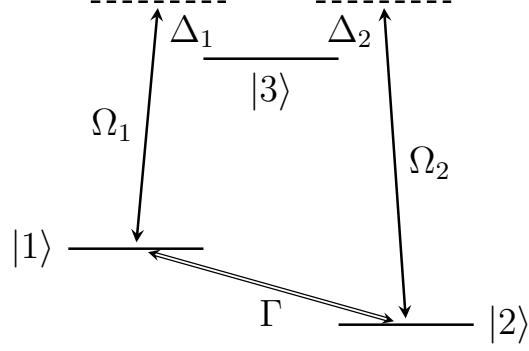


Figure 4.3.1: Raman transition in a three level system.

three level system is

$$\hat{H}^{(e)} = -\hbar\omega_1 |1\rangle \langle 1| - \hbar\omega_2 |2\rangle \langle 2| \quad (4.3.1)$$

and the interaction Hamiltonian is

$$\hat{H}^{(i)} = \hbar\Omega_1 \cos((\omega_1 + \Delta_1)t + \phi_1) |1\rangle \langle 3| \quad (4.3.2)$$

$$+ \hbar\Omega_2 \cos((\omega_2 + \Delta_2)t + \phi_2) |2\rangle \langle 3| + h.c. \quad (4.3.3)$$

In the interaction picture of $\hat{H}^{(e)}$, the Hamiltonian becomes

$$\begin{aligned} \hat{H}_I(t) &= e^{i\hat{H}^{(e)}t/\hbar} \hat{H}^{(i)} e^{-i\hat{H}^{(e)}t/\hbar} \\ &= (e^{-i\omega_1 t} |1\rangle \langle 1| + e^{-i\omega_2 t} |2\rangle \langle 2| + |3\rangle \langle 3|) \\ &\quad \cdot \frac{\hbar}{2} (\Omega_1 e^{i(\omega_1 + \Delta_1)t + \phi_1} |1\rangle \langle 3| + \Omega_2 e^{i(\omega_2 + \Delta_2)t + \phi_2} |2\rangle \langle 3| + h.c.) \\ &\quad \cdot (e^{i\omega_1 t} |1\rangle \langle 1| + e^{i\omega_2 t} |2\rangle \langle 2| + |3\rangle \langle 3|) \\ &= \frac{\hbar\Omega_1}{2} (e^{i(\Delta_1 t + \phi_1)} + e^{-i[(2\omega_1 + \Delta_1)t + \phi_1]}) |1\rangle \langle 3| \\ &\quad + \frac{\hbar\Omega_2}{2} (e^{i(\Delta_2 t + \phi_2)} + e^{-i[(2\omega_2 + \Delta_2)t + \phi_2]}) |2\rangle \langle 3| + h.c. \end{aligned}$$

Applying rotating wave approximation, we have

$$\hat{H}_I(t) \approx \frac{\hbar\Omega_1}{2} e^{i(\Delta_1 t + \phi_1)} |1\rangle \langle 3| + \frac{\hbar\Omega_2}{2} e^{i(\Delta_2 t + \phi_2)} |2\rangle \langle 3| + h.c. \quad (4.3.4)$$

The effective Hamiltonian of $\hat{H}_I(t)$ is

$$\begin{aligned} \hat{H}_{eff} = & \frac{\hbar\Omega_1^2}{4\Delta_1} (|1\rangle \langle 1| - |3\rangle \langle 3|) + \frac{\hbar\Omega_2^2}{4\Delta_2} (|2\rangle \langle 2| - |3\rangle \langle 3|) \\ & + \frac{\hbar\Omega_1\Omega_2}{8} \left(\frac{1}{\Delta_1} + \frac{1}{\Delta_2} \right) (|1\rangle \langle 2| e^{i[(\Delta_1 - \Delta_2)t + (\phi_1 - \phi_2)]} - |2\rangle \langle 1| e^{-i[(\Delta_1 - \Delta_2)t + (\phi_1 - \phi_2)]}) \end{aligned} \quad (4.3.5)$$

The first two terms are A.C. Starks shifts associated with the two interactions. The second pair of terms represent the Raman transition between $|1\rangle \leftrightarrow |2\rangle$. The Raman transition has a Rabi frequency

$$\Omega(\Gamma) = \frac{\Omega_1\Omega_2}{8} \left(\frac{1}{\Delta_1} + \frac{1}{\Delta_2} \right) \quad (4.3.6)$$

a detuning

$$\Delta(\Gamma) = \Delta_1 - \Delta_2 \quad (4.3.7)$$

and a phase

$$\phi(\Gamma) = \phi_1 - \phi_2 + \frac{\pi}{2} \quad (4.3.8)$$

The additional $\pi/2$ phase comes from the different sign between $|1\rangle \langle 2|$ and $|2\rangle \langle 1|$. Since the approximation is only related to time, for travelling wave $\cos(\vec{k}_i \cdot \vec{x} - \nu_i t + \phi_i)$, the space dependent part $\vec{k}_i \cdot \vec{x}$ can also be merged into phase ϕ_i . So the Hamiltonian of this Raman transition is equivalent to the interaction Hamiltonian (after rotating wave approximation) of a wave field with frequency $\Delta\nu = \nu_1 - \nu_2$ and wave vector $\Delta\vec{k} = \vec{k}_1 - \vec{k}_2$. We can also drive Raman transition between ion's motional levels, as

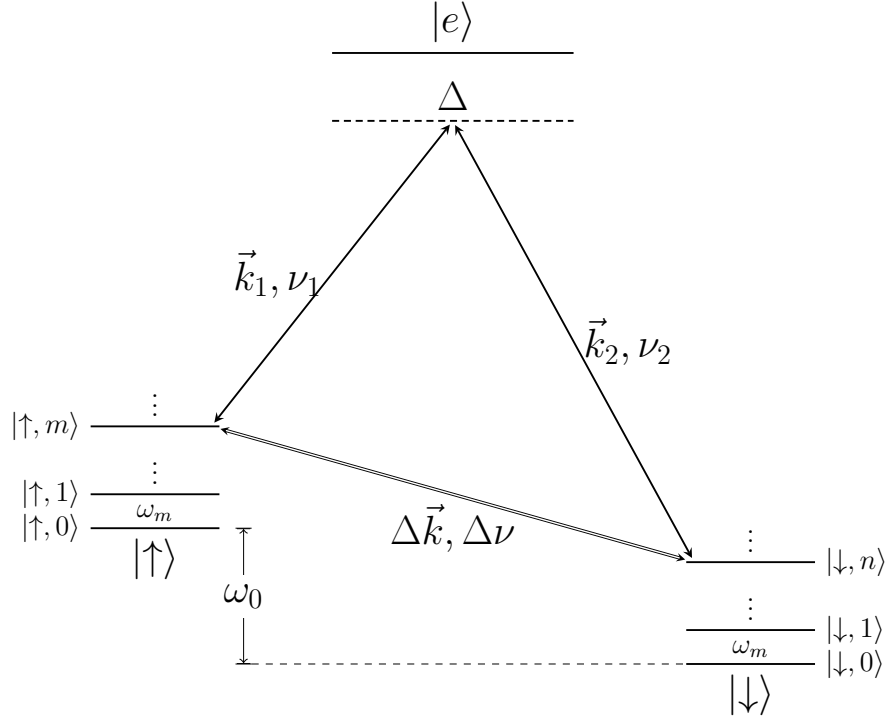


Figure 4.3.2: Raman transition between ion's motional levels.

it shows in Fig. 4.3.2.

A more intuitive way to understand ion's Raman transition is to think it as a two photons process. The ion first absorb a photon with frequency ν_1 coming from direction \vec{k}_1 , and jumps from $|\uparrow, m\rangle$ to an intermediate virtual level near to $|e\rangle$. Then it stimulatedly emits a photon with frequency ν_2 along direction \vec{k}_2 , and jumps to $|\downarrow, n\rangle$. In this whole process, ion's internal level energy changes by $\hbar\Delta\nu = \hbar(\nu_1 - \nu_2)$ and momentum changes by $\hbar\Delta\vec{k} = \hbar(\vec{k}_1 - \vec{k}_2)$.

4.3.2 Mode-locked pulse laser

Consider a resonant laser Raman transition between $^{171}\text{Yb}^+$ hyperfine levels $|1\rangle \leftrightarrow |3\rangle$, through the optical level $^2P_{1/2}$. Then we need two laser beams with wavelengths near 370nm. And the center frequency difference of this two laser beams have to be $\omega_{\text{HF}} \approx 12.6$ GHz. One way of generating this frequency difference is using a EOM driven by a 12.6 GHz RF source. However, an EOM working at this high frequency is not that efficient. Moreover, different sidebands after a EOM is not separated, which make a vanish Raman wave vector and have no coupling with motional levels. So instead of using EOM, we use another more efficient way which is based on mode-locked pulse laser's frequency comb. Mode-locked lasers can be used to produce a broadband optical frequency comb with overall bandwidth ranging from 10 GHz – 100 THz with comb teeth that are spaced by the repetition rate of the laser, typically in the range 0.1 – 1 GHz.

We already use a lot of CW (continuous wave) diode lasers in previous setup. Mode-locked pulse laser is also based on the CW laser. We know that a cavity with length L always have many equally spaced longitudinal modes. The minimal separation between these modes is

$$\delta\omega = \frac{\pi c}{L}$$

So the laser beam coming from a laser resonant cavity also contains many modes (frequency comb). Consider a laser with center frequency ω_0 and $2N + 1$ modes, which means its broadening is $2N\delta\omega$. The traveling wave electric field of this laser can be written as

$$E(z, t) = \sum_{n=-N}^N E_n e^{i[(\omega_0 + n\delta\omega)(t - z/c) + \phi_n]} \quad (4.3.9)$$

For normal CW laser there is no coherence between different modes, which means phase ϕ_n is randomly distributed. The laser power $I_{\text{cw}} = (2N + 1)I_0$ is just a summation of these modes. For a mode-locked laser, all phases are synchronized and locked to a same value. Setting this phase to be 0 and all $E_n = E_0$ (this approximation is valid near center frequency), add these modes coherently and we have

$$E(z, t) = E_0 e^{i\omega_0(t-z/c)} \frac{\sin((2N + 1)\delta\omega(t - z/c)/2)}{\sin(\delta\omega(t - z/c)/2)} \quad (4.3.10)$$

The beam power

$$I(z, t) \propto |E(z, t)|^2 = E_0^2 \frac{1 - \cos((2N + 1)\delta\omega(t - z/c))}{1 - \cos(\delta\omega(t - z/c))} \quad (4.3.11)$$

is a period pulse function with frequency $\delta\omega$ in time domain. The frequency $\delta\omega$ is also called repetition rate for a pulse laser. The peak power $I_{\text{peak}} = (2N + 1)^2 I_0$ is $2N + 1$ times of the normal CW laser output power.

Two different kinds of daily used mode-locked pulse lasers in our lab. The first one is “Mira-HP” from Coherent. It’s pumped by a green CW laser beam coming from a 10 Watts “Verdi 10” solid laser or a 18 Watts “G18” solid laser. Its center wavelength can be adjusted from 700nm to 980nm. A SHG accessory is installed to doubling laser’s frequency. After SHG, its output power is ~ 600 mW at 375 nm. Its cavity length can also be finely tuned through a PZT or a stepping motor, which results in a lockable repetition rate around 76 MHz. The second one is “Paladin”, also from Coherent. This is a industrial laser with a ~ 4 W output power at 355 nm. Its repetition rate is fixed at 120.15344 MHz. The working principles of this two lasers are basically the same. Fig. 4.3.3 shows optical paths related to the 355nm “Paladin” laser.

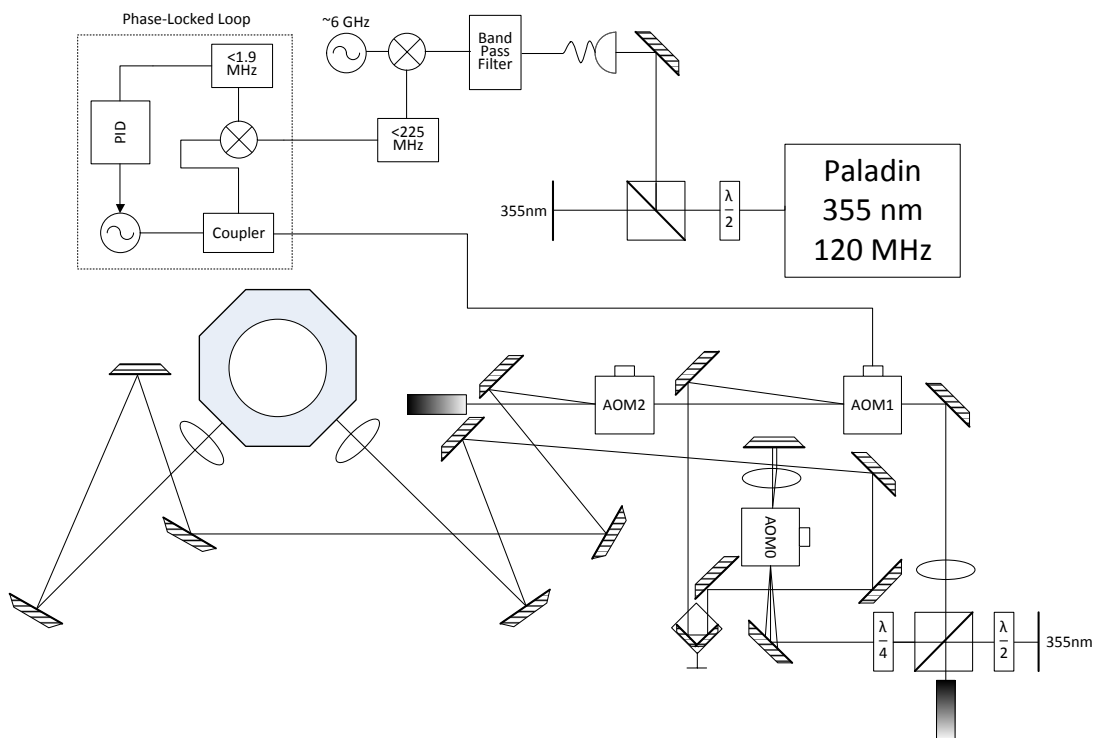


Figure 4.3.3: Diagram of optical paths for 355 nm pulse laser.

The 355nm laser beam is split into two paths at AOM1. The zero-th order beam passes through AOM2. AOM2's first order beam Raman2 then meets with AOM1's first order beam Raman1 at ion's position. The two AOMs: AOM1 and AOM2 are driven with different frequencies, let's say ν_1 and ν_2 . A pulse laser's frequency spectrum is a equally spaced comb. So all the possible Raman transitions driven by this two beams is

$$\omega = |\nu_1 - \nu_2 + k\delta\omega|, k \in \mathbb{Z} \quad (4.3.12)$$

For certain ω , this equation is equivalent to

$$|\omega - k\delta\omega| = |\nu_1 - \nu_2| \leq \nu_{\text{gap}}, k \in \mathbb{Z} \quad (4.3.13)$$

and

$$\frac{\omega - \nu_{\text{gap}}}{\delta\omega} \leq k \leq \frac{\omega + \nu_{\text{gap}}}{\delta\omega} \quad (4.3.14)$$

where ν_{gap} is the gap between maximal and minimal efficient driven frequency of AOM. We use AOMs from Brimrose with a center frequency 210 MHz and bandwidth 50 MHz. By real efficiency test we choose the working frequency interval to be [190, 230] MHz. So $\nu_{\text{gap}} = 40$ MHz. If $\omega = \omega_{\text{HF}} = 12642.81212$ MHz, then $104.889 \leq k \leq 105.555$. The only integer solution of k is $k = 105$. With this solution, $\Delta\nu = |\nu_1 - \nu_2| = 26.7$ MHz. We choose $\nu_1 = 193.3$ MHz and $\nu_2 = 220$ MHz, then

$$(\omega_0 + (n + 105)\delta\omega + \nu_2) - (\omega_0 + n\delta\omega + \nu_1) = \omega_{\text{HF}} \quad (4.3.15)$$

The $(n+105)$ th mode in Raman2 and the n th mode in Raman1 ($n = 0, \pm 1, \pm 2, \dots, \pm N$) makes a Raman transition between hyperfine levels $|1\rangle \leftrightarrow |3\rangle$. As it shows in Fig.

[4.3.4.](#)

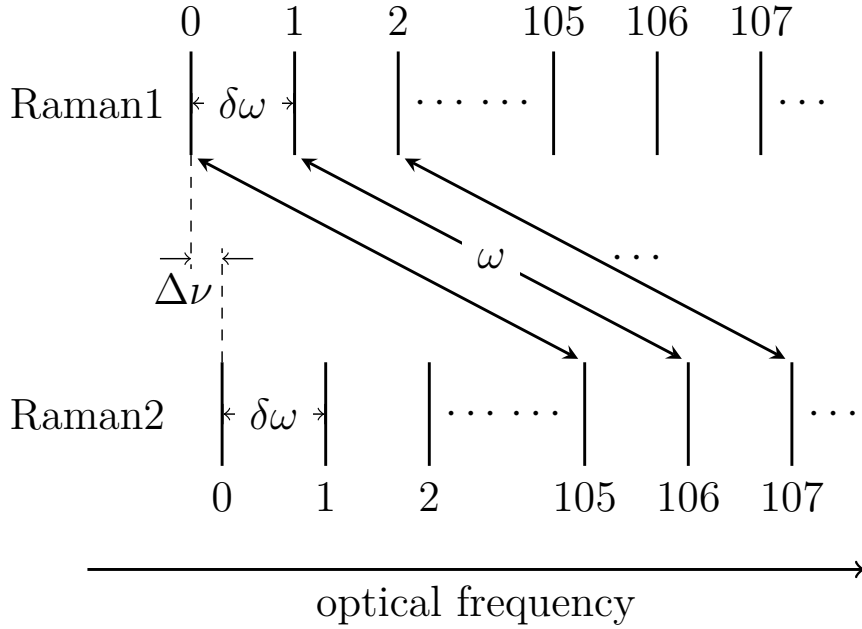


Figure 4.3.4: Frequency difference generated by pulse laser's frequency comb.

Note that the other direction of combs combination may also drive transitions:

$$|\nu_2 - \nu_1| = \Delta\nu \text{ or } \delta\omega - \Delta\nu$$

The corresponding resonance frequencies of ν_2 are

$$\nu_2 = \nu_1 \pm \Delta\nu \text{ or } \nu_1 \pm (\delta\omega - \Delta\nu)$$

In some experiments we need to manipulate all Zeeman levels simultaneously and we feed several driven frequencies to AOM2, within the range from ~ 210 MHz to ~ 230 MHz. Besides this frequency relationship, there are also constraints on the optical path lengths of Raman_{*i*} ($i = 1, 2$) from AOM1 to ion's position. The relative phase of Raman transition driven by the $(n+105)$ th mode in Raman2 and the n th

mode in Raman1 is

$$\phi_n = \frac{\delta\omega}{c}[(n + 105)z_2 - nz_1] = \frac{\delta\omega}{c}(n\Delta z + 105z_2), n = 0, \pm 1, \pm 2, \dots, \pm N \quad (4.3.16)$$

where $\Delta z = z_2 - z_1$. Define

$$\delta\phi = \frac{\delta\omega\Delta z}{c}$$

Assume all modes in b_i have the same amplitude, then the total Rabi frequency of these transitions is

$$\Omega = \left| \frac{1 - e^{i(2N+1)\delta\phi}}{1 - e^{i\delta\phi}} \right| \Omega_0 \quad (4.3.17)$$

where Ω_0 is Rabi frequency of the Raman transition driven by one pair of modes. Similar to pulse laser in frequency domain, this is a period pulse function with space frequency $\delta\omega/c$ as a function of Δz . The peak ratio of $\Omega/\Omega_0 = 2N + 1$ and occurs at $\Delta z = 2k\pi c/\delta\omega$, $k = 0, \pm 1, \pm 2, \dots$. An intuitive way to understand this constraint is two pulses for Raman transitions should arrive at the same time. Since $2k\pi c/\delta\omega \approx 15.7$ m is a very long distance, in our setup we simply choose $\Delta z = 0$. The first sideband beam Raman2 of AOM2 is lead to another side of the trap and has a longer natural optical path length. To compensate this difference, we setup several mirrors to make an additional U turn for the first sideband beam Raman1 of AOM1. We also put a pair of orthogonal mirrors mounted on a 1D transition stage to finely tune the optical length. To measure the optical length, we use a fishing line to simulate beam paths step by step and then measure the total length with a ruler. A more accurate way is to measure the difference of arriving time at the other side view ports of the trap, with a coincidence counting device such as our homemade TDC or a commercial device from PicoHarp. However, the fishing line method works amazingly well. After a coarse measurement and adjustment, we only fine tune the

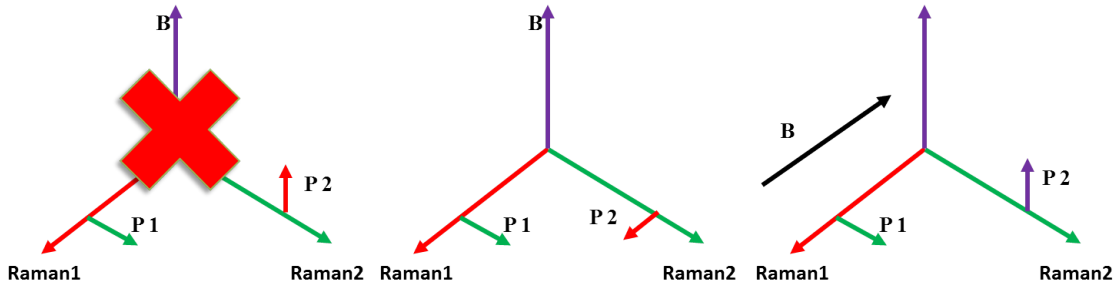


Figure 4.3.5: Polarization configurations of different Raman beams. The first polarization setup does not drive a transition between $|1\rangle \leftrightarrow |3\rangle$.

1D transition stage within several centimeters and can make the two pulses arrive at the same time.

Raman beams' polarizations with respect to magnetic field is also an important factor. For example, if one beam is π polarization, another beam is the orthogonal $|H\rangle = (\sigma_+ + \sigma_-)/\sqrt{2}$ polarization, then no Raman transition is driven between $|1\rangle \leftrightarrow |3\rangle$. Both $|1\rangle$ and $|3\rangle$ have a magnetic quantum number $m = 0$. π polarization makes a $\Delta m = 0$ transition while σ_{\pm} polarization makes a $\Delta m = \pm 1$ transition. So there is no compatible common level that can be reached from both $|1\rangle$ and $|3\rangle$ with proper polarizations. Fig. 4.3.5 shows this situation and some possible alternative polarization configurations.

The remaining problem of frequency comb scheme is that we need 105 times higher stability of repetition rate to make a frequency stable Raman transition. However, there is a smart way to get rid of the repetition rate stability problem. As we already know, the power envelop of a pulse laser is a period function with frequency same to the repetition rate. So we use a fast photo-diode to measure pulse laser's power. The power signal is mixed with a atomic clock referenced RF source to get a frequency difference between repetition rate's 52 th multiple frequency $52\delta\omega$ and

the reference RF frequency ω_{ref} . We pick out two times of this frequency difference as the driven frequency ν_1 of AOM1, through a frequency doubler and a low pass filter. A phase-locked loop [42] is used to generate a amplitude stable output and feed to AOM1. With this setup, we always have

$$\nu_1 = 2(52\delta\omega - \omega_{\text{ref}})$$

. The center frequency difference of beam Raman2 and Raman1 becomes

$$(\omega_0 + 105\delta\omega + \nu_2) - (\omega_0 + \nu_1) = 2\omega_{\text{ref}} + \delta\omega + \nu_2 \quad (4.3.18)$$

This frequency difference only depends on one time of $\delta\omega$, which usually has a fluctuation < 100 Hz under our lab temperature. For “Mira-HP”, we can also directly use the differential frequency as the error signal and make a feedback system to lock the cavity length through the PZT or stepping motor. With stabilized differential frequency, we can use Raman beams to drive different transitions by dynamically changing drive frequency of AOM1 just like using microwaves. Fig. 4.3.6 shows a graph of Raman spectrum data consisting of many peaks.

This data is taken without precise micromotion compensation and Zeeman levels compensation. So the spectrum is complex and includes $|1\rangle \leftrightarrow |3\rangle$ carrier transitions, first or more orders of X,Y mode blue and red sideband transitions, micromotion sideband transitions and Zeeman levels transitions. The lower figure shows a comparison of their measured positions and theoretic predict positions. As we already mentioned, micromotion sidebands can be minimized by carefully adjusting micromotion bias voltages. Zeeman levels transitions can also be eliminated by adjusting compensation magnetic coils’ currents and the polarization of input beams. After

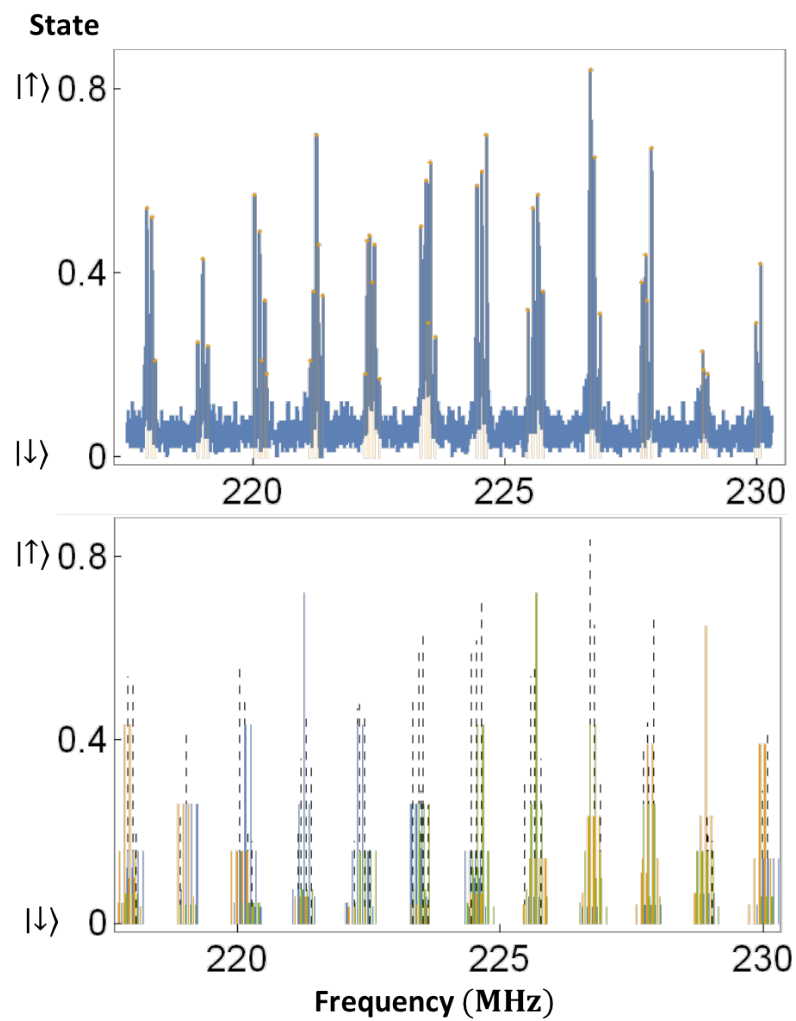


Figure 4.3.6: Raman spectrum depending on the frequency of AOM2.

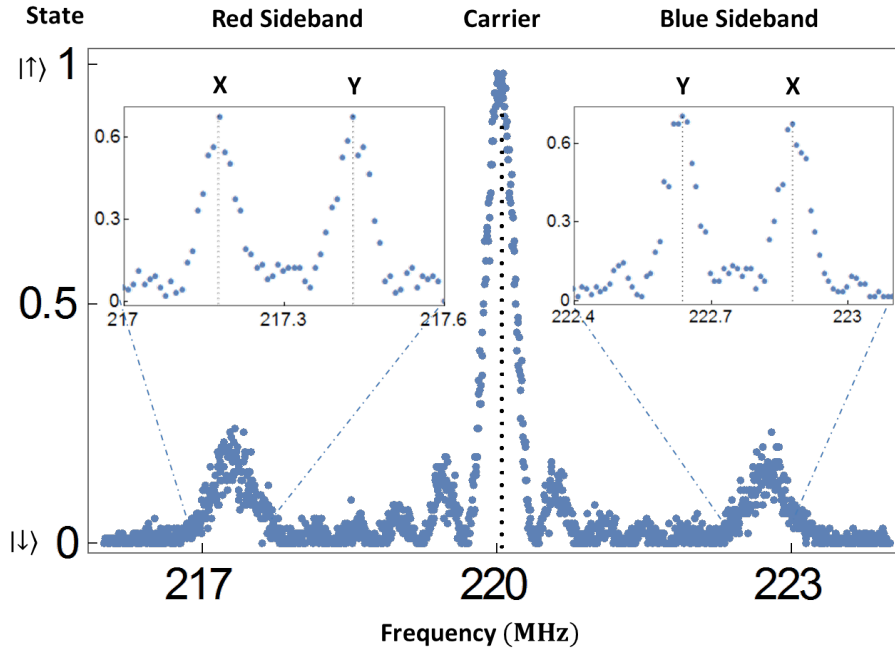


Figure 4.3.7: Raman spectrum of carrier transition, first blue sideband transitions and first red sideband transitions. We can see the two different trap modes along X and Y axis.

these optimization, we can get a graph of clear carrier transition and first sideband transitions of X,Y modes, as it shows in Fig. 4.3.7.

Both Raman beams are tightly focused at ion's position with lens to maximize power intensity and reduce possible fluctuations. The ion is put at the flat center of beams' Gaussian profiles, which can be measured with Rabi frequency measurements by sweeping 3D transition stage positions of lens. After carefully optimizing focus point of lens, we make a half beam waist $\sim 50 \mu\text{m}$ at ion's position. Under this condition, a $\sim 1 \mu\text{s}$ Rabi π time of carrier transition is achieved with each Raman beam power $\sim 30 \text{ mW}$.

A single pulse beam consists of many frequency components, so the Raman tran-

sition can also be driven with only one beam, except that the Raman wave vector is always zero. One beam Raman transition is useful during alignment. We can use it to align each beam to ion's position independently. The strength of one beam Raman transition is decided by the minimal frequency gap between the resonance frequency and integral multiples of repetition rate, which equals to $|\nu_1 - \nu_2|$. For Paladin case, this value is 26.7 MHz and is too far detuned to see any population oscillation signal. So we setup a double pass AOM0 to generate sidebands inside one beam. After the beam passes through AOM0 for the first time, both zero-th order and first order are parallel reflected by a combination of lens and mirror. They pass through AOM0 for the second time. Let's use an array (s_1, s_2) to label the final beam, where s_i represent the s_i th order sideband after the i th pass, $i = 1, 2$. Then $(1, 1)$ beam has a frequency shift of two times driven frequency and is merged with $(0, 0)$ beam which has no frequency shift. With this double pass scheme, AOM0 works just like a EOM and can also be used for amplitude stabilization. The power ratio of $(0, 0)$ and $(1, 1)$ among input power can be adjusted by changing driven signal's amplitude.

4.3.3 Sideband cooling

Define

$$\Omega_0 = e^{-\frac{\eta^2}{2}} \Omega \quad (4.3.19)$$

For carrier transition $|\downarrow, n\rangle \leftrightarrow |\uparrow, n\rangle$, Rabi frequency

$$\Omega_c \approx \Omega_0(1 - n\eta^2) \approx \Omega_0 \quad (4.3.20)$$

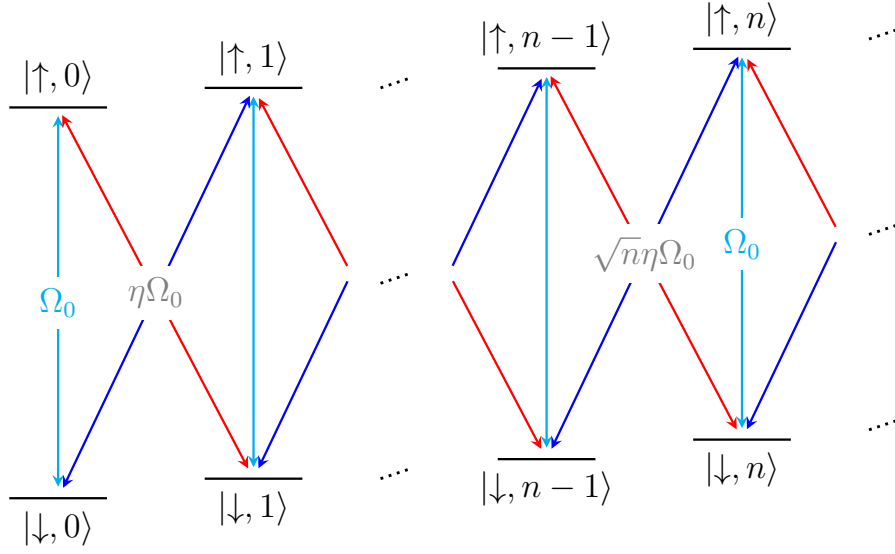


Figure 4.3.8: Carrier transitions (cyan), first blue sideband transitions (blue) and first red sideband transitions (red).

For first blue sideband transition $|\downarrow, n-1\rangle \leftrightarrow |\uparrow, n\rangle$ and first red sideband transition $|\downarrow, n\rangle \leftrightarrow |\uparrow, n-1\rangle$, Rabi frequency

$$\Omega_b = \Omega_r \approx \sqrt{n}\eta\Omega_0\left(1 - \frac{n-1}{2}\eta^2\right) \approx \sqrt{n}\eta\Omega_0 \quad (4.3.21)$$

The diagram for these three types of basic but important transition is showed in Fig. 4.3.8.

With red sideband transitions, we can further cool ion's vibrational mode to the ground state $|n=0\rangle$ by resolved sideband cooling [43]. The diagram of sideband cooling is showed in Fig. 4.3.9.

The duration for the k th red sideband transitions is t_k . We alternatively drive red sideband transitions and optical pumping transitions to lower down the average phonon number of ion's vibrational mode. After the initial Doppler cooling and

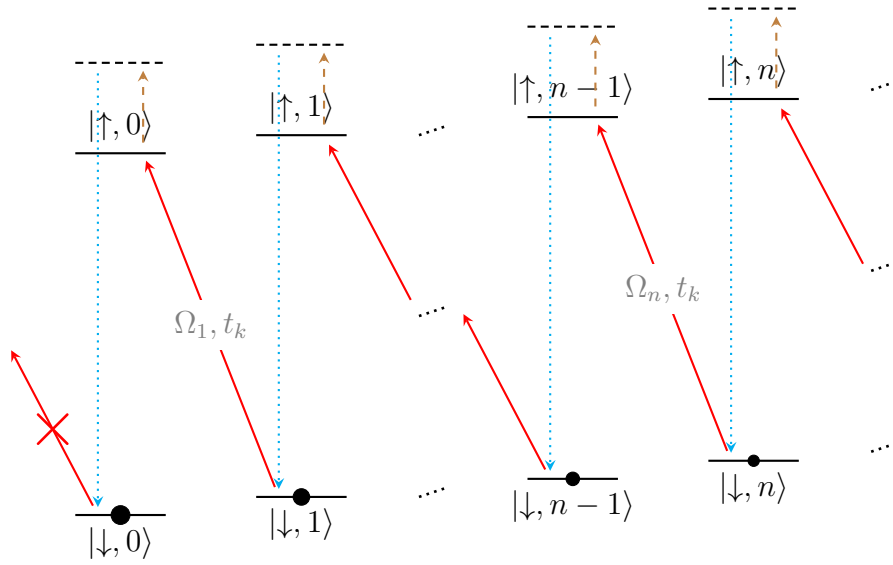


Figure 4.3.9: Diagram of sideband cooling. Dashed lines and dotted lines stand for optical pumping transitions. Solid lines stand for red sideband transitions.

optical pumping operation, the ion is in some down state $|\psi_0\rangle$. We can assume the ion to be in a pure state for simplicity, while a similar discussion can be easily extended for mixed states. Then it can be expressed as

$$|\psi_0\rangle = \sum_{n=0}^{\infty} c_n |\downarrow, n\rangle$$

It has an average phonon number

$$N_0 = \langle \psi_0 | a^\dagger a | \psi_0 \rangle = \sum_{n=0}^{\infty} n |c_n|^2$$

After the first red sideband transitions of duration t_1 , the state becomes

$$\begin{aligned} |\psi_0\rangle &\xrightarrow{t_1} \sum_{n=0}^{\infty} c_n \left(\cos\left(\frac{\Omega_n}{2}t_1\right) |\downarrow, n\rangle + \sin\left(\frac{\Omega_n}{2}t_1\right) |\uparrow, n-1\rangle \right) \\ &= \sum_{n=0}^{\infty} \left(c_n \cos\left(\frac{\Omega_n}{2}t_1\right) |\downarrow, n\rangle + c_{n+1} \sin\left(\frac{\Omega_{n+1}}{2}t_1\right) |\uparrow, n\rangle \right) \end{aligned}$$

Then an optical pumping beam is applied and all population of up states is merged into their corresponding down states. The state's density matrix becomes

$$\rho(\psi_1) = \sum_{n=0}^{\infty} \left(|c_n|^2 \cos^2\left(\frac{\Omega_n}{2}t_1\right) + |c_{n+1}|^2 \sin^2\left(\frac{\Omega_{n+1}}{2}t_1\right) \right) |\downarrow, n\rangle \langle \downarrow, n|$$

Its average phonon number is

$$\begin{aligned} N_1 = \text{Tr}(\rho_1 \cdot a^\dagger a) &= \sum_{n=0}^{\infty} n |c_n|^2 \cos^2\left(\frac{\Omega_n}{2}t_1\right) + \sum_{n=0}^{\infty} n |c_{n+1}|^2 \sin^2\left(\frac{\Omega_{n+1}}{2}t_1\right) \\ &= \sum_{n=0}^{\infty} n |c_n|^2 \cos^2\left(\frac{\Omega_n}{2}t_1\right) + \sum_{n=1}^{\infty} (n-1) |c_n|^2 \sin^2\left(\frac{\Omega_n}{2}t_1\right) \end{aligned}$$

After this process, the average phonon number is lowered by

$$N_0 - N_1 = \sum_{n=1}^{\infty} |c_n|^2 \sin^2\left(\frac{\Omega_n}{2}t_1\right) \geq 0$$

We can repeat this process for many times until the ion is cooled down. In reality, we can find a upper bound M of the maximal phonon number after the initial Doppler cooling and optical pumping, which means $c_{M+1} = c_{M+2} = \dots = 0$. We choose

$t_1 = \pi/\Omega_M$, then $\cos(\Omega_M t_1/2) = 0$ and

$$\rho(\psi_1) = \sum_{n=0}^{M-1} (|c_n|^2 \cos^2(\frac{\Omega_n}{2} t_1) + |c_{n+1}|^2 \sin^2(\frac{\Omega_{n+1}}{2} t_1)) |\downarrow, n\rangle \langle \downarrow, n|$$

The maximal phonon number of ψ_1 is lowered down to $M - 1$. Similarly, we choose $t_k = \pi/\Omega_{M+1-k}$, $k = 1, 2, \dots, M$. Then the maximal phonon number after the M th cycle is lowered down to 0, which means the ion is already in the ground state $|\downarrow, n = 0\rangle$. The effect of sideband cooling can be verified with an additional red sideband transition with duration $t_M = \pi/\Omega_1$ followed by a quantum state detection. If most population is already in the ground state $|\downarrow, n = 0\rangle$, then there is almost no excitation to $|\uparrow\rangle$, detection result is “dark”. Otherwise, there are some populations detected at $|\uparrow\rangle$ states. A graph of this verification process with different estimation of maximal phonon numbers is showed in Fig. 4.3.10.

From the graph, we find the initial maximal phonon number after Doppler cooling is more than 60, which matches with our Doppler cooling limit $\gamma = 19.7 \text{ MHz} \sim 60 \times \omega_m$ ($\omega_m \sim 3 \text{ MHz}$).

After sideband cooling, the accurate heating rate $\dot{\bar{n}}$ of our trapped-ion system can be determined by an additional probing cycle. Delays with no laser interaction are added between the cooling cycles and the probing cycle [44]. By comparing populations of the first blue sideband and the first red sideband with different delay time, we can fit and find that after sideband cooling the average phonon number

$$\bar{n}(t) \approx 0.016 + 0.0038t$$

, as it shows in Fig. 4.3.11.

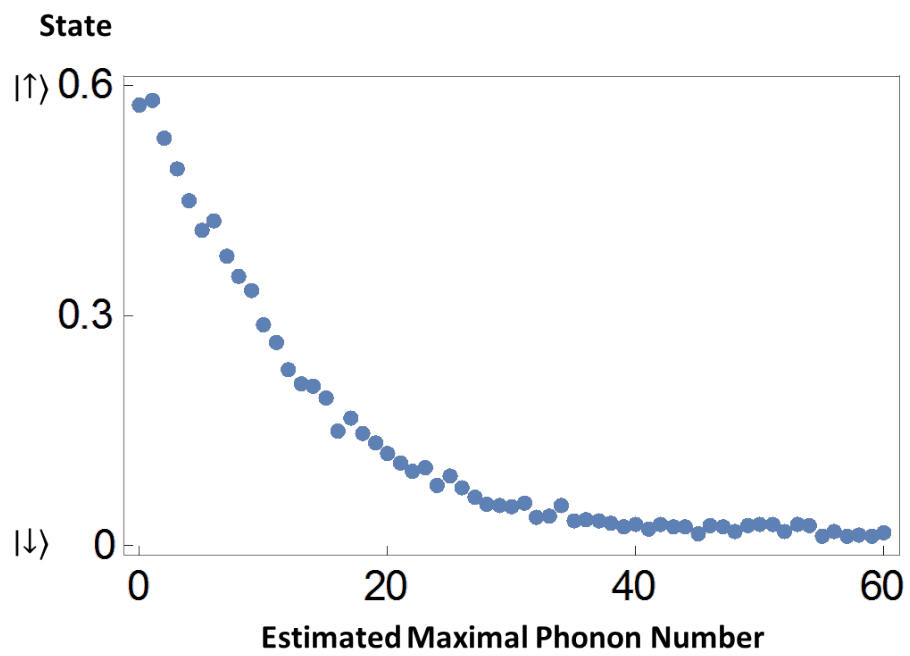


Figure 4.3.10: Performance of sideband cooling with different estimation of maximal phonon numbers.

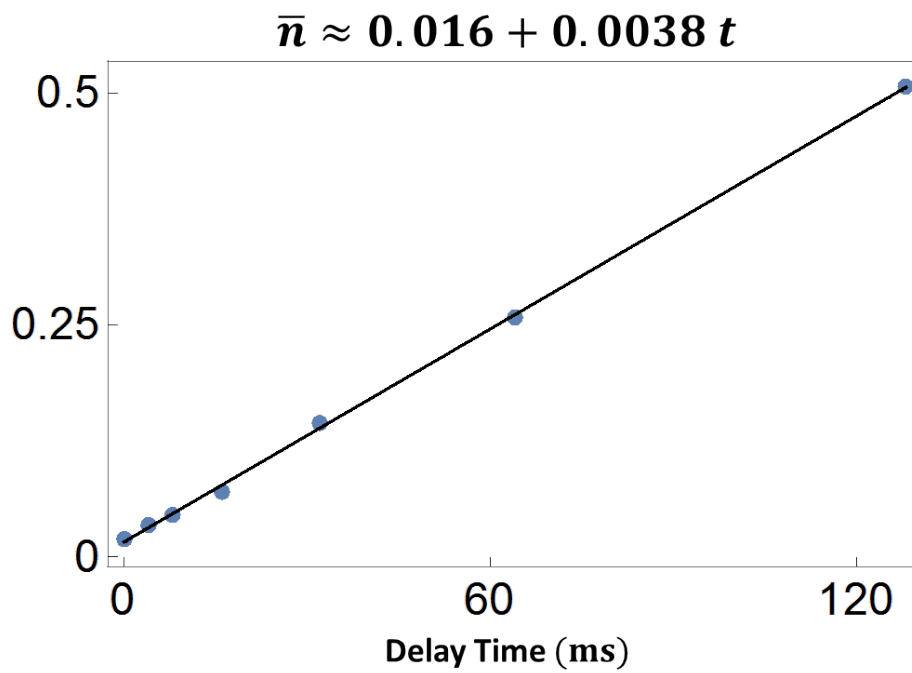


Figure 4.3.11: Heating rate measurement after sideband cooling. The solid line is fitted curve.

So our trap has a heating rate

$$\dot{\bar{n}} \approx 0.0038 \text{ phonon/ms}$$

which is low enough compared to our typical operation time.

Chapter 5

Control system

Once we have the ability to change all necessary properties of our traps and lasers, the next step is to build some accessible and reliable electronic units that have integrated control over all these apparatus. Control system is the integrated control unit of our trapped ion system. It provides a powerful software interface to operators. Such a system need to implement at least following functions.

1. **Equipment control** Programmable multi channel TTL generators and remote controllable signal generators to schedule microwaves and laser beams in nano seconds precision, with thousands repeat times.
2. **Data acquisition** Automatic data acquisition and store with TTL counters and control software.
3. **Waveform generation** Automatic experimental waveform and sequence generation, from simple parameter scan to complex Hamiltonian formula.

The key part of a integrated control system is communications, which include data transmissions and action synchronizations between different hardwares and soft-

wares. One example of this control system is the LabRAD ¹ system from Martinis superconducting quantum computation group at UCSB, which is an open source software written in Delphi and has a python binding. LabRAD is widely used in many labs and there is also a branch for AMO experiments ². However, we tried LabRAD at the very beginning but found it required a good training of general programming.

Most of us are not professional programmers but we use scientific computation software (such as Mathematica or MATLAB) a lot for physical theory simulations. So why not hide the complex hardware programming and let people run real experiments with the same set of formulas from their simulation code. Then they can use their familiar scientific software to do everything at the same place. From theory simulation, experiment sequence generation to data acquisition and result analysis, all automatically comes from some theory definitions defined by experimentalists. That's one of the main design principle when I develop our own control system. Another design principle is to combine the great part from two worlds: quick and powerful GUI building from graphical languages (e.g., LabVIEW), clear and familiar logic design from text-based languages. All software components are carefully designed and decoupled to fulfill this principle, which makes our system pretty easy to use. We make plenty of control panels for manually operations and display a variety of charts or images for real time monitoring. At the same time, all these control units are equipped with powerful scripting interfaces for automatic experimental control, which is essential for a long experiment running over nights.

¹<https://github.com/LabRAD/LabRAD/wiki>

²<https://github.com/AMOLabRAD/AMOLabRAD/wiki>

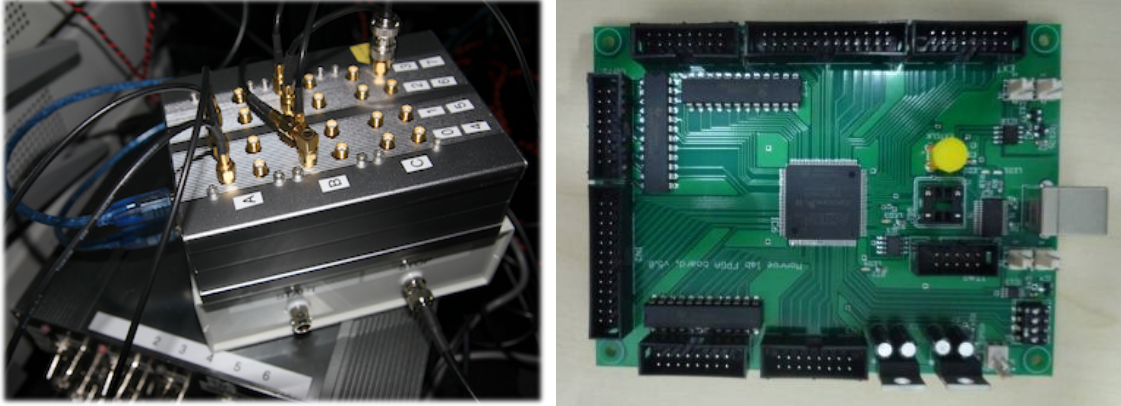


Figure 5.1.1: Left figure shows a 24 ports pulse sequencer on top of the RF switches box it controls. Right figure shows the inside FPGA board designed by Dizmitry.

5.1 Equipment control

For most experiments, the main kind of hardware that we finally control is AOM. As we already mentioned, AOMs are mainly served as optical switches to control duration of laser beam sidebands with nanosecond to microsecond level precisions. We use signal generators as drivers to control the modulation frequencies and strengths of them. Signal generator either from Agilent or “Rohde Schwarz” has a nice SCPI remote command interface that enables us to get or set parameters through network connections. The output signals of these signal generators are then controlled by RF switches which can be quickly opened or closed in < 5 ns through TTL signals.

A high performance TTL sequence generator is used to generate these synchronization TTL signals, as it shows in Fig. 5.1.1.

To maintain a stable time and phase relationship between operations, high frequency signal generators as well as TTL sequence generators are all finally referenced by a same 10 MHz Rb atomic clock reference ring. We build our own 20 channels TTL sequence generator [45], from a general-purpose Altera CycloneII EP2C5T144C6

FPGA board, which is now upgraded to a 28 channels version with much higher instruction capacity from a CycloneIII EP3C25 board. A 4 channels 24 (32 for upgraded version) bits gated counter is also programmed inside this pulse sequencer on the same board to output photon counts measured by PMT in real-time. To achieve high time resolution of output signals, the on-board PLL is used to divide input 50 MHz clock frequency up to 500 MHz. A 5 First-In-First-Out(FIFO)s assembly-line parallel scheme is implemented to distribute the read-convert procedure of about 10 ns into 5 clock cycles to achieve a minimal segment duration of 2 ns. The binary format of all instruction flows about time sequences or counters are carefully designed to be highly compact and easy to process and dispatch by FPGA circuits. With these hard optimizations, our pulse sequencer is able to manage 24 (32 for upgraded version) independent ports, with a range of durations from 2 ns to 4.2 ms (5497.5 s for upgraded version) and a maximum of 2560 (7680 for upgraded version) segments in length. The start time of TTL sequence output can be controlled by a trigger port, with which we can compensate the AC fluctuation with a line trigger circuit. Two pulse sequencers can be chained together also through this trigger port to overcome the segments number limitation.

The pulse sequences used in our experiments usually consists of many pulse segments, each pulse segment is a continuous period when all ports have constant states. The binary packet of each segment contains bits to describe its duration and each port's state. Each duration is a special encoded time stamp with a unit of minimal time resolution, which represents the number of clock cycles for this packet. The state bits are just the literally representation of all ports' boolean states. Every packet has the same fixed bit width. The start packet is unique and contains the number of repetitions for this whole pulse sequence, as well as a start flag bit and an external trigger flag bit. This binary protocol is of high efficiency and friendly to

FPGA circuits. A simple text-based language is also developed to add human readability and can be easily translated to its binary equivalent by computer programs. In the example sequence file in Fig. 5.1.2.

The “Chapter definitions” part associates chapter names with some boolean states of 24 ports in our pulse sequencer. In the “Sequence body” part, we can use the chapter name to represent the associated boolean state. Each argument number inside parentheses represents the duration of each state in the unit of microsecond. The corresponding time sequence diagram for the first 4 output channels A0 to A3 is showed in Fig. 5.1.3.

Note that its time scale has only relative meaning for better readability. Channel A0 is connected to the RF switch which controls the AOM of Doppler cooling beam path. The RF switch is reverse used and its state is ON by default, when the pulse sequencer outputs 0 so that the TTL input of RF switch is low level. channel A1 controls optical pumping beam path and channel A2 controls detection beam path. The Detection segment has another two $1 \mu\text{s}$ sub-segments after the detection beam path opens for $300 \mu\text{s}$. These 2 sub-segments have no output effects but internally they control the integrated gated counter to send TTL input counts data of the real detection segment back to the control computer. channel A3 connects to the external trigger input of our AWG board, thus controls the start time of microwaves.

From this simple example we notice that TTL signals are really good messengers which bridge the analog world with the digital world. In principle we can use TTL signals to control any finite state machines, which means any devices with finite and discrete possible operations. With this ability of precisely arranging the time order of all operations, the pulse sequencer actually serves as the center control unit of our trapped-ion system. The pulse sequencer, together with all these control units which can talk with computer as well as other devices, form the important bottom layer of

a Chapter definitions

```

1 Chapter(DopplerCooling,
2 00000000 00000000 00000000)
3 Chapter(OpticalPumping,
4 11000000 00000000 00000000)
5 Chapter(Detection,
6 10100000 00000000 00001111,
7 10000000 00000000 00000000,
8 10000000 00000000 00010000)
9 Chapter(AWG,
10 10010000 00000000 00000000)
11 Chapter(Zero,
12 10000000 00000000 00000000)

```

b Sequence body

```

1 DopplerCooling(1000)
2 OpticalPumping(5)
3 AWG(100)
4 Detection(300,1,1)
5 Zero(30)

```

Figure 5.1.2: Example sequence file for microwave experiments.

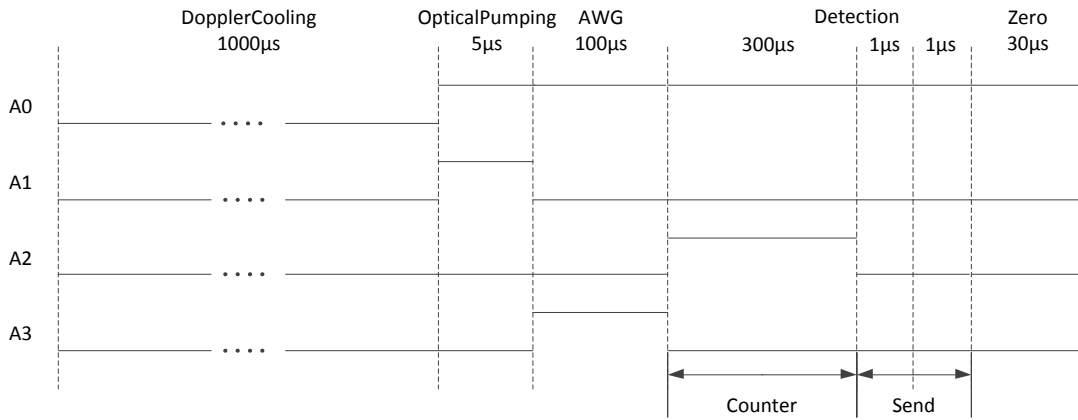


Figure 5.1.3: Time sequence diagram for the sequence file in Fig. 5.1.2.

our integrated control system.

5.2 Data acquisition

As the pulse sequencer serves as the center control unit, naturally the software that talks with the pulse sequencer should also be in the center of our software architecture. In our system, this main control software is a graphical interface program written in LabVIEW, as it shows in Fig. 5.2.1.

Its basic function is to communicate with the pulse sequencer through a 2 ~ 4 Mbps serial connection. We can load or edit sequence file on its left “Sequence” panel. The program can translate the text-based sequence language to binary bytes and send them to the pulse sequencer. If the sequence involves with gated counter channels which are usually used for collecting PMT counts, then the program can receive PMT counts data from the pulse sequencer and display average counts or states on the

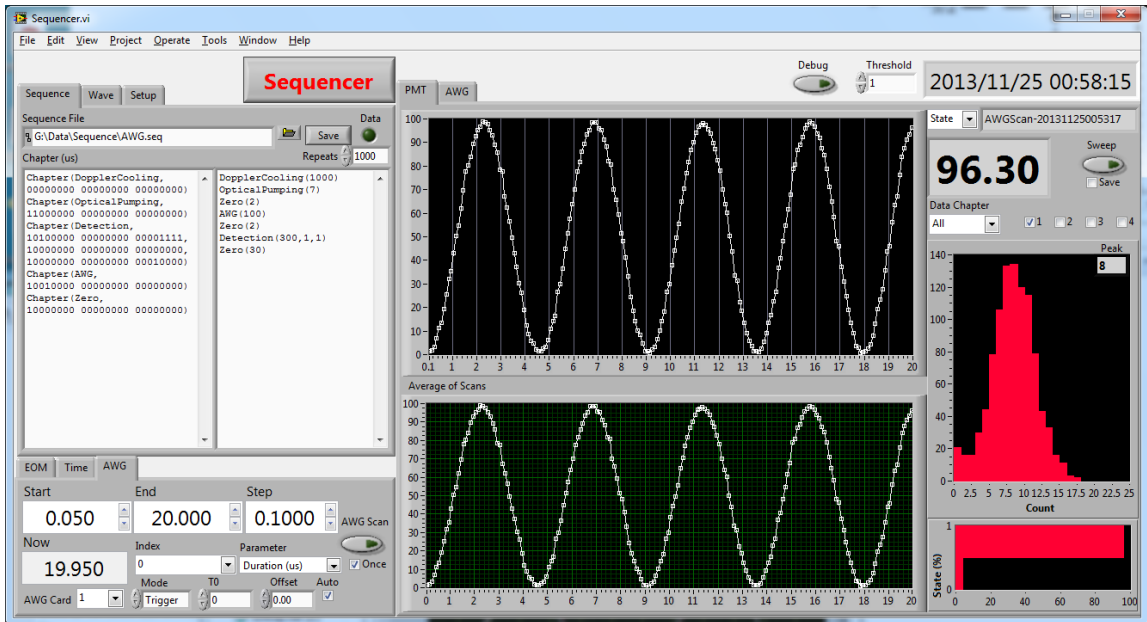


Figure 5.2.1: The main control program written in LabVIEW.

right “PMT” panel. The software also introduces some enhancements to overcome hardware limitation or increase usability. For sequence segments with long durations than the hardware single segment limit, it will split the single long segment into a lot of shorter segments. It will also resend sequence several times when it detects some PMT counts data is lost during transmission. The data acquisition process is also designed to be interruptible. We can press the emergency stop button at any time during a long operation. Later if we press the button again, then the operation will be recovered and continue to run just from the stop point. This is useful when something unexpected (e.g., the laser unlocks) happens during an experiment.

This basic input-output operation cycle is essential for all complex trapped-ion experiments. Usually one experiment is carried out repetitively with one parameter changing to obtain the relationship between the outcome and the parameter. The most common used two patterns are alignment sweeping and linear scanning. The

“Sweep” button is used to start an alignment sweeping. In this case the software just repeatedly sends sequences and receives data. So we can adjust some external parameters such as optical alignments, and use this “trapped-ion oscilloscope” as a reference. In the case of linear scanning, instead of manually changing external parameters, we can tell the software which parameter we want to scan as well as the scanning range. During the scan, every parameter and its corresponding original data is recorded and organized into a table. After the scan, this table is converted to a flexible structured text-based format and is stored into our network file system in a uniform naming/path manner. The scanning parameter can be the duration of some segment in the sequence (e.g., “Time Scan”), or parameter of some other device which is integrated controlled by the sequencer software (e.g., “EOM Scan”, “AWG Scan” or “RF Scan”). Currently we integrate 2 most commonly used devices into the sequencer software. The first one is the LabBrick signal generator for the fiber EOM, which is used to control the lock frequency of our 370 nm laser. Another one is the AWG board which can generate arbitrary waveforms for the implementation of complex Hamiltonians.

All experimental programs and data are put under a git version control system. Everyday at 6 : 00am, the data stored at the main control computer synchronize with a RAID data disk of FTP computer. Then at 7 : 00am, the data snapshot and git repository at FTP computer synchronize with another remote server mirror to ensure data security. The git repositories are managed by a lab management website based on Trac ³, which provides an enhanced wiki and issue tracking system. We often use its nice version control interface to recover corrupted programs or data to their historic version.

An auxiliary data service website is built with NodeJS and PHP to let us safely

³<http://trac.edgewall.org>

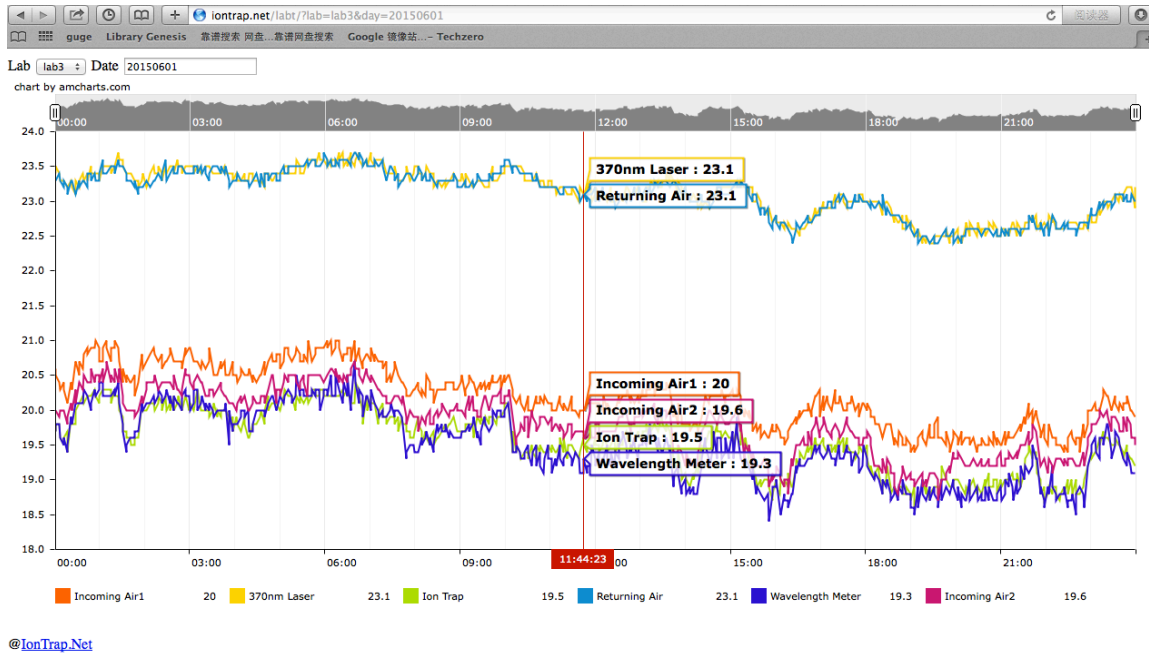


Figure 5.2.2: Screen shot of lab temperature website.

browse and manage real time temperature, wavelengths, experimental data and log from outside labs. This is useful when we share devices across different labs or run long experiments over nights. A screen shot of our lab temperature website is showed in Fig. 5.2.2.

For unattended long operations, a ion check program is also built to periodically check ion's status. When the ion becomes dark, we will receive notifications through alarms or phone calls. At the same time, a protection sequence will be automatically launched and try to bring the ion back.

5.3 Waveform generation

The sequence file or waveform file can be edited manually for some simple experiments such as the example Ramsey measurement. But as we mentioned in design principles, we can generate experimental sequences or waveforms directly from some theory definitions.

Some experiments only involved with standard quantum gates which are then implemented with microwaves. In $^{171}\text{Yb}^+$'s four level system, a standard quantum gate between $|i\rangle \leftrightarrow |j\rangle$ can be represented as a four parameter tuple

$$(i, j, \theta, \phi)$$

, where θ is rotation angle, ϕ is rotation phase. For example, $(1, 2, \pi/2, \pi/2)$ represents a $\pi/2$ σ_y quantum unitary gate from $|1\rangle$ to $|2\rangle$. This representation works for any combination of σ_x and σ_y type gates. A work around for σ_z type gates can be implemented based on the equation

$$\sigma_z(\theta) = \sigma_x\left(-\frac{\pi}{2}\right)\sigma_y(\theta)\sigma_x\left(\frac{\pi}{2}\right) \quad (5.3.1)$$

A complex experiments may consist of a lot of these parameter tuples. A sequence of these parameter tuples can be translated into a total rotation matrix by “DefToMat” function defined in our “IonTrap”Mathematica library. This rotation matrix is then used by “DefToAlg” function in our “algebraic” simulator to get a quick estimation of the final state.

The four parameter tuples can also be translated into a wave file by “DefToWave” function. The angle and phase translates to wave definition’s duration and phase field. Each wave definition’s frequency corresponds to the transition resonance fre-

quency between each tuple’s two states. The generated wave file then can be used for real experiments or numerical simulation. Numerical simulation is done by “DefToNum” function, which loads wave files and then simulate trapped-ion dynamics in a virtual trapped-ion simulator. The master equation simulator shares a lot of parameters with the real experimental setup and can be very accurate.

For experiments involved with phonons or multiple ions, the transition parameters of parameter tuples are extended to include more types of operations. For some experiments, waveform’s frequency or amplitude changes continuously with time. Sometimes the waveform function is not a standard sine function and can be very complex. Then we can add a user defined formula term to the parameter tuples. The “DefToWave” or “DefToNum” functions can handle these variants automatically. No matter what changes, the basic idea keeps the same: using one uniform representation for both simulation and experiment.

5.4 Software architecture

From point view of software engineering, all devices in the lab makes a complex heterogeneous system. Unlike computers, most devices doesn’t run an operating system. Many devices even doesn’t have a single chip on it. Also there are a bunch of different kinds of physical communication methods for different devices, from the simplest TTL trigger signal to network connections. Fortunately, on top of the abstract layer of control units, we only need to deal with devices which are able to talk with computers.

The main control program is released with a rich set of remote control interfaces so that it’s very easy to write some other software to share and make use of this main control resource. For example, we build a special control program for

the conditional sequential measurement without breaking any existing code, by exchanging data with the main control program through a shared memory interface. Through its network interface, we can even run quantum operations and take data from another personal computer outside our lab. Note that this interface is for the experimental data layer instead of the user interface layer and is different from any remote desktop tricks. In this manner, the main control program effectively acts as a virtual device for other programs. All of these graphical interface programs form the second layer of our integrated control system. Up to this graphical interface layer, we can already handle all the daily operations and do many experiments. However, for experiments with very complex logic, a text-based script language is desired to organize all complex operations. At first we use an embedded Lua engine based on LuaVIEW ⁴ to script our LabVIEW programs. It saves us a lot of time when we take data for the quantum contextuality and random number experiments. But it's still not a perfect solution since we have to manually convert our quantum gates or Hamiltonians into some form of program statements. I finally solve this problem by building a Mathematica-LabVIEW bridge. On top of this bridge, we develop an easy to use theory to experiment framework, including numerical simulation, experimental sequence/wave generation, parameter calibration, data taking, data analysis and plotting, all of which are totally automatic once we write the initial theory definitions in Mathematica. The logic diagram of this package is showed in Fig. 5.4.1.

The Mathematica-LabVIEW bridge is based on Mathematica's "NETLink" package and LabVIEW's Active/X server. This interface can be used to invoke any LabVIEW function VIs from Mathematica. For normal non-function VIs, I build some helper LabVIEW function VIs. The first one is "GetAllCtrls" to get all pairs of control names and its LabVIEW refnums on any VI front panel. Control name is

⁴<http://luaview.tm-solutions.eu/>

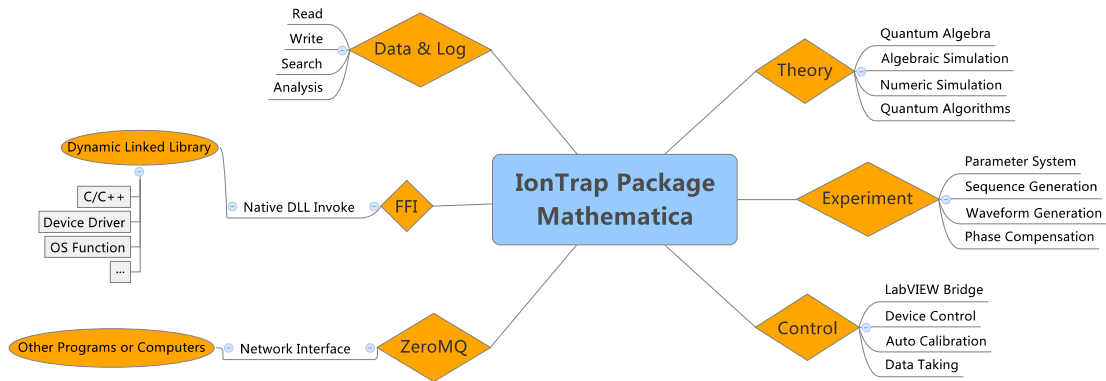


Figure 5.4.1: Diagram of IonTrap package written in Mathematica.

prefixed with its sub panel name or tab name if necessary. The others are “CtrlGetValue”, “CtrlSetValue” and “CtrlSignalValue” to get, set or “signal” a control’s value by its refnum. Here “signal” a control’s value means to set this control’s value and generate a corresponding “Value Change” signal to be captured in LabVIEW event structures.

From the other direction, we can also invoke Mathematica from LabVIEW to perform some complex calculations. The default behavior is to start a new background Mathematica kernel. In a more recent work of our bridge, we can let LabVIEW connect to the active front end session of Mathematica. We can also dynamically generate and implement LabVIEW’s event diagrams with VI scripting from text-based languages. In this way, LabVIEW acts as a graphical extension of Mathematica and they work together seamlessly. We can run a LabVIEW panel from a Mathematica notebook for graphical operations or real time charts display. All LabVIEW panel actions are then handled by this Mathematica kernel and can be logged to this Mathematica notebook.

Since Mathematica is not originally designed for device control, we extend its

hardware interoperability with the VISA COM library through “NETLink”, which is the same underlying hardware library of LabVIEW. A Mathematica package that provide a Foreign Language Interface (FFI) function is also developed, with which we can invoke native Dynamic Linked Libraries (DLL) and communicate with physical devices directly for efficiency critical reasons. Through these interfaces, we can use Mathematica to directly control pulse sequencer, AWG board or signal generators and perform rather complex experiments.

Sometimes other text-based languages are also used mainly for their high efficiencies or rich libraries. We use LuaJIT to build background running tasks and use Python/Qt or NodeJS/Webkit to build helper applications. Similar bridges between LabVIEW, Mathematica and these text-based languages are also built to maximally reusing software components.

Now this automated control framework is the unified top layer of our integrated control system. A lot of fancy quantum computation and simulation experiments have been done with the help of this control system. But a lot of parts still need improvements. We need a more robust exception reporting and recovery strategy to handle experimental accidents. We also need to extend our system a lot for multiple ions experiments. However, I believe we are already on the right way towards the ultimated software architecture of a quantum computer. For more details, some related code snippets and software screen shots can be found in Appendix A.

THIS PAGE INTENTIONALLY LEFT BLANK

Chapter 6

Experimental tests of quantum contextuality

In this experiment, we experimentally observed state-independent violations of Kochen-Specker inequalities for the simplest indivisible quantum system manifesting quantum contextuality, a three-level (qutrit) system. We performed the experiment with a single trapped $^{171}\text{Yb}^+$ ion, by mapping three ground states of the $^{171}\text{Yb}^+$ ion to a qutrit system and carrying out quantum operations by applying microwaves resonant to the qutrit transition frequencies (see in Fig. 6.0.1). Our results are free from the detection loophole and cannot be explained by the non-contextual hidden variable models.

6.1 Quantum contextuality

It is a long-standing debate whether quantum mechanics gives a complete description for all the properties of physical systems. In the world view of classical reality, the

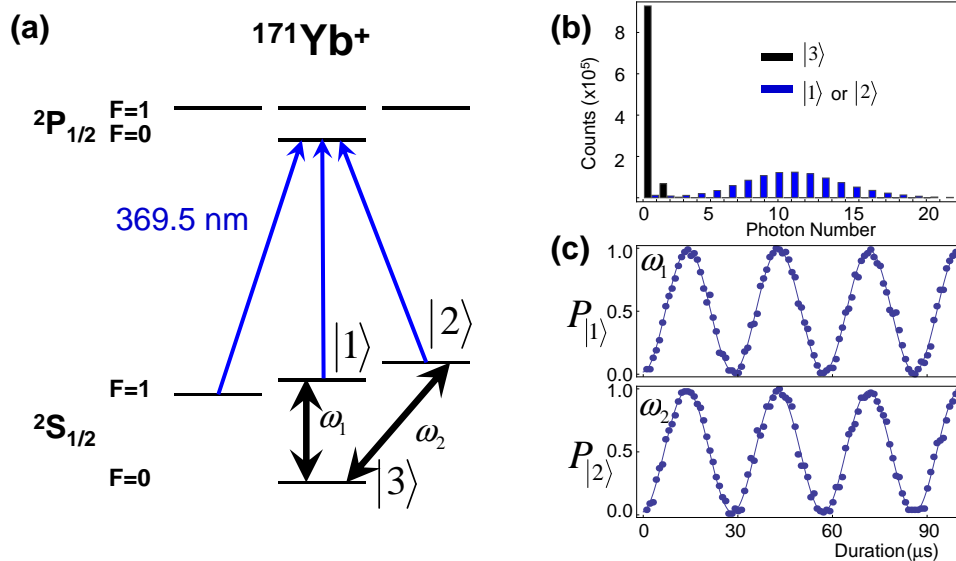


Figure 6.0.1: Microwave operations for qutrit system.

measurement outcomes on physical properties are noncontextual, i.e., predetermined independent of other compatible measurements that can be performed simultaneously, while in quantum mechanics measurements are contextual. This quantum contextuality provides one of the most fundamental characterizations of uniquely quantum phenomena.

Definition 6.1.1 (Non-Contextuality). Observables' probability distribution are **independent of measurement**.

Kochen, Specker, and Bell proved that quantum mechanics and any theory based on noncontextual classical reality give conflicting predictions [46]. The conflict is rooted in the structure of quantum mechanics and independent of the states of the system. This conflict was later reformulated as experimentally testable inequalities, in general referred to as the Kochen-Specker (KS) inequalities. Kochen and Specker showed that any quantum state in larger than 2 dimensions would reveal conflict

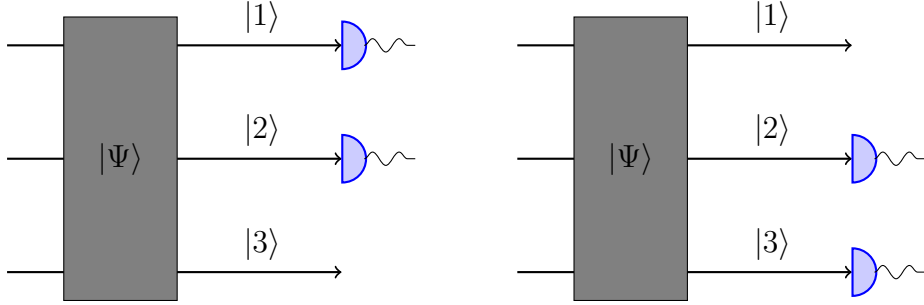


Figure 6.1.1: Simultaneously measurement & contextuality

with the non-contextual theories. The demonstration of the conflict in a simplest three dimensional quantum system, a qutrit, has fundamental importance since it would naturally imply the contraction in higher dimensions.

The conventional Bell inequalities can be considered a special type of the KS inequalities, where the contextuality is enforced by nonlocality. While Bell inequalities can be violated only by entangled states, the violation of the KS inequalities in principle can be observed for any state of the system.

A number of recent experiments have demonstrated the Kochen-Specker inequality for two qubit, using photons, ions, neutrons, or nuclear spin ensembles. In particular, the experiment carried by Roos closes the important detection efficiency loophole for experimental tests of quantum contextuality on two qubits using trapped ions [47].

On the other hand, it is known that two qubits are not the simplest system to show quantum contextuality. A single three-level system, called a qutrit, is the most fundamental system manifesting the conflict between quantum mechanics and noncontextual hidden variable theory. The test of the KS inequality with qutrits is of special interest for several reasons [48] [49]. Firstly, a qutrit is the simplest system to show quantum contextuality. Secondly, a violation of the KS inequality

in a three-level system would imply its violation in higher dimensions with $d > 3$; however, the reverse is not true. In this sense, it is more fundamental to test the KS inequality in the qutrit system. Finally, the qutrit system is intrinsically indivisible with no tensor product structure for its Hilbert space and thus has absolutely no entanglement. A violation of the KS inequality in qutrits clearly shows that quantum contextuality is not based on entanglement or particular quantum states but rooted in the fundamental structure of quantum mechanics.

6.2 State-independent experimental test

In this work, we experimentally observed state-independent violations of Kochen-Specker inequalities for the simplest indivisible quantum system manifesting quantum contextuality, a three-level (qutrit) system [50]. We performed the experiment with a single trapped $^{171}\text{Yb}^+$ ion, by mapping three ground states of the $^{171}\text{Yb}^+$ ion to a qutrit system and carrying out quantum operations by applying microwaves resonant to the qutrit transition frequencies. Our results are free from the detection loophole and cannot be explained by the non-contextual hidden variable models.

We use a significantly simplified state-independent version of the KS inequality was proposed by Yu and Oh recently [51], using 13 measurement settings, and 13 has been proven to be the minimum number of settings required for tests of quantum contextuality in a qutrit system. This inequality can be derived through an exhaustive check of all possible assignments of values ± 1 to the 13 variables. The basis vectors and their orthogonal relationships is showed in Fig. 6.2.1.

Theorem 6.2.1 (State-independent Inequality in Hidden Variable Theory). *Let A_i*

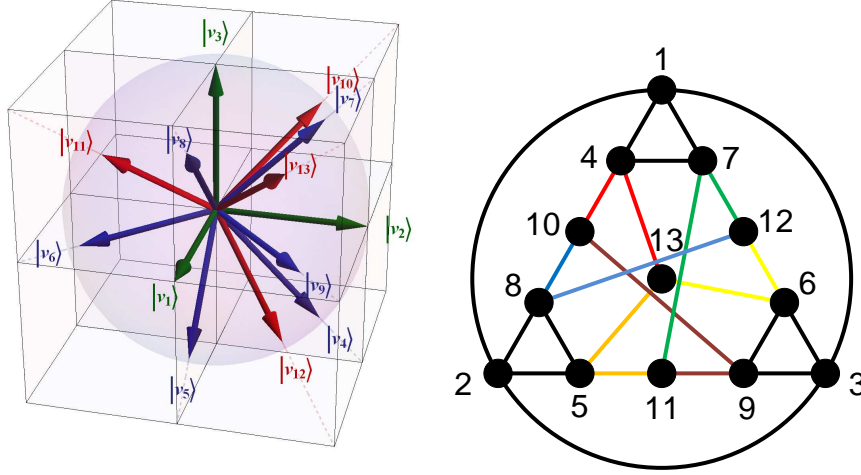


Figure 6.2.1: State-independent measurement basis and orthogonal relationships.

($i = 1, \dots, 13$) be observables taking values ± 1 . Then

$$\langle \chi_{13} \rangle := \sum_{i \in V} \mu_i \langle A_i \rangle - \sum_{(i,j) \in E} \mu_{ij} \langle A_i A_j \rangle - \sum_{(i,j,k) \in C} \mu_{ijk} \langle A_i A_j A_k \rangle \leq 25.$$

In quantum mechanics, let $|v_i\rangle$ be basis vectors, $A_i = I - 2|v_i\rangle\langle v_i|$ be observables. Then for any initial state $|\Psi\rangle$, we have

$$\langle \chi_{13} \rangle = \frac{83}{3} \approx 27.67.$$

For the hidden variable models that preserve algebraic structures of compatible observables, the inequality would be simplified to [51],

$$\langle \chi_4 \rangle = \sum_{i=10}^{13} \langle V_i \rangle \leq 1. \quad (6.2.1)$$

The inequality is valid, assuming the productrule and the sumrule still hold. The

productrule means the product of compatible observables are zero and the *sumrule* means the sum of all compatible observables are one. The $\chi_4 = (1 + \frac{1}{3}) I$ for the quantum mechanics, which breaks the inequality (6.2.1) regardless of initial states.

We test the KS inequalities (6.2.1) and (6.2.1) using a single trapped $^{171}\text{Yb}^+$ ion in a four-rod Paul trap with the setup similar to the one described in Ref. [40]. The basis vectors of a qutrit are represented by the three hyperfine levels of the $^{171}\text{Yb}^+$ ion in the $S_{1/2}$ ground-state manifold, with $|1\rangle = |F = 1, m_F = 0\rangle$, $|2\rangle = |F = 1, m_F = 1\rangle$, and $|3\rangle = |F = 0, m_F = 0\rangle$, as shown in Fig 6.2.2(a).

The experiment takes the following procedure: after 1 ms Doppler cooling, the state of the ion is initialized to $|3\rangle$ by 3 μs standard optical pumping [40]. The states for the test are coherently prepared by the microwaves ω_1 and ω_2 that are resonant to the transitions between $|1\rangle$ and $|3\rangle$, and between $|2\rangle$ and $|3\rangle$, respectively with high fidelity [52]. The pulse sequences for the preparations of different initial states are shown in Table 6.1. The coherent rotations of the microwaves are represented by the matrices $R_1(\theta_1, \phi_1)$, $R_2(\theta_2, \phi_2)$ shown in Fig. 6.2.2(b). Here θ_1 , θ_2 and ϕ_1 , ϕ_2 are controlled by the duration and the phase of the applied microwaves. The 2π times for both Rabi oscillations are adjusted to 29.5 μs , that is, the Rabi frequency $\Omega_{1,2} = (2\pi) 33.9$ kHz. The separation $\omega_2 - \omega_1 = (2\pi) 7.6372$ MHz with the magnetic field $B = 5.455$ G. The maximum probability of off-resonant excitation $\Omega^2/(\omega_2 - \omega_1)^2$ is about 1.6×10^{-5} , small enough to ensure the independence of each Rabi oscillation.

6.3 Experimental measurements

We measure the expectation values of single observables, $\langle A_i \rangle$ in Eq. (6.2.1) or $\langle V_i \rangle$ in Eq. (6.2.1), by rotating the measurement axis $|v_i\rangle$ to the state $|3\rangle$ through a unitary rotation U_i implemented with microwaves as shown in Fig. 6.2.2(c). Then

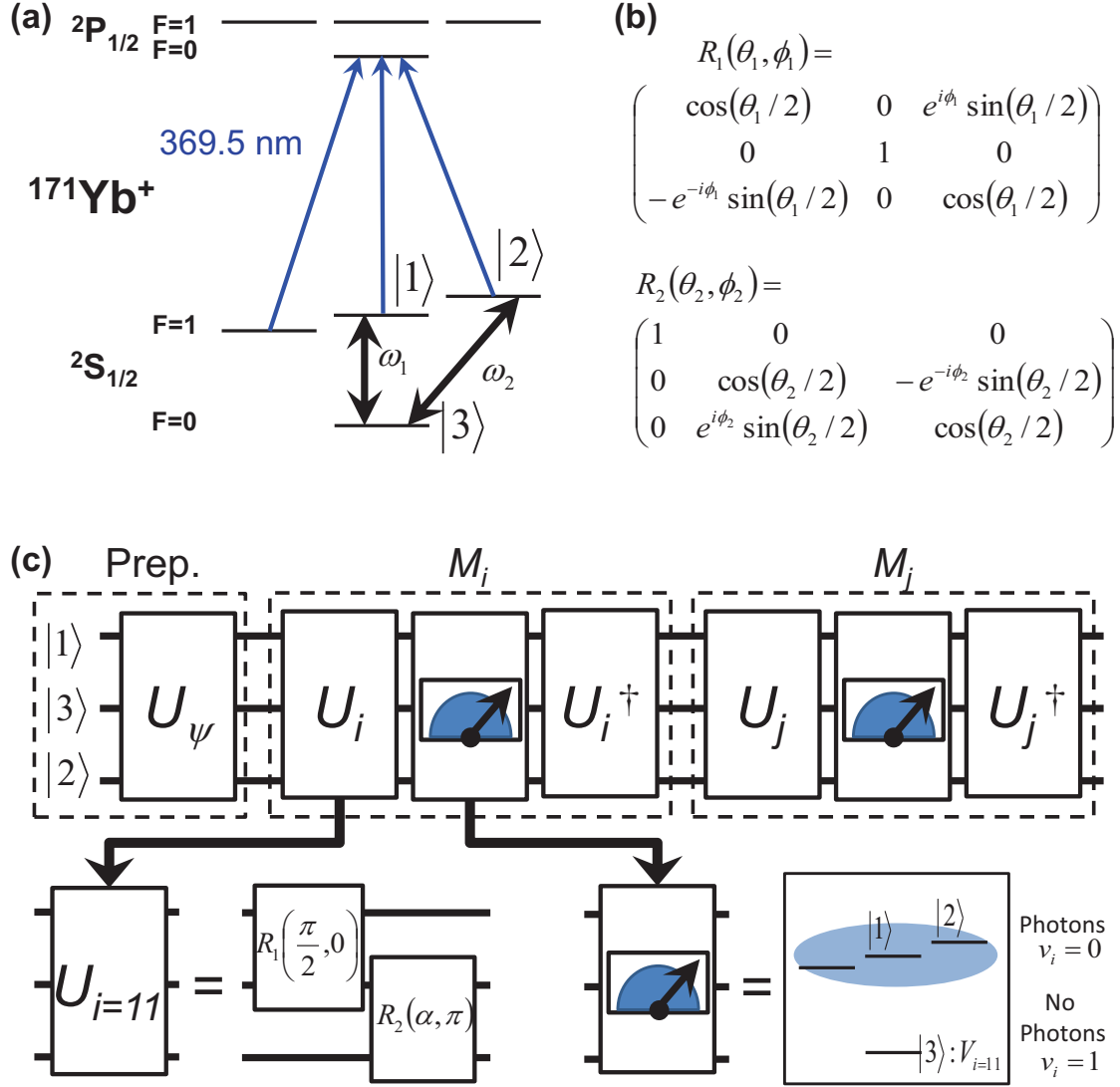


Figure 6.2.2: The $^{171}\text{Yb}^+$ ion system and the measurement scheme. (a) The energy diagram of $^{171}\text{Yb}^+$. Qutrit states $|1\rangle$, $|2\rangle$, and $|3\rangle$ are mapped onto $|F = 1, m_F = 0\rangle$, $|F = 1, m_F = 1\rangle$, and $|F = 0, m_F = 0\rangle$ in the $S_{1/2}$ ground state manifold, respectively. The transition frequencies are: $\omega_1 = (2\pi)12642.8213$ MHz and $\omega_2 = \omega_1 + (2\pi)7.6372$ MHz. (b) The matrix representations of $R_1(\theta_1, \phi_1)$, $R_2(\theta_2, \phi_2)$ rotations, which are realized by applying microwave pulses with the frequencies of ω_1 and ω_2 . Here θ_1 , θ_2 and ϕ_1 , ϕ_2 are controlled by the duration and the phase of the applied microwaves. (c) The sequential measurement scheme to detect the correlations $\langle V_i V_j \rangle$, where M_i and M_j denote the measurement boxes associated with the observables V_i and V_j , respectively.

Prep. Sequences (1 st 2 nd 3 rd)	Meas. Sequences (1 st 2 nd)
$\psi_1: R_1(\pi, 0)$	$U_1 = R_1(\pi, \pi)$
$\psi_2: R_2(\pi, 0)$	$U_2 = R_2(\pi, 0)$
$\psi_3: \text{no rotation}$	$U_3 = \text{no rotation}$
$\psi_4: R_1(\pi/2, \pi)$	$U_4 = R_2(\pi/2, \pi)$
$\psi_5: R_2(\pi/2, \pi)$	$U_5 = R_1(\pi/2, 0)$
$\psi_6: R_1(\alpha, 0) R_2(\pi/2, \pi)$	$U_6 = R_2(\pi, \pi) R_1(\pi/2, \pi)$
$\psi_7: R_1(0.304\pi, 0)$	$U_7 = R_2(\pi/2, 0)$
$\psi_8: R_2(0.288\pi, \pi) R_1(0.533\pi, 0)$	$U_8 = R_1(\pi/2, \pi)$
$\psi_9: R_1(\pi/2, \pi/2) R_2(\pi, 0)$	$U_9 = R_2(\pi, 0) R_1(\pi/2, \pi)$
$\rho_{10}: R_1(\pi/2, 0) R_2(\pi, 0) [0.5\text{ms}]$	$U_{10} = R_2(\pi/2, 0) R_1(\alpha, 0)$
$\rho_{11}: R_1(\alpha, 0) R_2(\pi/2, 0) [0.5\text{ms}]$	$U_{11} = R_1(\pi/2, \pi) R_2(\alpha, \pi)$
$\rho_{12}: R_1(\alpha, 0) R_2(\pi/2, 0) [1.0\text{ms}]$	$U_{12} = R_1(\pi/2, 0) R_2(\alpha, \pi)$
$R_2(\pi, \pi) [1.0\text{ms}] R_2(\pi, 0)$	$U_{13} = R_1(\pi/2, \pi) R_2(\alpha, 0)$

Table 6.1: (Left side): The pulse sequences to prepare different initial states from the simple basis states. We tested the inequalities for a total of 12 different states, including superposition states and mixed states, to check for the state independence. The state tomography results for the mixed states ρ_{10} , ρ_{11} , ρ_{12} are shown in Fig. 6.3.1. (Right side): The pulse sequences to generate the unitary rotations U_i ($i = 1, 2, \dots, 13$) for the sequential measurements illustrated in Fig. 2(c), where $\alpha = 0.392\pi$. Each unitary rotation U_i is uniquely associated with the observable V_i and implemented by the same pulse sequence independent of the context of the measurement of the observable V_i .

we measure the projection probability $P_{|3\rangle} = \langle V_i \rangle$ to the state $|3\rangle$, which gives $\langle A_i \rangle$ through $A_i = 1 - 2V_i$. The standard quantum jump detection based on the state-dependent fluorescence through a cycling transition can distinguish the $|F = 0\rangle$ level from the three $|F = 1\rangle$ levels. We observe on average 10 photons for the $|1\rangle$ or $|2\rangle$ states (referred to as the bright states) and basically no photon for the $|3\rangle$ state (referred to as the dark state) by collecting photons through objective lens with high numerical aperture at the front side and backside of the ion trap system. We assign value 1 to V_i when no photons are detected and value 0 when photons are detected. Therefore, the probability $P_{|3\rangle}$ is obtained by dividing the number of no-photon events by the number of total repetitions. The state detection error rates for wrongly registering the state $|3\rangle$ and missing the state $|3\rangle$ are 0.5% and 1.5%, respectively, with the discrimination threshold set at $n_{ph} = 1$.

Quantum state detection of a single $^{171}\text{Yb}^+$ ion is performed by the standard fluorescence detections distinguishing $F = 1$ and $F = 0$ states in $S_{1/2}$ ground state manifold. The probability of detecting a bright state ($|1\rangle$ or $|2\rangle$) as dark state ($|3\rangle$) is $C_{BD} = 2.1\%$, and that of detecting a dark state as dark state is $C_{DD} = 99.0\%$. We take into account the detection errors and transform the measured average value of a observable $\langle V_i \rangle_M$ to the actual value $\langle V_i \rangle_A$ by using the relation $\langle V_i \rangle_M = C_{DD} \langle V_i \rangle_A + C_{DB}(1 - \langle V_i \rangle_A)$. The simple applications of the transformation generate unphysical results due to the fluctuations of the infidelities. To avoid unphysical values, we assume they are Gaussian variables with the mean values C_{DD} , C_{BD} and the same standard deviations. Then we try to get the most probable estimate of C_{DD} and C_{BD} with two constraints: (a) Observables should be non-negative values. (b) The total sum of three orthogonal observables should be one. After correcting the average values of single observables, we apply the method to the results of the correlation measurements. The average value

$\langle V_i V_j \rangle$ can be written as $P(V_i = 1) P(V_j = 1 | V_i = 1)$, where $P(V_i = 1) = \langle V_i \rangle$. We transform the measured $P(V_j = 1 | V_i = 1)_M$ to corrected probabilities by the relation $P(V_j = 1 | V_i = 1)_M = C'_{DD} P(V_j = 1 | V_i = 1)_A + C'_{DB} (1 - P(V_j = 1 | V_i = 1)_A)$. The error coefficients C'_{DD} and C'_{DB} are not necessarily the same to those for $\langle V_i \rangle$.

To measure the correlations, we use the following relation,

$$\langle A_i A_j \rangle = \langle (1 - 2V_i)(1 - 2V_j) \rangle = 1 - 2\langle V_i \rangle - 2\langle V_j \rangle + 4\langle V_i V_j \rangle,$$

where $\langle V_i \rangle$ and $\langle V_j \rangle$ are obtained by the method described above. The correlation term $\langle V_i V_j \rangle$ is measured sequentially shown in Fig. 6.2.2(c), composed of two consecutive measurement boxes M_i and M_j associated with the observables V_i and V_j , respectively. Each measurement box M_i is implemented by a unitary rotation U_i , followed by a measurement in the standard basis which detects projection to the state $|3\rangle$ and an inverse unitary rotation U_i^\dagger . The rotation U_i and thus the measurement box M_i is uniquely determined by the observable V_i and is implemented in the same way in the experiment when we measure correlation of V_i with other compatible observables to assure context-independence. The unitary U_i is realized with one or two microwave rotations and the corresponding pulse sequences for U_i ($i = 1, 2, \dots, 13$) are listed in Table 6.1 for all the 13 different observables V_i . As an example, we illustrate the measurement of the correlation $\langle V_i V_j \rangle$ with $i = 11$ in Fig. 6.2.2(c).

For the last terms in the equality (6.2.1), we apply the similar methods described above. The correlations $-\langle A_i A_j A_k \rangle$ are expanded to $-1 + 2\langle V_i \rangle + 2\langle V_j \rangle + 2\langle V_k \rangle - 4\langle V_i V_j \rangle - 4\langle V_j V_k \rangle - 4\langle V_k V_i \rangle + 8\langle V_i V_j V_k \rangle$. We can ignore the terms $\langle V_i V_j V_k \rangle$ because they should not have negative values and the inequality without these terms should be bounded by the same value, 25. Note that we do not discard any measured data to

construct the inequality, which ensures that the experiment requires no fair-sampling assumption and thus is free from the detection efficiency loophole.

We measure a state's density matrix by performing qudit state tomography[53]. The density matrix of a state in the 4-level system can be written as

$$\hat{\rho}_4 = \frac{1}{2} \sum_{j=1}^{15} r_j \hat{\lambda}_j + \frac{1}{4} \hat{I}_4,$$

where $\hat{\lambda}_j$ are the SU(4) generators, which are referred as four dimensional generalized Gell-Mann matrices[54]. They have following properties:

$$\text{Tr}(\hat{\lambda}_j) = 0, \text{Tr}(\hat{\lambda}_j \hat{\lambda}_k) = 2\delta_{jk}.$$

Thus we can have

$$r_j = \text{Tr}(\hat{\rho}_4 \hat{\lambda}_j) = \langle \hat{\lambda}_j \rangle,$$

and the density matrix $\hat{\rho}_4$ can be reconstructed by measure all expectation values $\langle \hat{\lambda}_j \rangle$.

In our trapped-ion system, the florescence detecting method can only directly measure population on state $|1\rangle$. But it can be easily extended to measure the population on other state $|n\rangle$ by state flipping with a π pulse resonant at $|1\rangle \leftrightarrow |n\rangle$ transition. For a diagonal operator $\hat{A} = \text{diag}\{a_1, a_2, a_3, a_4\}$, its expectation value can be calculated by

$$\langle \hat{A} \rangle = \text{Tr}(\hat{\rho}_4 \hat{A}) = \sum_{j=1}^4 a_j \rho_{jj},$$

where ρ_{jj} is the population on state $|j\rangle$. For a off-diagonal operator \hat{B} , we can diagonalize \hat{B} to $\hat{B}_d = \hat{U} \hat{B} \hat{U}^\dagger$. The expectation value of \hat{B} on state ψ can be written

as

$$\langle \hat{B} \rangle = \langle \psi | \hat{B} \psi \rangle = \langle \hat{U} \psi | \hat{B}_d | \hat{U} \psi \rangle,$$

which is just the expectation value of diagonal operator \hat{B}_d on state $\hat{U}\psi$. Since $\hat{\lambda}_j$ is one of Pauli matrices extending to a higher dimension, the corresponding unitary operation \hat{U} is always pretty simple. So we can first perform the unitary operation \hat{U} on state ψ , then measure populations and calculate the expectation value of \hat{B}_d . Each population measurement is repeated by 1000 times. For the uncertainty of the measurements, we mainly consider the quantum projection noise and use the standard deviation of projection outcomes. The measurement result of the final physical observable can be always written as a function of expectation values of $\hat{\lambda}_j$ operators. We finally find the error bar by using the standard error propagating method.

We perform the measurements of 24 pairs of correlations of compatible observables under each given initial state. We repeat the same measurements 10,000 times for the same correlation, which results in 480,000 repetitions for one given initial state. To show that the inequalities (6.2.1) and (6.2.1) can be violated independent of the system state, we prepare 12 different initial states shown in Table 6.1 and Fig. 6.3.1 and repeat the measurements described in Fig. 6.2.2(c) and Table 6.1. We observe the fidelities of the prepared states on average of 98%.

From our observation, the inequalities (6.2.1) and (6.2.1) are clearly violated for all the input states that we tested, including the mixed states, as summarized in Fig. 6.3.1.

The average of $\langle \chi_{13} \rangle = 27.38(\pm 0.21)$ and $\langle \chi_4 \rangle = 1.35(\pm 0.04)$, significantly larger than the limits set by non-contextual hidden variable models. For some of the input states, $\langle \chi_4 \rangle$ and $\langle \chi_{13} \rangle$ are even larger than the quantum bounds, but this is of no

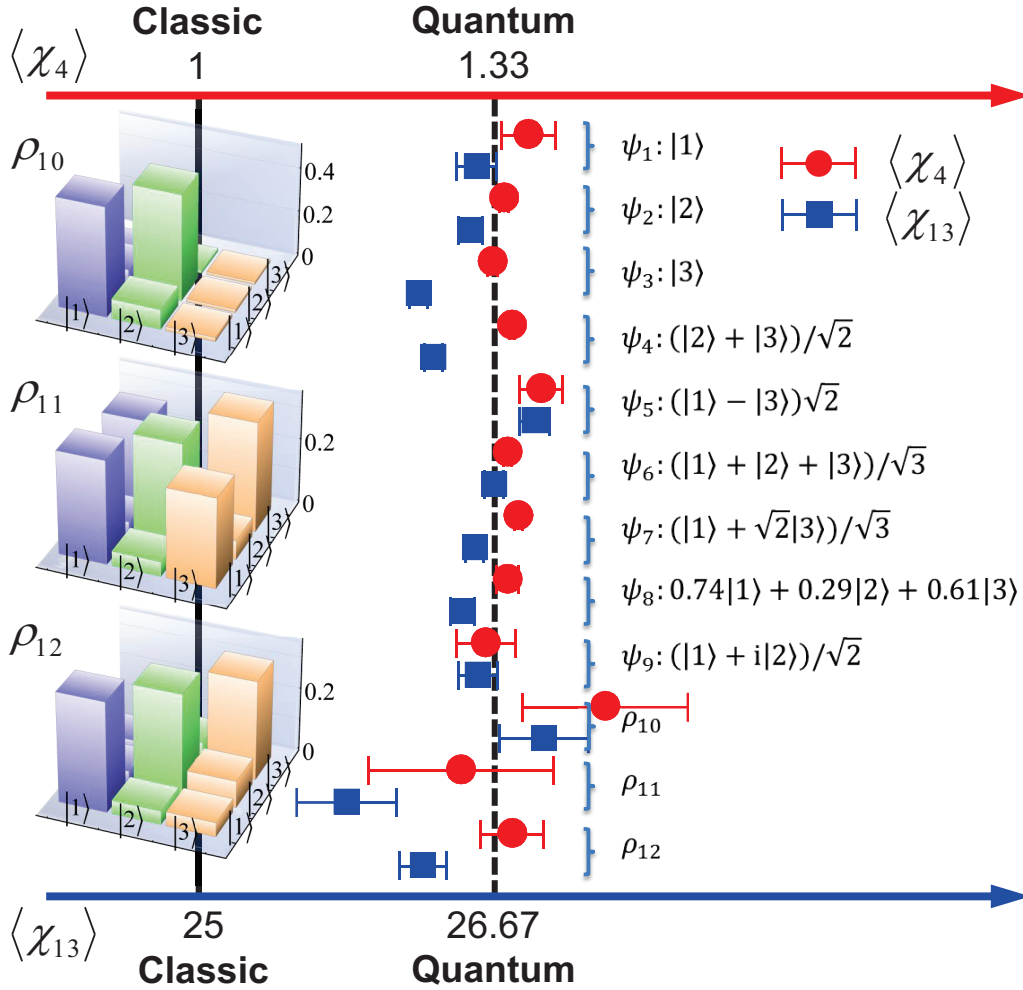


Figure 6.3.1: State-independent test of the KS inequalities $\langle \chi_4 \rangle$ and $\langle \chi_{13} \rangle$ for a qutrit system. The inequalities (6.2.1) and (6.2.1) are tested with 12 different initial states, including simple product states ψ_1 to ψ_3 , superposition states at the axis of the observables ψ_4 to ψ_6 , outside of the axis of the observables ψ_7 to ψ_9 , and mixed states ψ_{10} to ψ_{12} . We measure the density matrix of all the states by performing quantum state tomography for a qutrit [53], and confirm the prepared states with an average fidelity of 99.5% for the pure states ψ_1 to ψ_9 . The mixed state fidelities are around 97% shown in the figure. All the raw measurement data for $\langle \chi_{13} \rangle = 27.38(\pm 0.21)$ shown as blue filled squares violate the classical limit of 25 by 11.2σ , confirming the quantum contextuality for various states of the system. For each state, 480,000 realizations are used to obtain the value of $\langle \chi_{13} \rangle$. For the inequality (6.2.1), the observed value averaged over all the measured initial states is $\langle \chi_4 \rangle = 1.35(\pm 0.04)$. And the average value of all measured initial states is $\langle \chi_{13} \rangle = 27.38 \pm 0.21$.

physical significance as the results are within the error bar. All experimental data for state preparations and correlation measurements are listed in Appendix B.

In summary, we have observed violation of the KS inequality for the indivisible qutrit system using a single trapped ion, closing the detection efficiency loophole for this fundamental system that manifests quantum contextuality. The measurement results are in agreement with quantum mechanical predictions and violate the bounds set by any non-contextual hidden variable models by a significant margin. The compatibility loophole of the sequential measurements could be handled in the extended contextual models [55].

Let's summarize what we have done:

- experimental test of a state-independent Kochen-Specker inequality
- with a single trapped ion (indivisible system, no entanglement)
- close detection efficiency loophole

An important application of quantum contextuality experiment is to make a 'true' random number generator [56]. Later we will implement simultaneously measurement with Ba ions and $^{171}\text{Yb}^+$ ions together and using Ba ions' shielding level to protect certain state during measurement, thus make a loophole-free experiment.

Chapter 7

Quantum simulation of symmetry operations

Computation is the process of deriving the desired output from a given input, with some sort of modeling and calculation. Simulation is a generic scheme that mimic what's going on in one system, from another system. The classical universal Turing machine is always chosen as the most basic computation model and is able to simulate any other Turing machine. However, Feynman showed that a classical universal Turing machine would experience an exponential slowdown when simulating quantum phenomena, while a universal quantum simulator would not[8].

A quantum simulator is a device engineered to reproduce the properties of an ideal quantum model[57]. It's the universality of physical laws that makes physics simulation possible. This still emerging topical area has generated a remarkable exchange of scientific knowledge between apparently unconnected subfields of physics[58]. In terms of applications, it allows for the study of quantum systems that can not be efficiently simulated on classical computers. While a quantum computer would also

implement a universal quantum simulator[59], only particular systems have been simulated up to now using dedicated quantum simulators. Examples include black holes in Bose-Einstein condensates, quantum field theories[60] and recent quantum simulations of relativistic quantum effects as Zitterbewegung, Klein paradox and interacting relativistic particles in trapped ions.

In this chapter, we present the first experimental quantum simulation of “unphysical” operations beyond the regime of unitary and dissipative evolutions through the embedding of the dynamics in the electronic multi-levels of an $^{171}\text{Yb}^+$ ion. Despite of the fundamental usefulness of antilinear operations such as the complex conjugate, their implementation in a quantum device is considered to be impossible due to the linear character of quantum mechanics. For the first time to our knowledge, we observe the dynamics of the Majorana equation in a physical system and perform time reversal and charge conjugation, which are paradigmatic examples of antiunitary symmetry operators, during the evolution of a Majorana particle. Our implementation of time reversal and charge conjugation does not require the tomographic knowledge of the evolving state, thus can be applied regardless of the size of the system. In this way, our approach offers the possibility to add “unphysical” operations to the toolbox of quantum simulation and quantum computation, therefore providing a new route to efficiently compute otherwise intractable quantities as entanglement monotonones or time correlation functions.

7.1 Majorana equation and “unphysical” operation

Appearing at the same period of Dirac equation, the Majorana equation is a relativistic wave equation similar to the Dirac equation but includes the charge conjugate ψ_c of a spinor ψ . It is named after the mysterious Italian physicist Ettore Majorana.

Definition 7.1.1 (The Majorana Equation).

$$i\hbar\gamma^\mu\partial_\mu\psi = mc\psi_c$$

ψ_c is the charge conjugate of the spinor ψ .

It’s another relativistic wave equation for fermions derived from first principles. Unlike Dirac equation, it preserves helicity and has no stationary solutions. Actually, even today whether neutrinos are Dirac or Majorana particles still remains a open question. Many relativistic quantum effects such as *Zitterbewegung* can be observed from Majorana dynamics. All these interesting things are partial because of the non-hermitian nature of Majorana equation’s Hamiltonian. The quantum simulator obeys Schoedinger equation and always has a hermitian Hamiltonian. Its time evolution operator is always unitary. So generally it’s impossible to directly simulate the Majorana equation in a quantum simulator. However, a “unphysical” operation method is introduced recently to solve this kind of problems[58].

The Majorana equation for 1 + 1 dimensions can be written as

$$i\hbar\partial_t\psi = c\hat{\sigma}_x\hat{p}_x\psi - imc^2\hat{\sigma}_y\psi^*$$

With the “unphysical” operation, we map the state space to an enlarged Hilbert

space

$$\psi = \begin{pmatrix} \psi_1 \\ \psi_2 \end{pmatrix} \in \mathbb{C}_2 \rightarrow \Psi = \begin{pmatrix} \psi_1^r \\ \psi_2^r \\ \psi_1^i \\ \psi_2^i \end{pmatrix} \in \mathbb{R}_4$$

$$\psi = M\Psi = \begin{pmatrix} 1 & 0 & i & 0 \\ 0 & 1 & 0 & i \end{pmatrix} \Psi$$

Then the 1 + 1-dimensional Majorana equation becomes a 3 + 1-dimensional Dirac equation

$$i\hbar\partial_t\Psi = [\hat{p}_x c(\mathbf{1} \otimes \sigma_x) - mc^2(\sigma_x \otimes \sigma_y)]\Psi,$$

which has a hermitian Hamiltonian and is suitable for a quantum simulator.

The 3 + 1-dimensional Dirac equation's Hamiltonian can be implemented in a 4-level system, with initial state always being a momentum eigenstate

$$H_{\text{Majorana}} = \hat{p}_x c(\mathbf{1} \otimes \sigma_x) - mc^2(\sigma_x \otimes \sigma_y) \rightarrow \underbrace{pc(\sigma_{12}^x + \sigma_{34}^x)}_{H_1} + \underbrace{mc^2(\sigma_{23}^y - \sigma_{14}^y)}_{H_2}$$

Quantum computers or quantum simulators are important quantum devices that may enable us to experimentally address intriguing phenomena that are not directly tractable in the laboratory [61] or may outperform current classical computations for analyzing complex quantum systems [62, 63]. In recent years, various physical platforms such as neutral atoms [64], ions [65], photons [66], and superconducting circuits [67] have been fruitfully developed for the purpose of quantum simulation. However,

they are not yet able to perform some basic arithmetic calculations such as the complex conjugate, which changes the sign of the imaginary part of the coefficients of the state in a certain basis. Though we are used to compute the transformation with classical resources for useful scientific calculations, operations involving the complex conjugate require an anti-unitary process, which is impossible to be implemented in a quantum system. Moreover, the complex conjugate is not scalable in classical calculation, since it requires full knowledge of the quantum state, and the number of measurements grows exponentially with the size of the system.

The complex conjugate is deeply inherent to the important concepts of discrete symmetries. Wigner proved that any symmetry operation acts as a unitary or antiunitary transformation in the Hilbert space [68], while an antiunitary transformation can always be decomposed into a unitary transformation together with the complex conjugate. The study of symmetries has profoundly shaped our comprehension of physical laws in the quantum field theory, which unifies quantum mechanics and special relativity. Charge conjugation and time reversal are paradigmatic examples of antiunitary discrete symmetry operations [69, 70]. The charge conjugation together with the parity symmetry is not conserved in the weak interaction [71, 72], just as the time-reversal symmetry. The discovery of the violation of these symmetries has been a decisive breakthrough of quantum field theory leading to the standard model. Recently, several important algorithms for the simulation of relativistic quantum mechanics and quantum field theory have been discovered [73–78]. So far, however, quantum simulators of unitary and dissipative processes, the only physically allowed dynamics, have been realized [79–81].

Here, we perform the complex conjugate and these symmetry operations in our multi-level $^{171}\text{Yb}^+$ ion system through the use of the novel concept of embedding quantum simulator (EQS) [82–84]. As far as we know, this work is the first ex-

perimental demonstration of quantum simulation containing antiunitary evolutions beyond the boundary of the unitary operations. Our demonstration is scalable, where we can apply the time reversal or charge conjugation operations in systems of any size, since they do not require the tomographical knowledge of the state. The essence of the EQS is based on the finding that antiunitary operations can be implemented in a physical system by doubling the associated Hilbert space [82]. The scheme of the EQS enables us to efficiently compute entanglement monotones [83] or multi-time correlation functions [84, 85]. The reconstruction of these quantities would otherwise require a number of measurements that grows exponentially with the system size. We comment that the measurement of such quantities can be considered as an intractable task even for medium-size systems composed by, for example, only a dozen of qubits, whereas the EQS scheme provides the solution at the expense of one additional qubit to double the Hilbert space.

Before implementing antiunitary symmetry operations, we first simulate the Majorana dynamics to show the “unphysical” capability of the EQS. The Majorana equation [86], one of the representative relativistic equations,

$$i\hbar\rlap{/}\partial\psi = mc\psi_c, \tag{7.1.1}$$

where the Feynman slash notation $\rlap{/}\partial \equiv \gamma^\mu \partial_\mu$ with γ^μ being the Dirac matrices [87], describes the dynamics of a non-Hamiltonian system. Note that the spinor ψ and its charge conjugation ψ_c are present simultaneously in (7.2.1). Majorana envisioned that the Majorana equation together with the Majorana condition $\psi = \psi_c$ would be the fundamental equation describing neutrinos [86], which exhibit the novel phenomenon as “neutrino oscillation” [88]. Besides, the Majorana equation (7.2.1) has its own theoretical importance in exploring physics beyond the standard model. More-

over, the utility of the relativistic equations is not limited to relativistic quantum mechanics and quantum field theory. For example, electrons propagating through graphene are described by the $(2+1)$ -dimensional Dirac equation [89], and the symmetry breaking induced by tachyon condensation is described by a $(1+1)$ -dimensional Dirac-like equation with imaginary mass [90], a non-Hamiltonian system. Recently, a quantum simulation of the Majorana dynamics was performed in a photonic quantum platform, by decomposing its evolution in two Dirac equations [91, 92]. Through the quantum simulation of the inherently “unphysical” Majorana equation, we demonstrate various unique features, such as violation of charge and momentum conservation, broken orthogonality, and nontrivial effect of the state’s global phase.

Quantum computers or quantum simulators are important quantum devices that may enable us to experimentally address intriguing phenomena that are not directly tractable in the laboratory [61] or may outperform current classical computations for analyzing complex quantum systems [62, 63]. In recent years, various physical platforms such as neutral atoms [64], ions [65], photons [66], and superconducting circuits [67] have been fruitfully developed for the purpose of quantum simulation. However, they are not yet able to perform some basic arithmetic calculations such as the complex conjugate, which changes the sign of the imaginary part of the coefficients of the state in a certain basis. Though we are used to compute the transformation with classical resources for useful scientific calculations, operations involving the complex conjugate require an anti-unitary process, which is impossible to be implemented in a quantum system. Moreover, the complex conjugate is not scalable in classical calculation, since it requires full knowledge of the quantum state, and the number of measurements grows exponentially with the size of the system.

The complex conjugate is deeply inherent to the important concepts of discrete symmetries. Wigner proved that any symmetry operation acts as a unitary or antiu-

unitary transformation in the Hilbert space [68], while an antiunitary transformation can always be decomposed into a unitary transformation together with the complex conjugate. The study of symmetries has profoundly shaped our comprehension of physical laws in the quantum field theory, which unifies quantum mechanics and special relativity. Charge conjugation and time reversal are paradigmatic examples of antiunitary discrete symmetry operations [69, 70]. The charge conjugation together with the parity symmetry is not conserved in the weak interaction [71, 72], just as the time-reversal symmetry. The discovery of the violation of these symmetries has been a decisive breakthrough of quantum field theory leading to the standard model. Recently, several important algorithms for the simulation of relativistic quantum mechanics and quantum field theory have been discovered [73–78]. So far, however, quantum simulators of unitary and dissipative processes, the only physically allowed dynamics, have been realized [79–81].

7.2 Realization of embedding quantum simulator

Here, we perform the complex conjugate and these symmetry operations in our multi-level $^{171}\text{Yb}^+$ ion system through the use of the novel concept of embedding quantum simulator (EQS) [82–84]. As far as we know, this work is the first experimental demonstration of quantum simulation containing antiunitary evolutions beyond the boundary of the unitary operations. Our demonstration is scalable, where we can apply the time reversal or charge conjugation operations in systems of any size, since they do not require the tomographical knowledge of the state. The essence of the EQS is based on the finding that antiunitary operations can be implemented in a physical system by doubling the associated Hilbert space [82]. The scheme of the EQS enables us to efficiently compute entanglement monotones [83] or multi-time

correlation functions [84, 85]. The reconstruction of these quantities would otherwise require a number of measurements that grows exponentially with the system size. We comment that the measurement of such quantities can be considered as an intractable task even for medium-size systems composed by, for example, only a dozen of qubits, whereas the EQS scheme provides the solution at the expense of one additional qubit to double the Hilbert space.

Before implementing antiunitary symmetry operations, we first simulate the Majorana dynamics to show the “unphysical” capability of the EQS. The Majorana equation [86], one of the representative relativistic equations,

$$i\hbar\rlap{/}\partial\psi = mc\psi_c, \tag{7.2.1}$$

where the Feynman slash notation $\rlap{/}\partial \equiv \gamma^\mu \partial_\mu$ with γ^μ being the Dirac matrices [87], describes the dynamics of a non-Hamiltonian system. Note that the spinor ψ and its charge conjugation ψ_c are present simultaneously in (7.2.1). Majorana envisioned that the Majorana equation together with the Majorana condition $\psi = \psi_c$ would be the fundamental equation describing neutrinos [86], which exhibit the novel phenomenon as “neutrino oscillation” [88]. Besides, the Majorana equation (7.2.1) has its own theoretical importance in exploring physics beyond the standard model. Moreover, the utility of the relativistic equations is not limited to relativistic quantum mechanics and quantum field theory. For example, electrons propagating through graphene are described by the (2 + 1)-dimensional Dirac equation [89], and the symmetry breaking induced by tachyon condensation is described by a (1+1)-dimensional Dirac-like equation with imaginary mass [90], a non-Hamiltonian system. Recently, a quantum simulation of the Majorana dynamics was performed in a photonic quantum platform, by decomposing its evolution in two Dirac equations [91, 92]. Through the

quantum simulation of the inherently “unphysical” Majorana equation, we demonstrate various unique features, such as violation of charge and momentum conservation, broken orthogonality, and nontrivial effect of the state’s global phase.

The experimental scheme of the EQS is based on an important theoretical breakthrough in 2011, which is the discovery that unphysical operations can be implemented in a physical system by doubling the associated Hilbert space [82]. The proposed scheme facilitates the exploration of discrete symmetry operations which are unphysical in nature, such as time-reversal and charge-conjugation symmetries. It also relieves the requirement of tomographic information in some computational tasks in quantum information processing, such as the entanglement monotones [83] and noncausal kinematic transformations [84].

The essential idea of an EQS is the mapping from the original Hilbert space \mathbb{C}^2 to the enlarged one \mathbb{R}^4 for spinors in 1 + 1 spacetime dimension, $\mathcal{M} : \mathbb{C}^2 \rightarrow \mathbb{R}^4$. In the position basis, as shown in Fig. 7.2.1, the EQS mapping is defined as

$$\psi(x) = \langle x|\psi\rangle = \begin{pmatrix} \psi_1^{\text{re}}(x) + i\psi_1^{\text{im}}(x) \\ \psi_2^{\text{re}}(x) + i\psi_2^{\text{im}}(x) \end{pmatrix} \xrightarrow{\mathcal{M}} \Psi(x) = \langle x|\Psi\rangle = \begin{pmatrix} \psi_1^{\text{re}}(x) \\ \psi_2^{\text{re}}(x) \\ \psi_1^{\text{im}}(x) \\ \psi_2^{\text{im}}(x) \end{pmatrix} \quad (7.2.2)$$

where $\psi_{1(2)}^{\text{re(im)}}(x)$ are real functions satisfying the overall normalization condition $\int \left(|\psi_1^{\text{re}}(x)|^2 + |\psi_1^{\text{im}}(x)|^2 + |\psi_2^{\text{re}}(x)|^2 + |\psi_2^{\text{im}}(x)|^2 \right) dx = 1$. Inversely, as depicted in Fig. 7.2.1, the original spinor is retrieved through a matrix multiplication after evol-

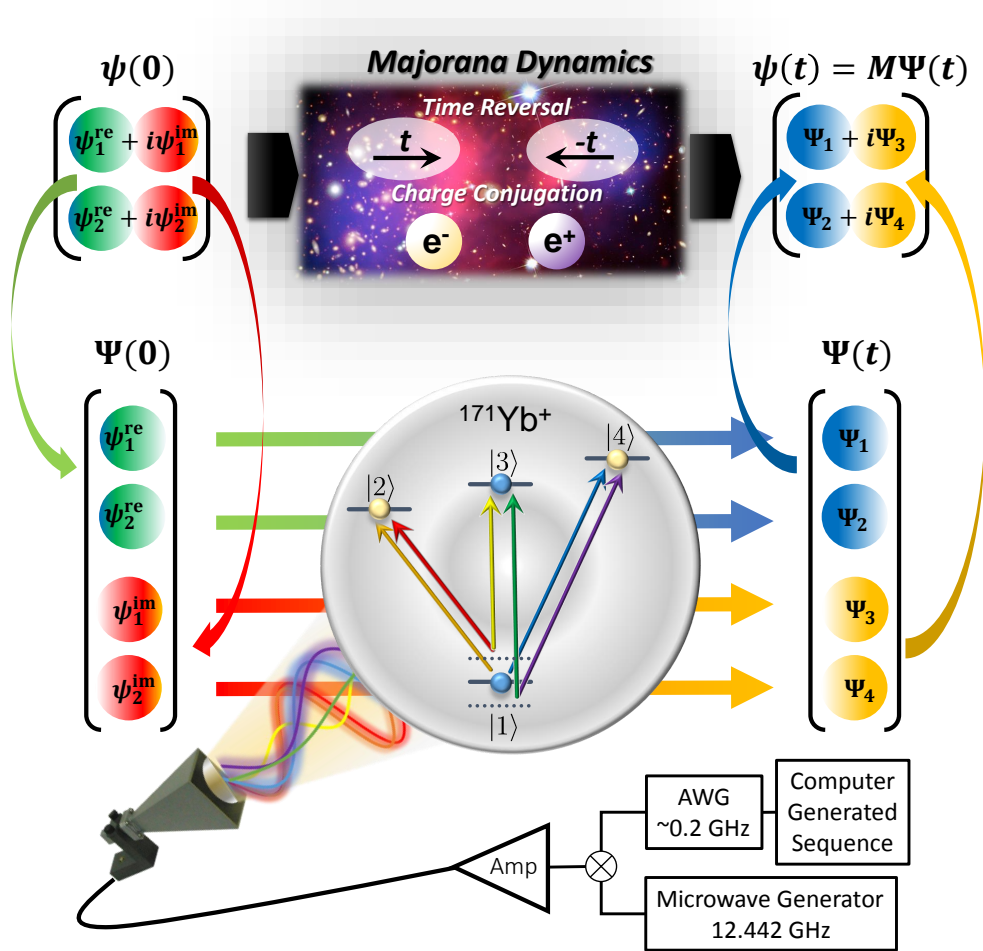


Figure 7.2.1: **Schematic of the EQS.** The upper and lower parts represent the original and enlarged spaces, respectively. Unphysical processes, which are forbidden by the laws of quantum mechanics, are mapped to unitary operations in the enlarged space. The EQS is built in a single $^{171}\text{Yb}^+$ ion trapped in a linear Paul trap, where the enlarged space is encoded in the ground-state manifold of the ion. The unitary operations are implemented by applying microwaves with six frequencies from a microwave horn.

ing in the EQS for certain duration,

$$\psi(x) = M\Psi(x), \quad M = \begin{pmatrix} 1 & 0 & i & 0 \\ 0 & 1 & 0 & i \end{pmatrix}. \quad (7.2.3)$$

Through the EQS mapping (7.2.3), the complex conjugate operation, $\hat{K} : \psi \rightarrow \psi^*$, is represented by a unitary operator $\hat{\mathcal{K}} = \hat{\sigma}_z \otimes \hat{\mathbb{I}}$ in the enlarged Hilbert space, which can be implemented directly in a quantum system.

With certain choice of the Dirac matrices in $(1 + 1)$ -dimension, $\gamma^0 = \hat{\sigma}_z$ and $\gamma^1 = i\hat{\sigma}_y$, the charge-conjugate spinor is properly defined as $\psi_c = i\hat{\sigma}_y\sigma_z\psi^*$. The Majorana equation in $1 + 1$ dimensions,

$$i\partial_t\psi(x, t) = \left(\hat{\sigma}_x\hat{p}_x - im\hat{\sigma}_y\hat{K}\right)\psi(x, t), \quad (7.2.4)$$

inherently contains the complex conjugate operator \hat{K} , which makes the Majorana dynamics prohibited by nature. For simplicity, we introduce a set of dimensionless units, i.e. mc^2 for the energy, mc for the momentum, and $\frac{\hbar}{mc^2}$ for the time.

In the enlarged Hilbert space, the original non-Hamiltonian system is mapped to a Hamiltonian one governed by an effective Hamiltonian,

$$\hat{\mathcal{H}} \equiv i\text{Im} \left[M^\dagger \left(c\hat{\sigma}_x\hat{p}_x - im\hat{\sigma}_y\hat{K} \right) M \right] = \hat{p}_x \left(\hat{\mathbb{I}} \otimes \hat{\sigma}_x \right) - m \left(\hat{\sigma}_x \otimes \hat{\sigma}_y \right). \quad (7.2.5)$$

Note that the equation of motion in the enlarged space, $i\partial_t\Psi(x, t) = \hat{\mathcal{H}}\Psi(x, t)$, keeps $\Psi(x, t)$ evolving inside \mathbb{R}^4 . Because the effective Hamiltonian (7.2.5) does not contain position operator, we perform the experimental implementation in momentum representation, where the dynamics of the Fourier transformed spinor $\tilde{\Psi}(p, t = 0) \equiv \frac{1}{\sqrt{2\pi}} \int \Psi(x, 0) e^{-ipx} dx$ is governed by a simpler Hamiltonian \mathcal{H}_p obtained by substi-

tuting the momentum operator with its eigenvalue in (7.2.5).

Along the same line, some discrete symmetry operations, *i.e.* the time reversal $\hat{T} : t \rightarrow (-t)$ and the charge conjugation $\hat{C} : \psi \rightarrow \psi_c$ take forms of unitary two-qubit gate operations in the enlarged Hilbert space: $\hat{\mathcal{T}} = i\hat{\sigma}_z \otimes \hat{\sigma}_y$, and $\hat{\mathcal{C}} = -\hat{\sigma}_z \otimes \hat{\sigma}_x$, respectively.

The EQS is built in an ion-trap system, which is a leading platform for quantum simulation [65]. The system consists of a single $^{171}\text{Yb}^+$ ion confined in a linear Paul trap [93], subjected to multi-frequency microwaves. As shown in Fig. 7.2.1, the four internal states of the ground-state manifold $^2S_{1/2}$ are encoded as $|F = 0, m_F = 0\rangle \equiv |1\rangle$ and $|F = 1, m_F = -1, 0, 1\rangle \equiv |m_F + 3\rangle, |1\rangle$ and $\{|2\rangle, |3\rangle, |4\rangle\}$ are separated by the hyperfine splitting $\omega_{\text{HF}} = (2\pi) 12.642812\text{GHz}$, and a uniform static magnetic field $B = 9.694\text{G}$ is applied to define the quantization axis and causes Zeeman splitting $\omega_Z = (2\pi) 13.586\text{MHz}$ among the upper states. As shown in the Fig. 7.2.1 the couplings between $|1\rangle$ and the upper states can be directly driven by microwave with frequencies as ω_{HF} and $\omega_{\text{HF}} \pm \omega_Z$, respectively. The couplings among the equally spaced upper states, *i.e.* $|2\rangle, |3\rangle$ and $|4\rangle$, are implemented by the stimulated Raman process of microwaves (see Methods). Based on the multi-fold microwave technique, we achieve ultimate controllability over the Hilbert space spanned by all of the four internal states. In other words, we construct a *ququad*, an elementary unit of quantum information processing consisting of four basis states. In principle, large-scale EQS can always be constructed by substituting one of the *qubits* in an array by a *ququad*, and the requisite microwave techniques involved in the control of the *ququad* have been developed in this work.

With the ability to perform any single-ququad operations, we implement the

effective Hamiltonian (7.2.5) in the momentum space,

$$\hat{\mathcal{H}}_p = p(|1\rangle\langle 2| + |3\rangle\langle 4|) + im(|1\rangle\langle 4| - |2\rangle\langle 3|) + \text{h.c.}, \quad (7.2.6)$$

on top of the EQS.

In the following, we use a plane-wave initial state $\psi_p(x)$ as an example of the encoding of states in the enlarged Hilbert space,

$$\begin{aligned} \psi_p(x) &= \begin{pmatrix} C_1 \\ C_2 \end{pmatrix} \otimes \frac{1}{\sqrt{2\pi}} e^{ipx/\hbar} \\ \xrightarrow{\mathcal{M}} \Psi_p(x) &= \frac{1}{2} \begin{pmatrix} C_1^* \\ C_2^* \\ iC_1^* \\ iC_2^* \end{pmatrix} \otimes \frac{1}{\sqrt{2\pi}} e^{-ipx/\hbar} + \frac{1}{2} \begin{pmatrix} C_1 \\ C_2 \\ -iC_1 \\ -iC_2 \end{pmatrix} \otimes \frac{1}{\sqrt{2\pi}} e^{ipx/\hbar} \\ &\equiv \Psi_p^{(-)}(x) + \Psi_p^{(+)}(x), \end{aligned} \quad (7.2.7)$$

where $\Psi_p^\pm(x)$ corresponds to plane-wave states (unnormalized) with momentum $\pm p$. Here we want to emphasize two points: (i) although $\Psi_p(x)$ is real, the components $\Psi_p^\pm(x)$ are usually composed of complex functions; (ii) there are always $+p$ and $-p$ components in the enlarged space to guarantee $\Psi_p(x)$ is real.

7.3 Experimental procedures

The experimental procedure is as follows. First, we map an initial Majorana spinor $\psi(x, t = 0)$ to a real bispinor $\Psi(x, t = 0)$ in the enlarged space. The momentum representation of the bispinor $\tilde{\Psi}(p, t = 0)$ evolves according to the enlarged space

Hamiltonian $\hat{\mathcal{H}}_p$. After encoding the initial condition $\tilde{\Psi}(p, 0)$ into the EQS, we implement \hat{H}_p for certain duration to simulate the Majorana dynamics. Then we perform quantum state tomography to obtain the enlarged space density matrix $\hat{\rho}(p, t)$, which can be mapped to the original space density matrix $\hat{\rho}(p, t)$. The average value of a diagonal operator A_d in the momentum space can be directly obtained via integration over the momentum, $\langle \hat{A}_d \rangle = \int \text{Tr} [\hat{A}_d \hat{\rho}(p, t)] dp$.

To obtain the average value of an off-diagonal operator in the momentum space, for example the average position of the Majorana particle, we change the four-component equation of motion in the enlarged Hilbert space into a pair of decoupled two-component equations by diagonalizing the first qubit. By coherently evolving a couple of two-dimensional equations with different momenta, we obtain the phase information between different momentum components. We repeat each measurement 1000 times to get the expectation value. The statistical errors, which are mainly due to quantum projection, are estimated by the standard deviation of mean value.

7.3.1 Stimulated Raman couplings

We implement a microwave Raman scheme for the transitions between $|2\rangle$ to $|3\rangle$ and $|3\rangle$ to $|4\rangle$. The strengths of effective Raman couplings are given by $\tilde{\Omega}_{23} = \frac{\Omega_{12}\Omega_{13}}{4} \left(\frac{1}{\Delta_{23}} + \frac{1}{\Delta_{23} + \delta_{23}} \right)$ and $\tilde{\Omega}_{34} = -\frac{\Omega_{13}\Omega_{14}}{4} \left(\frac{1}{\Delta_{34}} + \frac{1}{\Delta_{34} - \delta_{34}} \right)$, where Ω_{12} , Ω_{13} , and Ω_{14} are Rabi frequencies between $|1\rangle$ to $|2\rangle$, $|1\rangle$ to $|3\rangle$, and $|1\rangle$ to $|4\rangle$, respectively, $\Delta_{23(34)} \approx \pm 5 \max\{\Omega_{12(14)}, \Omega_{13}\}$ are the detuning from $|1\rangle$ to $|2\rangle(|4\rangle)$ and $\delta_{23(34)}$ are frequency shifts for the compensation of AC-stark effect between $|1\rangle$ to $|3\rangle$. The strengths of the Raman transitions are balanced to the direct transitions, which have around $(2\pi)3$ kHz. The cross talks between two transitions $\tilde{\Omega}_{23}$ and $\tilde{\Omega}_{34}$ are negligible because $\tilde{\Omega}_{23}$ ($\tilde{\Omega}_{34}$) is produced by the combination of σ_- (σ_+) and π polarizations of

microwave, which is impossible to couple to $|3\rangle \leftrightarrow |4\rangle$ transition ($|2\rangle \leftrightarrow |3\rangle$). The AC stark shifts from all the microwave transitions are carefully compensated by properly adjusting the microwave frequencies (see the appendix C).

In our $^{171}\text{Yb}^+$ ion system, only $|1\rangle \leftrightarrow |2\rangle, |3\rangle, |4\rangle$ transitions are naturally available. $|2\rangle \leftrightarrow |3\rangle, |4\rangle$ transitions can't be implemented directly, because the energy gap between $|2\rangle \leftrightarrow |3\rangle$ and $|3\rangle \leftrightarrow |4\rangle$ are very close. They are differed by a $\sim 310.8B^2\text{Hz/gauss}^2$ second-order Zeeman effect, which turns out to be only 31kHz. So instead of directly driving transitions, we use a microwave Raman scheme similar to the widely used Raman laser scheme. In this scheme, 6 different microwaves are mixed and simultaneously apply to the trap. The effective Hamiltonian method[94] is applied to analyze phases and amplitudes of Raman transitions. Then an equation system consists of all AC Stark shifts is solved to get the exact amplitudes and frequencies of all 6 microwave components.

One problem in this scheme is the slowing down of operations. The Raman transition is ~ 10 times slower than normal Rabi flopping, even with full power. But now we need 6 microwaves together. Decoherence occurs when the whole microwave duration are longer than $600\mu\text{s}$. This decoherence problem is later solved by apply a line trigger[95] to the pulse sequencer.

7.3.2 Mapping between original and enlarged spaces

In order to implement unphysical operations, such as the time reversal and charge conjugation, in our prototype of the embedding quantum simulator, we first consider the mapping \mathcal{M} which transforms the state vector in the original n -dimensional

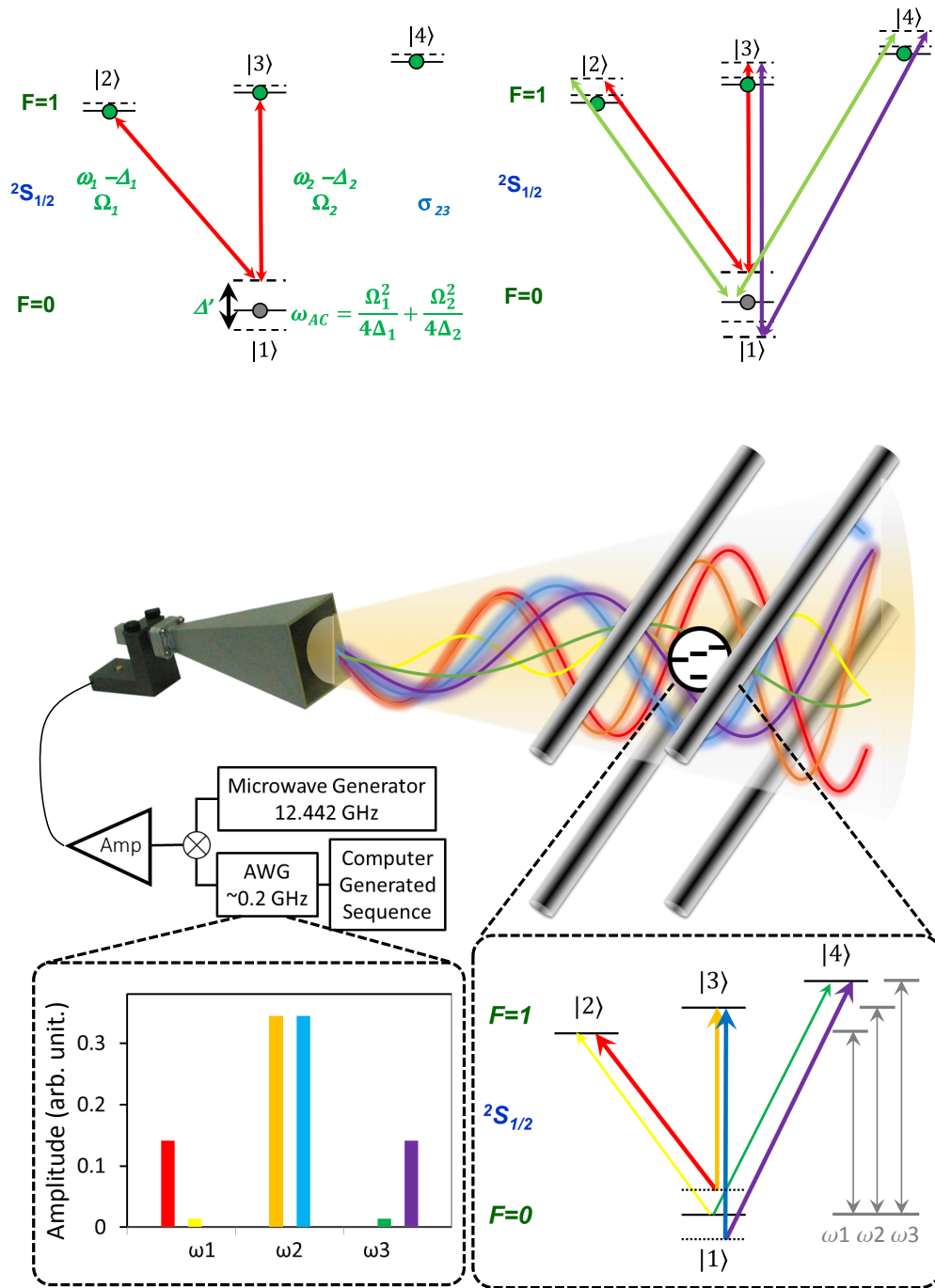


Figure 7.3.1: Microwave Raman transition

complex Hilbert space \mathbb{C}^n onto an enlarged $2n$ -dimensional real Hilbert space \mathbb{R}^{2n} ,

$$\psi(x) = \begin{pmatrix} \psi_1(x) \\ \vdots \\ \psi_n(x) \end{pmatrix} \longrightarrow \mathcal{M}\Psi(x) = \frac{1}{2} \begin{pmatrix} \psi_1(x) + \psi_1^*(x) \\ \vdots \\ \psi_n(x) + \psi_n^*(x) \\ i(\psi_1^*(x) - \psi_1(x)) \\ \vdots \\ i(\psi_n^*(x) - \psi_n(x)) \end{pmatrix} \equiv \begin{pmatrix} \psi_1^{\text{re}}(x) \\ \vdots \\ \psi_n^{\text{re}}(x) \\ \psi_1^{\text{im}}(x) \\ \vdots \\ \psi_n^{\text{im}}(x) \end{pmatrix} \quad (7.3.1)$$

In the $1 + 1$ dimension case, we consider the specific mapping $\mathcal{M} : \mathbb{C}^2 \rightarrow \mathbb{R}^4$. In the following, we use a plane-wave initial state $\psi_p(x)$ as an example of the encoding of states in the enlarged Hilbert space,

$$\begin{aligned} \psi_p(x) &= \begin{pmatrix} C_1 \\ C_2 \end{pmatrix} \otimes \frac{1}{\sqrt{2\pi}} e^{ipx/\hbar} \\ \longrightarrow \mathcal{M}\Psi_p(x) &= \frac{1}{2} \begin{pmatrix} C_1^* \\ C_2^* \\ iC_1^* \\ iC_2^* \end{pmatrix} \otimes \frac{1}{\sqrt{2\pi}} e^{-ipx/\hbar} + \frac{1}{2} \begin{pmatrix} C_1 \\ C_2 \\ -iC_1 \\ -iC_2 \end{pmatrix} \otimes \frac{1}{\sqrt{2\pi}} e^{ipx/\hbar} \\ &\equiv \Psi_p^{(-)}(x) + \Psi_p^{(+)}(x), \end{aligned} \quad (7.3.2)$$

where $\Psi_p^\pm(x)$ corresponds to plane-wave states (unnormalized) with momentum $\pm p$. Here we want to emphasize two points: (i) although $\Psi_p(x)$ is real, the components $\Psi_p^\pm(x)$ are usually composed of complex functions; (ii) there are always $+p$ and $-p$ components in the enlarged space to guarantee $\Psi_p(x)$ is real.

7.3.3 Quasi-quantum treatment of the momentum

The 1 + 1 Majorana equation for a two-component complex spinor $\psi(x) = \begin{pmatrix} \psi_1(x) \\ \psi_2(x) \end{pmatrix}$ is mapped onto a 3 + 1 Dirac equation for a four-component real bispinor $\Psi(x) = \begin{pmatrix} \psi_1^{\text{re}}(x) \\ \psi_2^{\text{re}}(x) \\ \psi_1^{\text{im}}(x) \\ \psi_2^{\text{im}}(x) \end{pmatrix}$ in the enlarged space, which takes the following form,

$$i\hbar\partial_t\Psi(x,t) = \hat{\mathcal{H}}\Psi(x,t) = \left[c\hat{p}_x \left(\hat{\mathbb{I}} \otimes \hat{\sigma}_x \right) - mc^2 (\hat{\sigma}_x \otimes \hat{\sigma}_y) \right] \Psi(x,t), \quad (7.3.3)$$

where $\hat{p}_x = -i\hbar\partial_x$ is the momentum operator.

In the momentum space, the bispinor $\tilde{\Psi}(p,t)$ is obtained via the Fourier transformation,

$$\tilde{\Psi}(p,t) = \frac{1}{\sqrt{2\pi}} \int \Psi(x,t) e^{-ipx/\hbar} dx, \quad (7.3.4)$$

and the equation of motion becomes

$$i\hbar\partial_t\tilde{\Psi}(p,t) = \hat{\mathcal{H}}_p\tilde{\Psi}(p,t) = \left[cp \left(\hat{\mathbb{I}} \otimes \hat{\sigma}_x \right) - mc^2 (\hat{\sigma}_x \otimes \hat{\sigma}_y) \right] \tilde{\Psi}(p,t), \quad (7.3.5)$$

where the momentum operator \hat{p}_x is substituted by its eigenvalue p . It is clear that the dynamics governed by $\hat{\mathcal{H}}_p$ is ready to be implemented in a quantum four-level system.

7.3.4 Physical observables

In this part, we will describe in detail the procedure to extract the information of various physical observables from experimental data. The time-dependent enlarged

four-component spinor can be formally written in the momentum space as follows,

$$|\Psi(t)\rangle = \int \Psi(p) |\chi_p(t)\rangle \otimes |p\rangle, \quad (7.3.6)$$

with $|p\rangle$ being the momentum basis, i.e. the plane-wave states, and $|\chi_p(t)\rangle$ describing the internal state $|\chi_p(t)\rangle = \sum_{j=1}^4 \chi_{p,j}(t) |j\rangle$. Note that the wave function in the momentum space $\Psi(p)$ does not depend on time and is fully determined by the initial condition $|\psi(0)\rangle$ in the original space, because the effective Hamiltonian $\hat{\mathcal{H}}$ commutes with the momentum operator \hat{p}_x . The only time-dependent part in Eq. (7.3.6) is the internal state $|\chi_p(t)\rangle$, whose dynamics is determined by the enlarged space Hamiltonian $\hat{\mathcal{H}}_p = pc(|1\rangle\langle 2| + |3\rangle\langle 4|) + imc^2(|1\rangle\langle 4| - |2\rangle\langle 3|) + \text{H.c.}$. The equation of motion for $|\chi_p(t)\rangle$, given by $i\hbar\partial_t |\chi_p(t)\rangle = \hat{\mathcal{H}}_p |\chi_p(t)\rangle$, can be simulated in a quantum four-level system. Using quantum state tomography, we experimentally obtain the density matrix $\hat{\rho}_p(t)$ corresponding to $|\chi_p(t)\rangle\langle\chi_p(t)|$.

7.3.5 Diagonal operators in the momentum space

The general form of a diagonal operator $\hat{\mathcal{O}}_{\text{dg}}$ in the momentum space can be written as follows,

$$\hat{\mathcal{O}}_{\text{dg}} = \hat{\Sigma} \otimes f(\hat{p}), \quad (7.3.7)$$

with $\hat{\Sigma} = c_0\hat{\mathbb{I}} + c_1\hat{\sigma}_x + c_2\hat{\sigma}_y + c_3\hat{\sigma}_z$ and $f(\cdot)$ being an arbitrary algebraic function, $\langle p|f(\hat{p})|p'\rangle = f(p)\delta(p-p')$. The expectation value of this operator at arbitrary

time t can be obtained as follows,

$$\begin{aligned} \langle \Psi(t) | M^\dagger \hat{\mathcal{O}}_{\text{dg}} M | \Psi(t) \rangle &= \int dp dp' \Psi^*(p) \Psi(p') \langle p | f(\hat{p}) | p' \rangle \langle \chi_p(t) | M^\dagger \hat{\Sigma} M | \chi_{p'}(t) \rangle \\ &= \int dp |\Psi(p)|^2 f(p) \text{Tr} \left[\hat{\rho}_p(t) \hat{M}^\dagger \hat{\Sigma} \hat{M} \right]. \end{aligned} \quad (7.3.8)$$

We may take the average momentum as a simple example,

$$\begin{aligned} p(t) &\equiv \langle \psi(t) | \hat{p} | \psi(t) \rangle \\ &= \langle \Psi(t) | M^\dagger \hat{p} M | \Psi(t) \rangle \\ &= \int dp p |\Psi(p)|^2 \text{Tr} \left[\hat{\rho}_p(t) \hat{M}^\dagger \hat{M} \right]. \end{aligned} \quad (7.3.9)$$

The quantum simulation for each $|\chi_p(t)\rangle$ will be as follows.

1. Prepare the initial state $|\chi_p(0)\rangle = \sum_{j=1}^4 \chi_{p,j}(t) |j\rangle$.
2. Implement the Hamiltonian $\hat{\mathcal{H}}_p$ and let the system evolve for certain time duration t ,

$$\hat{\mathcal{H}}_p = \begin{pmatrix} 0 & cp & 0 & imc^2 \\ cp & 0 & -imc^2 & 0 \\ 0 & imc^2 & 0 & cp \\ -imc^2 & 0 & cp & 0 \end{pmatrix}. \quad (7.3.10)$$

3. Perform the quantum state tomography and obtain $\hat{\rho}_p(t) = |\chi_p(t)\rangle \langle \chi_p(t)|$.

Then the matrix element mentioned above can be obtained straightforwardly,

$$\langle \chi_p(t) | M^\dagger \hat{\Sigma} M | \chi_p(t) \rangle = \text{Tr} \left[\hat{\rho}_p(t) M^\dagger \hat{\Sigma} M \right]. \quad (7.3.11)$$

7.3.6 Off-diagonal operators in the momentum space

Then we turn to investigate the method to obtain the expectation value of some off-diagonal operators $\hat{\mathcal{O}}_{\text{od}}$ in the momentum space. We will take position-dependent operators as examples, i.e.,

$$\hat{\mathcal{O}}_{\text{od}} = \hat{\Sigma} \otimes f(\hat{x}). \quad (7.3.12)$$

As mentioned above, the expectation value can be written as

$$\begin{aligned} & \langle \Psi(t) | M^\dagger \hat{\mathcal{O}}_{\text{dg}} M | \Psi(t) \rangle \\ &= \int dp dp' \Psi^*(p) \Psi(p') \langle p | f(\hat{x}) | p' \rangle \langle \chi_p(t) | M^\dagger \hat{\Sigma} M | \chi_{p'}(t) \rangle. \end{aligned} \quad (7.3.13)$$

Since $f(\hat{x})$ is not diagonal in the momentum space, the above expression will involve off-diagonal matrix-element as $\langle \chi_p(t) | M^\dagger \hat{\Sigma} M | \chi_{p'}(t) \rangle$. If we stick to the previous scheme, we will obtain two independent density matrices $\hat{\rho}_p(t)$ and $\hat{\rho}_{p'}(t)$, from which we can not construct the off-diagonal matrix element between two distinct momenta.

Inspired by the effective Hamiltonian $\hat{\mathcal{H}}_p$ for some definite momentum p ,

$$\begin{aligned} \hat{\mathcal{H}}_p &= pc(|1\rangle\langle 2| + |3\rangle\langle 4|) + imc^2(|1\rangle\langle 4| - |2\rangle\langle 3|) + \text{H.c.} \\ &\equiv pc(\hat{\mathbb{I}} \otimes \hat{\sigma}_x) - mc^2(\hat{\sigma}_x \otimes \hat{\sigma}_z), \end{aligned} \quad (7.3.14)$$

we notice that the first qubit can be diagonalized in the $\hat{\sigma}_x$ -basis. The quantum states and operators in the new basis $\{|+\rangle|0\rangle, |+\rangle|1\rangle, |-\rangle|0\rangle, |-\rangle|1\rangle\}$ and the old basis $\{|0\rangle|0\rangle, |0\rangle|1\rangle, |1\rangle|0\rangle, |1\rangle|1\rangle\}$, where $|0\rangle$ and $|1\rangle$ are the eigenstates of $\hat{\sigma}_z$, are related

by the following transform matrix \hat{S} ,

$$\hat{S} = \frac{\sqrt{2}}{2} \begin{pmatrix} 1 & 0 & 1 & 0 \\ 0 & 1 & 0 & 1 \\ 1 & 0 & -1 & 0 \\ 0 & 1 & 0 & -1 \end{pmatrix}, \quad (7.3.15)$$

where $|\pm\rangle \equiv \frac{1}{\sqrt{2}}(|0\rangle \pm |1\rangle)$ are eigenstates of $\hat{\sigma}_x$. In other words, the equation of motion for $|\chi_p(t)\rangle$ can be written in the new basis as follows,

$$i\hbar \frac{\partial}{\partial t} \begin{pmatrix} \chi_p^+(t) \\ \chi_p^-(t) \end{pmatrix} = \begin{pmatrix} \hat{H}_p^+ & 0 \\ 0 & \hat{H}_p^- \end{pmatrix} \begin{pmatrix} \chi_p^+(t) \\ \chi_p^-(t) \end{pmatrix} \quad (7.3.16)$$

with

$$\begin{pmatrix} \hat{H}_p^+ & 0 \\ 0 & \hat{H}_p^- \end{pmatrix} = \hat{S}^\dagger \hat{H}(p) \hat{S} = \begin{pmatrix} 0 & pc + imc^2 & 0 & 0 \\ pc - imc^2 & 0 & 0 & 0 \\ 0 & 0 & 0 & pc - imc^2 \\ 0 & 0 & pc + imc^2 & 0 \end{pmatrix} \quad (7.3.17)$$

and

$$\begin{pmatrix} \chi_p^+(t) \\ \chi_p^-(t) \end{pmatrix} = \begin{pmatrix} \chi_{p,1}^+(t) \\ \chi_{p,2}^+(t) \\ \chi_{p,1}^-(t) \\ \chi_{p,2}^-(t) \end{pmatrix} = \hat{S}^\dagger \begin{pmatrix} \chi_{p,1}(t) \\ \chi_{p,2}(t) \\ \chi_{p,3}(t) \\ \chi_{p,4}(t) \end{pmatrix}, \quad (7.3.18)$$

where $\chi_p^\pm(t)$ are column vectors with two entries and \hat{H}_p^\pm are 2×2 matrices in the new basis. As shown in Eq. (7.3.16), we note that the dynamics for $\chi_p^\pm(t)$ are

totally decoupled from each other, and can be separately simulated in quantum two-level systems. In order to obtain off-diagonal matrix elements between two distinct momenta p and p' , we have to simulate $\chi_p(t)$ and $\chi_{p'}(t)$ coherently. We obtain the following equations of motion by rearranging Eq. (7.3.16),

$$\begin{aligned} i\hbar \frac{\partial}{\partial t} \begin{pmatrix} \chi_p^+(t) \\ \chi_{p'}^+(t) \end{pmatrix} &= \begin{pmatrix} \hat{H}_p^+ & 0 \\ 0 & \hat{H}_{p'}^+ \end{pmatrix} \begin{pmatrix} \chi_p^+(t) \\ \chi_{p'}^+(t) \end{pmatrix}, \\ i\hbar \frac{\partial}{\partial t} \begin{pmatrix} \chi_p^-(t) \\ \chi_{p'}^-(t) \end{pmatrix} &= \begin{pmatrix} \hat{H}_p^- & 0 \\ 0 & \hat{H}_{p'}^- \end{pmatrix} \begin{pmatrix} \chi_p^-(t) \\ \chi_{p'}^-(t) \end{pmatrix}, \end{aligned} \quad (7.3.19)$$

which can be simulated in quantum four-level systems.

In the following investigation, we will use the average position $\langle \hat{x} \rangle \equiv \langle \psi(t) | \hat{x} | \psi(t) \rangle$ as an example. The detailed derivation is as follows,

$$\begin{aligned} \langle \hat{x} \rangle &= \langle \Psi(t) | M^\dagger \hat{x} M | \Psi(t) \rangle \\ &= \int dp dp' \Psi^*(p) \Psi(p') \langle p | \hat{x} | p' \rangle \langle \chi_p(t) | M^\dagger M | \chi_{p'}(t) \rangle \\ &= \int dp dp' \Psi^*(p) \Psi(p') \\ &\quad \times \langle p | \hat{x} | p' \rangle [\langle \chi_p^+(t) | \chi_{p'}^+(t) \rangle + \langle \chi_p^-(t) | \chi_{p'}^-(t) \rangle - i (\langle \chi_p^+(t) | \chi_{p'}^-(t) \rangle - \langle \chi_p^-(t) | \chi_{p'}^+(t) \rangle)] \\ &= \int \frac{dx dp dp'}{2\pi\hbar} x \exp[-(p-p')x/\hbar] \Psi^*(p) \Psi(p') [\langle \chi_p^+(t) | \chi_{p'}^+(t) \rangle + \langle \chi_p^-(t) | \chi_{p'}^-(t) \rangle]. \end{aligned}$$

The last line in the above equation is valid because of the following identity,

$$\int \frac{dp dp'}{2\pi\hbar} \exp[-(p-p')x/\hbar] \Psi^*(p) \Psi(p') [\langle \chi_p^+(t) | \chi_{p'}^-(t) \rangle - \langle \chi_p^-(t) | \chi_{p'}^+(t) \rangle] \quad (7.3.20)$$

which can be verified using $\rho_E(p) = \rho_E(-p)$ and $\chi_p^\pm(t) = [\chi_{-p}^\pm(t)]^*$.

The experiment procedure would be as follows.

1. Prepare the initial state determined by the initial condition $[\chi_{p,1}^\pm(0), \chi_{p,2}^\pm(0), \chi_{p',1}^\pm(0), \chi_{p',2}^\pm(0)]^T$.
2. Implement $\hat{H}_{p,p'}^\pm$ and let the system evolve for some time period t ,

$$\hat{H}_{p,p'}^\pm = \begin{pmatrix} \hat{H}_p^\pm & 0 \\ 0 & \hat{H}_{p'}^\pm \end{pmatrix} = \begin{pmatrix} 0 & pc \pm imc^2 & 0 & 0 \\ pc \mp imc^2 & 0 & 0 & 0 \\ 0 & 0 & 0 & p' \pm imc^2 \\ 0 & 0 & p' \mp imc^2 & 0 \end{pmatrix} \quad (7.3.21)$$

3. Perform the quantum state tomography and obtain $\rho_{p,p'}^\pm$,

$$\rho_{p,p'}^\pm = \begin{pmatrix} |\chi_{p,1}^\pm|^2 & \chi_{p,1}^\pm (\chi_{p,2}^\pm)^* & \chi_{p,1}^\pm (\chi_{p',1}^\pm)^* & \chi_{p,1}^\pm (\chi_{p',2}^\pm)^* \\ \chi_{p,2}^\pm (\chi_{p,1}^\pm)^* & |\chi_{p,2}^\pm|^2 & \chi_{p,2}^\pm (\chi_{p',1}^\pm)^* & \chi_{p,2}^\pm (\chi_{p',2}^\pm)^* \\ \chi_{p',1}^\pm (\chi_{p,1}^\pm)^* & \chi_{p',1}^\pm (\chi_{p,2}^\pm)^* & |\chi_{p',1}^\pm|^2 & \chi_{p',1}^\pm (\chi_{p',2}^\pm)^* \\ \chi_{p',2}^\pm (\chi_{p,1}^\pm)^* & \chi_{p',2}^\pm (\chi_{p,2}^\pm)^* & \chi_{p',2}^\pm (\chi_{p',1}^\pm)^* & |\chi_{p',2}^\pm|^2 \end{pmatrix}. \quad (7.3.22)$$

Sweeping the momenta p and p' over all possible values, we would obtain all of the information that is needed to calculate the expectation value $x(t) \equiv \langle \psi(t) | \hat{x} | \psi(t) \rangle$. The number of separate simulations for different (p, p') pairs for both signs will be N_P^2 , where N_P is the number of points with which we discretize the momentum axis.

7.3.7 Charge conservation and charge conjugation

The non-Hermitian Majorana Hamiltonian does not have eigenstates. However, we can define the concepts of particle and antiparticle from the eigenstates of the corresponding Dirac Hamiltonian, which is obtained by substituting the Majorana mass term with the Dirac mass term. Under the same convention, the 1+1 Dirac equation

takes the following dimensionless form,

$$i\partial_t |\psi\rangle = (\hat{\sigma}_x \hat{p}_x + m \hat{\sigma}_z) |\psi\rangle, \quad (7.3.23)$$

with the eigenvalues $\pm\sqrt{p^2 + m^2}$ and the corresponding eigenstates

$$\begin{aligned} |\psi_p^{(+)}\rangle &= \frac{1}{\sqrt{2}(p^2 + m^2)^{1/4}} \begin{pmatrix} \sqrt{\sqrt{p^2 + m^2} + m} \\ (p/|p|) \sqrt{\sqrt{p^2 + m^2} - m} \end{pmatrix} \otimes |p\rangle, \\ |\psi_p^{(-)}\rangle &= \frac{1}{\sqrt{2}(p^2 + m^2)^{1/4}} \begin{pmatrix} \sqrt{\sqrt{p^2 + m^2} - m} \\ -(p/|p|) \sqrt{\sqrt{p^2 + m^2} + m} \end{pmatrix} \otimes |p\rangle. \end{aligned} \quad (7.3.24)$$

Starting from an initial Majorana spinor $|\psi(0)\rangle = \begin{pmatrix} u_1(0) \\ u_2(0) \end{pmatrix} \otimes |p\rangle$, the time-dependent Majorana spinor can be formally written as follows,

$$|\psi(t)\rangle = \begin{pmatrix} v_1(t) \\ v_2(t) \end{pmatrix} \otimes |-p\rangle + \begin{pmatrix} u_1(t) \\ u_2(t) \end{pmatrix} \otimes |p\rangle. \quad (7.3.25)$$

Note that the appearance of the negative momentum component is originated from the charge conjugation in the Majorana mass term. By definition, the time-dependent charge is obtained as follows,

$$C(t) = |\langle \psi_p^{(+)} | \psi(t) \rangle|^2 + |\langle \psi_{-p}^{(+)} | \psi(t) \rangle|^2 - |\langle \psi_p^{(-)} | \psi(t) \rangle|^2 - |\langle \psi_{-p}^{(-)} | \psi(t) \rangle|^2 \quad (7.3.26)$$

By setting $\begin{pmatrix} u_1(0) \\ u_2(0) \end{pmatrix} = \begin{pmatrix} 1 \\ 0 \end{pmatrix}$, we obtain the theoretical and experimental data shown in Fig. 2 (b) in the main text.

Besides the violation of the charge conservation of plane-wave initial states, we investigate the charge conjugation on top of the Majorana dynamics of an initial

moving Gaussian wave packet as shown in Figs. 3 e-h in the main text. The initial Majorana spinor takes form of $\psi(x, t = 0) = \frac{1}{2}\pi^{-1/4}e^{-x^2/8-ip_0x} \begin{pmatrix} 1 \\ 1 \end{pmatrix}$ with $p_0 = 1$ in the position space. By definition, the charge conjugation interchanges the particle and antiparticle components in Eq. (7.3.25). In addition to the results in the main text, here we show the theoretical result for the dynamics of the internal degree of freedom in Fig. 7.3.2. In Fig. 7.3.2 B, we can clearly see that the populations of the particle and antiparticle components are interchanged right after the implementation of the charge-conjugation operator. Fig. 7.3.2 C shows the momentum distributions for the particle and antiparticle components at different times above and below the base lines, respectively. We clearly see from the Majorana dynamics of the internal degree of freedom that the evolution is continued after the implementation of the charge conjugation, although the roles of the particle and antiparticle are interchanged.

7.4 Experimental results

7.4.1 Majorana dynamics

In a quantum system, global phase can always be ignored because of its unobservability. However, under Majorana dynamics, for parallel initial states with different global phase.

$$|\psi_\theta(t = 0)\rangle := e^{i\theta} \begin{pmatrix} 1 \\ 0 \end{pmatrix} \otimes |p\rangle$$

the fidelity defined as $F(t) = |\langle \psi_\theta(t) | \psi_0(t) \rangle|^2$ is not conserved. In the enlarged Hilbert space, in $p = 0$ case

$$\Psi_\theta(t = 0) = (\cos \theta, 0, \sin \theta, 0)$$

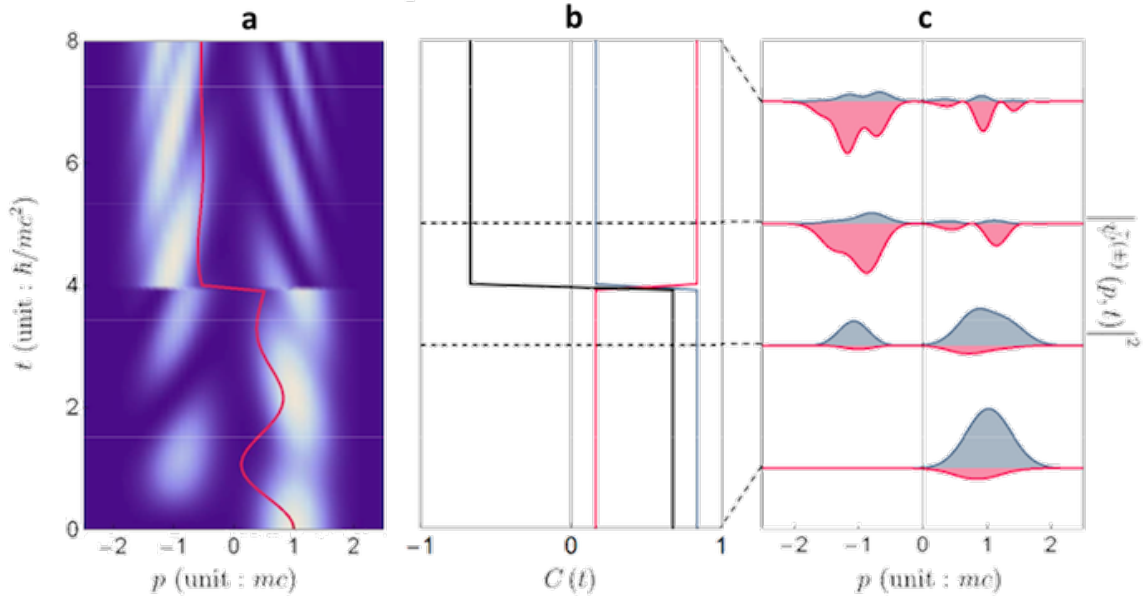


Figure 7.3.2: **Charge conjugation on top of the Majorana dynamics. a.** Time-dependent density distributions in momentum space. We implement the charge conjugation at the intermediate time $t = 4$. The solid line represents the average value of the momentum. **b.** Time-dependent charge (black) as well as populations of the particle (blue) and antiparticle (red) components. **c.** Momentum distributions of the particle (blue) and antiparticle (red) components at different times $t = 0, 3, 5$, and 8 . The curves are displaced along the vertical axis for better visualization.

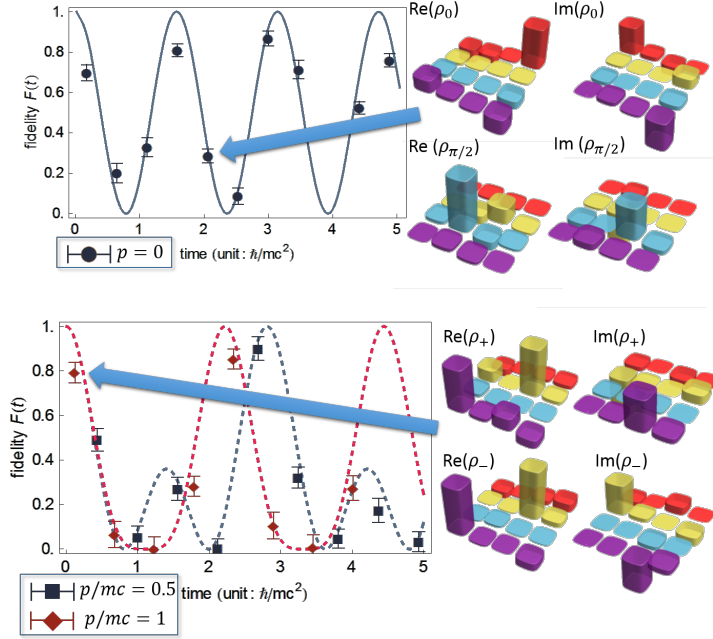


Figure 7.4.1: Global phase effect

And the fidelity

$$F(t) \equiv \text{Tr}(|\psi_\theta\rangle \langle \psi_\theta| |\psi_0\rangle \langle \psi_0|) = \text{Tr}(M\rho_\theta M^\dagger M\rho_0 M^\dagger)$$

in $p \neq 0$ case

$$\Psi_+(t=0) = (1, 0, -i, 0) \otimes |p\rangle, \quad \Psi_-(t=0) = (1, 0, i, 0) \otimes |-p\rangle$$

$$4F(t) \equiv \text{Tr}(M\rho_+ M^\dagger)^2 + \text{Tr}(M\rho_- M^\dagger)^2 + 2\text{Tr}(M\rho_+ M^\dagger)\text{Tr}(M\rho_- M^\dagger) \cos 2\theta$$

We experimentally observed this 'global phase effect' as showed in 7.4.1.

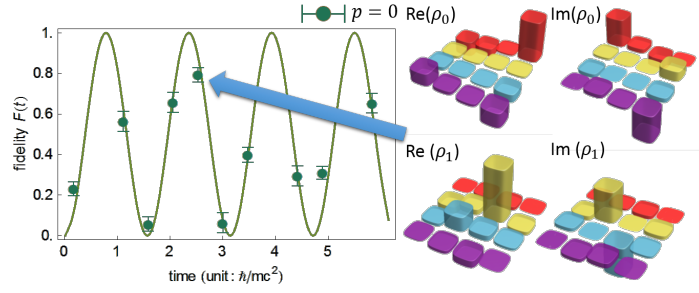


Figure 7.4.2: Orthogonality non-preservation

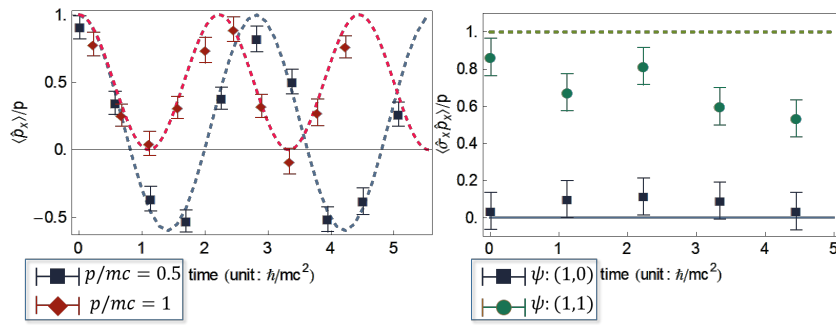


Figure 7.4.3: Momentum *Zitterbewegung* and helicity conservation

Another effect is the orthogonality non-preservation for initially orthogonal states

$$|\psi_0(t=0)\rangle := \begin{pmatrix} 1 \\ 0 \end{pmatrix} \otimes |p\rangle, |\psi_1(t=0)\rangle := \begin{pmatrix} 0 \\ 1 \end{pmatrix} \otimes |p\rangle$$

as showed in 7.4.2.

Average momentum $\langle \hat{p}_x \rangle$ oscillates but pseudo-helicity $\langle \hat{\sigma}_x \hat{p}_x \rangle$ conserves for initial state

$$\psi(x, t=0) = \frac{1}{\sqrt{2\pi}} e^{ipx/\hbar} \begin{pmatrix} 1 \\ 0 \end{pmatrix}$$

as showed in 7.4.3.

Fig. 7.4.4 shows our experimental results of the Majorana dynamics, where the initial spinors are chosen to be plane-wave states with $\psi_2 = 0$, i.e. $|\psi(0)\rangle = \begin{pmatrix} 1 \\ 0 \end{pmatrix} \otimes |p\rangle$.

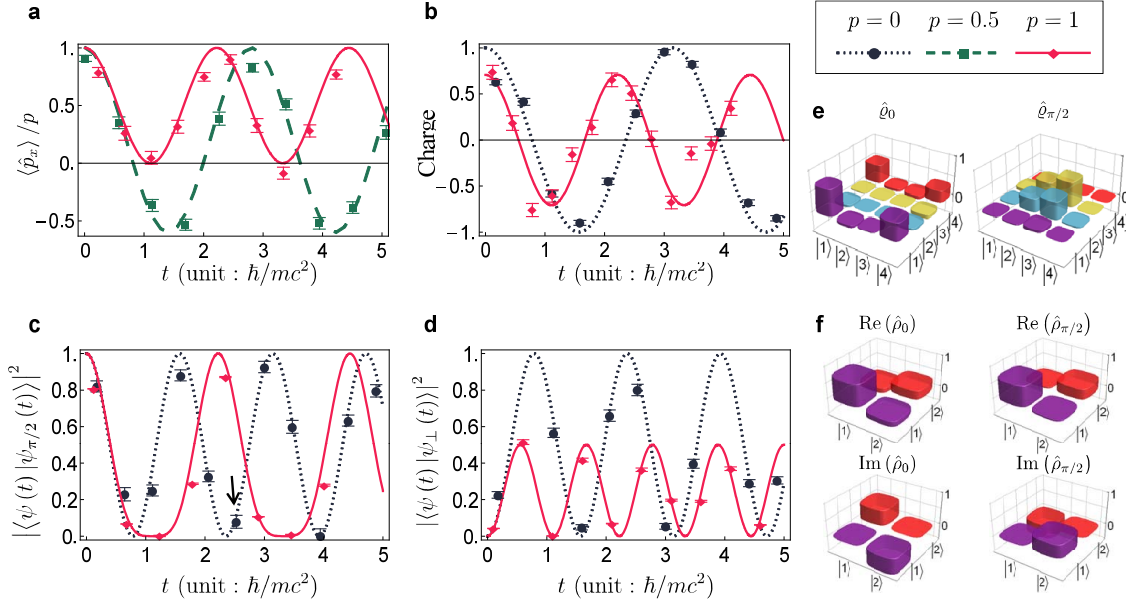


Figure 7.4.4: **Majorana dynamics.** **a**, Momentum space *Zitterbewegung*. **b**, Violation of charge conservation. The average values of the physical observables in **a** and **b** are measurement results of the Majorana spinor $|\psi(t)\rangle$ evolving from the initial state $\begin{pmatrix} 1 \\ 0 \end{pmatrix} \otimes |p\rangle$. **c**, Nonconserved fidelity caused by an initial global phase. The Majorana spinors $|\psi_{\theta}(t)\rangle$ evolve from the initial states $e^{i\theta} \begin{pmatrix} 1 \\ 0 \end{pmatrix} \otimes |p\rangle$ with $\theta = \pi/2$. **d**, Nonconserved orthogonality for initially perpendicular Majorana spinors. The Majorana spinors $|\psi_{\perp}(t)\rangle$ evolve from initial states $\begin{pmatrix} 0 \\ 1 \end{pmatrix} \otimes |-p\rangle$. We choose the momenta of the initial plane-wave states as $p = 0$ (black dotted), 0.5 (green dashed), and 1 (red solid), and set the Majorana mass $m = 1$. Curves are from theoretical simulation, and dots are from experimental data. **e**, Density matrices in the enlarged space obtained by quantum state tomography, related to the data point marked by the black arrow in **c**. **f**, Reconstructed density matrices in the original space. Error bars, 1σ .

Fig. 7.4.4a shows the momentum space *Zitterbewegung* for a Majorana particle. Due to the existence of the complex conjugate operator in the Majorana equation, the momentum, which is conserved for free Dirac particles, is no longer a conserved quantity in the Majorana dynamics. Because the violation of momentum conservation is originated by the Majorana mass term, the amplitude of the oscillation is inversely proportional to the magnitude of the momentum of the initial state. Meanwhile, the frequency of the oscillation is determined by the relativistic dispersion relation $\sqrt{p^2 + m^2}$, so the initial plane wave with larger momentum will oscillate faster. As shown in Fig. 7.4.4b, the Majorana dynamics also violates charge conservation, which may lead to physics beyond the standard model [96]. In the rest frame, the charge operator measures the difference between the populations of the internal states, which is equivalent to the $\hat{\sigma}_z$ operator [97]. For the non-zero momentum case, the particle and antiparticle basis is obtained by diagonalizing the corresponding Dirac equation with the same momentum, and the charge of a Majorana spinor is defined as the difference between the populations of the particle and antiparticle components (see Supplementary Materials). For the same reason, the amplitude and frequency of the charge oscillation exhibits similar momentum dependence as that of the momentum space *Zitterbewegung*.

Besides the above physical consequences, the dynamics governed by Majorana equation also shows unphysical phenomena. For example, the fidelity $|\langle \psi(t) | \psi_\theta(t) \rangle|^2$, where $|\psi(t)\rangle$ and $|\psi_\theta(t)\rangle$ are two Majorana spinors that evolve from initial states differing only in a global phase, $|\psi_\theta(0)\rangle = e^{i\theta} |\psi(0)\rangle$, will not always be unity as shown in Fig 7.4.4c. In other words, a Majorana spinor does not have the freedom to choose an arbitrary global phase. The reason for this surprising effect is the existence of the complex conjugate \hat{K} in the Majorana equation in Eq. (7.2.4). This effect can be more explicitly shown in the mapping \mathcal{M} in Eq. (7.2.2), i.e. the global

phase actually changes the initial four-component spinor in the enlarged Hilbert space. Figs. 7.4.4e and f show an example of the experimental results of the density matrices in the enlarged and original Hilbert spaces, which are indeed different from each other. In Fig. 7.4.4d, we experimentally observe the non-conservation of the orthogonality defined as $|\langle\psi(t)|\psi_{\perp}(t)\rangle|^2$, with $|\psi_{\perp}(t)\rangle$ being the Majorana spinor evolved from an orthogonal initial state $\begin{pmatrix} 0 \\ 1 \end{pmatrix} \otimes |-p\rangle$. During the evolution, the initial Majorana spinor will be coupled to $\begin{pmatrix} 0 \\ 1 \end{pmatrix} \otimes |p\rangle$ through the Hermitian relativistic kinetic term $\hat{\sigma}_x \hat{p}_x$, and $\begin{pmatrix} 0 \\ 1 \end{pmatrix} \otimes |-p\rangle$ through the non-Hermitian Majorana mass term $-im\hat{\sigma}_y \hat{K}$. The orthogonality $\langle\psi(t)|\psi'_{\perp}(t)\rangle$, where $|\psi'_{\perp}(t)\rangle$ is the Majorana spinor that evolves from the initial state $\begin{pmatrix} 0 \\ 1 \end{pmatrix} \otimes |p\rangle$, is always zero. This clearly indicates that the non-conservation of the orthogonality $|\langle\psi(t)|\psi_{\perp}(t)\rangle|^2$ stems from the non-Hermitian part of the Majorana Hamiltonian. As a result, given the same Majorana mass, we understand that the amplitude of the orthogonality oscillation is inversely proportional to the initial momentum.

7.4.2 Symmetry operations

Other than the plane waves, we also implement Majorana dynamics with realistic initial wave packets in our EQS. For example, the initial states for the Majorana dynamics in Fig. 7.4.5 are moving Gaussian states with momentum distributions centered around $p_0 = 1$ with internal state $\frac{1}{\sqrt{2}} \begin{pmatrix} 1 \\ 1 \end{pmatrix}$. The first part of the time axis ($0 \leq t < 4$) in Fig. 7.4.5 represents the Majorana dynamics of a moving wave packet, where we observe damping oscillation in the momentum space and *Zitterbewegung* in the position space. The reason of the damping in the momentum space is that a Gaussian wave packet has distribution over many different momentum components, and each momentum component oscillates with different frequency. To our surprise,

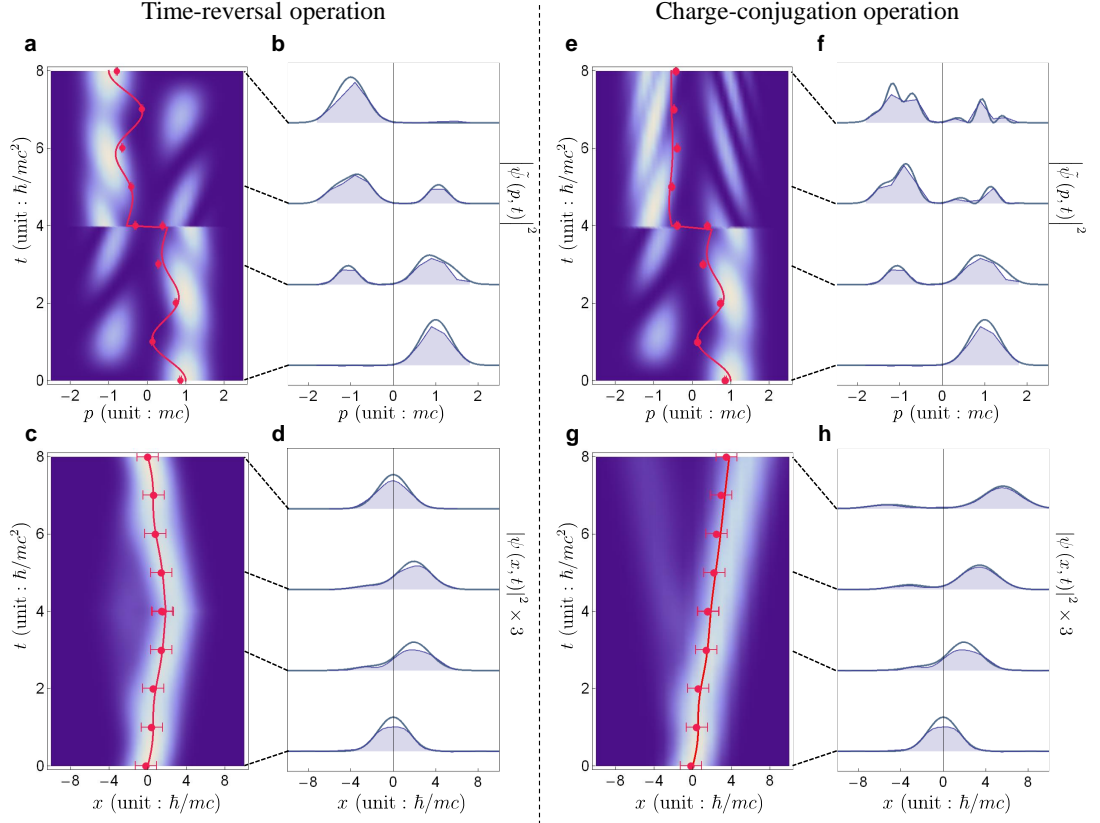


Figure 7.4.5: **Time reversal and charge conjugation.** **a-d**, Time reversal during the Majorana evolution. **e-h**, Charge conjugation on top of Majorana dynamics. The initial state is a moving Gaussian wave packet $\psi(x, t = 0) = \frac{1}{2}\pi^{-1/4}e^{-x^2/8 - ip_0x}$ ($\frac{1}{1}$) with initial average momentum $p_0 = 1$. The evolution is governed by the Majorana equation and the symmetry operations are performed at the midpoint $t = 4$. **a, e**, The time-dependent density distributions in the momentum space. **c, g**, The time-dependent density distributions in the position space. The solid curve represents the theoretical results of the average momentum $\langle \hat{p}_x \rangle$ in **a, c** and the average position $\langle \hat{x} \rangle$ in **e, g**, while the red dots with error bars are experimental results. **b, f**, The density distributions in the momentum space at given times. **d, h**, The density distributions in the position space at given times. From bottom to top, the times are $t = 0, 3, 5$ and 8 , respectively. The Solid curves are from theoretical calculation while the shades are from experiment. The curves are displaced along the vertical axis for better visualization, and the distributions in the position space are amplified by 3 times. The corresponding data points are marked by blue dashed lines.

although the average momentum of a Majorana particle behaves quite different from that of a Dirac particle, there is no visible difference in the behaviors of the average position as well as the probability distribution in position space. This is because a Majorana particle oscillates between the particle and antiparticle components with inverse momentum, but the positions as well as the velocities of the particle and antiparticle are exactly the same [69].

During the evolution of the Majorana equation, we implement the antiunitary time-reversal and charge-conjugation operations. Figs. 7.4.5a-d show our experimental results of the time-reversal operation during the Majorana time evolution. As shown in Fig. 7.4.5a, right after the time-reversal operation, the momentum as well as the velocity changes sign. As a result, the direction of the wave packet is reversed as shown in Fig. 7.4.5c. The damped average momentum as well as the position center of the wave packet is revived, which clearly shows that time is indeed reversed. Figs. 7.4.5e-f demonstrate the experimental implementation of the charge-conjugation operation. The latter interchanges the particle and antiparticle components, which are defined from the corresponding Dirac equation with the same momentum as discussed in Fig. 7.4.4b. By definition, the particle and corresponding antiparticle have opposite momentum but the same velocity. As a result, right after the charge-conjugation operation, the average momentum is reversed but not the velocity. Therefore, the trajectory in position space remains intact, which is different from the time-reversal operation.

7.5 Conclusion

In this chapter, we have experimentally constructed a prototype of the EQS capable of implementing unphysical evolution and operations. The crucial ideal is the

mapping from the original Hilbert space to the enlarged Hilbert space with doubled dimensions. The enlarged Hilbert space is encoded in the four internal states of the ground-state manifolds of a trapped $^{171}\text{Yb}^+$ ion. As a preliminary test, we simulate the unphysical Majorana dynamics, which manifests extraordinary phenomena, such as violations of momentum conservation and charge conservation. Further, we explore the capability of performing symmetry operations, i.e. time reversal and charge conjugation, at arbitrary evolution time. Our demonstration gives an unequivocal answer to the problem of implementing unphysical operations in a physical system.

The demonstrated embedding scheme would potentially reduce the computational complexity of ordinary quantum simulations in the sense that it eliminates the requirements for tomographic information. By enlarging the EQS, the demonstrated symmetry operations, can be potentially scaled up to many-particle systems in higher space-time dimensions, in which the conventional quantum state tomography is theoretically impossible. The EQS for multipartite systems only requires doubling the original Hilbert space dimension, which can be achieved by replacing a single *qubit* in an array of coupled *qubits* by a *ququad* (quantum four-level system). The proposed embedding scheme for the implementation of time reversal and charge conjugation operations may be extended to parity symmetry operations [84]. This enhanced toolbox for quantum simulators will be valuable for studying conservation laws and improving the computational capabilities of current quantum platforms.

Chapter 8

Quantum simulation of quantum field theory

In this chapter, we report on the first experimental quantum simulation of interacting quantum field modes with trapped ions, using a model of a fermion and an antifermion field modes interacting via bosonic field modes. Interesting features of quantum field theory (QFT) including particle pair creation and annihilation, self energy interactions, and non-perturbative phenomenon in the ultrastrong coupling (USC) or deep strong coupling (DSC) regimes are experimentally observed and studied by manipulating a $^{171}\text{Yb}^+$ ion's four internal levels as fermionic modes and motional phonon modes as bosonic modes. Jordan-Wigner transformation is used to map fermionic modes to internal qudits. Our experimental study represents an avenue towards going beyond classical computers by its scalability to add more bosonic and fermionic modes, which is an “exponential explosion” for classical computers.

8.1 Quantum field theory simulation

Quantum simulators are devices designed to simulate the properties of quantum models [5, 8]. The intrinsic physical behaviors fully governed by the laws of quantum mechanics make them possible to efficiently study complex quantum systems which asymptotically could not be solved by classical formula-based computation [62, 63]. Recent trapped-ions or super-conducting experimental progress for Ising models [98], relativistic Dirac equations [74, 79], embedded quantum simulators [58, 99] and fermionic models [100, 101] have demonstrated the feasibility of simulating numerous kinds of quantum many-body systems. However, the full experimental simulation have not been done for quantized fields described by quantum field theory (QFT), which applies quantum mechanics to functions of space-time and successfully give rise to the standard model of elementary particles. As far as we know, this work is the first experimental quantum simulation of interacting quantum field modes. Our approach is scalable by adding progressively more fermionic and bosonic field modes, which leads to a full quantum simulation of quantum field theories such as quantum electrodynamics (QED).

The classical ways to analyze QFT are Dyson series expansion in perturbation theory and Feynman diagrams [102]. When the coupling parameter is too large the perturbative methods will fail for a finite-mode Dyson expansion, mainly because only a reduced number of perturbative Feynman diagrams can be calculated. While a trapped-ion quantum simulator with the high degree of quantum control [6] could overcome these limitations and finally simulate QFTs faster than classical computers. Based on the proposal of Ref. [75], our experimental quantum simulation of finite-number interacting quantized field modes will include all terms of the Dyson expansion. In particular, We consider a basic model of

- Only one fermion and one anti-fermion
- Interacting through bosonic field modes

which already reveals interesting features such as self-interactions, particle creation and annihilation and non-perturbative regimes. The Hamiltonian for this simplified model is

$$\begin{aligned}
H &= \omega(b_p^\dagger b_p + d_p^\dagger d_p) + \int dk \omega_k a_k^\dagger a_k \\
&+ g \int dx \psi^\dagger(0, x) \psi(0, x) A(0, x)
\end{aligned} \tag{8.1.1}$$

where b_p and d_p are fermionic and antifermionic annihilation operators while a_k are the bosonic annihilation operators.

As a stepped experimental demonstration, we first consider the simplest situation with only one bosonic mode, which can be easily represented as a single ion's phonon mode along X or Y direction. Fermion and antifermion are considered as two comoving modes with incoming Gaussian wave packets which are centered in the average momentum with distant average initial positions. They are also assumed to make single excitation when applied to the vacuum. These modes describes self-interaction dressed states by emission and absorption of virtual bosons. They also represent the lowest order free evolution of the incoming wave packets which will collide in a certain region of spacetime. The pair creation and annihilation is local and takes place only when the two wave packets of fermion and antifermion overlap. There is also a distant interaction between fermion and antifermion mediated by the coupling to the bosons. A diagram of these interactions similar to the Feynman diagram is showed in Fig. 8.1.1.

Note that the loop of this diagram includes all terms in a finite-mode Dyson

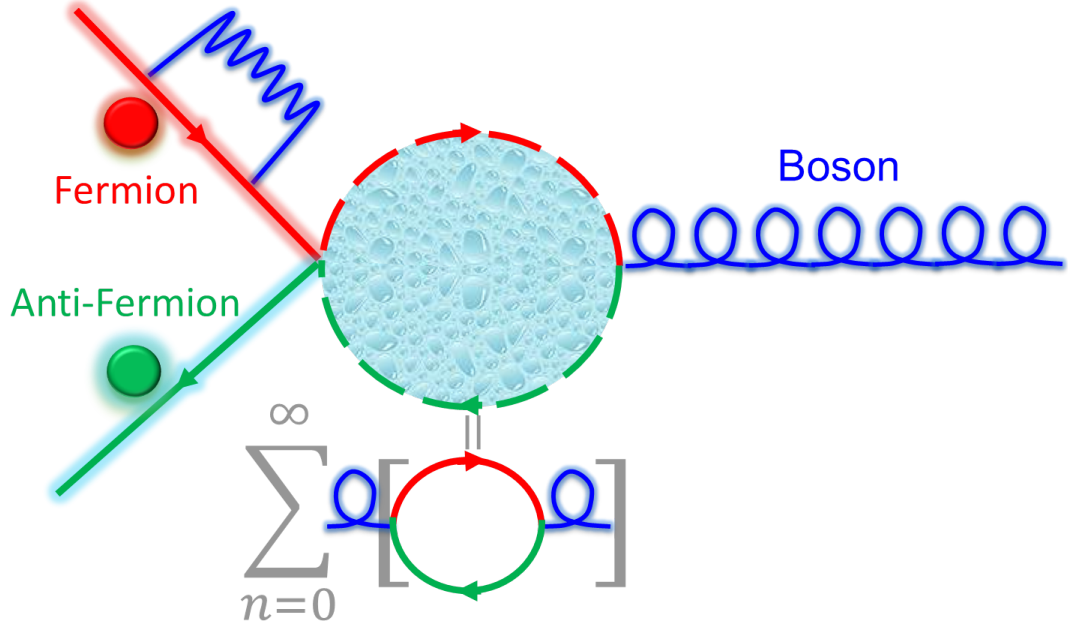


Figure 8.1.1: Diagram of interactions between fermion, antifermion and bosons.

expansion, which is very different from the standard perturbative Feynman diagram with only a reduced number of terms. By applying slow massive bosons and some other reasonable approximations described by Ref. [75], the interaction Hamiltonian that we want to realize becomes

$$\begin{aligned}
 H &= g_1 e^{-i\omega_0 t} (b^\dagger b a_0 + d d^\dagger a_0) + g_2 e^{-(t-T/2)^2 / (2\sigma_t^2)} \\
 &\cdot (e^{i\delta t} b^\dagger d^\dagger a_0 + e^{-i(2\omega_0 + \delta)t} d b a_0) + h.c.
 \end{aligned}
 \tag{8.1.2}$$

where $\delta = \omega_f + \omega_{\bar{f}} - \omega_0$. ω_f , $\omega_{\bar{f}}$ and ω_0 represent the energy of fermion operator b , antifermion operator d and boson operator a_0 . g_2/g_1 gives the relative strength ratio between pair creation and self-interaction. T is the total time of pair-creation process while σ_t is the temporal interval of the interaction region. Applying a standard Jordan-Wigner mapping from fermionic modes into four internal levels of a single

$^{171}\text{Yb}^+$ ion

$$\begin{aligned} b^\dagger &= I \otimes \sigma^+, b = I \otimes \sigma^-, \\ d^\dagger &= \sigma^+ \otimes \sigma_z, d = \sigma^- \otimes \sigma_z \end{aligned} \quad (8.1.3)$$

then the Hamiltonian becomes

$$\begin{aligned} H_I &= g_1(|1\rangle\langle 1| + 2|2\rangle\langle 2| + |4\rangle\langle 4|)a_0e^{-i\omega_0t} \\ &- g(t)(|1\rangle\langle 4|a_0^\dagger e^{-i\delta t} + |1\rangle\langle 4|a_0e^{-i(2\omega_0+\delta)t}) + h.c. \end{aligned} \quad (8.1.4)$$

where

$$g(t) = g_2e^{-(t-T/2)^2/(2\sigma_t^2)}.$$

The vacuum state and fermionic states are represented as

$$|1\rangle = |\text{vacuum}\rangle, |2\rangle = |f\rangle, |3\rangle = -|\bar{f}\rangle, |4\rangle = -|f, \bar{f}\rangle \quad (8.1.5)$$

The experimental diagram for this implementation is showed in Fig. 8.1.2.

This internal state labels differ from previous experiments by swapping Zeeman state $|4\rangle$ with clock state $|3\rangle$ for the ease of experimental realization. The Hamiltonian can be implemented with following trapped ion operations

- $(|1\rangle\langle 1| + 2|2\rangle\langle 2| + |4\rangle\langle 4|)a_0e^{-i\omega_0t}$: ω_0 detuned displacement operators with σ_+ polarization Raman beams, as it shows in Fig. 8.1.3.
- $|1\rangle\langle 4|a_0^\dagger e^{-i\delta t}$: δ detuned blue sideband transition between $|1\rangle \leftrightarrow |4\rangle$.
- $|1\rangle\langle 4|a_0e^{-i(2\omega_0+\delta)t}$: $2\omega_0 + \delta$ detuned red sideband transition between $|1\rangle \leftrightarrow |4\rangle$.

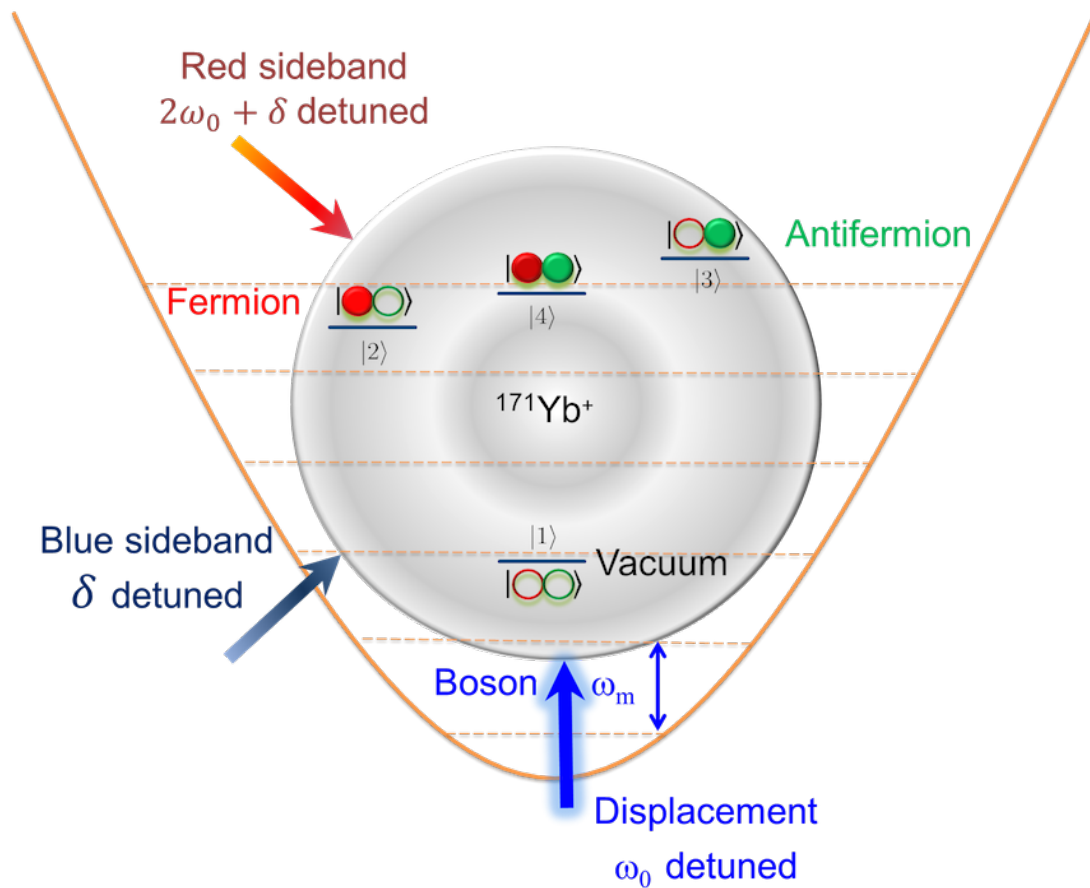


Figure 8.1.2: Diagram of QFT experiment.

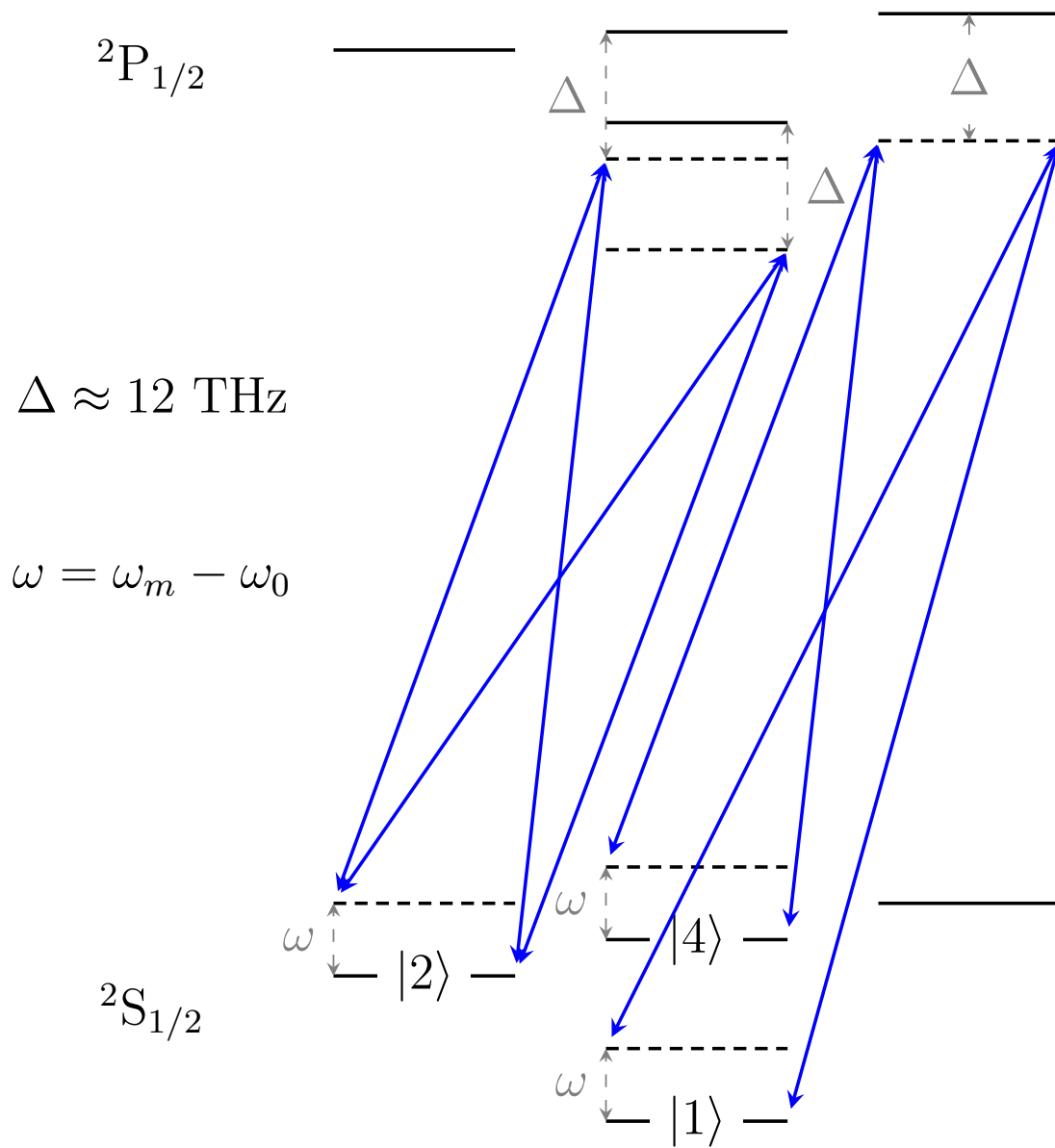


Figure 8.1.3: Diagram of displacement operator with σ_+ polarization Raman beams.

As we already calculated in Chapter 3, all optical transitions between $^2S_{1/2} \leftrightarrow ^2P_{1/2}$ states have the same transition strength factor respect to absolute values. For this experiment case, the σ_+ polarization Raman beams with frequency difference $\omega_m - \omega_0$ gives exactly the desired displacement Hamiltonian $(|1\rangle\langle 1| + 2|2\rangle\langle 2| + |4\rangle\langle 4|)a_0e^{-i\omega_0t}$. In principle we can also implement other kinds of displacement Hamiltonians by applying additional σ_- and π polarization Raman beams with specified ratios.

8.2 Experimental results

This experiment is realized with stimulated Raman transitions implemented by a 375 nm “MiraHP” mode-locked pulse laser. We first cool down vibrational modes and initialize the ion to the vacuum state $|1, n = 0\rangle$ by resolved sideband cooling [43]. Then a phonon displacement Raman beam component for all internal levels, a detuned blue sideband Raman beam component and a detuned red sideband Raman beam component (both for the clock transition), are applied simultaneously to realize this Hamiltonian in our trapped $^{171}\text{Yb}^+$ ion system. All these Raman laser beams introduce state-dependent forces and push the ion along $\pm\Delta k$ direction for certain internal states. After the evolution process, we measure the final distribution of phonon number states by applying the blue and the red sideband transitions and fitting the signals through the maximal likelihood method with parameters of the Fock state populations. For the measurement step, we observe the followed time evolution of blue and red sideband transitions up to 250 μs with 1 μs step by averaging 200 repetitions of each step.

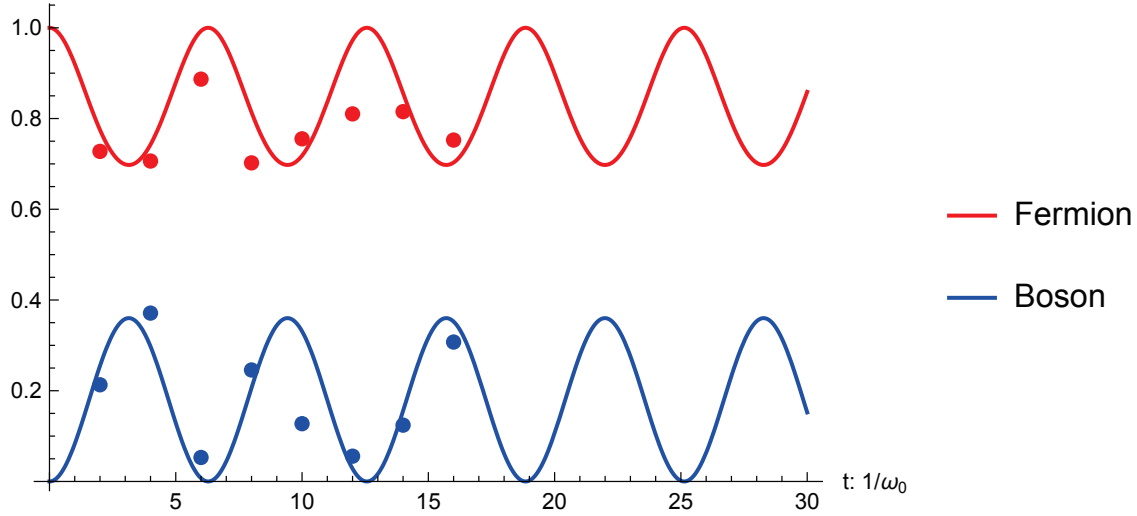


Figure 8.2.1: Experimental data of self-interaction process. Solid curve is theoretical simulation curve.

We first realize the fermion self-interactions process with parameter

$$g_1 = 0.15\omega_0, g_2 = 0, \sigma_t = 3/\omega_0.$$

The experimental data is showed in Fig. 8.2.1.

We observe that the initial fermion emits and reabsorbs bosons at a period $2\pi/\omega_0$. The experimental result match well with the theoretical simulation curve. For the average boson (phonon) number measurement, we first use optical pumping to trace out internal states and then make a phonon number fitting measurement with blue sideband time sweep. Fig. 8.2.2 shows the corresponding phonon number fitting data at $t = 2/\omega_0$.

We then realize the pair annihilation process with parameter

$$g_1 = 0.01\omega_0, g_2 = 0.21\omega_0, \sigma_t = 3/\omega_0.$$

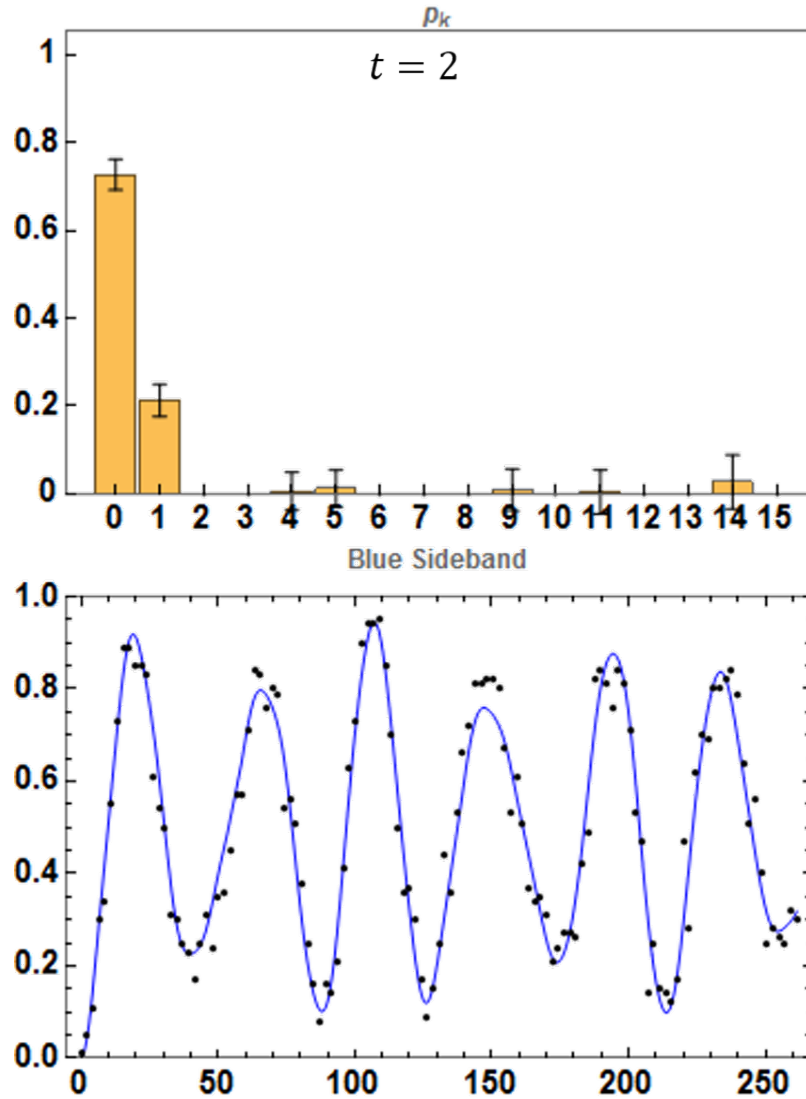


Figure 8.2.2: Experimental data of phonon number fitting at $t = 2/\omega_0$. The upper histogram is phonon number distribution. The lower data and curve are experimental data and theoretical curve of blue sideband time sweep.

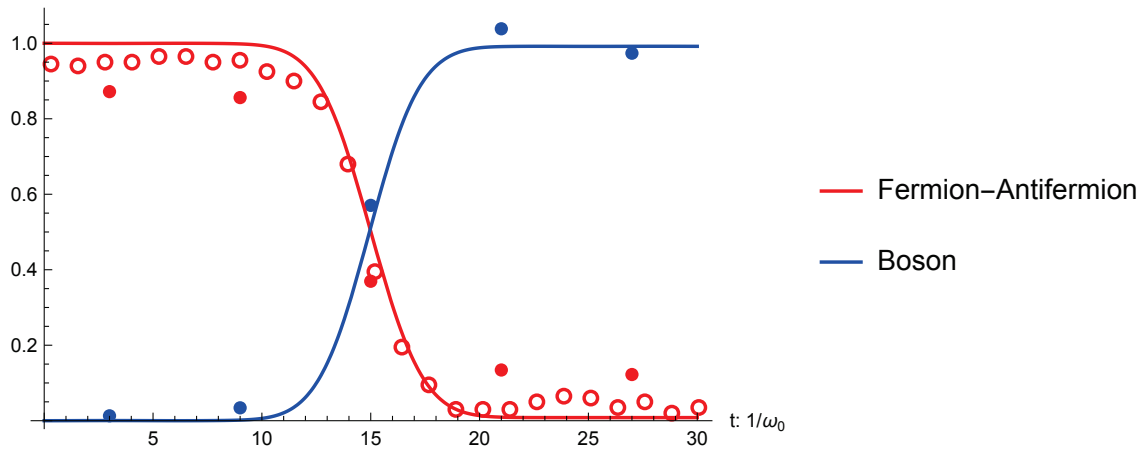


Figure 8.2.3: Experimental data of pair annihilation process. Solid dots and hollow dots are data of two experiments. Solid curve is theoretical simulation curve.

The experimental data is showed in Fig. 8.2.3.

We observe that the initial fermion and antifermion pair annihilates when the two modes overlap and enter the interaction region. This process gives rise to the population of bosonic mode. The projection population of fermion mode or fermion-antifermion pair at bosonic mode $|n = 0\rangle$ are measured based on the population measurement of state $|1, 0\rangle$. And following experimental steps are for population measurement of $|1, 0\rangle$.

- Collapse bright states' population to dark state $|1\rangle$ by standard detection process
- A “uniform red sideband” transition to transfer states $|1, n \neq 0\rangle$ to bright state $|3, n - 1\rangle$ with same Rabi frequency
- Carrier transition to swap bright state $|3\rangle$ and dark state $|1\rangle$
- Standard detection process to measure bright states' population, which should be equal to the original population of $|1, 0\rangle$

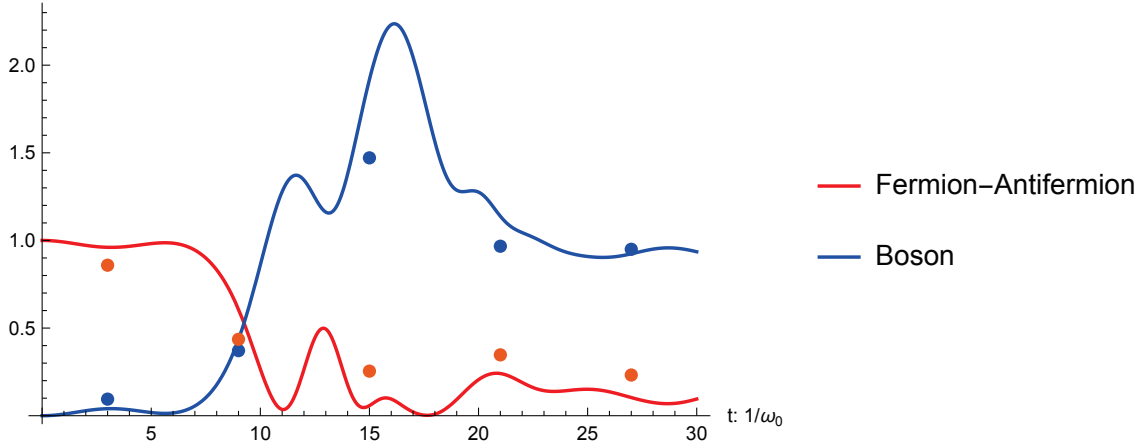


Figure 8.2.4: Experimental data of non-perturbative regimes interaction process. Solid curve is theoretical simulation curve.

Finally we realize the non-perturbative regimes interaction process with parameter

$$g_1 = 0.1\omega_0, g_2 = \omega_0, \sigma_t = 4/\omega_0$$

The experimental data is showed in Fig. 8.2.4.

For large g_2 values ($g_2 \geq \omega_0$), we enter into the non-perturbative regime, in which Feynman-diagram techniques are of little help. Here, we obtain that the number of created bosons is much larger due to the non-resonant terms. The dynamics becomes more complex and strongly dependent on the specific coupling values.

All these experimental data are summarized as Fig. 8.2.5.

In conclusion, this work is featured as the first experimental quantum simulation of interacting quantum field modes. Our approach is scalable by adding progressively more fermionic and bosonic field modes, which leads to a full quantum simulation of quantum field theories such as quantum electrodynamics (QED).

In our current experimental system, an extension to multi phonon (bosonic) modes should be straightforward by loading a chain of ions and shining Raman laser

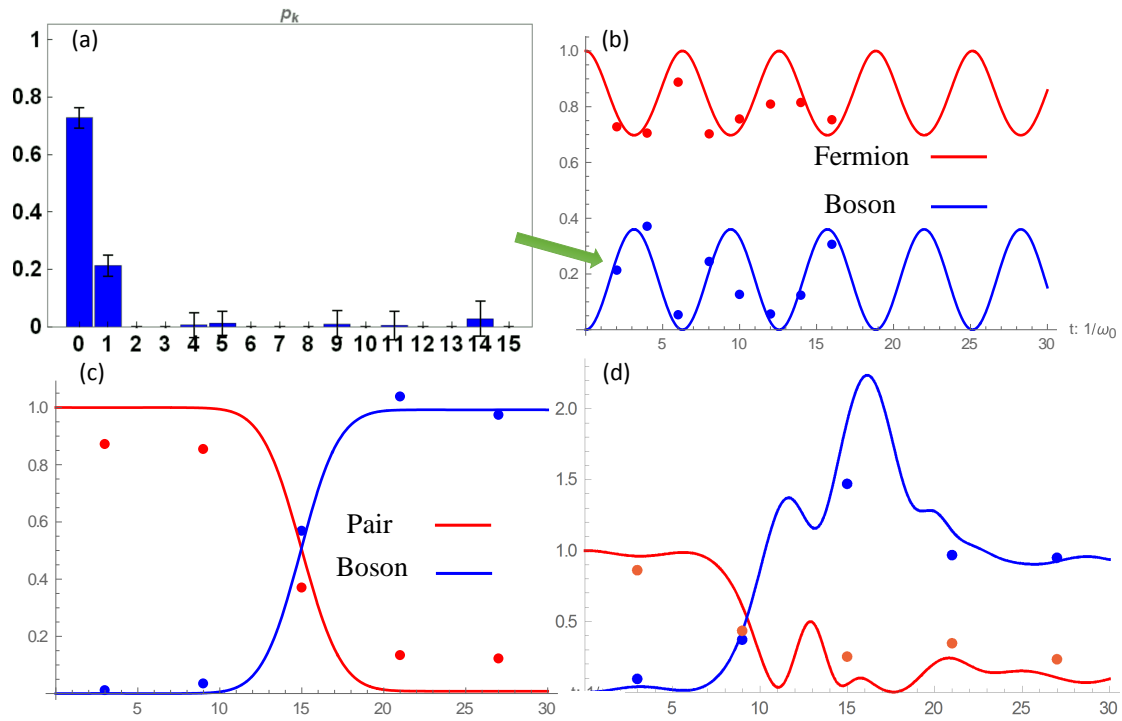


Figure 8.2.5: Experimental data of quantum field theory simulation.

beam on one end of the ion chain. Then we can effectively simulate open system Markov process with these bosonic modes.

In this way, the experimental study represents an avenue towards going beyond the exponential explosion limit of classical computers. We point out that already with 10 two-level ions and 5 phonons per ion, one could perform quantum simulations of interacting quantum field modes that are beyond the reach of classical computers, that is, a Hilbert space dimension of $10^{10} \sim 2^{33}$.

Chapter 9

Conclusion and outlook

In conclusion, we have built a $^{171}\text{Yb}^+$ trapped-ion system with various quantum operations. The high fidelity attained in these operations and the ultimate controllability of our integrated control system shows the high performance of our $^{171}\text{Yb}^+$ system as a promising candidate of quantum computer. Several fundamental and important experiments on quantum computation and simulation are demonstrated with these systems. The observation of experimental violation of Kochen-Specker inequalities shows quantum contextuality is rooted in the fundamental structure of quantum mechanics. The simulation of relativistic effects and anti-unitary operations under non-Hamiltonian Majorana dynamics in a Hamiltonian system greatly extend the applicability of quantum simulator. For a higher degree of control in quantum regime, motional degrees of freedom are then added to our system with stimulated Raman transitions implemented by a mode-locked pico-second pulse laser. With this new functionality, we make an experimental quantum simulation of interacting bosonic and fermionic quantum field modes, which reveals interesting features such as self interactions, particle creation and annihilation and non-perturbative regimes. All

these work can be summarized as this:

- Build a $^{171}\text{Yb}^+$ trapped-ion system
- Implement a diverse set of quantum operations
- Experimental violation of quantum contextuality
- Quantum simulation of symmetry operations and quantum field theory

For trap system, a detailed implementation of our integrated control system is discussed. A lot of fancy quantum computation and simulation experiments have been done with the help of this system. In a recent plan, an extension to multiple ions as well as a more robust exception reporting and recovery strategy to handle experimental accidents will be added to this system.

For quantum contextuality experiment, later we will implement simultaneously measurement with Ba ions and $^{171}\text{Yb}^+$ ions together and using Ba ions' shielding level to protect certain state during measurement, thus make a loophole-free quantum contextuality verification.

For quantum simulation of anti-unitary operations, our scheme is straightforward to scale up by replacing the momentum eigenvalue scheme with the real momentum operator and simulate multiple Majorana particles with more ions.

For quantum simulation of quantum field theory, our experimental scheme is a scalable approach and can be extended beyond the limit of classical computation of quantum field theory when more fermions and bosons are included.

Appendix A

Control software

A.1 Code snippets

Talk is cheap, show me the code – Linus Tovalds

Listing 1: Diople transition elements calculation.

```
1 ReducedMatrixElement[{l1_}, {l2_}] := (l1 - l2) Sqrt[Max[l1, l2]];
2 ReducedMatrixElement[{ls1___, l1_, s1_, j1_}, {ls2___, l2_, s2_,
3   j2_}] := (
4   (-1)^(l1 + s1 + j2 + 1) Sqrt[(2 j1 + 1) (2 j2 + 1)]
5   SixJSymbol @@ ( {
6     {l1, j1, s1},
7     {j2, l2, 1}
8   } ) ReducedMatrixElement[{ls1, l1}, {ls2, l2}]
9   );
10
11 DiopleTransitionElement[{ls1__, j1_, m1_}, {ls2__, j2_, m2_}] := (
```

```

12      (-1)^(j1 - m1) ThreeJSymbol @@ ( Transpose@{
13          {j1, 1, j2},
14          {-m1, m1 - m2, m2}
15      } ) ReducedMatrixElement[{ls1, j1}, {ls2, j2}]
16  );

```

Listing 2: Call LabVIEW function VI from Mathematica.

```

1  AppCls = NETLink`NETNew["LabVIEW.ApplicationClass"];
2
3  LoadVI[viname_String, option_Integer: 16, resv_Symbol: False] :=
4  Module[{vipath, r},
5      vipath =
6          If[StringLength@viname > 3 &&
7              StringTake[viname, -3] == ".vi" && !
8              StringFreeQ[viname, "\\\" | \"/"], viname,
9              VIDir <> viname <> ".vi"];
10     r = AppCls@GetVIREference[vipath, "", resv, option];
11     If[r != $Failed, LoadVI[viname] = r]; r
12 ];
13
14 MakeAndCastNETObject[obj_Integer, type_] := NETLink`CastNETObject[
15     NETLink`MakeNETObject[obj, "System.UInt32"], type];
16 MakeAndCastNETObject[obj_, type_] := Module[{r = obj},
17     If[! NETLink`NETObjectQ[r], r = NETLink`MakeNETObject[r]];
18     If[r === $Failed, obj,

```

```

19     If[NETLink`InstanceOf[r, "System.__ComObject"], r,
20         NETLink`CastNETObject[r, type]]]
21 ];
22
23 CallVI[vi_?NETLink`NETObjectQ, paramNames_List, paramVals_List] :=
24     Module[{param1, param2, r},
25         NETLink`BeginNETBlock[];
26         param1 =
27             NETLink`CastNETObject[
28                 NETLink`MakeNETObject[paramNames], "object"];
29         param2 =
30             NETLink`ReturnAsNETObject[
31                 MakeAndCastNETObject[
32                     MakeAndCastNETObject[#, "object"] & /@ paramVals, "object"]];
33         vi@Call[param1, param2];
34         r = NETLink`NETObjectToExpression[param2];
35         NETLink`EndNETBlock[]; r
36     ];
37 CallVI[viname_String, paramNames_List, paramVals_List] :=
38     CallVI[LoadVI[viname], paramNames, paramVals];

```

Listing 3: Data operations.

```

1 Each[lst_, expr_] := (expr @@ #) & /@ lst
2
3 Spread[lst_] :=

```

```

4   If[Head[lst][[1, 2]]] === List, Transpose[Thread /@ lst], lst]
5
6   DateFolder[date_String] :=
7     FileNameJoin[{DataFolder[], StringTake[date, 4],
8       If[StringLength[date] >= 6, StringTake[date, 6], ""],
9       If[StringLength[date] >= 8, StringTake[date, 8], ""]}];
10  DateFolder[date_List; DateList[]] := DateFolder@DateString[date,
11    Take[{"Year", "Month", "Day"}, Min[3, Length[date]]]];
12
13  DataDateString[s_String] := StringTake[FileName[s], {-14, -7}];
14
15  DataDate[s_String] := DateList@DataDateString[s];
16
17  DateTime[s_String] := ToExpression /@ StringTake[FileName[s],
18    {{-14, -11}, {-10, -9}, {-8, -7}, {-6, -5}, {-4, -3}, {-2, -1}}];
19
20  DataFolder[] = FileNameJoin[{DriveLetter[], "Data"}];
21  DataFolder[s_String] :=
22    If[! StringFreeQ[s, "\\\" | "/"], DataFolder[],
23      DateFolder@DataDateString[s]];
24
25  DataPath[s_String] :=
26    If[! StringFreeQ[s, ":"], s, FileNameJoin[{DataFolder[s],
27      If[FileExtension[s] === "" &&
28        StringFreeQ[StringTake[s, -1], "\\\" | "/"], s <> ".txt", s]}]

```

```

29     ];
30
31 LoadData[stream_InputStream] := Module[
32     {items = {}, item = "", value = "", mode = 0, depth = 0,
33     separator = "", lines, line, pos},
34     lines = ReadList[stream, String];
35     Do[
36         Switch[mode,
37             0, If[StringTake[line, -1] == "=",
38                 item = StringTake[line, {1, -2}];
39                 mode = 1,
40                 If[(pos = StringPosition[line, "=") != {}],
41                     item = StringTake[line, pos[[1, 1]] - 1];
42                     value = StringTake[line, {pos[[1, 2]] + 1, -1}];
43                     AppendTo[items, item -> value];
44                 ]],
45             1, If[StringTake[line, -1] == "{",
46                 value = "";
47                 mode = 2;
48                 depth = 1;
49                 separator = StringTake[line, {1, -2}]],
50             2, If[line == separator <> "{", ++depth,
51                 If[line == "}" <> separator, --depth]];
52     If[depth == 0,
53         AppendTo[items, item -> value]; mode = 0,

```

```

54     value = value <> line <> "\n"]
55     ], {line, lines}];
56     items
57     ];
58 LoadData[s_String] := Module[{file = DataPath[s], data},
59     If[FileExistsQ[file], file = OpenRead[file], Return[]];
60     data = LoadData[file];
61     Close[file];
62     If[StringFreeQ[s, "\\\" | "/"], LoadData[s] = data];
63     data
64     ]
65 LoadData[s_String, item_String] := item /. LoadData[s]
66 LoadData[s_String, item__String] := List[item] /. LoadData[s]
67
68 CountsData[s_String] :=
69     Module[{data = LoadData[s, "Counts"], variable, count},
70     data = StringSplit[data, "\n"];
71     data = Transpose[Table[StringSplit[x], {x, data}]];
72     variable = ToExpression[Take[data, 1][[1]]];
73     count = ToExpression[Transpose[Take[data, {3, -1}]]];
74     CountsData[s] = Table[variable[[i]] -> Partition[count[[i]]/
75         If[# >= 256, #, 1] &[GCD @@ (count[[i])]], 4], {i,
76         Length[variable]}]
77     ]
78

```

```

79 SplitCounts[s_String] :=
80   Module[{steps =
81     Floor[(#2 - #1)/#3 + 1 & @@
82     ToExpression[LoadData[s, "Start", "End", "Step"]]],
83     totalsteps = Length[CountsData[s]]},
84     Table[CountsData[s][[(i - 1)*steps + 1 ;; i*steps]],
85     {i, Floor[totalsteps/steps]}]
86   ];
87
88 FromCounts[lst_List, expr_] := Each[lst, #1 -> Each[#2, expr] &]
89 FromCounts[s_String, expr_] := FromCounts[CountsData[s], expr]
90
91 ToState[x_?NumberQ] := If[x > DarkThreshold, 1., 0.]
92 ToState[lst_List] := (If[# > DarkThreshold, 1., 0.] &) /@ lst
93 ToState[lst_?
94   NumberQ] := (If[# > DarkThreshold, 1., 0.] &) /@ (List@lst)
95
96 Average[lst_List, n_Integer, func_[: Mean] :=
97   Each[lst, {#1, func[Partition[#2, n]]} &]
98 Average[s_String, expr_, n_Integer, func_[: Mean] :=
99   Average[FromCounts[s, expr], n, func]
100 Average[lst_List, func_[: Mean] := Each[lst, {#1, func[#2]} &]
101 Average[s_String, expr_, func_[: Mean] :=
102   Average[FromCounts[s, expr], func]
103

```



```

104 C1 = #1 &;
105 C2 = #2 &;
106 C3 = #3 &;
107 C4 = #4 &;
108 C0 = (#1 + #2 + #3 + #4) &;
109
110 S1 = ToState[#1] &;
111 S2 = ToState[#2] &;
112 S3 = ToState[#3] &;
113 S4 = ToState[#4] &;
114 S0 = ToState[#1 + #2 + #3 + #4] &;
115
116 CurrentDateString[offset : (_?NumberQ) : 0] :=
117   DateString[DatePlus[DateList[], offset],
118     {"Year", "Month", "Day"}]
119
120 CurrentTimeString[offset : (_?NumberQ) : 0] :=
121   DateString[DatePlus[DateList[], offset],
122     {"Year", "Month", "Day", "Hour", "Minute", "Second"}]
123
124 NewData[prefix_String] := Module[{data, path, dir},
125   data = prefix <> CurrentTimeString[];
126   path = DataPath[data];
127   dir = DirectoryName[path];
128   If[! DirectoryQ[dir], CreateDirectory[dir]];

```

```

129   Close[OpenAppend[path]];
130   data
131   ];
132
133   DataString[item_, value_] := ToString[item] <> "=" <>
134     (If[StringPosition[#, "\n"] === {}, #, "\n{\n" <> # <> "\n}"] &@
135       ToString[value]) <> "\n";
136   DataString[items_List] := StringJoin @@ Each[items, DataString];
137
138   WriteData[s_String, items_List] :=
139     Module[{fp = OpenWrite[DataPath[s]]},
140       WriteString[fp, DataString[items]];
141       Close[fp]; s
142     ];
143
144   AppendData[s_String, items_List] :=
145     Module[{fp = OpenAppend[DataPath[s]]},
146       WriteString[fp, DataString[items]];
147       Close[fp]; s
148     ];

```

Listing 4: Microwave files import and export.

```

1   ToFormula[x_Integer] := x;
2   ToFormula[x : (_Real | _Rational)] :=
3     Module[{xr = Round[x]},

```

```

4     If[Abs[xr - x] < 10^-6, xr, SetAccuracy[x, 8]];
5 ToFormula[x_Complex] := Complex @@ (ToFormula /@ {Re[x], Im[x]});
6 ToFormula[sym_Symbol] := (sym /. FormulaConvention);
7 ToFormula[expr_] :=
8     ToFormula[expr[[0]]] @@ (ToFormula /@ List @@ expr);
9
10 ToFormulaString[Null] := "";
11 ToFormulaString[str_String] := str;
12 ToFormulaString[expr_] :=
13     StringReplace[
14         ToString[ToFormula[expr],
15             FortranForm], {RegularExpression["([0-9\\.])e([0-9\\+\\-])" ->
16                 "$1E$2", "**" -> "^"}];
17 ToFormulaString[expr_, n_Integer] :=
18     If[NumberQ[expr], ToNumberString[expr, n], ToFormulaString[expr]];
19
20 ToNumberString[x_?NumberQ] :=
21     If[x == 0, "0", ToString[x, FortranForm]];
22 ToNumberString[x_?NumberQ, n_Integer] :=
23     ToNumberString[SetAccuracy[x, n]];
24
25 ToWaveString[] := Sequence[];
26 ToWaveString[frequency_, duration_?NumberQ, amplitude_, phase_,
27     gap_?NumberQ, formula_ : Null] := {ToFormulaString[frequency, 5],
28     ToNumberString[duration, 4], ToFormulaString[amplitude, 4],

```

```

29     ToFormulaString[phase, 4], ToNumberString[gap, 2],
30     ToFormulaString[formula]};
31 ToWaveString[waves_List] := Each[waves, ToWaveString];
32
33 ExportWaveString[] := "\n";
34 ExportWaveString[frequency_, duration_?NumberQ, amplitude_, phase_,
35     gap_?NumberQ, formula_ : Null] :=
36     StringJoin @@ (Riffle[
37         ToWaveString[frequency, duration, amplitude, phase, gap,
38         formula], ",") <> "\n";
39 ExportWaveString[waves_List] :=
40     WaveHead <> StringJoin @@ Each[waves, ExportWaveString];
41
42 ExportWaveFile[path_String, expr_] :=
43     If[StringQ[#], Export[DataPath[path], #]] &@ExportWaveString[expr];
44
45 FromFormula[str_String] :=
46     Module[{parens, funcs,
47         formula = StringReplace[str, "w" -> "2*Pi*f"]},
48     parens =
49         SortBy[Join#[[1]] & /@ StringPosition[formula, "("], -#[[1]] &
50         /@ StringPosition[formula, ")"], Abs];
51     parens =
52     NestWhile[
53         Replace[#, {a___, x_?Positive, y_?Negative, b___} :> {a, b,

```

```

54     x -> y}] &, parens, ! FreeQ[#, _?IntegerQ, 1] &];
55     funcs = #[[2]] & /@
56     StringPosition[formula, WordCharacter .. ~~ "(",
57     Overlaps -> False];
58     formula = StringReplacePart[formula, "[", {#, #} & /@ funcs];
59     formula =
60     StringReplacePart[formula, "]", -{#, #} & /@ (funcs /. parens)];
61     StringReplace[
62     formula, {d : {DigitCharacter, "."} .. ~~ "E" ~~
63     n : {DigitCharacter, "+", "-"} .. :> d <> "*10^" <> n}];
64 FromFormula[expr_] := (expr /. (Reverse /@ FormulaConvention));
65
66 FromFormulaString[str_String] :=
67     FromFormula@ToExpression@FromFormula[str];
68 FromFormulaString[x_?NumberQ] := x;
69
70 WaveVariable[wave_List] :=
71     Join @@ Table[
72     Each[Transpose@{Symbol[
73     "Global`" <> # <> ToString[i - 1]] & /@
74     {"f", "d", "a", "p", "g"},
75     List @@ (wave[[i]][[1 ;; 5]])}, Rule], {i,
76     Length[wave]}}];
77
78 FromWaveString[wavestr_?MatrixQ] := (# /. WaveVariable[#]) &[

```

```

79     FromWaveString /@ wavestr];
80 FromWaveString[
81     wavestr_List] := {FromFormulaString@#1, ToExpression@#2,
82     FromFormulaString@#3, FromFormulaString@#4, ToExpression@#5,
83     FromFormulaString@#6} & @@ wavestr;
84
85 ImportWaveString[str_String] :=
86     FromWaveString@ImportString[str, "CSV"][[2 ;; -1]];
87
88 ImportWaveFile[path_String] :=
89     FromWaveString@Import[DataPath[path], "CSV"][[2 ;; -1]];

```

A.2 Software screenshots

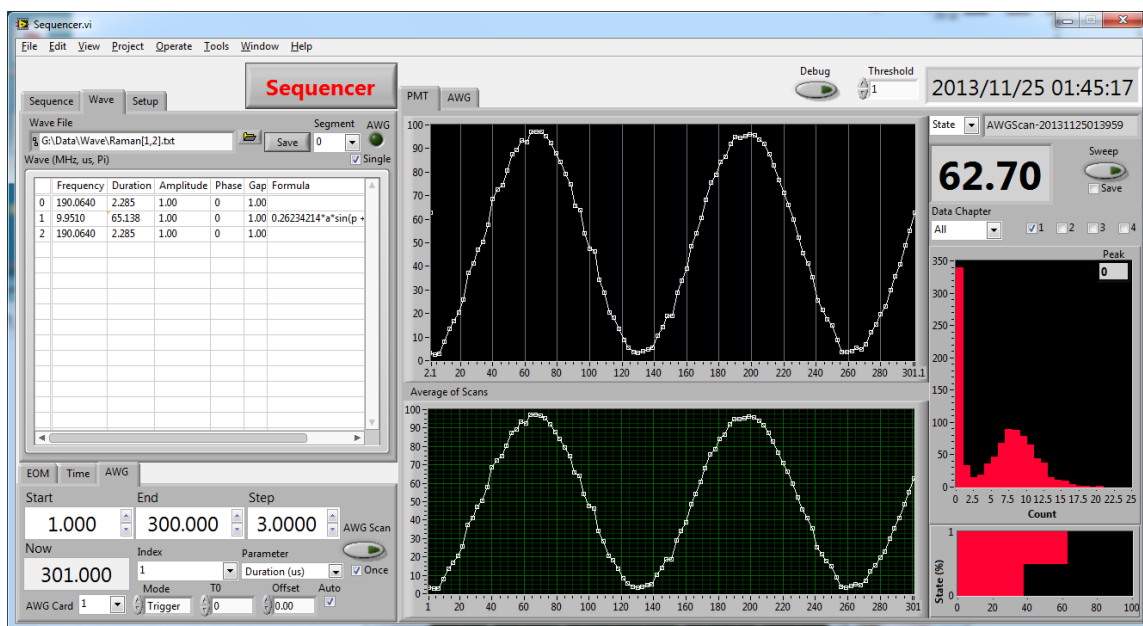


Figure A.2.1: Another picture of the main control program.

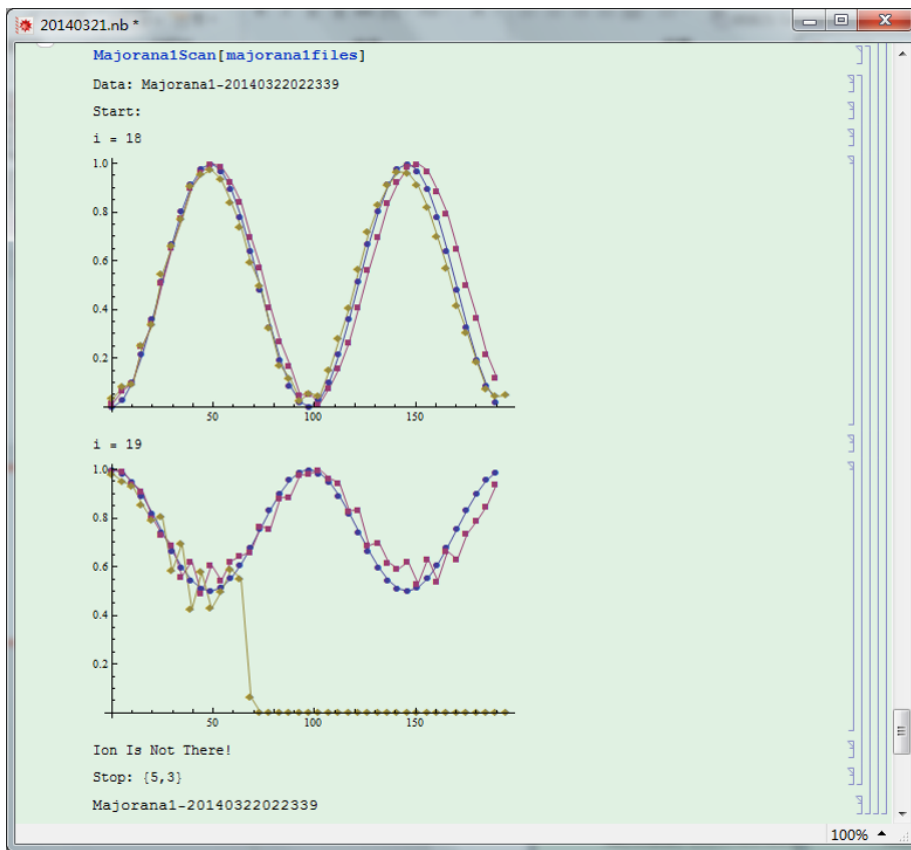


Figure A.2.2: Automated data taking with Mathematica.

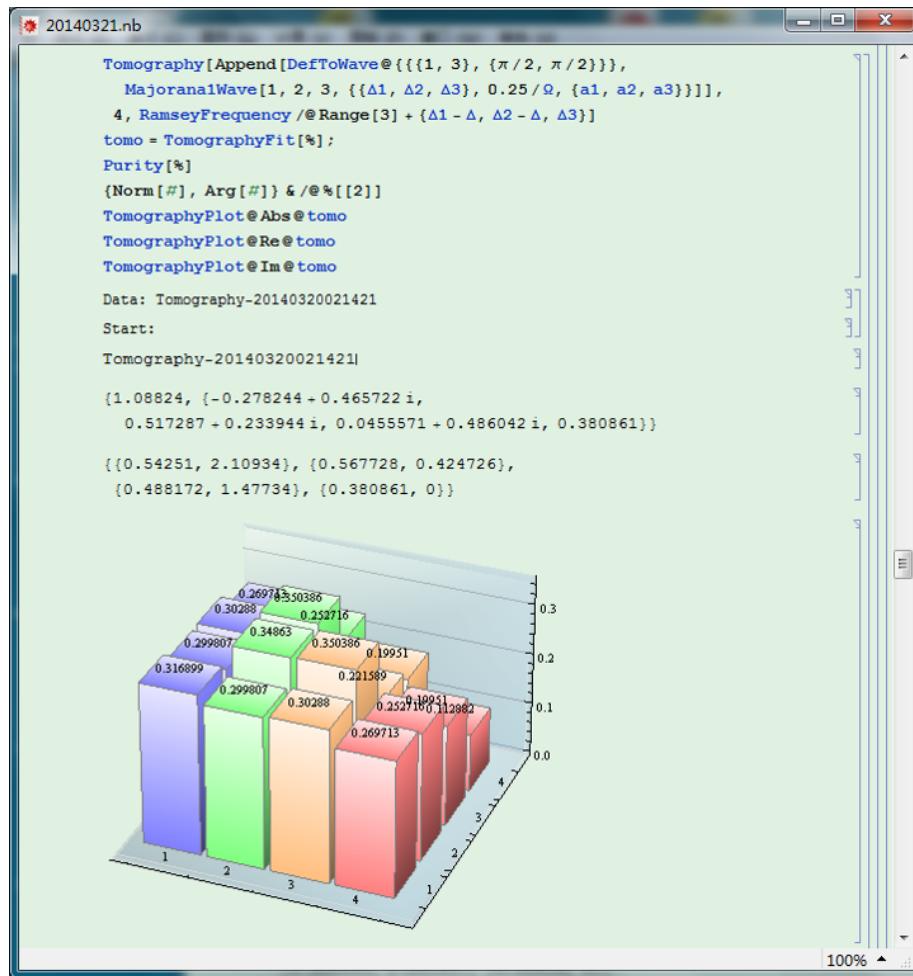


Figure A.2.3: Data analysis and plot with Mathematica.

Appendix B

Quantum contextuality experimental data

The first table shows the 12 different initial states' density matrices, including theoretical values and experimental results. After this are state-independent KS inequality measurement results for each initial state.

State	Theory	Raw	Correct	Fidelity
ψ_1	$\begin{pmatrix} 1.000 & 0.000 & 0.000 \\ 0.000 & 0.000 & 0.000 \\ 0.000 & 0.000 & 0.000 \end{pmatrix}$	$\begin{pmatrix} 0.957 & 0.027 & 0.010 \\ 0.027 & 0.024 & 0.003 \\ 0.010 & 0.003 & 0.019 \end{pmatrix}$	$\begin{pmatrix} 1.000 & 0.028 & 0.011 \\ 0.028 & 0.000 & 0.000 \\ 0.011 & 0.000 & 0.000 \end{pmatrix}$	100%
ψ_2	$\begin{pmatrix} 0.000 & 0.000 & 0.000 \\ 0.000 & 1.000 & 0.000 \\ 0.000 & 0.000 & 0.000 \end{pmatrix}$	$\begin{pmatrix} 0.028 & 0.006 & 0.002 \\ 0.006 & 0.950 & 0.020 \\ 0.002 & 0.020 & 0.021 \end{pmatrix}$	$\begin{pmatrix} 0.009 & 0.006 & 0.003 \\ 0.006 & 0.989 & 0.022 \\ 0.003 & 0.022 & 0.002 \end{pmatrix}$	98.9%
ψ_3	$\begin{pmatrix} 0.000 & 0.000 & 0.000 \\ 0.000 & 0.000 & 0.000 \\ 0.000 & 0.000 & 1.000 \end{pmatrix}$	$\begin{pmatrix} 0.016 & 0.006 & 0.005 \\ 0.006 & 0.028 & 0.009 \\ 0.005 & 0.009 & 0.956 \end{pmatrix}$	$\begin{pmatrix} 0.000 & 0.005 & 0.006 \\ 0.005 & 0.000 & 0.009 \\ 0.006 & 0.009 & 1.000 \end{pmatrix}$	100%
ψ_4	$\begin{pmatrix} 0.500 & 0.000 & 0.500 \\ 0.000 & 0.000 & 0.000 \\ 0.500 & 0.000 & 0.500 \end{pmatrix}$	$\begin{pmatrix} 0.492 & 0.016 & 0.465 \\ 0.016 & 0.027 & 0.012 \\ 0.465 & 0.012 & 0.481 \end{pmatrix}$	$\begin{pmatrix} 0.496 & 0.019 & 0.496 \\ 0.019 & 0.019 & 0.013 \\ 0.496 & 0.013 & 0.485 \end{pmatrix}$	98.7%
ψ_5	$\begin{pmatrix} 0.000 & 0.000 & 0.000 \\ 0.000 & 0.500 & 0.500 \\ 0.000 & 0.500 & 0.500 \end{pmatrix}$	$\begin{pmatrix} 0.032 & 0.013 & 0.002 \\ 0.013 & 0.489 & 0.451 \\ 0.002 & 0.451 & 0.479 \end{pmatrix}$	$\begin{pmatrix} 0.016 & 0.015 & 0.002 \\ 0.015 & 0.497 & 0.491 \\ 0.002 & 0.491 & 0.487 \end{pmatrix}$	98.4%
ψ_6	$\begin{pmatrix} 0.333 & 0.333 & 0.333 \\ 0.333 & 0.333 & 0.333 \\ 0.333 & 0.333 & 0.333 \end{pmatrix}$	$\begin{pmatrix} 0.325 & 0.302 & 0.299 \\ 0.302 & 0.342 & 0.269 \\ 0.299 & 0.269 & 0.333 \end{pmatrix}$	$\begin{pmatrix} 0.324 & 0.333 & 0.324 \\ 0.333 & 0.343 & 0.314 \\ 0.324 & 0.314 & 0.333 \end{pmatrix}$	98.1%
ψ_7	$\begin{pmatrix} 0.333 & 0.000 & 0.471 \\ 0.000 & 0.000 & 0.000 \\ 0.471 & 0.000 & 0.667 \end{pmatrix}$	$\begin{pmatrix} 0.352 & 0.015 & 0.446 \\ 0.015 & 0.024 & 0.024 \\ 0.446 & 0.024 & 0.624 \end{pmatrix}$	$\begin{pmatrix} 0.346 & 0.017 & 0.473 \\ 0.017 & 0.000 & 0.027 \\ 0.473 & 0.027 & 0.654 \end{pmatrix}$	99.8%
ψ_8	$\begin{pmatrix} 0.553 & 0.217 & 0.447 \\ 0.217 & 0.085 & 0.176 \\ 0.447 & 0.176 & 0.362 \end{pmatrix}$	$\begin{pmatrix} 0.545 & 0.167 & 0.426 \\ 0.167 & 0.092 & 0.135 \\ 0.426 & 0.135 & 0.363 \end{pmatrix}$	$\begin{pmatrix} 0.576 & 0.197 & 0.461 \\ 0.197 & 0.051 & 0.154 \\ 0.461 & 0.154 & 0.373 \end{pmatrix}$	100.9%
ψ_9	$\begin{pmatrix} 0.500 & 0.500 & 0.000 \\ 0.500 & 0.500 & 0.000 \\ 0.000 & 0.000 & 0.000 \end{pmatrix}$	$\begin{pmatrix} 0.494 & 0.457 & 0.006 \\ 0.457 & 0.483 & 0.001 \\ 0.006 & 0.001 & 0.023 \end{pmatrix}$	$\begin{pmatrix} 0.506 & 0.494 & 0.006 \\ 0.494 & 0.494 & 0.001 \\ 0.006 & 0.001 & 0.000 \end{pmatrix}$	99.4%
ρ_{10}	$\begin{pmatrix} 0.500 & 0.000 & 0.000 \\ 0.000 & 0.500 & 0.000 \\ 0.000 & 0.000 & 0.000 \end{pmatrix}$	$\begin{pmatrix} 0.495 & 0.007 & 0.020 \\ 0.007 & 0.451 & 0.022 \\ 0.020 & 0.022 & 0.054 \end{pmatrix}$	$\begin{pmatrix} 0.509 & 0.007 & 0.023 \\ 0.007 & 0.462 & 0.023 \\ 0.023 & 0.023 & 0.030 \end{pmatrix}$	97.0%
ρ_{11}	$\begin{pmatrix} 0.333 & 0.000 & 0.333 \\ 0.000 & 0.333 & 0.000 \\ 0.333 & 0.000 & 0.333 \end{pmatrix}$	$\begin{pmatrix} 0.334 & 0.006 & 0.272 \\ 0.006 & 0.286 & 0.021 \\ 0.272 & 0.021 & 0.381 \end{pmatrix}$	$\begin{pmatrix} 0.334 & 0.007 & 0.303 \\ 0.007 & 0.283 & 0.022 \\ 0.303 & 0.022 & 0.383 \end{pmatrix}$	94.3%
ρ_{12}	$\begin{pmatrix} 0.333 & 0.000 & 0.000 \\ 0.000 & 0.333 & 0.000 \\ 0.000 & 0.000 & 0.333 \end{pmatrix}$	$\begin{pmatrix} 0.331 & 0.013 & 0.014 \\ 0.013 & 0.326 & 0.002 \\ 0.014 & 0.002 & 0.343 \end{pmatrix}$	$\begin{pmatrix} 0.331 & 0.014 & 0.014 \\ 0.014 & 0.326 & 0.002 \\ 0.014 & 0.002 & 0.343 \end{pmatrix}$	99.9%

Table B.1: Density matrices of the 12 initial states.

	$P_{ 1\rangle}$				$P_{ 2\rangle}$				$P_{ 3\rangle}$			
	Basis	Theory	Raw	Correct	Basis	Theory	Raw	Correct	Basis	Theory	Raw	Correct
M_1	V_1	1.000	0.989	0.999	V_2	0.000	0.025	0.001	V_3	0.000	0.025	0.000
M_2	V_8	0.500	0.528	0.509	V_2	0.000	0.026	0.000	V_5	0.500	0.511	0.491
M_3	V_1	1.000	0.989	0.998	V_7	0.000	0.025	0.000	V_4	0.000	0.027	0.002
M_4	V_6	0.500	0.512	0.504	V_3	0.000	0.024	0.000	V_9	0.500	0.504	0.496
M_5		0.667	0.656	0.655	V_4	0.000	0.024	0.000	V_{10}	0.333	0.356	0.345
M_6		0.667	0.675	0.672	V_4	0.000	0.026	0.000	V_{13}	0.333	0.342	0.328
M_7	V_5	0.500	0.506	0.504		0.167	0.179	0.160	V_{11}	0.333	0.345	0.336
M_8	V_5	0.500	0.503	0.499		0.167	0.188	0.167	V_{13}	0.333	0.346	0.334
M_9	V_6	0.500	0.507	0.500		0.167	0.183	0.157	V_{12}	0.333	0.357	0.343
M_{10}	V_6	0.500	0.505	0.499	V_{13}	0.333	0.351	0.339		0.167	0.186	0.162
M_{11}		0.667	0.663	0.659	V_7	0.000	0.024	0.000	V_{11}	0.333	0.356	0.341
M_{12}	V_{12}	0.333	0.347	0.332	V_7	0.000	0.025	0.000		0.667	0.671	0.668
M_{13}	V_8	0.500	0.499	0.496		0.167	0.190	0.171	V_{10}	0.333	0.342	0.333
M_{14}	V_8	0.500	0.508	0.501	V_{12}	0.333	0.358	0.344		0.167	0.181	0.155
M_{15}	V_9	0.333	0.352	0.342	V_{10}	0.500	0.509	0.506		0.167	0.173	0.153
M_{16}		0.167	0.178	0.163	V_9	0.500	0.503	0.504	V_{11}	0.333	0.340	0.334
M_1	$V_1 V_2$	0.000	0.023	0.000	$V_2 V_3$	0.000	0.001	0.000	$V_3 V_1$	0.000	0.001	0.000
M_2	$V_8 V_2$		0.011	0.000	$V_2 V_5$		0.001	0.000	$V_5 V_8$		0.012	0.000
M_3	$V_1 V_7$		0.020	0.000	$V_7 V_4$		0.001	0.000	$V_4 V_1$		0.001	0.000
M_4	$V_6 V_3$		0.013	0.000	$V_3 V_9$		0.001	0.000	$V_9 V_6$		0.011	0.000
M_5			0.015	0.000	$V_4 V_{10}$		0.001	0.000	$V_{10} V_4$		0.010	0.001
M_6			0.017	0.000	$V_4 V_{13}$		0.001	0.000	$V_{13} V_4$		0.008	0.000
M_7	$V_5 V_{11}$		0.011	0.000			0.004	0.000	$V_{11} V_5$		0.006	0.000
M_8	$V_5 V_{13}$		0.011	0.000			0.005	0.000	$V_{13} V_5$		0.007	0.000
M_9	$V_6 V_{12}$		0.011	0.000			0.005	0.000	$V_{12} V_6$		0.008	0.000
M_{10}	$V_6 V_{13}$		0.012	0.000	$V_{13} V_6$		0.008	0.000			0.005	0.000
M_{11}			0.016	0.000	$V_7 V_{11}$		0.001	0.000	$V_{11} V_7$		0.007	0.000
M_{12}	$V_{12} V_7$		0.010	0.001	$V_7 V_{12}$		0.001	0.000			0.016	0.000
M_{13}	$V_8 V_{10}$		0.012	0.000			0.004	0.000	$V_{10} V_8$		0.008	0.000
M_{14}	$V_8 V_{12}$		0.014	0.001	$V_{12} V_8$		0.009	0.000			0.004	0.000
M_{15}	$V_9 V_{10}$		0.007	0.000	$V_{10} V_9$		0.010	0.000			0.004	0.000
M_{16}			0.004	0.000	$V_9 V_{11}$		0.011	0.000	$V_{11} V_9$		0.008	0.000
		Theory			Raw			Correct				
$\langle\chi_4\rangle$		1.333			1.207 ± 0.011			1.301 ± 0.011				
$\langle\chi_{13}\rangle$		27.667			28.137 ± 0.181			27.814 ± 0.172				

Table B.2: ψ_1

	$P_{ 1\rangle}$				$P_{ 2\rangle}$				$P_{ 3\rangle}$			
	Basis	Theory	Raw	Correct	Basis	Theory	Raw	Correct	Basis	Theory	Raw	Correct
M_1	V_1	0.000	0.029	0.003	V_2	1.000	0.989	0.997	V_3	0.000	0.027	0.000
M_2	V_8	0.000	0.029	0.005	V_2	1.000	0.985	0.995	V_5	0.000	0.025	0.001
M_3	V_1	0.000	0.025	0.000	V_7	0.500	0.520	0.509	V_4	0.500	0.502	0.491
M_4	V_6	0.500	0.494	0.485	V_3	0.000	0.033	0.000	V_9	0.500	0.523	0.515
M_5		0.167	0.190	0.164	V_4	0.500	0.508	0.501	V_{10}	0.333	0.350	0.335
M_6		0.167	0.181	0.163	V_4	0.500	0.499	0.497	V_{13}	0.333	0.349	0.340
M_7	V_5	0.000	0.027	0.003		0.667	0.659	0.664	V_{11}	0.333	0.339	0.333
M_8	V_5	0.000	0.024	0.000		0.667	0.672	0.669	V_{13}	0.333	0.347	0.331
M_9	V_6	0.500	0.504	0.501		0.167	0.172	0.153	V_{12}	0.333	0.354	0.346
M_{10}	V_6	0.500	0.504	0.501	V_{13}	0.333	0.346	0.336		0.167	0.183	0.163
M_{11}		0.167	0.190	0.164	V_7	0.500	0.504	0.497	V_{11}	0.333	0.352	0.338
M_{12}	V_{12}	0.333	0.342	0.332	V_7	0.500	0.504	0.501		0.167	0.187	0.168
M_{13}	V_8	0.000	0.028	0.000		0.667	0.682	0.677	V_{10}	0.333	0.340	0.323
M_{14}	V_8	0.000	0.026	0.000	V_{12}	0.333	0.352	0.335		0.667	0.670	0.665
M_{15}	V_9	0.333	0.346	0.331	V_{10}	0.500	0.509	0.502		0.167	0.191	0.166
M_{16}		0.167	0.183	0.159	V_9	0.500	0.507	0.501	V_{11}	0.333	0.353	0.340
M_1	$V_1 V_2$	0.000	0.002	0.000	$V_2 V_3$	0.000	0.024	0.000	$V_3 V_1$	0.000	0.001	0.000
M_2	$V_8 V_2$		0.001	0.000	$V_2 V_5$		0.022	0.000	$V_5 V_8$		0.001	0.000
M_3	$V_1 V_7$		0.001	0.000	$V_7 V_4$		0.012	0.000	$V_4 V_1$		0.010	0.000
M_4	$V_6 V_3$		0.014	0.001	$V_3 V_9$		0.001	0.000	$V_9 V_6$		0.012	0.000
M_5			0.003	0.000	$V_4 V_{10}$		0.013	0.001	$V_{10} V_4$		0.009	0.000
M_6			0.004	0.000	$V_4 V_{13}$		0.013	0.001	$V_{13} V_4$		0.008	0.000
M_7	$V_5 V_{11}$		0.001	0.000			0.014	0.000	$V_{11} V_5$		0.008	0.000
M_8	$V_5 V_{13}$		0.001	0.000			0.016	0.000	$V_{13} V_5$		0.008	0.000
M_9	$V_6 V_{12}$		0.011	0.000			0.005	0.001	$V_{12} V_6$		0.009	0.000
M_{10}	$V_6 V_{13}$		0.014	0.001	$V_{13} V_6$		0.008	0.000			0.005	0.001
M_{11}			0.003	0.000	$V_7 V_{11}$		0.012	0.000	$V_{11} V_7$		0.009	0.000
M_{12}	$V_{12} V_7$		0.009	0.000	$V_7 V_{12}$		0.012	0.000			0.006	0.001
M_{13}	$V_8 V_{10}$		0.001	0.000			0.017	0.000	$V_{10} V_8$		0.008	0.000
M_{14}	$V_8 V_{12}$		0.001	0.000	$V_{12} V_8$		0.009	0.000			0.013	0.000
M_{15}	$V_9 V_{10}$		0.009	0.000	$V_{10} V_9$		0.012	0.000			0.005	0.000
M_{16}			0.006	0.001	$V_9 V_{11}$		0.012	0.000	$V_{11} V_9$		0.008	0.000
		Theory	Raw				Correct					
$\langle\chi_4\rangle$		1.333	1.221 ± 0.011				1.320 ± 0.011					
$\langle\chi_{13}\rangle$		27.667	27.932 ± 0.182				27.695 ± 0.172					

Table B.3: ψ_2

	$P_{ 1\rangle}$				$P_{ 2\rangle}$				$P_{ 3\rangle}$			
	Basis	Theory	Raw	Correct	Basis	Theory	Raw	Correct	Basis	Theory	Raw	Correct
M_1	V_1	0.000	0.025	0.000	V_2	0.000	0.025	0.000	V_3	1.000	0.992	1.000
M_2	V_8	0.500	0.519	0.503	V_2	0.000	0.025	0.000	V_5	0.500	0.513	0.497
M_3	V_1	0.000	0.028	0.000	V_7	0.500	0.515	0.508	V_4	0.500	0.499	0.492
M_4	V_6	0.000	0.029	0.005	V_3	1.000	0.984	0.994	V_9	0.000	0.025	0.001
M_5		0.167	0.190	0.168	V_4	0.500	0.504	0.500	V_{10}	0.333	0.343	0.331
M_6		0.167	0.184	0.165	V_4	0.500	0.501	0.499	V_{13}	0.333	0.345	0.336
M_7	V_5	0.500	0.506	0.502		0.167	0.182	0.161	V_{11}	0.333	0.348	0.337
M_8	V_5	0.500	0.515	0.507		0.167	0.184	0.156	V_{13}	0.333	0.353	0.338
M_9	V_6	0.000	0.029	0.000		0.667	0.673	0.667	V_{12}	0.333	0.350	0.333
M_{10}	V_6	0.000	0.026	0.000	V_{13}	0.333	0.366	0.343		0.667	0.665	0.657
M_{11}		0.167	0.191	0.172	V_7	0.500	0.497	0.494	V_{11}	0.333	0.344	0.334
M_{12}	V_{12}	0.333	0.356	0.341	V_7	0.500	0.513	0.505		0.167	0.182	0.154
M_{13}	V_8	0.500	0.507	0.498		0.167	0.194	0.166	V_{10}	0.333	0.352	0.336
M_{14}	V_8	0.500	0.506	0.500	V_{12}	0.333	0.350	0.337		0.167	0.188	0.163
M_{15}	V_9	0.333	0.339	0.326	V_{10}	0.000	0.025	0.000		0.667	0.675	0.674
M_{16}		0.667	0.679	0.677	V_9	0.000	0.025	0.000	V_{11}	0.333	0.337	0.323
M_1	$V_1 V_2$	0.000	0.001	0.000	$V_2 V_3$	0.000	0.001	0.000	$V_3 V_1$	0.000	0.023	0.000
M_2	$V_8 V_2$		0.014	0.001	$V_2 V_5$		0.001	0.000	$V_5 V_8$		0.012	0.000
M_3	$V_1 V_7$		0.001	0.000	$V_7 V_4$		0.013	0.000	$V_4 V_1$		0.012	0.000
M_4	$V_6 V_3$		0.001	0.000	$V_3 V_9$		0.024	0.000	$V_9 V_6$		0.000	0.000
M_5			0.004	0.000	$V_4 V_{10}$		0.013	0.000	$V_{10} V_4$		0.008	0.000
M_6			0.006	0.001	$V_4 V_{13}$		0.011	0.000	$V_{13} V_4$		0.009	0.000
M_7	$V_5 V_{11}$		0.012	0.000			0.003	0.000	$V_{11} V_5$		0.007	0.000
M_8	$V_5 V_{13}$		0.012	0.000			0.004	0.000	$V_{13} V_5$		0.009	0.000
M_9	$V_6 V_{12}$		0.001	0.000			0.015	0.000	$V_{12} V_6$		0.008	0.000
M_{10}	$V_6 V_{13}$		0.001	0.000	$V_{13} V_6$		0.008	0.000			0.015	0.000
M_{11}			0.005	0.000	$V_7 V_{11}$		0.012	0.000	$V_{11} V_7$		0.008	0.000
M_{12}	$V_{12} V_7$		0.007	0.000	$V_7 V_{12}$		0.012	0.000			0.004	0.000
M_{13}	$V_8 V_{10}$		0.012	0.000			0.004	0.000	$V_{10} V_8$		0.007	0.000
M_{14}	$V_8 V_{12}$		0.011	0.000	$V_{12} V_8$		0.006	0.000			0.004	0.000
M_{15}	$V_9 V_{10}$		0.011	0.002	$V_{10} V_9$		0.001	0.000			0.016	0.000
M_{16}			0.015	0.000	$V_9 V_{11}$		0.000	0.000	$V_{11} V_9$		0.010	0.001
		Theory			Raw			Correct				
$\langle\chi_4\rangle$		1.333			1.211 ± 0.011			1.323 ± 0.011				
$\langle\chi_{13}\rangle$		27.667			27.990 ± 0.182			27.708 ± 0.172				

Table B.4: ψ_3

	$P_{ 1\rangle}$				$P_{ 2\rangle}$				$P_{ 3\rangle}$			
	Basis	Theory	Raw	Correct	Basis	Theory	Raw	Correct	Basis	Theory	Raw	Correct
M_1	V_1	0.500	0.499	0.489	V_2	0.000	0.024	0.000	V_3	0.500	0.520	0.511
M_2	V_8	1.000	0.991	1.000	V_2	0.000	0.025	0.000	V_5	0.000	0.024	0.000
M_3	V_1	0.500	0.511	0.506	V_7	0.250	0.259	0.241	V_4	0.250	0.270	0.253
M_4	V_6	0.250	0.263	0.246	V_3	0.500	0.504	0.500	V_9	0.250	0.270	0.254
M_5		0.083	0.106	0.084	V_4	0.250	0.260	0.248	V_{10}	0.667	0.665	0.668
M_6		0.750	0.745	0.746	V_4	0.250	0.270	0.254	V_{13}	0.000	0.027	0.000
M_7	V_5	1.000	0.989	0.999		0.000	0.023	0.000	V_{11}	0.000	0.025	0.001
M_8	V_5	1.000	0.991	1.000		0.000	0.026	0.000	V_{13}	0.000	0.025	0.000
M_9	V_6	0.250	0.256	0.245		0.083	0.110	0.090	V_{12}	0.667	0.660	0.665
M_{10}	V_6	0.250	0.280	0.261	V_{13}	0.000	0.029	0.000		0.750	0.741	0.739
M_{11}		0.750	0.752	0.750	V_7	0.250	0.269	0.250	V_{11}	0.000	0.025	0.000
M_{12}	V_{12}	0.667	0.659	0.661	V_7	0.250	0.270	0.256		0.083	0.108	0.083
M_{13}	V_8	0.000	0.027	0.007		0.333	0.332	0.327	V_{10}	0.667	0.659	0.666
M_{14}	V_8	0.000	0.029	0.004	V_{12}	0.667	0.657	0.662		0.333	0.340	0.334
M_{15}	V_9	0.667	0.671	0.671	V_{10}	0.250	0.274	0.258		0.083	0.101	0.072
M_{16}		0.750	0.751	0.752	V_9	0.250	0.264	0.248	V_{11}	0.000	0.024	0.000
M_1	$V_1 V_2$	0.000	0.012	0.000	$V_2 V_3$	0.000	0.001	0.000	$V_3 V_1$	0.000	0.012	0.000
M_2	$V_8 V_2$		0.022	0.000	$V_2 V_5$		0.001	0.000	$V_5 V_8$		0.001	0.000
M_3	$V_1 V_7$		0.013	0.000	$V_7 V_4$		0.007	0.001	$V_4 V_1$		0.006	0.000
M_4	$V_6 V_3$		0.006	0.000	$V_3 V_9$		0.011	0.000	$V_9 V_6$		0.006	0.000
M_5			0.003	0.000	$V_4 V_{10}$		0.005	0.000	$V_{10} V_4$		0.016	0.000
M_6			0.016	0.000	$V_4 V_{13}$		0.006	0.000	$V_{13} V_4$		0.001	0.000
M_7	$V_5 V_{11}$		0.024	0.000			0.001	0.000	$V_{11} V_5$		0.001	0.000
M_8	$V_5 V_{13}$		0.024	0.000			0.001	0.000	$V_{13} V_5$		0.000	0.000
M_9	$V_6 V_{12}$		0.006	0.000			0.003	0.000	$V_{12} V_6$		0.017	0.001
M_{10}	$V_6 V_{13}$		0.006	0.000	$V_{13} V_6$		0.001	0.000			0.015	0.000
M_{11}			0.017	0.000	$V_7 V_{11}$		0.007	0.000	$V_{11} V_7$		0.001	0.000
M_{12}	$V_{12} V_7$		0.017	0.000	$V_7 V_{12}$		0.006	0.000			0.003	0.000
M_{13}	$V_8 V_{10}$		0.001	0.000			0.008	0.000	$V_{10} V_8$		0.015	0.000
M_{14}	$V_8 V_{12}$		0.001	0.000	$V_{12} V_8$		0.014	0.000			0.007	0.000
M_{15}	$V_9 V_{10}$		0.015	0.000	$V_{10} V_9$		0.006	0.000			0.003	0.000
M_{16}			0.016	0.000	$V_9 V_{11}$		0.008	0.001	$V_{11} V_9$		0.001	0.000
		Theory	Raw				Correct					
$\langle\chi_4\rangle$		1.333	1.249 ± 0.008				1.338 ± 0.008					
$\langle\chi_{13}\rangle$		27.667	27.811 ± 0.178				27.722 ± 0.168					

Table B.5: ψ_4

	$P_{ 1\rangle}$				$P_{ 2\rangle}$				$P_{ 3\rangle}$			
	Basis	Theory	Raw	Correct	Basis	Theory	Raw	Correct	Basis	Theory	Raw	Correct
M_1	V_1	0.000	0.024	0.000	V_2	0.500	0.502	0.499	V_3	0.500	0.503	0.501
M_2	V_8	0.250	0.272	0.255	V_2	0.500	0.503	0.498	V_5	0.250	0.265	0.247
M_3	V_1	0.000	0.024	0.000	V_7	0.000	0.026	0.000	V_4	1.000	0.991	1.000
M_4	V_6	0.250	0.274	0.253	V_3	0.500	0.508	0.500	V_9	0.250	0.268	0.247
M_5		0.333	0.325	0.319	V_4	0.000	0.025	0.001	V_{10}	0.667	0.674	0.680
M_6		0.333	0.349	0.339	V_4	0.000	0.025	0.000	V_{13}	0.667	0.660	0.661
M_7	V_5	0.250	0.261	0.249		0.750	0.746	0.750	V_{11}	0.000	0.030	0.001
M_8	V_5	0.250	0.280	0.261		0.083	0.110	0.076	V_{13}	0.667	0.666	0.663
M_9	V_6	0.250	0.264	0.252		0.750	0.744	0.748	V_{12}	0.000	0.026	0.000
M_{10}	V_6	0.250	0.269	0.253	V_{13}	0.667	0.672	0.672		0.083	0.104	0.075
M_{11}		0.000	0.028	0.004	V_7	1.000	0.984	0.993	V_{11}	0.000	0.027	0.002
M_{12}	V_{12}	0.000	0.031	0.005	V_7	1.000	0.984	0.992		0.000	0.029	0.003
M_{13}	V_8	0.250	0.254	0.240		0.083	0.105	0.081	V_{10}	0.667	0.675	0.678
M_{14}	V_8	0.250	0.258	0.248	V_{12}	0.000	0.025	0.000		0.750	0.746	0.752
M_{15}	V_9	0.667	0.671	0.675	V_{10}	0.250	0.257	0.246		0.083	0.101	0.080
M_{16}		0.750	0.740	0.745	V_9	0.250	0.264	0.252	V_{11}	0.000	0.031	0.003
M_1	$V_1 V_2$	0.000	0.001	0.000	$V_2 V_3$	0.000	0.012	0.000	$V_3 V_1$	0.000	0.011	0.000
M_2	$V_8 V_2$		0.007	0.000	$V_2 V_5$		0.012	0.000	$V_5 V_8$		0.007	0.000
M_3	$V_1 V_7$		0.001	0.000	$V_7 V_4$		0.002	0.000	$V_4 V_1$		0.020	0.000
M_4	$V_6 V_3$		0.007	0.000	$V_3 V_9$		0.014	0.001	$V_9 V_6$		0.007	0.001
M_5			0.007	0.000	$V_4 V_{10}$		0.001	0.000	$V_{10} V_4$		0.016	0.000
M_6			0.008	0.000	$V_4 V_{13}$		0.001	0.000	$V_{13} V_4$		0.016	0.000
M_7	$V_5 V_{11}$		0.007	0.000			0.016	0.000	$V_{11} V_5$		0.001	0.000
M_8	$V_5 V_{13}$		0.007	0.000			0.003	0.000	$V_{13} V_5$		0.016	0.000
M_9	$V_6 V_{12}$		0.005	0.000			0.015	0.000	$V_{12} V_6$		0.001	0.000
M_{10}	$V_6 V_{13}$		0.006	0.000	$V_{13} V_6$		0.015	0.000			0.002	0.000
M_{11}			0.001	0.000	$V_7 V_{11}$		0.022	0.000	$V_{11} V_7$		0.000	0.000
M_{12}	$V_{12} V_7$		0.001	0.000	$V_7 V_{12}$		0.024	0.000			0.001	0.000
M_{13}	$V_8 V_{10}$		0.005	0.000			0.002	0.000	$V_{10} V_8$		0.015	0.000
M_{14}	$V_8 V_{12}$		0.007	0.000	$V_{12} V_8$		0.001	0.000			0.019	0.000
M_{15}	$V_9 V_{10}$		0.015	0.000	$V_{10} V_9$		0.008	0.001			0.002	0.000
M_{16}			0.017	0.000	$V_9 V_{11}$		0.006	0.000	$V_{11} V_9$		0.001	0.000
		Theory			Raw			Correct				
$\langle\chi_4\rangle$		1.333			1.209 ± 0.008			1.307 ± 0.008				
$\langle\chi_{13}\rangle$		27.667			27.768 ± 0.179			27.680 ± 0.168				

Table B.6: ψ_5

	$P_{ 1\rangle}$				$P_{ 2\rangle}$				$P_{ 3\rangle}$			
	Basis	Theory	Raw	Correct	Basis	Theory	Raw	Correct	Basis	Theory	Raw	Correct
M_1	V_1	0.333	0.344	0.330	V_2	0.333	0.344	0.330	V_3	0.333	0.352	0.339
M_2	V_8	0.000	0.024	0.000	V_2	0.333	0.344	0.330	V_5	0.667	0.673	0.670
M_3	V_1	0.333	0.344	0.327	V_7	0.000	0.028	0.000	V_4	0.667	0.678	0.673
M_4	V_6	0.667	0.673	0.666	V_3	0.333	0.354	0.334	V_9	0.000	0.026	0.000
M_5		0.889	0.873	0.881	V_4	0.000	0.024	0.000	V_{10}	0.111	0.136	0.119
M_6		0.000	0.026	0.000	V_4	0.000	0.027	0.002	V_{13}	1.000	0.990	0.998
M_7	V_5	0.000	0.025	0.000		0.889	0.887	0.888	V_{11}	0.111	0.138	0.112
M_8	V_5	0.000	0.025	0.000		0.000	0.026	0.001	V_{13}	1.000	0.990	0.999
M_9	V_6	0.000	0.029	0.004		0.889	0.880	0.888	V_{12}	0.111	0.127	0.108
M_{10}	V_6	0.000	0.027	0.003	V_{13}	1.000	0.984	0.994		0.000	0.026	0.003
M_{11}		0.222	0.247	0.230	V_7	0.667	0.669	0.669	V_{11}	0.111	0.127	0.101
M_{12}	V_{12}	0.111	0.131	0.110	V_7	0.667	0.660	0.663		0.222	0.241	0.227
M_{13}	V_8	0.667	0.670	0.669		0.222	0.241	0.222	V_{10}	0.111	0.137	0.110
M_{14}	V_8	0.667	0.661	0.660	V_{12}	0.111	0.135	0.109		0.222	0.249	0.231
M_{15}	V_9	0.111	0.138	0.110	V_{10}	0.667	0.678	0.676		0.222	0.234	0.213
M_{16}		0.222	0.242	0.231	V_9	0.667	0.648	0.653	V_{11}	0.111	0.133	0.116
M_1	$V_1 V_2$	0.000	0.009	0.000	$V_2 V_3$	0.000	0.009	0.000	$V_3 V_1$	0.000	0.009	0.000
M_2	$V_8 V_2$		0.001	0.000	$V_2 V_5$		0.010	0.001	$V_5 V_8$		0.016	0.000
M_3	$V_1 V_7$		0.009	0.000	$V_7 V_4$		0.002	0.000	$V_4 V_1$		0.016	0.000
M_4	$V_6 V_3$		0.017	0.000	$V_3 V_9$		0.008	0.000	$V_9 V_6$		0.001	0.000
M_5			0.021	0.000	$V_4 V_{10}$		0.001	0.000	$V_{10} V_4$		0.004	0.000
M_6			0.001	0.000	$V_4 V_{13}$		0.001	0.000	$V_{13} V_4$		0.025	0.000
M_7	$V_5 V_{11}$		0.001	0.000			0.018	0.000	$V_{11} V_5$		0.003	0.000
M_8	$V_5 V_{13}$		0.001	0.000			0.001	0.000	$V_{13} V_5$		0.022	0.000
M_9	$V_6 V_{12}$		0.001	0.000			0.023	0.001	$V_{12} V_6$		0.003	0.000
M_{10}	$V_6 V_{13}$		0.001	0.000	$V_{13} V_6$		0.022	0.000			0.001	0.000
M_{11}			0.006	0.000	$V_7 V_{11}$		0.016	0.000	$V_{11} V_7$		0.003	0.000
M_{12}	$V_{12} V_7$		0.004	0.000	$V_7 V_{12}$		0.014	0.000			0.006	0.000
M_{13}	$V_8 V_{10}$		0.017	0.000			0.005	0.000	$V_{10} V_8$		0.004	0.000
M_{14}	$V_8 V_{12}$		0.018	0.001	$V_{12} V_8$		0.003	0.000			0.006	0.000
M_{15}	$V_9 V_{10}$		0.004	0.001	$V_{10} V_9$		0.016	0.000			0.005	0.000
M_{16}			0.005	0.000	$V_9 V_{11}$		0.016	0.000	$V_{11} V_9$		0.004	0.000
		Theory	Raw				Correct					
$\langle\chi_4\rangle$		1.333	1.223 ± 0.007				1.344 ± 0.006					
$\langle\chi_{13}\rangle$		27.667	27.883 ± 0.177				27.587 ± 0.165					

Table B.7: ψ_6

	$P_{ 1\rangle}$				$P_{ 2\rangle}$				$P_{ 3\rangle}$			
	Basis	Theory	Raw	Correct	Basis	Theory	Raw	Correct	Basis	Theory	Raw	Correct
M_1	V_1	0.333	0.345	0.334	V_2	0.000	0.027	0.000	V_3	0.667	0.665	0.666
M_2	V_8	0.029	0.057	0.029	V_2	0.000	0.026	0.000	V_5	0.971	0.965	0.971
M_3	V_1	0.333	0.356	0.339	V_7	0.333	0.350	0.333	V_4	0.333	0.346	0.328
M_4	V_6	0.167	0.189	0.167	V_3	0.667	0.675	0.674	V_9	0.167	0.182	0.159
M_5		0.648	0.648	0.648	V_4	0.333	0.355	0.344	V_{10}	0.019	0.042	0.008
M_6		0.019	0.043	0.012	V_4	0.333	0.349	0.339	V_{13}	0.648	0.649	0.649
M_7	V_5	0.029	0.053	0.022		0.324	0.340	0.329	V_{11}	0.648	0.647	0.648
M_8	V_5	0.029	0.051	0.019		0.324	0.340	0.329	V_{13}	0.648	0.651	0.652
M_9	V_6	0.167	0.197	0.176		0.814	0.812	0.812	V_{12}	0.019	0.047	0.012
M_{10}	V_6	0.167	0.177	0.157	V_{13}	0.648	0.650	0.651		0.186	0.209	0.192
M_{11}		0.019	0.040	0.011	V_7	0.333	0.352	0.343	V_{11}	0.648	0.644	0.646
M_{12}	V_{12}	0.019	0.047	0.011	V_7	0.333	0.361	0.350		0.648	0.641	0.639
M_{13}	V_8	0.971	0.963	0.972		0.010	0.035	0.011	V_{10}	0.019	0.041	0.017
M_{14}	V_8	0.971	0.960	0.969	V_{12}	0.019	0.043	0.019		0.010	0.036	0.012
M_{15}	V_9	0.019	0.049	0.022	V_{10}	0.167	0.179	0.161		0.814	0.812	0.817
M_{16}		0.186	0.214	0.192	V_9	0.167	0.186	0.161	V_{11}	0.648	0.649	0.647
M_1	$V_1 V_2$	0.000	0.009	0.000	$V_2 V_3$	0.000	0.001	0.000	$V_3 V_1$	0.000	0.016	0.000
M_2	$V_8 V_2$		0.002	0.000	$V_2 V_5$		0.001	0.000	$V_5 V_8$		0.022	0.000
M_3	$V_1 V_7$		0.009	0.000	$V_7 V_4$		0.007	0.000	$V_4 V_1$		0.008	0.000
M_4	$V_6 V_3$		0.006	0.001	$V_3 V_9$		0.018	0.001	$V_9 V_6$		0.004	0.000
M_5			0.014	0.000	$V_4 V_{10}$		0.009	0.000	$V_{10} V_4$		0.001	0.000
M_6			0.001	0.000	$V_4 V_{13}$		0.007	0.000	$V_{13} V_4$		0.016	0.000
M_7	$V_5 V_{11}$		0.001	0.000			0.009	0.000	$V_{11} V_5$		0.016	0.000
M_8	$V_5 V_{13}$		0.002	0.000			0.008	0.000	$V_{13} V_5$		0.014	0.000
M_9	$V_6 V_{12}$		0.005	0.000			0.017	0.000	$V_{12} V_6$		0.002	0.000
M_{10}	$V_6 V_{13}$		0.005	0.000	$V_{13} V_6$		0.014	0.000			0.005	0.000
M_{11}			0.001	0.000	$V_7 V_{11}$		0.011	0.002	$V_{11} V_7$		0.014	0.000
M_{12}	$V_{12} V_7$		0.002	0.000	$V_7 V_{12}$		0.006	0.000			0.014	0.000
M_{13}	$V_8 V_{10}$		0.024	0.000			0.001	0.000	$V_{10} V_8$		0.001	0.000
M_{14}	$V_8 V_{12}$		0.025	0.001	$V_{12} V_8$		0.001	0.000			0.001	0.000
M_{15}	$V_9 V_{10}$		0.001	0.000	$V_{10} V_9$		0.005	0.001			0.020	0.000
M_{16}			0.004	0.000	$V_9 V_{11}$		0.005	0.000	$V_{11} V_9$		0.018	0.001
		Theory			Raw			Correct				
$\langle\chi_4\rangle$		1.333			1.227 ± 0.008			1.345 ± 0.008				
$\langle\chi_{13}\rangle$		27.667			28.016 ± 0.179			27.593 ± 0.166				

Table B.8: ψ_7

	$P_{ 1\rangle}$				$P_{ 2\rangle}$				$P_{ 3\rangle}$			
	Basis	Theory	Raw	Correct	Basis	Theory	Raw	Correct	Basis	Theory	Raw	Correct
M_1	V_1	0.553	0.559	0.558	V_2	0.085	0.108	0.083	V_3	0.362	0.368	0.359
M_2	V_8	0.010	0.037	0.017	V_2	0.085	0.103	0.087	V_5	0.905	0.886	0.897
M_3	V_1	0.553	0.564	0.562	V_7	0.048	0.078	0.050	V_4	0.399	0.395	0.388
M_4	V_6	0.536	0.536	0.535	V_3	0.362	0.362	0.353	V_9	0.102	0.136	0.112
M_5		0.945	0.930	0.938	V_4	0.048	0.076	0.054	V_{10}	0.008	0.033	0.008
M_6		0.059	0.091	0.067	V_4	0.048	0.079	0.054	V_{13}	0.894	0.873	0.879
M_7	V_5	0.010	0.038	0.016		0.620	0.608	0.612	V_{11}	0.369	0.375	0.372
M_8	V_5	0.010	0.042	0.011		0.096	0.127	0.103	V_{13}	0.894	0.882	0.886
M_9	V_6	0.102	0.131	0.105		0.835	0.830	0.832	V_{12}	0.063	0.091	0.063
M_{10}	V_6	0.102	0.122	0.105	V_{13}	0.894	0.868	0.878		0.005	0.039	0.017
M_{11}		0.231	0.247	0.230	V_7	0.399	0.405	0.397	V_{11}	0.369	0.382	0.373
M_{12}	V_{12}	0.063	0.086	0.064	V_7	0.399	0.397	0.392		0.538	0.543	0.544
M_{13}	V_8	0.905	0.892	0.899		0.088	0.113	0.092	V_{10}	0.008	0.036	0.009
M_{14}	V_8	0.905	0.890	0.898	V_{12}	0.063	0.085	0.063		0.033	0.063	0.040
M_{15}	V_9	0.008	0.041	0.002	V_{10}	0.536	0.547	0.542		0.456	0.464	0.456
M_{16}		0.094	0.118	0.095	V_9	0.536	0.532	0.531	V_{11}	0.369	0.380	0.373
M_1	$V_1 V_2$	0.000	0.014	0.000	$V_2 V_3$	0.000	0.004	0.001	$V_3 V_1$	0.000	0.007	0.000
M_2	$V_8 V_2$		0.001	0.000	$V_2 V_5$		0.003	0.000	$V_5 V_8$		0.018	0.000
M_3	$V_1 V_7$		0.014	0.000	$V_7 V_4$		0.003	0.000	$V_4 V_1$		0.009	0.000
M_4	$V_6 V_3$		0.013	0.000	$V_3 V_9$		0.010	0.001	$V_9 V_6$		0.002	0.000
M_5			0.021	0.000	$V_4 V_{10}$		0.002	0.000	$V_{10} V_4$		0.001	0.000
M_6			0.003	0.000	$V_4 V_{13}$		0.003	0.000	$V_{13} V_4$		0.020	0.000
M_7	$V_5 V_{11}$		0.001	0.000			0.015	0.000	$V_{11} V_5$		0.011	0.002
M_8	$V_5 V_{13}$		0.001	0.000			0.003	0.000	$V_{13} V_5$		0.022	0.000
M_9	$V_6 V_{12}$		0.003	0.000			0.018	0.000	$V_{12} V_6$		0.003	0.001
M_{10}	$V_6 V_{13}$		0.002	0.000	$V_{13} V_6$		0.019	0.000			0.001	0.000
M_{11}			0.006	0.000	$V_7 V_{11}$		0.010	0.000	$V_{11} V_7$		0.009	0.000
M_{12}	$V_{12} V_7$		0.002	0.000	$V_7 V_{12}$		0.009	0.000			0.014	0.001
M_{13}	$V_8 V_{10}$		0.020	0.000			0.003	0.000	$V_{10} V_8$		0.002	0.000
M_{14}	$V_8 V_{12}$		0.021	0.000	$V_{12} V_8$		0.002	0.000			0.002	0.000
M_{15}	$V_9 V_{10}$		0.002	0.000	$V_{10} V_9$		0.011	0.000			0.011	0.000
M_{16}			0.004	0.001	$V_9 V_{11}$		0.014	0.000	$V_{11} V_9$		0.007	0.000
		Theory	Raw				Correct					
$\langle\chi_4\rangle$		1.333	1.244 ± 0.008				1.354 ± 0.007					
$\langle\chi_{13}\rangle$		27.667	27.514 ± 0.179				27.577 ± 0.168					

Table B.9: ψ_8

	$P_{ 1\rangle}$				$P_{ 2\rangle}$				$P_{ 3\rangle}$			
	Basis	Theory	Raw	Correct	Basis	Theory	Raw	Correct	Basis	Theory	Raw	Correct
M_1	V_1	0.500	0.521	0.510	V_2	0.500	0.501	0.490	V_3	0.000	0.025	0.000
M_2	V_8	0.250	0.267	0.253	V_2	0.500	0.507	0.505	V_5	0.250	0.256	0.242
M_3	V_1	0.500	0.512	0.510	V_7	0.250	0.253	0.239	V_4	0.250	0.265	0.251
M_4	V_6	0.500	0.483	0.475	V_3	0.000	0.026	0.000	V_9	0.500	0.532	0.525
M_5		0.417	0.410	0.403	V_4	0.250	0.255	0.239	V_{10}	0.333	0.368	0.358
M_6		0.417	0.450	0.440	V_4	0.250	0.261	0.241	V_{13}	0.333	0.333	0.318
M_7	V_5	0.250	0.274	0.256		0.417	0.405	0.394	V_{11}	0.333	0.363	0.350
M_8	V_5	0.250	0.266	0.252		0.417	0.431	0.426	V_{13}	0.333	0.332	0.322
M_9	V_6	0.500	0.513	0.514		0.167	0.184	0.169	V_{12}	0.333	0.325	0.317
M_{10}	V_6	0.500	0.529	0.523	V_{13}	0.333	0.337	0.322		0.167	0.181	0.155
M_{11}		0.417	0.415	0.408	V_7	0.250	0.264	0.250	V_{11}	0.333	0.351	0.342
M_{12}	V_{12}	0.333	0.335	0.318	V_7	0.250	0.276	0.255		0.417	0.439	0.427
M_{13}	V_8	0.250	0.276	0.255		0.417	0.411	0.399	V_{10}	0.333	0.360	0.346
M_{14}	V_8	0.250	0.266	0.251	V_{12}	0.333	0.323	0.311		0.417	0.444	0.438
M_{15}	V_9	0.333	0.343	0.336	V_{10}	0.500	0.485	0.484		0.167	0.196	0.180
M_{16}		0.167	0.181	0.154	V_9	0.500	0.509	0.502	V_{11}	0.333	0.359	0.345
M_1	$V_1 V_2$	0.000	0.011	0.000	$V_2 V_3$	0.000	0.011	0.000	$V_3 V_1$	0.000	0.001	0.000
M_2	$V_8 V_2$		0.007	0.000	$V_2 V_5$		0.015	0.002	$V_5 V_8$		0.006	0.000
M_3	$V_1 V_7$		0.013	0.000	$V_7 V_4$		0.007	0.000	$V_4 V_1$		0.007	0.000
M_4	$V_6 V_3$		0.010	0.000	$V_3 V_9$		0.001	0.000	$V_9 V_6$		0.012	0.000
M_5			0.010	0.000	$V_4 V_{10}$		0.008	0.001	$V_{10} V_4$		0.009	0.000
M_6			0.010	0.000	$V_4 V_{13}$		0.006	0.000	$V_{13} V_4$		0.007	0.000
M_7	$V_5 V_{11}$		0.007	0.000			0.009	0.000	$V_{11} V_5$		0.007	0.000
M_8	$V_5 V_{13}$		0.006	0.000			0.010	0.000	$V_{13} V_5$		0.008	0.000
M_9	$V_6 V_{12}$		0.011	0.000			0.006	0.001	$V_{12} V_6$		0.008	0.000
M_{10}	$V_6 V_{13}$		0.012	0.000	$V_{13} V_6$		0.008	0.000			0.004	0.000
M_{11}			0.010	0.000	$V_7 V_{11}$		0.006	0.000	$V_{11} V_7$		0.011	0.002
M_{12}	$V_{12} V_7$		0.008	0.000	$V_7 V_{12}$		0.006	0.000			0.011	0.000
M_{13}	$V_8 V_{10}$		0.005	0.000			0.010	0.000	$V_{10} V_8$		0.009	0.000
M_{14}	$V_8 V_{12}$		0.007	0.000	$V_{12} V_8$		0.008	0.000			0.010	0.000
M_{15}	$V_9 V_{10}$		0.008	0.000	$V_{10} V_9$		0.011	0.000			0.005	0.000
M_{16}			0.006	0.001	$V_9 V_{11}$		0.012	0.000	$V_{11} V_9$		0.008	0.000
		Theory			Raw			Correct				
$\langle\chi_4\rangle$		1.333			1.247 ± 0.011			1.344 ± 0.011				
$\langle\chi_{13}\rangle$		27.667			27.669 ± 0.214			27.652 ± 0.206				

Table B.10: ψ_9

	$P_{ 1\rangle}$				$P_{ 2\rangle}$				$P_{ 3\rangle}$			
	Basis	Theory	Raw	Correct	Basis	Theory	Raw	Correct	Basis	Theory	Raw	Correct
M_1	V_1	0.500	0.532	0.532	V_2	0.500	0.430	0.427	V_3	0.000	0.062	0.041
M_2	V_8	0.250	0.300	0.288	V_2	0.500	0.434	0.428	V_5	0.250	0.294	0.283
M_3	V_1	0.500	0.528	0.527	V_7	0.250	0.236	0.224	V_4	0.250	0.259	0.248
M_4	V_6	0.500	0.487	0.482	V_3	0.000	0.066	0.040	V_9	0.500	0.483	0.478
M_5		0.417	0.440	0.443	V_4	0.250	0.226	0.224	V_{10}	0.333	0.332	0.333
M_6		0.417	0.438	0.432	V_4	0.250	0.230	0.215	V_{13}	0.333	0.363	0.354
M_7	V_5	0.250	0.290	0.280		0.417	0.374	0.368	V_{11}	0.333	0.358	0.352
M_8	V_5	0.250	0.285	0.275		0.417	0.378	0.372	V_{13}	0.333	0.359	0.352
M_9	V_6	0.500	0.465	0.468		0.167	0.235	0.230	V_{12}	0.333	0.305	0.302
M_{10}	V_6	0.500	0.462	0.460	V_{13}	0.333	0.346	0.341		0.167	0.211	0.199
M_{11}		0.417	0.427	0.422	V_7	0.250	0.239	0.226	V_{11}	0.333	0.359	0.352
M_{12}	V_{12}	0.333	0.358	0.341	V_7	0.250	0.245	0.221		0.417	0.452	0.439
M_{13}	V_8	0.250	0.335	0.337		0.417	0.342	0.344	V_{10}	0.333	0.318	0.319
M_{14}	V_8	0.250	0.351	0.341	V_{12}	0.333	0.311	0.299		0.417	0.370	0.361
M_{15}	V_9	0.333	0.321	0.310	V_{10}	0.500	0.467	0.462		0.167	0.244	0.229
M_{16}		0.167	0.190	0.184	V_9	0.500	0.447	0.449	V_{11}	0.333	0.366	0.366
M_1	$V_1 V_2$	0.000	0.014	0.003	$V_2 V_3$	0.000	0.010	0.002	$V_3 V_1$	0.000	0.001	0.000
M_2	$V_8 V_2$		0.007	0.001	$V_2 V_5$		0.010	0.001	$V_5 V_8$		0.005	0.000
M_3	$V_1 V_7$		0.012	0.002	$V_7 V_4$		0.004	0.000	$V_4 V_1$		0.005	0.000
M_4	$V_6 V_3$		0.010	0.000	$V_3 V_9$		0.003	0.001	$V_9 V_6$		0.009	0.000
M_5			0.009	0.000	$V_4 V_{10}$		0.007	0.003	$V_{10} V_4$		0.008	0.001
M_6			0.009	0.000	$V_4 V_{13}$		0.006	0.001	$V_{13} V_4$		0.008	0.001
M_7	$V_5 V_{11}$		0.006	0.000			0.007	0.000	$V_{11} V_5$		0.006	0.000
M_8	$V_5 V_{13}$		0.005	0.000			0.008	0.000	$V_{13} V_5$		0.007	0.000
M_9	$V_6 V_{12}$		0.009	0.000			0.005	0.000	$V_{12} V_6$		0.007	0.000
M_{10}	$V_6 V_{13}$		0.010	0.001	$V_{13} V_6$		0.005	0.000			0.003	0.000
M_{11}			0.010	0.002	$V_7 V_{11}$		0.006	0.001	$V_{11} V_7$		0.008	0.000
M_{12}	$V_{12} V_7$		0.008	0.001	$V_7 V_{12}$		0.006	0.001			0.006	0.000
M_{13}	$V_8 V_{10}$		0.006	0.000			0.007	0.000	$V_{10} V_8$		0.008	0.001
M_{14}	$V_8 V_{12}$		0.011	0.004	$V_{12} V_8$		0.007	0.001			0.007	0.000
M_{15}	$V_9 V_{10}$		0.007	0.001	$V_{10} V_9$		0.010	0.001			0.004	0.000
M_{16}			0.004	0.000	$V_9 V_{11}$		0.009	0.000	$V_{11} V_9$		0.009	0.002
		Theory	Raw				Correct					
$\langle \chi_4 \rangle$		1.333	1.268 ± 0.011				1.320 ± 0.011					
$\langle \chi_{13} \rangle$		27.667	27.049 ± 0.216				27.371 ± 0.210					

Table B.11: ρ_{10}

	$P_{ 1\rangle}$				$P_{ 2\rangle}$				$P_{ 3\rangle}$			
	Basis	Theory	Raw	Correct	Basis	Theory	Raw	Correct	Basis	Theory	Raw	Correct
M_1	V_1	0.333	0.357	0.340	V_2	0.333	0.301	0.281	V_3	0.333	0.393	0.379
M_2	V_8	0.000	0.106	0.088	V_2	0.333	0.289	0.282	V_5	0.667	0.623	0.629
M_3	V_1	0.333	0.346	0.336	V_7	0.333	0.341	0.330	V_4	0.333	0.346	0.335
M_4	V_6	0.333	0.324	0.305	V_3	0.333	0.400	0.386	V_9	0.333	0.327	0.309
M_5		0.556	0.509	0.504	V_4	0.333	0.348	0.335	V_{10}	0.111	0.186	0.161
M_6		0.111	0.181	0.161	V_4	0.333	0.343	0.334	V_{13}	0.556	0.507	0.505
M_7	V_5	0.000	0.114	0.085		0.444	0.412	0.405	V_{11}	0.556	0.513	0.510
M_8	V_5	0.000	0.121	0.097		0.444	0.403	0.397	V_{13}	0.556	0.506	0.505
M_9	V_6	0.333	0.319	0.311		0.556	0.527	0.529	V_{12}	0.111	0.177	0.160
M_{10}	V_6	0.333	0.335	0.310	V_{13}	0.556	0.542	0.529		0.111	0.200	0.162
M_{11}		0.111	0.183	0.155	V_7	0.333	0.346	0.331	V_{11}	0.556	0.521	0.514
M_{12}	V_{12}	0.111	0.174	0.152	V_7	0.333	0.350	0.340		0.556	0.510	0.508
M_{13}	V_8	0.667	0.602	0.606		0.222	0.240	0.226	V_{10}	0.111	0.185	0.168
M_{14}	V_8	0.667	0.609	0.610	V_{12}	0.111	0.188	0.168		0.222	0.238	0.222
M_{15}	V_9	0.111	0.195	0.173	V_{10}	0.333	0.338	0.325		0.556	0.506	0.502
M_{16}		0.111	0.206	0.196	V_9	0.333	0.329	0.325	V_{11}	0.556	0.477	0.479
M_1	$V_1 V_2$	0.000	0.008	0.000	$V_2 V_3$	0.000	0.008	0.000	$V_3 V_1$	0.000	0.010	0.000
M_2	$V_8 V_2$		0.003	0.000	$V_2 V_5$		0.008	0.000	$V_5 V_8$		0.019	0.001
M_3	$V_1 V_7$		0.011	0.001	$V_7 V_4$		0.008	0.000	$V_4 V_1$		0.010	0.000
M_4	$V_6 V_3$		0.010	0.000	$V_3 V_9$		0.010	0.000	$V_9 V_6$		0.010	0.001
M_5			0.016	0.001	$V_4 V_{10}$		0.010	0.000	$V_{10} V_4$		0.005	0.000
M_6			0.006	0.001	$V_4 V_{13}$		0.008	0.000	$V_{13} V_4$		0.014	0.000
M_7	$V_5 V_{11}$		0.003	0.000			0.012	0.001	$V_{11} V_5$		0.015	0.000
M_8	$V_5 V_{13}$		0.004	0.000			0.013	0.001	$V_{13} V_5$		0.016	0.001
M_9	$V_6 V_{12}$		0.010	0.001			0.015	0.000	$V_{12} V_6$		0.005	0.000
M_{10}	$V_6 V_{13}$		0.010	0.000	$V_{13} V_6$		0.057	0.041			0.006	0.000
M_{11}			0.006	0.000	$V_7 V_{11}$		0.010	0.000	$V_{11} V_7$		0.014	0.000
M_{12}	$V_{12} V_7$		0.005	0.000	$V_7 V_{12}$		0.010	0.000			0.013	0.000
M_{13}	$V_8 V_{10}$		0.017	0.000			0.008	0.001	$V_{10} V_8$		0.005	0.000
M_{14}	$V_8 V_{12}$		0.017	0.000	$V_{12} V_8$		0.006	0.000			0.008	0.001
M_{15}	$V_9 V_{10}$		0.006	0.000	$V_{10} V_9$		0.010	0.000			0.014	0.000
M_{16}			0.005	0.000	$V_9 V_{11}$		0.011	0.001	$V_{11} V_9$		0.015	0.001
		Theory			Raw			Correct				
$\langle \chi_4 \rangle$		1.333			1.220 \pm 0.010			1.317 \pm 0.010				
$\langle \chi_{13} \rangle$		27.667			27.351 \pm 0.216			27.689 \pm 0.207				

Table B.12: ρ_{11}

	$P_{ 1\rangle}$				$P_{ 2\rangle}$				$P_{ 3\rangle}$			
	Basis	Theory	Raw	Correct	Basis	Theory	Raw	Correct	Basis	Theory	Raw	Correct
M_1	V_1	0.333	0.340	0.334	V_2	0.333	0.345	0.338	V_3	0.333	0.335	0.328
M_2	V_8	0.333	0.340	0.338	V_2	0.333	0.337	0.336	V_5	0.333	0.328	0.326
M_3	V_1	0.333	0.341	0.340	V_7	0.333	0.328	0.326	V_4	0.333	0.335	0.334
M_4	V_6	0.333	0.348	0.343	V_3	0.333	0.321	0.316	V_9	0.333	0.346	0.341
M_5		0.333	0.346	0.338	V_4	0.333	0.328	0.319	V_{10}	0.333	0.351	0.343
M_6		0.333	0.347	0.340	V_4	0.333	0.331	0.323	V_{13}	0.333	0.344	0.337
M_7	V_5	0.333	0.342	0.333		0.333	0.343	0.333	V_{11}	0.333	0.343	0.334
M_8	V_5	0.333	0.353	0.347		0.333	0.344	0.337	V_{13}	0.333	0.324	0.316
M_9	V_6	0.333	0.356	0.347		0.333	0.331	0.322	V_{12}	0.333	0.340	0.331
M_{10}	V_6	0.333	0.370	0.356	V_{13}	0.333	0.333	0.318		0.333	0.341	0.326
M_{11}		0.333	0.338	0.328	V_7	0.333	0.338	0.328	V_{11}	0.333	0.352	0.344
M_{12}	V_{12}	0.333	0.323	0.319	V_7	0.333	0.330	0.326		0.333	0.358	0.355
M_{13}	V_8	0.333	0.335	0.332		0.333	0.327	0.323	V_{10}	0.333	0.348	0.345
M_{14}	V_8	0.333	0.339	0.332	V_{12}	0.333	0.330	0.322		0.333	0.353	0.346
M_{15}	V_9	0.333	0.357	0.350	V_{10}	0.333	0.323	0.314		0.333	0.344	0.336
M_{16}		0.333	0.335	0.328	V_9	0.333	0.333	0.326	V_{11}	0.333	0.352	0.346
M_1	$V_1 V_2$	0.000	0.006	0.000	$V_2 V_3$	0.000	0.008	0.000	$V_3 V_1$	0.000	0.008	0.000
M_2	$V_8 V_2$		0.008	0.001	$V_2 V_5$		0.006	0.000	$V_5 V_8$		0.007	0.000
M_3	$V_1 V_7$		0.008	0.000	$V_7 V_4$		0.008	0.000	$V_4 V_1$		0.009	0.002
M_4	$V_6 V_3$		0.008	0.000	$V_3 V_9$		0.006	0.000	$V_9 V_6$		0.009	0.001
M_5			0.008	0.000	$V_4 V_{10}$		0.006	0.000	$V_{10} V_4$		0.006	0.000
M_6			0.009	0.001	$V_4 V_{13}$		0.007	0.000	$V_{13} V_4$		0.007	0.000
M_7	$V_5 V_{11}$		0.008	0.000			0.008	0.000	$V_{11} V_5$		0.008	0.000
M_8	$V_5 V_{13}$		0.009	0.001			0.008	0.001	$V_{13} V_5$		0.009	0.002
M_9	$V_6 V_{12}$		0.008	0.000			0.010	0.003	$V_{12} V_6$		0.007	0.000
M_{10}	$V_6 V_{13}$		0.010	0.002	$V_{13} V_6$		0.008	0.001			0.009	0.001
M_{11}			0.008	0.001	$V_7 V_{11}$		0.010	0.003	$V_{11} V_7$		0.010	0.002
M_{12}	$V_{12} V_7$		0.009	0.002	$V_7 V_{12}$		0.008	0.001			0.007	0.000
M_{13}	$V_8 V_{10}$		0.007	0.000			0.008	0.001	$V_{10} V_8$		0.010	0.002
M_{14}	$V_8 V_{12}$		0.009	0.002	$V_{12} V_8$		0.007	0.000			0.009	0.001
M_{15}	$V_9 V_{10}$		0.009	0.001	$V_{10} V_9$		0.008	0.000			0.007	0.000
M_{16}			0.009	0.002	$V_9 V_{11}$		0.010	0.003	$V_{11} V_9$		0.011	0.003
		Theory			Raw			Correct				
$\langle\chi_4\rangle$		1.333			1.268 ± 0.011			1.331 ± 0.011				
$\langle\chi_{13}\rangle$		27.667			26.506 ± 0.223			27.463 ± 0.220				

Table B.13: ρ_{12}

Appendix C

Ququad Operations

In our $^{171}\text{Yb}^+$ ion system, we use the microwaves for the transitions between $|1\rangle$ and $|2\rangle, |3\rangle, |4\rangle$ levels. We use a microwave Raman scheme similar to the widely used Raman laser scheme for the transitions between $|2\rangle$ to $|3\rangle$ and $|3\rangle$ to $|4\rangle$ transitions. We cannot apply a radio frequency for the operations of these transitions, since the energy gap between $|2\rangle \leftrightarrow |3\rangle$ and $|3\rangle \leftrightarrow |4\rangle$ is very close, which is $(2\pi)31$ kHz for our experimental condition. As shown in Fig. 1 of the main text, 6 different frequencies of microwaves are combined and simultaneously applied to the trap. For the control of 6 microwaves, we use a PCI-board arbitrary waveform generator (AWG) with 1 GHz sampling rate, which is mixed with a 12442.8213 MHz microwave. The AWG generates the signal of 6 frequencies from 186 ~ 214 MHz.

The system is described by the Hamiltonian $\hat{H} = \hat{H}_A + \hat{H}_{AL}$, with atomic part \hat{H}_A being

$$\hat{H}_A = (\hbar\omega_{\text{hf}} - \hbar\omega_z) |2\rangle \langle 2| + (\hbar\omega_{\text{hf}} + \omega_q) |3\rangle \langle 3| + (\hbar\omega_{\text{hf}} + \hbar\omega_z) |4\rangle \langle 4|, \quad (\text{C.0.1})$$

and the interaction part \hat{H}_{AL} being

$$\hat{H}_{AL}(t) = \sum_{n=1}^6 \sum_{j=2}^4 \hbar \Omega_{1j}^{(n)} \cos(\omega_n t + \phi_n) \hat{\sigma}_x^{(j)}, \quad (\text{C.0.2})$$

respectively. We set the 6 frequencies in the microwave as follows,

$$\begin{aligned} \omega_1 &= \omega_{\text{hf}} - \omega_z - \delta_1, & \omega_2 &= \omega_{\text{hf}} + \omega_z - \delta_2, \\ \omega_3 &= \omega_{\text{hf}} - \omega_z - \Delta, & \omega_4 &= \omega_{\text{hf}} + \omega_q - \Delta - \delta_3, \\ \omega_5 &= \omega_{\text{hf}} + \omega_q + \Delta, & \omega_6 &= \omega_{\text{hf}} + \omega_z + \Delta - \delta_4, \end{aligned} \quad (\text{C.0.3})$$

where Δ is the detuning for the stimulated Raman transitions and δ_i are the frequency shifts used to compensate the AC Stark effect. Using the method in Ref. [94], we obtain the effective Hamiltonian $\hat{\mathcal{H}}_{\text{eff}} = \hat{\mathcal{H}}_{\text{st}} + \hat{\mathcal{H}}_{\text{cp}}$ in the interaction picture defined

by \hat{H}_A , where $\hat{\mathcal{H}}_{\text{st}}$ includes all of the AC Stark shifts,

$$\begin{aligned}
\hat{\mathcal{H}}_{\text{st}} &= \frac{\hbar \left(\Omega_{13}^{(1)}\right)^2}{4(\omega_z + \omega_q + \delta_1)} (|3\rangle\langle 3| - |1\rangle\langle 1|) + \frac{\hbar \left(\Omega_{14}^{(1)}\right)^2}{4(2\omega_z + \delta_1)} (|4\rangle\langle 4| - |1\rangle\langle 1|) \\
&\quad - \frac{\hbar \left(\Omega_{12}^{(2)}\right)^2}{4(2\omega_z - \delta_2)} (|2\rangle\langle 2| - |1\rangle\langle 1|) - \frac{\hbar \left(\Omega_{13}^{(2)}\right)^2}{4(\omega_z - \omega_q - \delta_2)} (|3\rangle\langle 3| - |1\rangle\langle 1|) \\
&\quad + \frac{\hbar \left(\Omega_{12}^{(3)}\right)^2}{4\Delta} (|2\rangle\langle 2| - |1\rangle\langle 1|) + \frac{\hbar \left(\Omega_{13}^{(3)}\right)^2}{4(\omega_z + \Delta + \omega_q)} (|3\rangle\langle 3| - |1\rangle\langle 1|) \\
&\quad + \frac{\hbar \left(\Omega_{14}^{(3)}\right)^2}{4(2\omega_z + \Delta)} (|4\rangle\langle 4| - |1\rangle\langle 1|) \\
&\quad - \frac{\hbar \left(\Omega_{12}^{(4)}\right)^2}{4(\omega_z - \Delta + \omega_q - \delta_3)} (|2\rangle\langle 2| - |1\rangle\langle 1|) + \frac{\hbar \left(\Omega_{13}^{(4)}\right)^2}{4(\Delta + \delta_3)} (|3\rangle\langle 3| - |1\rangle\langle 1|) \\
&\quad + \frac{\hbar \left(\Omega_{14}^{(4)}\right)^2}{4(\omega_z + \Delta - \omega_q + \delta_3)} (|4\rangle\langle 4| - |1\rangle\langle 1|) \\
&\quad - \frac{\hbar \left(\Omega_{12}^{(5)}\right)^2}{4(\omega_z + \Delta + \omega_q)} (|2\rangle\langle 2| - |1\rangle\langle 1|) - \frac{\hbar \left(\Omega_{13}^{(5)}\right)^2}{4\Delta} (|3\rangle\langle 3| - |1\rangle\langle 1|) \\
&\quad + \frac{\hbar \left(\Omega_{14}^{(5)}\right)^2}{4(\omega_z - \Delta - \omega_q)} (|4\rangle\langle 4| - |1\rangle\langle 1|) \\
&\quad - \frac{\hbar \left(\Omega_{12}^{(6)}\right)^2}{4(\omega_z + \Delta - \delta_4)} (|2\rangle\langle 2| - |1\rangle\langle 1|) - \frac{\hbar \left(\Omega_{13}^{(6)}\right)^2}{4(\omega_z + \Delta - \omega_q - \delta_4)} (|3\rangle\langle 3| - |1\rangle\langle 1|) \\
&\quad - \frac{\hbar \left(\Omega_{14}^{(6)}\right)^2}{4(\Delta - \delta_4)} (|4\rangle\langle 4| - |1\rangle\langle 1|) \\
&= \hbar\omega_{\text{st}}^{(1)}|1\rangle\langle 1| + \hbar\omega_{\text{st}}^{(2)}|2\rangle\langle 2| + \hbar\omega_{\text{st}}^{(3)}|3\rangle\langle 3| + \hbar\omega_{\text{st}}^{(4)}|4\rangle\langle 4|, \tag{C.0.4}
\end{aligned}$$

and $\hat{\mathcal{H}}_{\text{cp}}$ includes all coupling terms with frequencies much smaller than Δ ,

$$\begin{aligned} \hat{\mathcal{H}}_{\text{cp}} = & \frac{\hbar\tilde{\Omega}_{12}e^{-i\delta_1 t+i\phi_1}}{2}|1\rangle\langle 2| + \frac{\hbar\tilde{\Omega}_{14}e^{-i\delta_2 t+i\phi_2}}{2}|1\rangle\langle 4| \\ & + \frac{\hbar\tilde{\Omega}_{23}e^{-i\delta_3 t+i\phi_{43}}}{2}|2\rangle\langle 3| + \frac{\hbar\tilde{\Omega}_{34}e^{-i\delta_4 t+i\phi_{65}}}{2}|3\rangle\langle 4| \\ & + \frac{\hbar\Omega_{13}^{(3)}\Omega_{14}^{(4)}(\omega_z + \Delta)}{4[(\omega_z + \Delta)^2 - \omega_q^2]}|3\rangle\langle 4|e^{i(2\omega_q - \delta_3)t+i\phi_{43}} - \frac{\hbar\Omega_{12}^{(5)}\Omega_{13}^{(6)}(\omega_z + \Delta)}{4[(\omega_z + \Delta)^2 - \omega_q^2]}|2\rangle\langle 3|e^{-i(2\omega_q + \delta_4)t+i\phi_{65}} + \text{H.c.} \end{aligned} \quad (\text{C.0.5})$$

The effective couplings $\tilde{\Omega}_{23}$ and $\tilde{\Omega}_{34}$ are defined as follows,

$$\tilde{\Omega}_{23} = \frac{\Omega_{12}^{(3)}\Omega_{13}^{(4)}}{4} \left(\frac{1}{\Delta} + \frac{1}{\Delta + \delta_3} \right), \quad \tilde{\Omega}_{34} = -\frac{\Omega_{13}^{(5)}\Omega_{14}^{(6)}}{4} \left(\frac{1}{\Delta} + \frac{1}{\Delta - \delta_4} \right). \quad (\text{C.0.6})$$

Transferring into the second rotating frame defined by $\hat{\mathcal{H}}_{\text{st}}$, one obtains the following rotating frame Hamiltonian

$$\hat{\mathcal{H}} = e^{i\hat{\mathcal{H}}_{\text{st}}t/\hbar}\hat{\mathcal{H}}_{\text{cp}}(t)e^{-i\hat{\mathcal{H}}_{\text{st}}t/\hbar}. \quad (\text{C.0.7})$$

In order to make the final rotating frame Hamiltonian time-independent, the additional detunings should satisfy the following relations,

$$\begin{aligned} \delta_1 &= \omega_{\text{st}}^{(1)} - \omega_{\text{st}}^{(2)}, \\ \delta_2 &= \omega_{\text{st}}^{(1)} - \omega_{\text{st}}^{(4)}, \\ \delta_3 &= \omega_{\text{st}}^{(2)} - \omega_{\text{st}}^{(3)}, \\ \delta_4 &= \omega_{\text{st}}^{(3)} - \omega_{\text{st}}^{(4)}. \end{aligned} \quad (\text{C.0.8})$$

Comparing to the Majorana equation, one obtains the following relations

$$\begin{aligned}\frac{\hbar\tilde{\Omega}_{12}}{2}e^{i\phi_1} &= \frac{\hbar\tilde{\Omega}_{34}}{2}e^{i\phi_{65}} = cp, \\ \frac{\hbar\tilde{\Omega}_{14}}{2}e^{i\phi_2} &= -\frac{\hbar\tilde{\Omega}_{23}}{2}e^{i\phi_{43}} = imc^2.\end{aligned}\tag{C.0.9}$$

One problem in this scheme is the slowing down of operations. The Raman transition is 10 times slower than normal Rabi flopping, even with full power. But now we need 6 microwaves together. Decoherence occurs when the whole microwave duration is longer than $600\mu s$. This decoherence problem is later solved by applying a line trigger [95] to the pulse sequencer.

THIS PAGE INTENTIONALLY LEFT BLANK

Bibliography

- [1] International Technology Roadmap for Semiconductors. Overall technology roadmap characteristics. Technical report, International Technology Roadmap for Semiconductors, 2010.
- [2] Nielsen Michael and Chuang Isaac. Quantum Computation and Quantum Information. Cambridge University Press, 2000.
- [3] Rolf Drechsler and Robert Wille. From truth tables to programming languages: Progress in the design of reversible circuits. In Proceedings of the 2011 41st IEEE International Symposium on Multiple-Valued Logic, ISMVL '11, pages 78–85, Washington, DC, USA, 2011. IEEE Computer Society.
- [4] P. W. Shor. Algorithms for quantum computation: discrete logarithms and factoring. In S. Goldwasser, editor, IEEE Foundations of Computer Science (FOCS), pages 124–134, 1994.
- [5] S. Lloyd. Universal quantum simulators. Science, 273:1073, 1996.
- [6] D. Leibfried, R. Blatt, C. Monroe, and D. Wineland. Quantum dynamics of single trapped ions. Rev. Mod. Phys, 75:281, 2003.
- [7] A. Friedenauer, H. Schmitz, J. T. Glueckert, D. Porras, and T. Schaetz. Simulating a quantum magnet with trapped ions. Nat. Phys.cs, 4:757–761, 2008.
- [8] Feynman Richard P. Simulating physics with computers. International Journal of Theoretical Physics, 21(6-7):467–488, 1982.
- [9] Alain Aspect, Philippe Grangier, and Gérard Roger. Experimental realization of einstein-podolsky-rosen-bohm gedanken experiment: A new violation of bell’s inequalities. Phys. Rev. Lett., 49:91–94, 1982.

- [10] T. Monz, K. Kim, W. Hänsel, M. Riebe, A. S. Villar, P. Schindler, M. Chwalla, M. Hennrich, and R. Blatt. Realization of the quantum toffoli gate with trapped ions. Phys. Rev. Lett., 102:040501, 2009.
- [11] René Heilmann, Markus Gräfe, Stefan Nolte, and Alexander Szameit. Arbitrary photonic wave plate operations on chip: Realizing hadamard, pauli-x, and rotation gates for polarisation qubits. Scientific Reports, 4, 2013.
- [12] Jerry M. Chow, Jay M. Gambetta, A. D. Córcoles, Seth T. Merkel, John A. Smolin, Chad Rigetti, S. Poletto, George A. Keefe, Mary B. Rothwell, J. R. Rozen, Mark B. Ketchen, and M. Steffen. Universal quantum gate set approaching fault-tolerant thresholds with superconducting qubits. Phys. Rev. Lett., 109:060501, 2012.
- [13] B. P. Lanyon, C. Hempel, D. Nigg, M. Müller, R. Gerritsma, F. Zähringer, P. Schindler, J. T. Barreiro, M. Rambach, G. Kirchmair, M. Hennrich, P. Zoller, R. Blatt, and C. F. Roos. Universal digital quantum simulation with trapped ions. Science, 334(6052):57–61, 2011.
- [14] Seth Lloyd and Samuel L. Braunstein. Quantum computation over continuous variables. Phys. Rev. Lett., 82:1784–1787, 1999.
- [15] Peter W. Shor. Polynomial-time algorithms for prime factorization and discrete logarithms on a quantum computer. SIAM J. Comput., 26(5):1484–1509, 1997.
- [16] Chao Li, Wei Ruan, Long Zhang, and Xiang Zhang. Mathematical Theory of Computer Algebra System. Tsinghua University Press, 2010.
- [17] Kazumaro Aoki, Jens Franke, Arjen K. Lenstra, Emmanuel Thomé, Joppe W. Bos, Pierrick Gaudry, Alexander Kruppa, Peter L. Montgomery, Dag Arne Osvik, Herman te Riele, Andrey Timofeev, and Paul Zimmermann. Factorization of a 768-bit rsa modulus. In International Association for Cryptologic Research, 2010.
- [18] J. M. Landsberg and L. Manivel. Generalizations of strassen’s equations for secant varieties of segre varieties. arXiv:math/0601097, 2006.
- [19] Lov K. Grover. A fast quantum mechanical algorithm for database search. arXiv:quant-ph/9605043, 1996.

- [20] Alejandro Perdomo-Ortiz, Neil Dickson, Marshall Drew-Brook, Geordie Rose, and Alán Aspuru-Guzik. Finding low-energy conformations of lattice protein models by quantum annealing. Scientific Reports, 2, 2012.
- [21] Xiang Zhang, Yangchao Shen, Junhua Zhang, Jorge Casanova, Lucas Lamata, Enrique Solano, Man-Hong Yung, Jing-Ning Zhang, and Kihwan Kim. Time reversal and charge conjugation in an embedding quantum simulator. Nat. Comm., 6, 7917, 2015.
- [22] David P. DiVincenzo. The physical implementation of quantum computation. Fortschritte der Physik, 48(9-11):771–783, 2000.
- [23] T. Rosenband. Frequency ratio of al^+ and hg^+ single-ion optical clocks; metrology at the 17th decimal place. Science, 319:1808, 2008.
- [24] W. Paul. Electromagnetic traps for charged and neutral particles. Rev. Mod. Phys., 62(3):531–540, 1990.
- [25] LD Landau and EM Lifshitz. Mechanics, vol. 1. Course of theoretical physics, 1976.
- [26] J. D. Siversns, L. R. Simkins, S. Weidt, and W. K. Hensinger. On the application of radio frequency voltages to ion traps via helical resonators. arXiv:1106.5013, 106, 327, 2012.
- [27] Jeroen Koelemeij. Ultrahigh vacuum is an ion’s best friend, 2013.
- [28] Brian E King. Quantum state engineering and information processing with trapped ions. PhD thesis, University of Colorado, 1999.
- [29] Andrew T. Grier, Marko Cetina, Fedja Oručević, and Vladan Vuletić. Observation of cold collisions between trapped ions and trapped atoms. Phys. Rev. Lett., 102:223201, 2009.
- [30] R. D. Levine. Introduction to reactive molecular collisions, 2003.
- [31] Liana D Socaciu-Siebert. Reaction Kinetics and Femtosecond Dynamics of Small Gold Clusters. PhD thesis, Freie Universität Berlin, 2004.
- [32] Zhang Peng and Dalgarno Alexander. Static dipole polarizability of ytterbium†. The Journal of Physical Chemistry A, 111(49):12471–12476, 2007. PMID: 17915845.

- [33] DJ Wineland, C Monroe, WM Itano, D Leibfried, BE King, and DM Meekhof. Experimental issues in coherent quantum-state manipulation of trapped atomic ions. Journal of Research of the National Institute of Standards and Technology, 103(3), 1998.
- [34] Y. Waseda and M. Isshiki. Purification Process and Characterization of Ultra High Purity Metals: Application of Basic Science to Metallurgical Processing. Springer Series in Materials Processing. Springer Berlin Heidelberg, 2012.
- [35] Steven Matthew Olmschenk. Quantum teleportation between distant matter qubits. PhD thesis, The University of Michigan, 2009.
- [36] Andrew Chew. Doppler-free spectroscopy of iodine at 739nm. Bachelor thesis, University of Maryland, 2008.
- [37] D. J. Berkeland, J. D. Miller, J. C. Bergquist, W. M. Itano, and D. J. Wineland. Minimization of ion micromotion in a paul trap. Journal of Applied Physics, 83(10):5025–5033, 1998.
- [38] Alexander Braun. Addressing Single Yb₁hn⁺ Ions: A New Scheme for Quantum Computing in Linear Ion Traps;[Experimente Durchgeführt Am Institut Für Laser-Physik Der Universität Hamburg]. Cuvillier Verlag, 2007.
- [39] R.W.P. Drever, J.L. Hall, F.V. Kowalski, J. Hough, G.M. Ford, A.J. Munley, and H. Ward. Laser phase and frequency stabilization using an optical resonator. Applied Physics B, 31(2):97–105, 1983.
- [40] S. Olmschenk, K. C. Younge, D. L. Moehring, D. N. Matsukevich, P. Maunz, and C. Monroe. Manipulation and detection of a trapped yb⁺ hyperfine qubit. Phys. Rev. A, 76:052314, 2007.
- [41] DF James and Jonathan Jerke. Effective hamiltonian theory and its applications in quantum information. Canadian Journal of Physics, 85(6):625–632, 2007.
- [42] Susan M. Clark, Rajibul Islam, Wesley C. Campbell, Taeyoung Choi, Shantanu Debnath, Emily E. Edwards, Fields Brian, David Hayes, David Hucul, Ismail V. Inlek, and et al. Beat note stabilization of mode-locked lasers for quantum information processing. Optics Letters, 39(11):3238–3241, 2014.

- [43] C. Monroe, D.M. Meekhof, B.E. King, S.R. Jefferts, W.M. Itano, D.J. Wineland, and P. Gould. Resolved-sideband raman cooling of a bound atom to the 3d zero-point energy. Phys. Rev. Lett., 75:4011–4014, 1995.
- [44] Q. A. Turchette, Kielpinski, B. E. King, D. Leibfried, D. M. Meekhof, C. J. Myatt, M. A. Rowe, C. Sackett, C. S. Wood, W. M. Itano, C. Monroe, and D. J. Wineland. Heating of trapped ions from the quantum ground state. Phys. Rev. A, 61:063418, 2000.
- [45] Junhua Zhang. Developing a control system for quantum information processing with trapped ions. Bachelor thesis, Peking University, 2012.
- [46] J. S. Bell. On the problem of hidden variables in quantum mechanics. Rev. Mod. Phys., 38:447–452, 1966.
- [47] G. Kirchmair, F. Zähringer, R. Gerritsma, M. Kleinmann, O. Gühne, A. Cabello, R. Blatt, and C. F. Roos. State-independent experimental test of quantum contextuality. Nature, 460:494–497, 2009.
- [48] Radek Lapkiewicz, Peizhe Li, Christoph Schaeff, Nathan K. Langford, Sven Ramelow, Marcin Wieśniak, and Anton Zeilinger. Experimental non-classicality of an indivisible quantum system. Nature, 474:490–493, 2011.
- [49] C. Zu, Y.-X. Wang, D.-L. Deng, X.-Y. Chang, K. Liu, P.-Y. Hou, H.-X. Yang, and L.-M. Duan. State-independent experimental test of quantum contextuality in an indivisible system. Phys. Rev. Lett., 109:150401, 2012.
- [50] Xiang Zhang, Mark Um, Junhua Zhang, Shuoming An, Ye Wang, Dong-ling Deng, Chao Shen, Lu-Ming Duan, and Kihwan Kim. State-independent experimental test of quantum contextuality with a single trapped ion. Phys. Rev. Lett., 110:070401, 2013.
- [51] Sixia Yu and C. H. Oh. State-independent proof of kochen-specker theorem with 13 rays. Phys. Rev. Lett., 108:030402, 2012.
- [52] K. R. Brown, A. C. Wilson, Y. Colombe, C. Ospelkaus, A. M. Meier, E. Knill, D. Leibfried, and D. J. Wineland. Single-qubit-gate error below 10^{-4} in a trapped ion. Phys. Rev. A, 84:030303(R), 2011.
- [53] R. T. Thew, K. Nemoto, A. G. White, and W. J. Munro. Qudit quantumstate tomography. Phys. Rev. A, 66:012303, 2002.

- [54] Reinhold A Bertlmann and Philipp Krammer. Bloch vectors for qudits. Journal of Physics A: Mathematical and Theoretical, 41(23):235303, 2008.
- [55] Otfried Gühne, Matthias Kleinmann, Adán Cabello, Jan Ake Larsson, Gerhard Kirchmair, Florian Zähringer, Rene Gerritsma, and Christian F. Roos. Compatibility and noncontextuality for sequential measurements. Phys. Rev. A, 81:022121, 2010.
- [56] Mark Um, Xiang Zhang, Junhua Zhang, Ye Wang, Shen Yangchao, D. L Deng, Lu-Ming Duan, and Kihwan Kim. Experimental certification of random numbers via quantum contextuality. Scientific Reports, 3(1627), 2013.
- [57] Junhua Zhang, Jingning Zhang, Xiang Zhang, and Kihwan Kim. Realization of geometric landau-zyener-stückelberg interferometry. Phys. Rev. A, 89:013608, 2014.
- [58] J. Casanova, C. Sabin, J. Leon, I. L. Egusquiza, R. Gerritsma, C. F. Roos, J. J. Garcia-Ripoll, and E. Solano. Quantum simulation of the majorana equation and unphysical operations. Phys. Rev. X, 1:021018, 2011.
- [59] Zhang Jingfu, Yung Man-Hong, and Laflamme Raymond. Digital quantum simulation of the statistical mechanics of a frustrated magnet. Nat. Comm., 3:880, 2012.
- [60] M. Gu, Karoline Wiesner, E. Rieper, and V. Vedral. Quantum mechanics can reduce the complexity of classical models. Nat. Comm., 3(762), 2012.
- [61] Ch. Schneider, D. Porras, and T. Schaetz. Experimental quantum simulations of many-body physics with trapped ions. Rep. Prog. Phys., 75:024401, 2012.
- [62] J. Ignacio Cirac and Peter Zoller. Goals and opportunities in quantum simulation. Nat. Phys., 8:264–266, 2012.
- [63] I. M. Georgescu, S. Ashhab, and Franco Nori. Quantum simulation. Rev. Mod. Phys., 86:153–185, 2014.
- [64] Immanuel Bloch, Jean Dalibard, and Sylvain Nascimbéne. Quantum simulations with ultracold quantum gases. Nat. Phys., 8:267–276, 2012.
- [65] R. Blatt and C. F. Roos. Quantum simulations with trapped ions. Nat. Phys., 8:277–284, 2012.

- [66] Alán Aspuru-Guzik and Philip Walther. Photonic quantum simulators. Nat. Phys., 8:285–291, 2012.
- [67] Andrew A. Houck, Hakan E. Türeci, and Jens Koch. On-chip quantum simulation with superconducting circuits. Nat. Phys., 8:292–299, 2012.
- [68] E. P. Wigner. Group Theory and its Application to the Quantum Mechanics of Atomic Spectra. New York: Academic Press, 1959.
- [69] J. J. Sakurai. Advanced Quantum Mechanics. Addison-Wesley, Los Angeles, 1967.
- [70] J. J. Sakurai. Modern Quantum Mechanics. Addison Wesley Longman, 1993.
- [71] T. D. Lee and C. N. Yang. Question of parity conservation in weak interactions. Phys. Rev., 104:254–258, 1956.
- [72] K Kleinknecht. Cp violation and k decays. Annual Review of Nuclear Science, 26(1):1–50, 1976.
- [73] Michael H. Freedman, Alexei Kitaev, and Zhenghan Wang. Simulation of topological field theories by quantum computers. Commun. Math. Phys., 227:587–603, 2002.
- [74] L. Lamata, J. León, T. Schätz, and E. Solano. Dirac equation and quantum relativistic effects in a single trapped ion. Phys. Rev. Lett., 98:253005, 2007.
- [75] J. Casanova, L. Lamata, I. L. Egusquiza, R. Gerritsma, C. F. Roos, J. J. García-Ripoll, and E. Solano. Quantum simulation of quantum field theories in trapped ions. Phys. Rev. Lett., 107:260501, 2011.
- [76] Stephen P. Jordan, Keith S. M. Lee, and John Preskill. Quantum algorithms for quantum field theories. Science, 336:1130–1133, 2012.
- [77] P. Hauke, D. Marcos, M. Dalmonte, and P. Zoller. Quantum simulation of a lattice schwinger model in a chain of trapped ions. Phys. Rev. X, 3:041018, 2013.
- [78] DaWei Lu, Jacob D. Biamonte, Jun Li, Hang Li, Tomi H. Johnson, Ville Bergholm, Mauro Faccin, Zoltán Zimborás, Raymond Laflamme, Jonathan Baugh, and Seth Lloyd. Chiral quantum walks. arXiv:1405.6209, 2014.

- [79] R. Gerritsma, G. Kirchmair, F. Zahringer, E. Solano, R. Blatt, and C. F. Roos. Quantum simulation of the dirac equation. Nature, 463:68–71, 2010.
- [80] Felix Dreisow, Matthias Heinrich, Robert Keil, Andreas Tünnermann, Stefan Nolte, Stefano Longhi, and Alexander Szameit. Classical simulation of relativistic zitterbewegung in photonic lattices. Phys. Rev. Lett., 105:143902, 2010.
- [81] R. Gerritsma, B. P. Lanyon, F. Zahringer G. Kirchmair, C. Hempel, J. Casanova, J. J. Garcia-Ripoll, E. Solano, R. Blatt, and C. F. Roos. Quantum simulation of the klein paradox with trapped ions. Phys. Rev. Lett., 106:060503, 2011.
- [82] J. Casanova, C. Sabín, J. León, I. L. Egusquiza, R. Gerritsma, C. F. Roos, J. J. García Ripoll, and E. Solano. Quantum simulation of the majorana equation and unphysical operations. Phys. Rev. X, 1:021018, 2011.
- [83] R. Di Candia, B. Mejia, H. Castillo, J. S. Pedernales, J. Casanova, and E. Solano. Embedding quantum simulators for quantum computation of entanglement. Phys. Rev. Lett., 111:240502, 2013.
- [84] U. Alvarez-Rodriguez, J. Casanova, L. Lamata, and E. Solano. Quantum simulation of noncausal kinematic transformations. Phys. Rev. Lett., 111:090503, 2013.
- [85] J. S. Pedernales, R. Di Candia, P. Schindler, T. Monz, M. Hennrich, J. Casanova, and E. Solano. Entanglement measures in ion-trap quantum simulators without full tomography. Phys. Rev. A, 90:012327, 2014.
- [86] Ettore Majorana. Teoria simmetrica dellélettrone e del positrone. Il Nuovo Cimento, 14, 1937.
- [87] B. Thrall. The Dirac Equation. Springer-Verlag, Berlin, 1992.
- [88] B Pontecorvo. Mesonium and anti-mesonium. Sov.Phys.JETP, 6:429, 1957.
- [89] A H Castro Neto, F Guinea, N M R Peres, K S Novoselov, and A K Geim. The electronic properties of graphene. Rev. Mod. Phys., 81:109, 2009.
- [90] A Marini, Tr X Tran, S Roy, S Longhi, and F Biancalana. Optical analog of spontaneous symmetry breaking induced by tachyon condensation in amplifying plasmonic arrays. Phys. Rev. A, 89:023840, 2014.

- [91] Changsuk Noh, B. M. Rodríguez-Lara, and Dimitris G. Angelakis. Proposal for realization of the majorana equation in a tabletop experiment. Phys. Rev. A, 87:040102(R), 2013.
- [92] J. Keil, C. Noh, A. Rai, S. Stüzer, S. Nolte, D. G. Angelakis, and A. Szaemelt. Experimental simulation of charge conservation violation and majorana dynamics. arXiv: 1404.5444, 2014.
- [93] Xiang Zhang, Mark Um, Junhua Zhang, Shuoming An, Ye Wang, Dong-ling Deng, Chao Shen, Lu-Ming Duan, and Kihwan Kim. State-independent experimental test of quantum contextuality with a single trapped ion. Phys. Rev. Lett., 110:070401, 2013.
- [94] Daniel James and Jonathan Jerke. Effective hamiltonian theory and its applications in quantum information. arXiv:0706.1090, 2007.
- [95] A Smith, B E Anderson, S Chaudhury, and P S Jessen. Three-axis measurement and cancellation of background magnetic fields to less than 50 ug in a cold atom experiment. Journal of Physics B: Atomic, Molecular and Optical Physics, 44(20):205002, 2011.
- [96] R. N. Mohapatra and P. B. Pal. Massive Neutrinos in Physics and Astrophysics, Lecture Notes in Physics. World Scientific Publishing Co., Singapore, 2004.
- [97] L Lamata, J Casanova, I L Egusquiza, and E Solano. The nonrelativistic limit of the majorana equation and its simulation in trapped ions. Phys. Scr., T147:014017, 2012.
- [98] K. Kim, M.-S. Chang, S. Korenblit, R. Islam, E. E. Edwards, J. K. Freericks, G.-D. Lin, L.-M. Duan, and C. Monroe. Quantum simulation of frustrated ising spins with trapped ions. Nature, 465:590–593, 2010.
- [99] Xiang Zhang, Yangchao Shen, Junhua Zhang, Jorge Casanova, Lucas Lamata, Enrique Solano, Man-Hong Yung, Jing-Ning Zhang, and Kihwan Kim. Time reversal and charge conjugation in an embedding quantum simulator. Nat. Comm., 2015.
- [100] L. García-Álvarez, J. Casanova, A. Mezzacapo, I. L. Egusquiza, L. Lamata, G. Romero, and E. Solano. Fermion-fermion scattering in quantum field theory with superconducting circuits. Phys. Rev. Lett., 114:070502, 2015.

- [101] R. Barends, L. Lamata, J. Kelly, L. Garcia-Alvarez, A. G. Fowler, A. Megrant, E. Jeffrey, T. C. White, D. Sank, J. Y. Mutus, B. Campbell, Yu Chen, Z. Chen, B. Chiaro, A. Dunsworth, I.-C. Hoi, C. Neill, P. J. J. OMalley, C. Quintana, P. Roushan, A. Vainsencher, J. Wenner, E. Solano, and John M. Martinis. Digital quantum simulation of fermionic models with a superconducting circuit. Nat. Comm., 6, 2015.
- [102] Michael Edward Peskin and Daniel V. Schroeder. An introduction to quantum field theory. Advanced book program. Westview Press Reading (Mass.), Boulder (Colo.), 1995.